Simulation of time-periodic and topological tight-binding systems with plasmonic waveguide arrays

Dissertation
zur
Erlangung des Doktorgrades (Dr. rer. nat.)
der
Mathematisch-Naturwissenschaftlichen Fakultät
der
Rheinischen Friedrich-Wilhelms-Universität Bonn

von
Zlata Fedorova, geb. Cherpakova
aus
Moskau, Russland

Bonn, 2021

Angefertigt mit Genehmigung der Mathematisch-Naturwissenschaftlichen Fakultät der Rheinischen Friedrich-Wilhelms-Universität Bonn.

1. Gutachter:	Prof. Dr. Stefan Linden
2. Gutachter:	Prof. Dr. Johann Kroha
Tag der Promotion:	26.08.2022
Erscheinungsjahr:	2022

Abstract

Floquet engineering, the control by external time-periodic forcing, is a powerful tool to manipulate different quantum systems. The underlying principle is that driving a system periodically with frequency ω induces hybridization of the eigenstates of a static system separated in energy by a multiple of $\hbar\omega$. By choosing a proper driving scheme one can thus take an advantage of this hybridization to create new synthetically designed properties, that would be inaccessible in equilibrium.

In this thesis Floquet engineering is utilized to tailor topological and transport properties of surface plasmon polaritons propagating in arrays of coupled waveguides. Evanescently coupled waveguides is a widely used experimental platform to study various coherent quantum phenomena encountered in atomic and condensed matter physics. Such experiments are based on the mathematical analogy between the paraxial Helmholtz equation for the electromagnetic field propagating in arrays of coupled waveguides and the Schrödinger equation that describes temporal evolution of a single particle wavefunction in tight-binding atomic lattices. Within this quantum-optical analogy the time axis of a quantum system is directly mapped into the propagation distance of surface plasmon polaritons. Therefore, periodically modulating the waveguide geometry along the propagation distance enables us to mimic the effect of external time-periodic field.

Under the scope of this thesis we investigate three periodically-driven one-dimensional tight-binding systems that illuminate different applications of the Floquet engineering. In order to make predictions about the dynamics of each system we perform numerical calculations based on the Floquet theory. The obtained theoretical findings are used to design the plasmonic structures, which are then fabricated by negative-tone electron beam lithography. The propagation of surface plasmon polaritons in the fabricated samples is monitored by real- and Fourier space leakage radiation microscopy.

As the first system, we consider a one-dimensional prototype of a topological insulator described by the Su-Schriefer-Heeger model. This model supports two topologically distinct phases that, when interfaced, give rise to a topologically protected edge state localized at the boundary. This is the manifestation of the so-called bulk boundary correspondence principle. The question we address here is what happens with the topological edge state if the boundary between the two phases is subject to local time-periodic perturbations while the bulk is kept static?

In the second project we deal with the topological transport quantization that emerges in the slowly driven Rice-Mele model. This phenomenon, known as the Thouless pumping, breaks down at the non-adiabatic conditions, which is the major limitation for the experimental realization of this effect. The reason is that finite driving frequencies induce coupling between the forward and backward propagating Floquet states. As a result, the system becomes topologically trivial and the transport deviates from perfect quantization. We are aimed to show that using sufficiently strong time-periodic losses the Thouless pumping can be restored at an arbitrary large driving frequency.

Inspired by the previously obtained results, in the third part of this thesis we demonstrate another application of time-periodic losses. In contrast to the previous example where losses were applied

globally, here, they are confined only to the few lattice sites and serve as a directional filter for a Hamiltonian, i.e. lossless, quantum ratchet. Ratchet is a system where broken space and time inversion symmetry gives rise to a directional transport without a bias force. As a ratchet system we consider a periodically-driven Su-Schrieffer-Heeger model, which for certain resonant driving frequencies supports directional current once the relevant symmetries are broken by initial conditions. On the example of this system we want to show that properly chosen time-periodic losses can transmit the current in one direction but strongly suppress it in the opposite direction.

Contents

CHAPTER 1

Introduction

Time-periodic driving via external fields is a powerful technique for coherent control of various quantum systems. Also known as Floquet engineering, this method mathematically relies on the Floquet theory, the formalism developed to systematically analyse Hamiltonians with discrete translational invariance in time. The primary goal of the Floquet approach is to transform the time-periodic problem into a time-independent one that yields the general quasi-stationary solution. This allows for an intuitive way to understand the behaviour of a driven system and thereby enables to find a proper driving scheme to confer the desired properties on it. Floquet engineering finds ever-widening applications to tailor cold atoms in optical lattices [1, 2]. The range of use also includes solid state [3], photonic [4, 5] and acoustic [6] systems. By choosing appropriate driving scheme one can, for instance, control single-particle tunnelling [7], tune transport regimes from ballistic to localised [8], create artificial gauge fields [9], induce quantum phase transitions [10], pump charge [11], and tailor the transmission across the modulated region [12, 13]. Furthermore, using periodic driving one can change the topological properties of a system [14]. Remarkably, some driven systems exhibit topological phenomena without any static counterparts [15].

Topology is an emergent concept in solid state physics to classify states of matter that do not fit into the Landau's paradigm of spontaneous symmetry breaking. Although most phase transitions in nature can be explained in the framework of the Ginsburg-Landau theory, the discovery of the quantum Hall effect by K. von Klitzing has shown that this paradigm is not completely exhaustive [16]. The stepwise change of the Hall conductivity in strong magnetic field at low temperature was a principally new kind of phase transition that happened without spontaneous symmetry breaking. Another surprising observation was that the conductivity on each quantum Hall plateau turned out to be a universal quantity independent of smooth variations of Hamiltonian parameters and cannot be changed unless the system undergoes a phase transition. Later on it was recognized that this universality comes from the fact that some physical observable, e.g. the conductance, can be associated with a certain topological invariant and thus is robust against a homotopy of the Hamiltonian, i.e. protected by topology [17, 18]. Until now a great variety of topological materials and phases has been discovered including topological insulators [19], topological superconductors [20], Dirac or Weyl semimetals [21]. The common feature of these phases is that the topological properties of the bulk material have a strong influence on the character of the states at the boundary, the so-called bulk boundary correspondence principle. For instance, topological insulators, like ordinary insulators, have an insulating energy gap in the bulk but, in addition, support metallic boundary states whose energy lies within the band

gap. These states are unidirectional and do not suffer from a scattering by impurities which makes them particularly interesting for practical applications in quantum computing [22], spintronics [19], acoustics [23] and photonics [24].
In this thesis Floquet engineering is employed to tailor topological and transport properties in arrays of evanescently coupled plasmonic waveguides. Over the past decades arrays of coupled waveguides have become a well-established experimental platform used to study certain coherent quantum phenomena encountered in atomic and condensed matter physics [25–27]. The underlying principle is that the propagation of light or, in our case surface plasmon polaritons, in such arrays mathematically realizes the single-particle Schrödinger equation on a tight-binding lattice with the waveguide axis playing the role of time [26, 28, 29]. Uncomplicated experimental setting, precise control over the system parameters during sample fabrication, and the possibility of a direct visualization are the major advantages of such quantum simulators. A great variety of quantum-optical analogies have been already realized on the basis of coupled waveguides. Restricting ourselves to phenomena related to solid-state physics we mention Zener tunnelling [30], Anderson localization [31], Bloch oscillations [32], dynamic localization [33], and various topological phenomena [24]. Periodically modulating a waveguide geometry along the propagation distance enables to mimic the effect of external periodic driving making arrays of coupled waveguides an ideal playground for Floquet engineering [4, 5]. In the context of quantum simulations, plasmonic waveguides provide an additional benefit in comparison to the conventional optical waveguides that is rooted in the specific detection technique, the so-called leakage radiation microscopy. This method does not only allow to capture full wavepacket evolution in real space by a single camera snapshot but also gives access to the momentum-resolved spectrum in Fourier space [28, 29]. The latter is a particularly interesting feature in the view of Floquet engineering as it allows to directly image the quasienergy bands of an equivalent driven system.
In this work we combine real- and Fourier space leakage radiation microscopy to characterize a number of plasmonic analogues of the periodically-driven one-dimensional tight-binding lattices. Prior to the optical experiments the behaviour of the systems of interest is predicted by numerical calculations based on the Floquet theory. The plasmonic waveguide arrays are designed with an eye on the results of the theoretical analysis and fabricated by negative-tone grayscale electron beam lithography. This thesis includes three research projects that illuminate different applications of Floquet engineering.
In the first project we investigate the robustness of a topological edge state against local time-periodic perturbations in the otherwise static one-dimensional plasmonic topological insulator. It is known that the bulk-boundary correspondence principle and the ensuing topological protection are in general valid only in the case of static deformations [34, 35]. The reason is that in the static case the coupling of the edge state to the bulk states is energetically forbidden due to the presence of the band gap. Dynamic perturbations, in contrast, can cause hybridisation of the states and drastically change their character. The question we address here is how far the topological protection can be extended to the case of local time-periodic perturbations if the bulk is kept static, i.e. the topological properties of the bulk are unchanged.
In the second project, non-Hermitian Floquet engineering is introduced as a tool to restore topological transport quantization in fast Thouless pumps. Thouless pumping is a robust quantized current that emerges in slowly driven one-dimensional lattices as a consequence of a non-trivial topological invariant, the so-called Chern number. Being the temporal analogue of the integer quantum Hall effect [36], Thouless pumping has played a prominent role in the development of topology as a concept in condensed matter physics. Up to date it remains an issue of intense research activities, both

theoretical and experimental [37–40]. The fundamental problem for experimental applications of this effect is the adiabaticity requirement. At nonzero driving frequencies, unavoidable in experiments, the system becomes topologically trivial due to non-adiabatic coupling between different bands and, as a result, the particle transport deviates from perfect quantization [15, 39, 41]. To overcome this limitation we will employ time-periodic modulation of dissipation. There are many examples how losses profoundly influence the system dynamics. In addition to ubiquitous exponential decay, they may cause such peculiar phenomena as unidirectional robust transport [42], asymmetric transmission or reflection [43, 44], and non-Hermitian topological edge states associated with exceptional points [45–47]. Dissipation has been utilized to probe topological quantities [48, 49]. Another fascinating example is the so-called non-Hermitian shortcut to adiabaticity [50–52], which describes faster evolution of a wavefunction in a system with an additional time-dependent gain or loss than in its Hermitian counterpart. The key feature of this work is that the losses are modulated periodically in a way that they could suppress non-adiabatic effects and thereby restore topological pumping at fast driving frequencies. Our plasmonic experiments is a perfect platform to study the effect of periodic losses because they can be easily implemented by tailoring a waveguide geometry.

Finally, in the last project we will demonstrate another application of non-Hermitian Floquet engineering by constructing a direction-dependent filter for a non-adiabatic Hamiltonian quantum ratchet. Ratchets are systems that convert periodic drive into directed motion without a bias force by breaking of space- and time-reversal symmetry [53]. Introduced by Smoluchowski [54] and Feynman [55], ratchets represent a wide class of microscopic motors, which operate in classical as well as in quantum systems. In particular, the ratchet effect was observed in microbiological [56] and molecular motion [57], semiconductor [58] and superconductor [59] heterostructures, irradiated graphene [60], electron pumps [61], photonic setups [62, 63], and Bose-Einstein condensates [64]. The common limitation that share all non-adiabatic Hamiltonian, i.e. lossless, quantum ratchets is that their efficiency sensitively depends on the initial conditions [64–67]. It turns out that non-optimal initial conditions lead to unwanted excitation of eigenstates that move opposite to the net current thereby reducing the ratchet performance. In contrast, it is often desired to achieve maximal current without the initial state preparation. In order to relax strict initial state requirements we will use local time-periodic losses that are aimed to selectively absorb the states moving in one direction but transmit in the opposite direction. Remarkably, the local character of the applied losses prevents additional dissipation into the bulk.

Outline

This thesis is structured as follows. Chapter 2 introduces the essential theoretical concepts from condensed matter physics relevant for this work. It starts with some basic definitions that are followed by the derivation of the Schrödinger equation in the tight-binding approximation. Next, we outline the principles of the Floquet approach in treating time-periodic systems and, lastly, we give a brief introduction to the topic of topological phases of matter. Chapter 3 summarizes the basic theory behind our plasmonic experiments. After describing the general properties of surface plasmon polaritons, we discuss the relevant excitation, detection and guiding techniques. The ultimate result of this part is the derivation of the coupled mode equations which yield the connection between the wavepacket dynamics in arrays of coupled waveguides and the tight-binding model for crystaline solids. The experimental methods are described in Chapter 4. Having laid out the background for our results, we present our first quantum-optical analogy in Chapter 5. Here, we explore the limits of topological protection under local periodic driving in the otherwise static Su-Schreefer-Heeger model. Chapter 6 is aimed to demonstrate that topological pumping in the driven Rice-Mele model can be restored outside of the adiabatic limit by making use of time-periodic losses. In Chapter 7 a dynamic dissipative impurity is designed such that it works as a direction-dependent filter in a Hamiltonian quantum ratchet based on the periodically-driven Su-Schrieffer-Heeger model.

CHAPTER 2

Time-periodic and topological tight-binding systems

This chapter provides a self-contained introduction to the relevant theoretical concepts needed to describe the systems of interest for the present thesis. In Section 2.1 we begin with elementary notions of condensed matter physics and then derive the tight-binding Hamiltonian that describes the evolution of an electron wave function in one-dimensional solids. Section 2.2 focuses on periodically driven systems and outlines the basics of the Floquet theory. Finally, Section 2.3 briefly introduces the topic of topological phenomena occurring in condensed matter systems.

2.1 Tight-binding systems

2.1.1 Basic notions of condensed matter physics

The key feature of crystalline solids is the regular arrangement of the constituting atoms. A crystal can be viewed as a basis of one or several atoms that repeats itself after any discrete translation by a vector of the form

$$\mathbf{R} = \sum_{j}^{d} n_j \mathbf{a}_j, \tag{2.1}$$

with d being the number of dimension, $\mathbf{a}_j$ being a primitive lattice vector, and $n_j \in \mathbb{Z}$, where symbol $\mathbb{Z}$ denotes the set of integers. The Fourier transform of the real-space lattice (2.1) is called the reciprocal lattice whose points in the momentum space are located at

$$\mathbf{G} = \sum_{j}^{d} m_j \mathbf{b}_j, \tag{2.2}$$

where the vectors $\mathbf{b}_j$ satisfy $\mathbf{a}_i \cdot \mathbf{b}_j = 2\pi\delta_{ij}$ and $m_j \in \mathbb{Z}$. An electron inside a crystal finds itself in the periodic potential, consequently, its Hamiltonian is translation invariant:

$$\hat{H}(\mathbf{r} + \mathbf{R}) = \hat{H}(\mathbf{r}) \tag{2.3}$$

for any $\mathbf{R}$ given by Eq. (2.1). The Bloch's theorem tells us that there exist the eigenstates of $\hat{H}$ called the Bloch states that can be written in the form [95]:

$$|\psi_{\alpha,k}(\mathbf{r})\rangle = e^{i\mathbf{k}\cdot\mathbf{r}}|u_{\alpha,\mathbf{k}}(\mathbf{r})\rangle. \tag{2.4}$$

Here, the Bloch modes $|u_{\alpha,\mathbf{k}}(\mathbf{r}+\mathbf{R})\rangle = |u_{\alpha,\mathbf{k}}(\mathbf{r})\rangle$ have the periodicity of the lattice, α is the band index, and $\mathbf{k}$ is the quasimomentum confined to the first Brillouin zone (BZ), i.e. $|\mathbf{k}| < |\mathbf{k}+\mathbf{G}|$ for any $\mathbf{G}$ given by Eq. (2.2). If we apply the time-independent Schrödinger equation (SE) to the Bloch states we obtain

$$\hat{H}_{\mathbf{k}}|u_{\alpha,\mathbf{k}}(\mathbf{r})\rangle = \epsilon_\alpha(\mathbf{k})|u_{\alpha,\mathbf{k}}(\mathbf{r})\rangle, \tag{2.5}$$

with $\hat{H}_k = e^{-i\mathbf{k}\cdot\mathbf{r}}\hat{H}e^{i\mathbf{k}\cdot\mathbf{r}}$ being the so-called Bloch or momentum-space Hamiltonian. The $\mathbf{k}$-periodic eigenvalues $\epsilon_\alpha(\mathbf{k}) = \epsilon_\alpha(\mathbf{k}+\mathbf{G})\ \forall\mathbf{G}$ are said to form the α^{th} energy band.
Sometimes it is convenient to operate in the real space rather than in the momentum space. In such a case, one can make use of the Wannier states. These are a set of orthonormal states localized on atomic sites that can be always constructed from the Bloch states and vice versa via the discrete Fourier transform [96]:

$$|w_\alpha(\mathbf{R}_j,\mathbf{r})\rangle = \frac{1}{\sqrt{N}}\sum_k e^{-i\mathbf{k}\cdot\mathbf{R}_j}|\psi_{\alpha,\mathbf{k}}(\mathbf{r})\rangle, \quad k \in 1^{\text{st}}\text{BZ} \tag{2.6}$$

with j ranging from 1 up to the number of lattice sites.

2.1.2 One-dimensional tight-binding model

Let $\phi_{\text{a}}(\mathbf{r})$ be the wave function of an electron at the outer shell of an isolated atom which satisfies the stationary SE:

$$\hat{H}_{\text{a}}\phi_{\text{a}}(\mathbf{r}) = \epsilon_{\text{a}}\phi_{\text{a}}(\mathbf{r}). \tag{2.7}$$

Here, the Hamiltoian:

$$\hat{H}_{\text{a}} = -\frac{\hbar^2}{2m}\nabla^2 + U_{\text{a}}(\mathbf{r}), \tag{2.8}$$

where $\hbar$ is the reduced Planck's constant, m is the mass of an electron and $U_{\text{a}}(\mathbf{r})$ is the atomic potential centered at $\mathbf{r} = 0$.
Next, consider a 1D crystal formed by N atoms sitting on the lattice sites $x_j = ja$ with a being

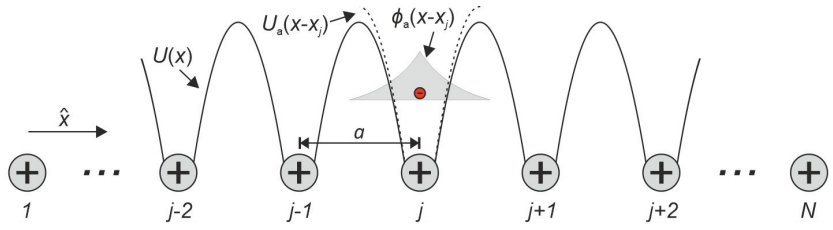

Figure 2.1: Schematic of the tight-binding chain composed of N atoms. Here, $U(x)$ is the potential of the whole lattice, $U_{\text{a}}(x-x_j)$ is the potential of an individual atom, a is the lattice constant, $\phi_{\text{a}}(x-x_j)$ is the atomic orbital which quickly decays away from $x = x_j$.

the lattice constant along the x-axis (see Fig. 2.1). For simplicity, we assume that all the atoms are identical and each separately can be described by the Hamiltonian (2.8). Electron spin is not taken into account. The crystal Hamiltonian then reads

$$\hat{H} = -\frac{\hbar^2}{2m}\frac{\partial^2}{\partial x^2} + U(x), \quad U(x) = \sum_j^N U_{\mathrm{a}}(x - x_j). \tag{2.9}$$

The approximate solution of this Hamiltonian can be found using the tight-binding (TB) approximation [95, 97]. Here, one starts with considering the extreme case of isolated atoms where the wave function of an electron on a site j is solely given by an atomic orbital $\phi_{\mathrm{a}}(x - x_j)$. When the atoms are brought together to form a crystal, the atomic orbitals start to overlap. However, if the overlap is small the electrons are still almost localized at the original orbitals but have a tiny probability to hop to the neighboring site. This idea is best seen in the position space spanned by the Wannier basis. Using atomic orbitals as an approximate form of the Wannier functions and, for brevity, denoting $|w(x_j, x)\rangle = |j\rangle$ we can rewrite the crystal Hamiltonian as follows [96]:

$$\hat{H} = \sum_{jj'} |j'\rangle\langle j'|\hat{H}|j\rangle\langle j|, \tag{2.10}$$

where the matrix elements are given by

$$\langle j'|\hat{H}|j\rangle = H_{jj'} \approx \int \mathrm{d}x \phi_a^*(x - x_{j'}) \left(-\frac{\hbar^2}{2m}\frac{\partial^2}{\partial x^2} + U(x)\right) \phi_a(x - x_j). \tag{2.11}$$

Since the atomic orbitals are highly localized, only diagonal elements and those that correspond to the nearest neighbors make a significant contribution while others can be neglected. Rewriting the crystal Hamiltonian (2.9) as a sum of the atomic Hamiltonian and the remaining potential $\hat{H} = \hat{H}_a(x - x_j) + \tilde{U}(x - x_j)$, where $\tilde{U}(x - x_j) = \sum_{j' \neq j} U_a(x - x_{j'})$ and using Eq. (2.7) we come to

$$H_{jj} \equiv E_j = E_a - \int \mathrm{d}x \phi_a^*(x - x_j)\tilde{U}(x - x_j)\phi_a(x - x_j) \tag{2.12}$$

and

$$H_{jj+1} \equiv J_{jj+1} \approx -\int \mathrm{d}x \phi_a^*(x - x_{j+1})\tilde{U}(x - x_j)\phi_a(x - x_j). \tag{2.13}$$

Then the tight-binding Hamiltonian can be written in a form:

$$\hat{H}_{\mathrm{TB}} = \sum_j E_j|j\rangle\langle j| - \sum_j J_{j+1j}(|j+1\rangle\langle j| + h.c.), \tag{2.14}$$

where $h.c.$ denotes Hermitian conjugate. Equation (2.14) shows that E_j represents an energy on site j which mainly consists of the atomic potential minus a constant correction due to interaction with the lattice, while J_{jj+1} measures the probability for an electron to hop to the neighboring site. It is clear, that if all atoms in a TB chain are equivalent then the on-site energies $E_j \equiv E$ and the coupling constants $J_{j\pm1j} \equiv J$ are just the same for all j. Although, in general, they can vary from site to site. In the case of all-identical atoms, the Hamiltonian (2.14) has a simple exact solution. Imposing the

periodic boundary conditions we satisfy the Bloch's theorem and can look for the eigenstates in a plane wave form:

$$|k\rangle = \frac{1}{\sqrt{N}} \sum_j e^{ikx_j} |j\rangle, \quad k \in 1^{\text{st}}\text{BZ} \tag{2.15}$$

with the inversion formula

$$|j\rangle = \frac{1}{\sqrt{N}} \sum_k e^{-ikx_j} |k\rangle, \quad k \in 1^{\text{st}}\text{BZ}. \tag{2.16}$$

Plugging Eq. (2.16) into (2.14) we obtain

$$\begin{aligned} \hat{H}_{\text{TB}}(k) = \frac{1}{N} \sum_j \sum_{kk'} E|k\rangle\langle k'|e^{-ija(k-k')} - \frac{1}{N} \sum_j \sum_{kk'} J|k\rangle\langle k'|e^{-ija(k-k')} \left(e^{-ika} + e^{ik'a}\right) \\ = \sum_k \epsilon(k)|k\rangle\langle k| \end{aligned} \tag{2.17}$$

with

$$\epsilon(k) = E - 2J \cos ka. \tag{2.18}$$

Eq. (2.18) gives the dispersion relation for the electron that is plotted in Fig. 2.2. In the beginning we have assumed that each atomic state contributes a single electron, while its maximum occupancy is limited by the Pauli principle to two. As a consequence, the band formed by this dispersion relation must be half filled and the Fermi energy $E_{\text{F}} = E$. Note, that in Fig. 2.2 E_{F} is set to zero. Since there is a single continuous band with no band gaps, one can always find allowed energy states arbitrary close to the Fermi energy. This system thus describes a metal. The band width, defined as the difference between the maximum and the minimum energy, equals to $4J$.

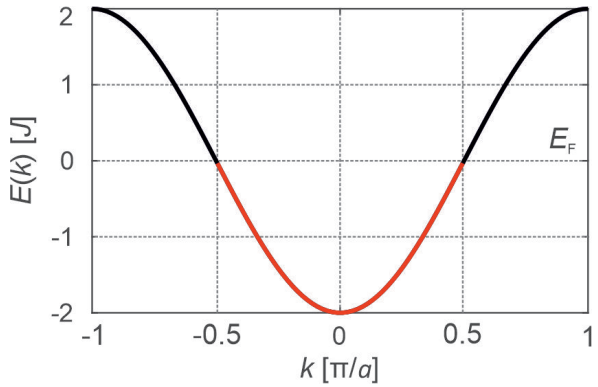

Figure 2.2: Dispersion relation $E(k)$ obtained from the TB Hamiltonian 2.14 with all-identical atoms. The Fermi energy E_{F} is set to zero. The red part of the curve highlights the filled part of the band.

Matrix form

The temporal evolution of an arbitrary electron state $|\Psi(t)\rangle$ in a 1D tight-binding lattice is found by solving the time-dependent SE:

$$i\frac{\mathrm{d}}{\mathrm{d}t}|\Psi(t)\rangle = \hat{H}_{\mathrm{TB}}|\Psi(t)\rangle, \tag{2.19}$$

which in the Wannier basis $\{|j\rangle\}$ can be viewed as a matrix problem, where

$$|\Psi(t)\rangle = \begin{pmatrix} \cdots & p_{j-1}(t) & p_j(t) & p_{j+1}(t) & \cdots \end{pmatrix}^{\mathrm{T}} \tag{2.20}$$

is a vector whose elements are time-dependent amplitudes $p_j(t) = \langle j|\Psi(t)\rangle$ and

$$\hat{H}_{\mathrm{TB}} = \begin{pmatrix} \ddots & \ddots & & & \\ \ddots & E_{j-1} & -J_{j-1j} & & \\ & -J_{j-1j} & E_j & -J_{jj+1} & \\ & & -J_{jj+1} & E_{j+1} & \ddots \\ & & & \ddots & \ddots \end{pmatrix} \tag{2.21}$$

is the matrix for the Hamiltonian (2.14). Note, that here and later on $\hbar$ is set to 1. If by ϵ_j and $|\Phi_j\rangle$ we denote the eigenvalues and corresponding eigenstate vectors of the matrix Hamiltonian (2.21), the solution of Eq. (2.19) can be written as:

$$|\Psi(t)\rangle = \sum_{j=1}^{N} c_j e^{-i\epsilon_j t}|\Phi_j\rangle, \tag{2.22}$$

where c_j are constants determined by initial conditions, i.e. $c_j = \langle\Phi_j|\Psi(t=0)\rangle$.

2.2 Time-periodic systems

In the previous section we dealt with a static one-dimensional tight-binding lattice. According to Eq. (2.22), the temporal evolution of an electron wave function in such a system is fully described by the eigenenergies and eigenstates of the time-independent Hamiltonian (2.14). Now imagine that a TB lattice is subject to some periodic external field oscillating with the frequency ω. As a result, the system's Hamiltonian inherits periodic behaviour:

$$\hat{H}(t) = \hat{H}(t+T), \tag{2.23}$$

where $T = 2\pi/\omega$ is the period of the driving. It is clear, that in such a case the static energy spectrum is no longer relevant, as energy is exchanged with the driving field. However, the symmetry of the Hamiltonian under discrete time translations, $t \longrightarrow t+T$ has an important consequence for the system's dynamics that can be systematically understood in the framework of the Floquet formalism.

2.2.1 Floquet theory

Central for the Floquet formalism is the Floquet theorem which was originally developed to solve linear differential equations with periodic coefficients. In the realm of quantum mechanics, the Floquet theory is the temporal analogue of Bloch's theorem. While Bloch's theorem suggests the form of the eigen wave functions based on the spatial periodicity of the crystal potential, the Floquet theorem gives an analogous result for Hamiltonians periodic in time.
Consider a quantum system whose Hamiltonian obeys the periodicity condition (2.23). According to the Floquet theorem [1, 99], there exist solutions of the corresponding time-dependent SE

$$i\frac{\mathrm{d}}{\mathrm{d}t}|\Psi(t)\rangle = \hat{H}(t)|\Psi(t)\rangle \tag{2.24}$$

called Floquet states that have the form:

$$|\Psi_j(t)\rangle = e^{-\mathrm{i}\epsilon_j t}|\Phi_j(t)\rangle, \tag{2.25}$$

where ϵ_j is a constant quasienergy and $|\Phi_j(t)\rangle$ is a T-periodic Floquet mode $|\Phi_j(t)\rangle = |\Phi_j(t+T)\rangle$. The term "quasienergy" arises from the analogy to the quasimomentum k associated with Bloch states in crystalline solids. Substituting the Floquet ansatz (2.25) into the SE (2.24) yields:

$$\left(\hat{H}(t) - \mathrm{i}\frac{\mathrm{d}}{\mathrm{d}t}\right)|\Phi_j(t)\rangle = \epsilon_j|\Phi_j(t)\rangle. \tag{2.26}$$

The equation above reveals that the quasienergies ϵ_j are eigenvalues of the so-called Floquet Hamiltonian $\hat{\mathcal{H}} \equiv \hat{H}(t) - \mathrm{i}\frac{\partial}{\partial t}$. It can be readily seen that multiplying a Floquet mode in Eq. 2.26 by $e^{in\omega t}$ with $n \in \mathbb{Z}$

$$|\tilde{\Phi}_j(t)\rangle \rightarrow |\Phi_j(t)\rangle e^{in\omega t} \tag{2.27}$$

shifts the corresponding eigenvalue by $n\omega$:

$$\tilde{\epsilon}_j = \epsilon_j + n\omega. \tag{2.28}$$

Crucially, this operation does not alter the corresponding Floquet state:

$$|\Psi_j(t)\rangle = e^{-\mathrm{i}\tilde{\epsilon}_j t}|\tilde{\Phi}_j(t)\rangle = e^{-\mathrm{i}\epsilon_j t}|\Phi_j(t)\rangle. \tag{2.29}$$

Hence, the quasienergies are defined up to integer multiples of ω and one can always choose all ϵ_j to lie within the interval $[-\omega/2, \omega/2)$, which is called the first Floquet Brillouin zone (FBZ) in analogy to the BZ for quasimomentum. From now on, we assume that index j counts only ϵ_j which lie in the same FBZ, so that each quasienergy represents a unique Floquet state.
The corresponding eigenvectors of $\hat{\mathcal{H}}$, the Floquet modes $|\Phi_j(t)\rangle$, are periodic in time. It suggests to consider the Floquet Hamiltonian as an operator acting in the extended Hilbert space $\mathcal{R} \otimes \mathcal{T}$ [100]. This space is composed of the usual Hilbert space $\mathcal{R}$ of square-integrable functions on configuration space $\mathbf{r}$ and the space of T-periodic functions $\mathcal{T}$ spanned by the Fourier basis $e^{in\omega t}$, $n \in \mathbb{Z}$. The direct

product $\mathcal{R} \otimes \mathcal{T}$ is in turn also a Hilbert space with the inner product defined as follows:

$$\langle\langle a|b\rangle\rangle = \frac{1}{T}\int_0^T \langle a(t)|b(t)\rangle \mathrm{d}t. \tag{2.30}$$

The orthonormality condition for the Floquet modes thus takes the form:

$$\langle\langle \Phi_j(t)|\Phi_{j'}(t)\rangle\rangle = \frac{1}{T}\int_0^T \mathrm{d}t \int_{-\infty}^{\infty} \mathrm{d}\mathbf{r}\Phi_j^*(\mathbf{r},t)\Phi_{j'}(\mathbf{r},t) = \delta_{jj'}. \tag{2.31}$$

In $\mathcal{R}\otimes\mathcal{T}$ the Floquet modes $\{|\Phi_j(t)\rangle\}$ form a complete set and for every time t, the temporal evolution of any state can be expressed as:

$$|\Psi(t)\rangle = \sum_j c_j e^{-i\epsilon_j t}|\Phi_j(t)\rangle, \tag{2.32}$$

where $c_j = \langle\Phi_j(0)|\Psi(0)\rangle$.

2.2.2 Time-independent representation of periodically driven systems

Since the quasienergies and the Floquet modes allow to fully reconstruct the dynamics of a time-periodic system for the given initial conditions, our main goal is to solve the eigenvalue problem (2.26). It turns out that with the help of the extended Hilbert space $\mathcal{R}\otimes\mathcal{T}$, one can map this time-dependent problem to a time-independent one with an extra dimension [101, 102]. Indeed, representing the Hamiltonian and the Floquet modes in the Fourier basis

$$\begin{aligned} \hat{H}(t) &= \sum_{n=-\infty}^{\infty} \mathrm{e}^{-\mathrm{i}n\omega t}\hat{H}_n, \\ |\Phi_j(t)\rangle &= \sum_{n=-\infty}^{\infty} \mathrm{e}^{-\mathrm{i}n\omega t}|\Phi_j^n\rangle, \end{aligned} \tag{2.33}$$

and plugging them into Eq. (2.26) we arrive at the time-independent Floquet equation:

$$\left(\hat{H}_0 - n\omega\right)|\Phi_j^n\rangle + \sum_{m\neq 0}\hat{H}_m|\Phi_j^{n-m}\rangle = \epsilon_j|\Phi_j^n\rangle, \quad \forall n\in\mathbb{Z}, \tag{2.34}$$

where the Floquet index n can be considered as a position in a fictitious spatial dimension. Denoting by $\hat{I}$ an identity matrix, we can rewrite Eq. (2.34) as the following eigenvalue problem with an infinite

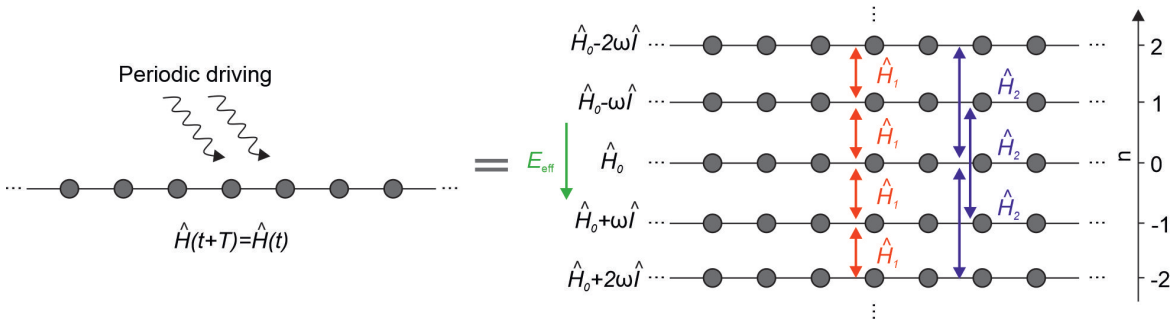

Figure 2.3: Schematic of the Floquet picture: a periodically driven 1D lattice is equivalent to a static lattice with an additional spatial dimension, in which the position is determined by the Floquet index n. The n^{th} layer has a potential offset of $n\omega$ relative to $\hat{H}_0$ as if the system was subject to a constant electric field $\mathbf{E}_{\text{eff}} \propto \omega$ along the Floquet direction n (green arrow). Red and blue arrows exemplify the coupling between the chains induced by $\hat{H}_1$ and $\hat{H}_2$, respectively (the higher order couplings are not shown).

block-matrix operator:

$$\begin{pmatrix} \ddots & \ddots & \ddots & \ddots & \\ \ddots & \hat{H}_0-(n-1)\omega\hat{I} & \hat{H}_{-1} & \hat{H}_{-2} & \ddots \\ \ddots & \hat{H}_1 & \hat{H}_0-n\omega\hat{I} & \hat{H}_{-1} & \ddots \\ \ddots & \hat{H}_2 & \hat{H}_1 & \hat{H}_0-(n+1)\omega\hat{I} & \ddots \\ & \ddots & \ddots & \ddots & \ddots \end{pmatrix} \begin{pmatrix} \vdots \\ |\Phi_j^{n-1}\rangle \\ |\Phi_j^{n}\rangle \\ |\Phi_j^{n+1}\rangle \\ \vdots \end{pmatrix} = \epsilon_j \begin{pmatrix} \vdots \\ |\Phi_j^{n-1}\rangle \\ |\Phi_j^{n}\rangle \\ |\Phi_j^{n+1}\rangle \\ \vdots \end{pmatrix}, \tag{2.35}$$

which can be readily solved numerically after reasonable truncation in the Floquet space.
Significantly, the above result does not only allow to compute the system's dynamics, but also provides an intuitive picture which helps to understand the behaviour of periodically driven systems. This is illustrated in Figure 2.3 on a 1D TB lattice subject to periodic driving. Here, the Hamiltonian is given by (2.21) with the only difference, that the on-site energies and/or hopping amplitudes are periodic functions of time. The Floquet equation (2.35) tells us that this system is equivalent to a time-independent $(1+1)$D lattice composed of an infinite number of TB chains labeled by the Floquet index n with the overall potential shifted by $n\omega$. This potential offset can be viewed as an effective constant electric field directed along the fictitious dimension (see green arrow in Fig. 2.3). In the static Floquet analogue, the coupling within each chain is described by $\hat{H}_0$ while the Fourier components $\hat{H}_n$ provide coupling between the chains. Using the Floquet picture one can transfer the concepts relevant for non-driven systems of higher dimensionality with the Hamiltonian being replaced by the Floquet operator and energy by quasienergy. In particular, it allows to systematically analyse energy bands of periodically driven lattices which can be obtained as described below.

Floquet-Bloch systems

If a system possesses translation symmetry in both space and time $\hat{H}(x,t) = \hat{H}(x+a,t) = \hat{H}(x,t+T)$, it satisfies Bloch's theorem and the Floquet theorem simultaneously. In the following chapters of this

thesis we take an advantage of such a two-fold translation symmetry to access quasienergy dispersion relations of periodically driven lattices. For that we proceed in two steps: First, we use the plane wave basis states $|k\rangle$ (see Eq. (2.15)) to diagonalize the Hamiltonian with respect to the quasimomentum k and obtain the Bloch Hamiltonian:

$$\hat{H}_k(t) = \langle k|\hat{H}|k\rangle. \tag{2.36}$$

In the second step, the Floquet theory is applied to $\hat{H}_k(t)$ at every fixed k value taken from the 1st BZ: $k \in [-\pi/a, \pi/a)$. Thus we look for the eigenstates of the form [2, 102]:

$$|\psi^F_{\alpha,k}(x,t)\rangle = e^{ikx - i\epsilon_\alpha(k)t}|\phi_{\alpha,k}(x,t)\rangle, \tag{2.37}$$

where the Floquet-Bloch modes are periodic in both space and time $|\phi_{\alpha,k}(x,t)\rangle = |\phi_{\alpha,k}(x+a,t)\rangle = |\phi_{\alpha,k}(x+a,t+T)\rangle$ and $\epsilon_\alpha(k)$ are the k-dependent quasienergies with α being a band index. The states (2.37) have all the properties of the Floquet states, i.e. the Floquet-Bloch modes obey the orthonormality condition (2.31) and the quasienergies are uniquely defined up to integer multiples of ω. Since the quasienergy spectrum is periodic along momentum and energy axes, one defines the two-dimensional Floquet-Bloch Brillouin zone (FBBZ) as $\{-\omega/2 \leq \epsilon < \omega/2; -\pi/a \leq k < \pi/a\}$. In order to find $|\phi_{\alpha,k}(x,t)\rangle$ and $\epsilon_\alpha(k)$, we follow the procedure described by Eqs. (2.33) - (2.35) replacing $\hat{H}(t)$ by $\hat{H}_k(t)$ and $|\Phi_j(t)\rangle$ by $|\phi_{\alpha,k}(x,t)\rangle$, respectively.
Eq. (2.35) then reveals the structure of the energy spectrum of a periodically driven system (see Fig. 2.4): The bands of the undriven system described by the zeroth Fourier component $\hat{H}_{k0}$ are split into infinitely many copies called Floquet replicas spaced by the driving frequency ω whereas the coupling between the bands depends on the driving regime as given by the higher-order Fourier components $\hat{H}_{kn}$. Depending on the magnitude of the driving frequency ω in comparison to the energy scales of $\hat{H}_{k0}$, different frequency regimes are realized. When ω is low the Floquet spectrum becomes denser extending the required size of the Floquet matrix (2.35) and hence the calculation time. As ω increases the coupling between the bands gets weaker which ultimately breaks the system into uncoupled 1D chains. We note that due to the used experimental platform, the extreme adiabatic

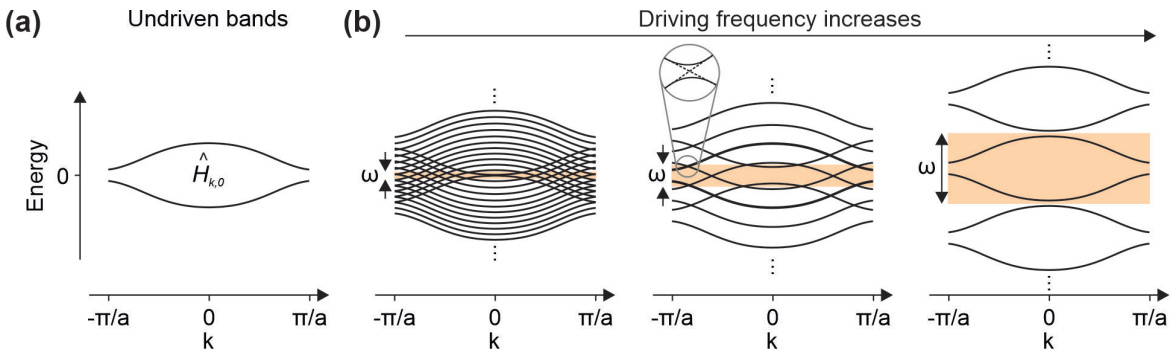

Figure 2.4: Principle of the Floquet-Bloch spectrum formation. (a) Schematic of bands of an arbitrary static system described by $\hat{H}_{k0}$. (b) Periodic driving splits these bands into the Floquet replicas spaced by the driving frequency ω. From left to right ω as well as the distance between the replicas increase. The orange rectangle highlights the 1st FBBZ. When the Floquet replicas of the bands intersect, they may couple, i.e. hybridize, and the avoided crossings appear as shown in the central picture. The strength of coupling and hence the width of a gap at an avoided crossing depends on a particular driving scheme.

($\omega \to 0$) or high frequency regimes ($\omega \to \infty$) are out of the scope of this thesis. In contrast, we will focus on the intermediate frequency regime, when the driving frequency remains comparable to the band width of the undriven Hamiltonian.

2.3 Topological systems

Topological phenomena in 1D TB systems will be of particular interest to us. In order to understand the origin of these phenomena, let us begin with the definition: Topology is a branch of mathematics that studies properties of continuity. In particular, those properties of geometric objects that are preserved under continuous deformations such as stretching, twisting or bending excluding those that imply creation or closure of holes and cutting or gluing parts together. A deformation of this kind is called a homotopy and the objects that can be smoothly deformed into each other are called homotopic, e.g. a torus and a cup in Fig. 2.5 (a). Figure 2.5 (b), in contrast, shows topologically distinct surfaces in $\mathbb{R}^3$. These objects can be distinguished by an integer number called genus (number of holes) that is a topological invariant. An important difference between geometry and topology is that geometric properties have local structure, while topological proprieties are defined by the geometry as a whole and thus have global structure.
In the last decades topology has been developed into a powerful concept to classify fundamentally new phases of matter that do not fit into the Landau paradigm of spontaneous symmetry breaking [103]. The example with a torus and a cup clearly shows that having the same topological invariant the objects can be of absolutely different shapes. In the same vein, physical properties associated with topological invariants have universal character and exhibit remarkable robustness against a wide range of deformations [104]. Topology was found to underlie various fascinating physical phenomena including integer and fractional quantum Hall effect [103], quantized charge pumping [36], topologically-protected edge states [19], Majorana bound states [105] etc.
The topological invariants of crystalline solids can be expressed in terms of the so-called geometric or Berry phase. This is the phase picked up by a quantum particle during an adiabatic loop in the Hamiltonian's parameter space. Below we derive it and discuss the most relevant for this thesis cases of one- and two-dimentional parameter space.

2.3.1 Berry phase and topological invariants

Consider a Hamiltonian that smoothly depends on time through a parameter $\mathbf{R}(t)$:

$$\hat{H}(t) = \hat{H}(\mathbf{R}(t)). \tag{2.38}$$

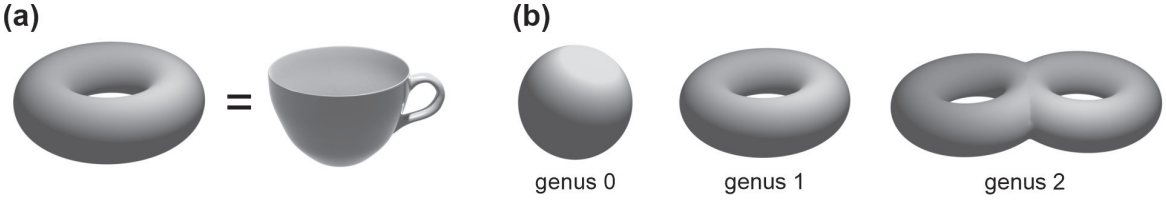

Figure 2.5: (a) Example of homotopic objects. (b) Topologically distinct surfaces in $\mathbb{R}^3$.

For every $\mathbf{R}$ we can define the instantaneous eigenvalues $E_\alpha(\mathbf{R})$ and the instantaneous eigenstates $|\alpha(\mathbf{R})\rangle$ as [106]:

$$\hat{H}(\mathbf{R})|\alpha(\mathbf{R})\rangle = E_\alpha(\mathbf{R})|\alpha(\mathbf{R})\rangle. \tag{2.39}$$

In the following we assume the energy spectrum to be discrete and non-degenerate. According to the adiabatic theorem, if $\mathbf{R}$ changes slowly enough then the system prepared in a state $|\Psi(0)\rangle = |\alpha(\mathbf{R}(0))\rangle$ at time $t = 0$ will remain in this state over time:

$$|\Psi(t)\rangle = e^{i\varphi_\alpha(t)}|\alpha(\mathbf{R}(t))\rangle. \tag{2.40}$$

with $\varphi_\alpha(t)$ being a pure phase factor. By "slow" is meant that the characteristic rate of change of the Hamiltonian is much smaller than the energy gap between E_α and the neighboring states. Plugging Eq. (2.40) into the time-dependent SE yields

$$i\left(\frac{\partial}{\partial t}\varphi_\alpha\right)|\alpha\rangle + \frac{\partial}{\partial t}|\alpha\rangle = \frac{\hat{H}}{i}|\alpha\rangle. \tag{2.41}$$

In order to find φ_α we multiply Eq. (2.41) by $\langle\alpha|$, use Eq. 2.39, and integrate over t. As a result, one finds that the phase φ_α consists of the two terms

$$\varphi_\alpha = \zeta_\alpha + \gamma_\alpha, \tag{2.42}$$

where

$$\zeta_\alpha = -\int_0^t E_\alpha(t')\mathrm{d}t' \tag{2.43}$$

and

$$\gamma_\alpha = i\int_0^t \langle\alpha(\mathbf{R}(t'))|\frac{\partial}{\partial t'}|\alpha((\mathbf{R}(t'))\rangle\mathrm{d}t'. \tag{2.44}$$

The first term ζ_α is the so-called dynamic phase. In order to make sense of the second term let us rewrite it as

$$\gamma_\alpha = i\int_C \langle\alpha(\mathbf{R})|\frac{\partial}{\partial\mathbf{R}}|\alpha(\mathbf{R})\rangle\cdot\mathrm{d}\mathbf{R} = \int_C \mathbf{A}^\alpha(\mathbf{R})\cdot\mathrm{d}\mathbf{R}, \tag{2.45}$$

with integration done over the path C that the vector $\mathbf{R}$ traverses in the parameter space. Importantly, substitution $\mathbf{R}(t') \to \mathbf{R}(\tau(t'))$: $\tau(0) = 0$ and $\tau(t) = t$ in Eq. (2.45) does not change γ_α meaning that this phase only depends on the path C, i.e. on the geometry of the parameter space, but not on how exactly the vector $\mathbf{R}$ depends on time. Therefore, as opposed to dynamic phase, γ_α is referred to as geometric or Berry phase. The integrand in Eq. (2.45)

$$A_j^\alpha = i\langle\alpha(\mathbf{R})|\partial_{R_j}\alpha(\mathbf{R})\rangle \tag{2.46}$$

is known as the Berry connection. It can be easily checked that the Berry connection and the geometric phase generally depend on the gauge. However, if the path C is a closed loop, i.e. $\mathbf{R}(0) = \mathbf{R}(t)$, then the Berry phase

$$\gamma_\alpha = \oint_C \mathbf{A}^\alpha\cdot\mathrm{d}\mathbf{R} \tag{2.47}$$

becomes gauge-invariant and, therefore, can be in principle linked to a physical observable.

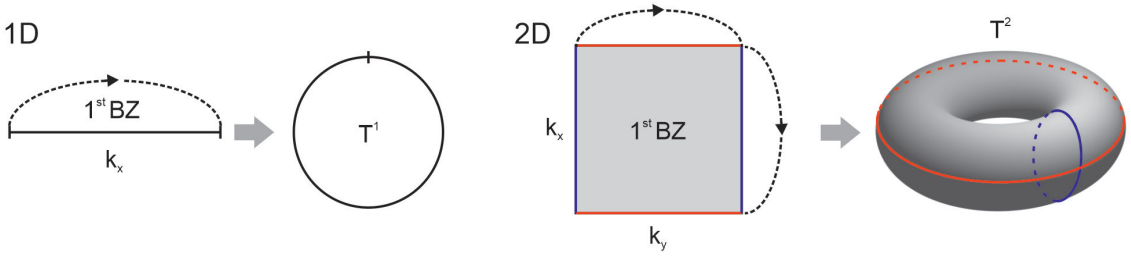

Figure 2.6: The first Brillouin zone in 1D turns into a ring and in 2D turns into a torus, upon connecting the boundaries as highlighted by dashed arrows.

It turns out that the ideas discussed above are directly applied to the energy bands in crystalline solids. Recall Eq. (2.5) that is the SE for the periodic part of the Bloch states $|u_{\alpha,\mathbf{k}}\rangle$. Due to periodicity of the Bloch Hamiltonian $\hat{H}_{\mathbf{k}}$ with respect to the quasimomentum $\mathbf{k}$, the opposite edges of the first BZ represent the same state and thus can be "glued" together. Thus, the 1D BZ is identified with a ring T^1, the 2D BZ is a torus T^2 (see Fig. 2.6). More generally, the n-dimensional BZ is the hypertorus T^n. From this perspective, $\mathbf{k}$ plays a role of the parameter that creates a loop when runs through the 1$^{\text{st}}$ BZ. Now one can readily define the Berry connection and the Berry phase of the α^{th} band by simply substituting $|\alpha(\mathbf{R})\rangle \to |u_{\alpha,\mathbf{k}}\rangle$ and $\partial/\partial R_j \to \partial/\partial k_j$ in Eqs. (2.46) and (2.47), respectively. The total Berry phase γ_α picked up by an electron moving through the BZ takes discrete moduli and is used to characterize topological properties of the energy bands.
The Berry phase in one-dimensional crystals is commonly called the Zak phase [107, 108]:

$$\gamma_Z^\alpha = i \oint_{-\pi/a}^{\pi/a} \mathrm{d}k \langle u_{\alpha,k} | \frac{\partial}{\partial k} | u_{\alpha,k} \rangle. \tag{2.48}$$

In Chapter 5 we will see that the value of the Zak phase is related to a topological invariant in the Su-Schrieffer-Heeger model and that, if it happens to be non-zero, underlies the existence of topologically-protected edge states.
In 1D TB systems a two-dimensional topological invariant can arise as well. Indeed, by adding an adiabatically varying time-periodic parameter $\theta: \ \theta(t) = \theta(t+T)$ to the Bloch Hamiltonian of a 1D lattice one essentially creates the two-dimensional parameter space. Let $\mathbf{R} = (k, \theta)$. Using the Stoke's theorem we can rewrite the Berry phase (2.47) as an area integral over an open surface $S(C)$ spanned by the loop C:

$$\oint_C \mathbf{A}^\alpha \cdot \mathrm{d}\mathbf{R} = \iint_{S(C)} \Omega^\alpha(k,\theta) \mathrm{d}k \mathrm{d}\theta, \tag{2.49}$$

with

$$\Omega^\alpha(k,\theta) = i \left[\langle \partial_\theta u_{\alpha,k} | \partial_k u_{\alpha,k} \rangle - \langle \partial_k u_{\alpha,k} | \partial_\theta u_{\alpha,k} \rangle \right] \tag{2.50}$$

being the so-called Berry curvature. Unlike the Berry connection, the Berry curvature is independent of a gauge and plays a role of the local geometric property of the energy band. The famous Gauss-Bonnet theorem provides a link between geometry and topology. It states that the curvature integrated over a

closed 2D surface is quantized in the units of 2π [104]. When applied to the Berry curvature it reads

$$\int_{-\pi/a}^{\pi/a} \mathrm{d}k \int_0^T \mathrm{d}t \Omega^\alpha(k, \theta(t)) = 2\pi \mathscr{C}, \tag{2.51}$$

where $\mathscr{C}$ is an integer called the Chern number. Equation (2.51) can be also rewritten as the winding of the Zak phase:

$$\oint \mathrm{d}\theta \frac{\partial \gamma_Z^\alpha}{\partial \theta} = 2\pi \mathscr{C}. \tag{2.52}$$

The Chern number is widely known as the topological invariant that characterises quantum Hall states. In Chapter 6 it will appear to be responsible for the topological transport quantization in a slowly varying 1D potential, the phenomenon called Thouless pumping.

The concept of the Berry phase and the Chern number might look a bit too abstract. In order to gain a better understanding of these ideas it is instructive to draw an analogy with more familiar physics, namely, with electromagnetism. Taking a closer look at Eq. (2.47), one may recognize that the Berry phase reminds the magnetic flux given by the loop integral of the gauge-dependent vector potential represented by the Berry connection. On the other hand, we know that the magnetic flux can be defined as the surface integral of the magnetic field. Consequently, Eq. (2.49) suggests that the Berry curvature is a kind of the magnetic field.

The implication of the Chern number we will illustrate on a simple example of a two-band system [104, 106]. Consider a Bloch Hamiltonian of a 2D lattice with two internal degrees of freedom which may arise e.g. from a double-site unit cell or the two spin states. Here, we have assumed two spatial dimensions in order to meet the necessary condition for the Chern number that is the 2D cyclically varying parameter given by the wavevector $\mathbf{k} = (k_x, k_y) \in 1^{\text{st}}\text{BZ}$. Due to the internal degrees of freedom, the Hilbert space is also two-dimensional, thus the general Bloch Hamiltonian can be written as a linear combination of the Pauli matrices

$$\hat{H}_\mathbf{k} = h_x \hat{\sigma}_x + h_y \hat{\sigma}_y + h_z \hat{\sigma}_z = \mathbf{h}(\mathbf{k}) \cdot \hat{\sigma}. \tag{2.53}$$

The spectrum of this Hamiltonian consists of the two energy bands $E_\pm = \pm|\mathbf{h}(\mathbf{k})|$ which cross at $\mathbf{h} = (0, 0, 0)$. Since the 2D BZ is a torus T^2, the function $\mathbf{h}(\mathbf{k})$ defines a continuous mapping $T^2 \to \mathbb{R}^3 \backslash (0, 0, 0)$, where the origin is excluded to avoid the degeneracy. Therefore, the endpoint of $\mathbf{h}(\mathbf{k})$ traces out a surface that is topologically equivalent to a torus as $\mathbf{k}$ runs through the first BZ. It turns out, that the Berry curvature of this system is given by [104, 106]

$$\Omega^\pm = \pm \frac{\mathbf{h}}{2|\mathbf{h}|^3}, \tag{2.54}$$

which looks exactly like the field of a point-like magnetic monopole sitting in the origin. Now it becomes clear why the Chern number must be integer: The Chern number of the band $E_-(\mathbf{k})$ (or $E_+(\mathbf{k})$) is the flux of the monopole field Ω^- (or Ω^+) through the deformed torus traced by $\mathbf{h}(\mathbf{k})$. If the origin is inside the "torus", then $\mathscr{C} = 1$ (or -1). If it lies outside, then $\mathscr{C} = 0$. Evidently, the Chern number is insensitive to local deformations of the "torus" and cannot be altered unless we cross the origin. At the transition point the band gap closes, the spectrum becomes degenerate and no adiabatic following is possible, hence, the Berry phase and the associated topological invariant are not defined. Note, that the "torus" can in principle intersect itself giving rise to the higher Chern

numbers $\mathscr{C} = 2, 3$, etc. To conclude this example, let us outline some important features of topological invariants. First, a topological invariant must take only quantized values. Second, it is robust in a sense that it cannot be changed under continuous deformation of the band. In fact, the only way to change the topological invariant of a static system lies through the closure of the band gap and breaking some global symmetries of the Hamiltonian. These symmetries will be introduced in the next section.
An important remark is that in the context of topological robustness we can only talk about static or slow adiabatic deformations of a system. Dynamic perturbations, in contrast, may pump enough energy to a system to overcome the band gap and the whole concept of topological robustness is, strictly saying, no longer valid. However, if perturbations are periodic in time, then a system can be effectively treated as a static system with a modified Hamiltonian in the framework of Floquet theory. This allows to define topological invariants for Floquet systems [109, 110]. As we have seen in the previous sections, time-periodic perturbations can drastically change the band structure of a system and open new band gaps. It underlies the remarkable richness of topological phases found in Floquet systems. When subject to time-periodic perturbations, a system, trivial in equilibrium, can become a topological insulator [111–113]. Also there exist Floquet systems that support topologically-protected edge states that do not have analogues in non-driven systems. Such states are known as anomalous edge modes [114].

2.3.2 Symmetries and topological classification

Having discussed the particular examples of topological invariants we can ask ourselves, which systems can exhibit non-trivial topological properties and which not? What are the different kinds of topological systems? The answers on these questions are found in the so-called periodic table of topological invariants (see Table 2.1), where the systems of non-interacting fermions are arranged according to dimensionality and special symmetry properties [115–117]. Here, if non-trivial topology is possible, it is indicated by the entries $\mathbb{Z}$ or $\mathbb{Z}_2$, if not, it is denoted by 0. $\mathbb{Z}$ and $\mathbb{Z}_2$ are the corresponding homotopy groups, i.e. the topological invariants characterized by an integer number or a binary quantity, respectively.
Let us consider the symmetries that underlie topological classification. We typically understand a symmetry as some unitary operator that commutes with the Hamiltonian, for instance, spin-rotation symmetry or space-translation symmetry. In practice, such symmetries can be always eliminated by writing the Hamiltonian in a block form and focusing the attention on one block, i.e. the reduced Hamiltonian. That is precisely what we did previously to obtain the Bloch Hamiltonian in the case of space-translation symmetry. However, the symmetries we are interested in are different because they cannot be made to disappear by any block decomposition [117]. They are sometimes called the generalized symmetries owing to the fact that they reflect very general, non-local characteristics of a system and thus persist even in utterly reduced Hamiltonians. Now imagine we have found all the unitary matrices that commute with some Hamiltonian $\hat{H}$ and thereby exhausted all the symmetries which are present. We block diagonalized $\hat{H}$ using these unitary transformations and obtained the blocks $\hat{h}$ that cannot be further reduced. Which symmetries are left for these blocks? The first two symmetries of this kind are time-reversal $\mathcal{T}$ and charge-conjugation C (or particle-hole) symmetries. When acting on the blocks $\hat{h}$, they are given by antiunitary matrices that can either commute or anticommute with $\hat{h}$. The combination of these two form a third symmetry called chiral (or sublattice, hence the notation $\mathcal{S}$). It is in turn given by a unitary matrix that anticommutes with $\hat{h}$. Based on

Class	$\mathcal{T}$	C	$\mathcal{S}$	$d=1$	$d=2$	$d=3$	$d=4$
A	0	0	0	0	$\mathbb{Z}$	0	$\mathbb{Z}$
AIII	0	0	+	$\mathbb{Z}$	0	$\mathbb{Z}$	0
AI	+	0	0	0	0	0	$\mathbb{Z}$
BDI	+	+	+	$\mathbb{Z}$	0	0	0
D	0	+	0	$\mathbb{Z}_2$	$\mathbb{Z}$	0	0
DIII	-	+	+	$\mathbb{Z}_2$	$\mathbb{Z}_2$	$\mathbb{Z}$	0
AII	-	0	0	0	$\mathbb{Z}_2$	$\mathbb{Z}_2$	$\mathbb{Z}$
CII	-	-	+	$\mathbb{Z}$	0	$\mathbb{Z}_2$	$\mathbb{Z}_2$
C	0	-	0	0	$\mathbb{Z}$	0	$\mathbb{Z}_2$
CI	+	-	+	0	0	$\mathbb{Z}$	0

Table 2.1: Periodic table of topological invariants [115]. The first column from the left side contains 10 symmetry classes labeled using the notations of Altland and Zirnbauer. Each class is characterized by the presence or absence of the time reversal ($\mathcal{T}$), charge conjugation or particle-hole (C), and chiral ($\mathcal{S}$) symmetry. If a symmetry is present, it is denoted by + or - depending on the sign of $\mathcal{T}^2$, C^2, and $\mathcal{S}^2$ if absent, it is denoted by 0. d is the spatial dimension. The possibility to find a topologically non-trivial system is indicated by $\mathbb{Z}$ or $\mathbb{Z}_2$ depending on the type of a topological invariant. Whereas if all the Hamiltonians in the chosen symmetry class of a certain dimensionality are topologically trivial, it is indicated by 0.

invariance (or not invariance) of the Hamiltonian under $\mathcal{T}$, C, and $\mathcal{S}$, a system can be assigned to one of the symmetry classes of the periodic Table 2.1.

It turns out that there can be only ten different symmetry classes and this list is exhaustive in accordance with the classification scheme of Altland and Zirnbauer [118]. To puzzle out why, we have to mention an important property of $\mathcal{T}$ and C, namely, both transformation matrices can square to plus or minus identity, more specifically, the Hamiltonian can be either not invariant under, e.g. $\mathcal{T}$, or invariant and $\mathcal{T}^2 = +1$, or invariant and $\mathcal{T}^2 = -1$, and the same holds for C. As a result, we get 9 options how the Hamiltonian can respond to time-reversal and charge conjugation. Finally, it is also necessary to consider the action of combination of $\mathcal{T}$ and C. Indeed, there can be a situation when that both $\mathcal{T}$ and C symmetries are violated, but the Hamiltonian is invariant under $\mathcal{S} = \mathcal{T}C$ (see class AIII). Note that square of $\mathcal{S}$ is always plus identity, $\mathcal{S}^2 = (\mathcal{T}C)^2 = +1$. Therefore, there are in total 10 options.

By looking at the action of $\mathcal{T}$, C, and $\mathcal{S}$ on the creation and annihilation operators and demanding that canonical commutation (or anticommutation) relations hold true, one can derive the criteria that help to determine whether a given single-particle Hamiltonian obeys a certain generalized symmetry or not. Below we list these criteria for static systems.

1. Time-reversal transformation can be represented as $\mathcal{T} = \mathcal{K}U_{\mathrm{T}}$, where $\mathcal{K}$ is complex conjugation and U_{T} is a unitary rotation. The real-space Hamiltonian H is said to be time-reversal symmetric if

$$\mathcal{T}: \quad U_{\mathrm{T}}^{\dagger} H^{*} U_{\mathrm{T}} = H, \tag{2.55}$$

where "$*$" denotes complex conjugation. In momentum space it holds

$$\mathcal{T}: U_{\mathrm{T}}^{\dagger} H_k^{*} U_{\mathrm{T}} = H_{-k}. \tag{2.56}$$

Note, that for spinless particles $U_{\mathrm{T}} \equiv \mathbb{I}$ and Eq. (2.55) simplifies to $H^{*} = H$. In this case, $\mathcal{T}$ always squares to +1 [119].

2. Charge conjugation reads $\mathcal{C} = \mathcal{K}U_{\mathrm{C}}$, where $\mathcal{K}$ is again complex conjugation and U_{C} is a unitary rotation. The real-space Hamiltonian H is said to be symmetric under charge conjugation if and only if there exist such U_{C} that

$$\mathcal{C}: \quad U_{\mathrm{C}}^{\dagger} H^{*} U_{\mathrm{C}} = -H. \tag{2.57}$$

   In momentum space this condition reads

$$\mathcal{C}: \quad U_{\mathrm{C}}^{\dagger} H_k^{*} U_{\mathrm{C}} = -H_{-k}. \tag{2.58}$$

3. For being chiral symmetric, H must obey

$$\mathcal{S}: \quad U_{\mathrm{S}}^{\dagger} H U_{\mathrm{S}} = -H. \tag{2.59}$$

   The fact that chiral transformation is a combination of time-reversal and charge conjugation imposes additional requirements on the operator U_{S}, namely it must be unitary, Hermitian, and local (act in the same way within each unit cell) [106]. In momentum space chiral symmetry requires

$$\mathcal{S}: \quad U_{\mathrm{S}}^{\dagger} H_k U_{\mathrm{S}} = -H_k. \tag{2.60}$$

For Floquet-Bloch systems the above criteria can be formulated as follows [120, 121]:

1. Time reversal symmetry is present if there exist such a time moment $t_0 \in [0, T]$ and a unitary operator U_{T} that

$$\mathcal{T}: U_{\mathrm{T}}^{\dagger} H_k^{*}(t_0 + t) U_{\mathrm{T}} = H_{-k}(t_0 - t); \tag{2.61}$$

2. Charge conjugation implies the existence of such a unitary matrix U_{C} that

$$\mathcal{C}: \quad U_{\mathrm{C}}^{\dagger} H_k(t)^{*} U_{\mathrm{C}} = -H_k(t); \tag{2.62}$$

3. Finally, for chiral symmetry there exist such a unitary operator U_{S} and a time point $t_0 \in [0, T]$ that

$$\mathcal{S}: \quad U_{\mathrm{S}}^{\dagger} H_k(t_0 + t) U_{\mathrm{S}} = -H_k(t_0 - t). \tag{2.63}$$

Presence of the generalized symmetries leads to important consequences for the energy (or quasienergy) spectrum of a system.

1. Namely, if time-reversal symmetry is satisfied, then the spectrum is symmetric around $k = 0$, in other words, the eigenenergies of the eigenstates with momenta k and $-k$ are equal $\epsilon(k) = \epsilon(-k)$;
2. If the Hamiltonian obeys charge conjugation symmetry then $\epsilon(k) = -\epsilon(-k)$;
3. If chiral symmetry is present, then the spectrum of a system is symmetric around $\epsilon = 0$, i.e. $\epsilon(k) = -\epsilon(k)$.

CHAPTER 3

Theoretical basics of surface plasmon polariton waveguides

The present chapter contains the essential theoretical background for understanding the working principle of our experimental platform that are arrays of dielectric loaded surface plasmon polariton waveguides. Section 3.1 is devoted to the introduction to surface plasmon polaritons (SPPs), the electromagnetic waves living at the interface between metal and dielectric. It begins with the fundamentals of electromagnetism and the optical properties of metals which give rise to the existence of SSPs. Next, the relevant methods of their excitation and detection are discussed. In Section 3.2 SPP propagation in dielectric waveguide structures is considered: from a single waveguide up to an array of N coupled waveguides. Lastly, we explain how arrays of plasmonic waveguides can be used as quantum simulators.

3.1 Introduction to surface plasmon polaritons

3.1.1 Fundamentals of electromagnetism

The existence of surface plasmon polaritons can be well understood within the framework of classical electromagnetism which firmly relies on the laws formulated by James Clerk Maxwell in early 1860s [68]. These laws link four macroscopic fields: the dielectric induction **D**, the electric field **E**, the magnetic induction **B**, and the magnetic field **H**. In the SI unit convention, the Maxwell's equations are given by [69]

$$\nabla \cdot \mathbf{D}(\mathbf{r}, t) = \rho(\mathbf{r}, t), \tag{3.1a}$$

$$\nabla \cdot \mathbf{B}(\mathbf{r}, t) = 0, \tag{3.1b}$$

$$\nabla \times \mathbf{E}(\mathbf{r}, t) = -\frac{\partial \mathbf{B}(\mathbf{r}, t)}{\partial t}, \tag{3.1c}$$

$$\nabla \times \mathbf{H}(\mathbf{r}, t) = \mathbf{j}(\mathbf{r}, t) + \frac{\partial \mathbf{D}(\mathbf{r}, t)}{\partial t}, \tag{3.1d}$$

where ρ is the charge density and $\mathbf{j}$ is the current density. The auxiliary fields $\mathbf{D}$ and $\mathbf{H}$ are defined as

$$\mathbf{D} = \varepsilon_0 \mathbf{E} + \mathbf{P}, \tag{3.2a}$$

$$\mathbf{H} = \frac{1}{\mu_0}\mathbf{B} + \mathbf{M}, \tag{3.2b}$$

where $\mathbf{P}$ is the volume density of electric dipole moments (polarization), $\mathbf{M}$ is the density of magnetic moments (magnetization), ε_0 [1] is the vacuum permittivity, and μ_0 [2] is the vacuum permeability. In the present thesis we can limit ourselves to consideration of linear, isotropic and non-magnetic media with $\mathbf{P}$ and $\mathbf{M}$ being proportional to the electric and magnetic field, respectively. As a result, the constitutive relations take a simple form

$$\mathbf{D} = \varepsilon_0 \varepsilon \mathbf{E}, \tag{3.3a}$$

$$\mathbf{B} = \mu_0 \mathbf{H}, \tag{3.3b}$$

with ε being the relative permittivity (also called dielectric function).
Later on it will be important to understand how the electromagnetic fields behave at an interface between two isotropic media. If there are no free charges and free currents at the interface, i.e. $\rho = 0$ and $\mathbf{j} = 0$, the boundary conditions imply the continuity of the tangential components of the electric and magnetic fields and the continuity of the normal components of the electric and magnetic inductions. These conditions follow from the Maxwell's equations and are summarized below [69]

$$\hat{\mathbf{n}} \times (\mathbf{E}_2 - \mathbf{E}_1) = 0, \tag{3.4a}$$

$$\hat{\mathbf{n}} \times (\mathbf{H}_2 - \mathbf{H}_1) = 0, \tag{3.4b}$$

$$\hat{\mathbf{n}} \cdot (\mathbf{D}_2 - \mathbf{D}_1) = 0, \tag{3.4c}$$

$$\hat{\mathbf{n}} \cdot (\mathbf{B}_2 - \mathbf{B}_1) = 0, \tag{3.4d}$$

where $\hat{\mathbf{n}}$ is a unit vector, normal to the interface and indices 1 and 2 label two media.
Another significant consequence of the Maxwell's equations is that the oscillating electric field creates an oscillating magnetic field and vice versa giving rise to propagation of electromagnetic waves in free space. The corresponding wave equations are obtained by applying curl ($\nabla\times$) to Eq. (3.1c) or (3.1d) and then using the vector identity $\nabla \times (\nabla \times \mathbf{E}) = \nabla(\nabla \cdot \mathbf{E}) - \nabla^2\mathbf{E}$. In the following we assume no external charges $\rho = 0$ and currents $\mathbf{j} = 0$ and take the constitutive relations form above (3.3a)-(3.3b) into account. Thus, we obtain the wave equation which for the electric field is given by

$$\frac{\varepsilon}{c_0^2}\frac{\partial^2 \mathbf{E}}{\partial t^2} - \nabla^2 \mathbf{E} = 0, \tag{3.5}$$

where $c_0 = 1/\sqrt{\varepsilon_0 \mu_0}$ is the speed of light in vacuum [3]. With the harmonic wave ansatz $\mathbf{E}(\mathbf{r}, t) =$

[1] $\varepsilon_0 \approx 8.854 \times 10^{-12} \frac{\mathrm{F}}{\mathrm{m}}$
[2] $\mu_0 \approx 1.257 \times 10^{-6} \frac{\mathrm{H}}{\mathrm{m}}$
[3] $c_0 \approx 2.998 \times 10^{8} \frac{\mathrm{m}}{\mathrm{s}}$

$\mathbf{E}(\mathbf{r})e^{-i\omega t}$ Eq. 3.5 reduces to the so-called Helmholtz equation [68]:

$$\left(\nabla^2 + \varepsilon k_0^2\right) \cdot \mathbf{E} = 0, \tag{3.6}$$

where by $k_0 = \omega/c_0$ we denoted the vacuum wave number.

3.1.2 Optical properties of metals

Electromagnetic response of metals is a complex interplay of different contributions. If the frequency of an external field is smaller than the energy of the interband transitions, the contribution of conducting electrons dominates and the optical properties can be well described by the classical model named after the German physicist Paul Drude [68, 70]. This model assumes that the electrons in a metal can move freely under the applied external field. The only damping force arises from the random collisions with the static ion cores which happen with the frequency γ_c. All the lattice effects are accounted by the effective electron mass m^* while other interactions are neglected. When the external oscillating field $\mathbf{E}(t) = \mathbf{E}_0 e^{-i\omega t}$ is applied, the equation of motion reads

$$m^*\ddot{\mathbf{x}} + m^*\gamma_c\dot{\mathbf{x}} = -e\mathbf{E}(t), \tag{3.7}$$

where e is the elementary charge[4]. Substituting the harmonic wave ansatz for the electron displacement $\mathbf{x}(t) = \mathbf{x}_0 e^{-i\omega t}$ into Eq. (3.7) one obtains

$$\mathbf{x}(t) = \frac{e\mathbf{E}(t)}{m^*}\frac{1}{\omega^2 + i\gamma_c\omega}. \tag{3.8}$$

The displacement of the electrons distributed with the density n induces the macroscopic polarization:

$$\mathbf{P} = -en\mathbf{x} = -\frac{e^2 n\mathbf{E}(t)}{m^*}\frac{1}{\omega^2 + i\gamma_c\omega}. \tag{3.9}$$

Inserting Eq. 3.9 into the definition (3.2a) and comparing the result with the constitutive relation (3.3a) yields the dielectric function

$$\varepsilon_D(\omega) = 1 - \frac{\omega_p^2}{\omega^2 + i\gamma_c\omega}, \tag{3.10}$$

where $\omega_p^2 = \frac{ne^2}{\varepsilon_0 m^*}$ denotes the plasma frequency.
Up to now we have only considered conducting electrons which turns out to be insufficient to describe the optical properties of the noble metals used in this work, i.e. gold and silver. There are two additional factors that have to be taken into account to make the model more accurate. First, the filled d-band of a noble metal results in a polarization offset which can be accounted by substituting 1 in Eq. (3.10) by $\varepsilon_\infty > 1$. Second, starting from the near infrared frequencies on there is an increasing contribution of the electronic transitions between the bands [71]. This effect however can be easily incorporated in the Drude model by adding the classical Lorenz-oscillator terms with the proper

[4] $e \approx 1.602 \times 10^{-19}$C

resonance frequency ω_j [72]. The resulting dielectric function is given by

$$\varepsilon_{\mathrm{DL}}(\omega) = \varepsilon_\infty + \frac{\omega_\mathrm{p}^2}{\omega^2 + i\gamma_\mathrm{c}\omega} - \sum_j \frac{f_j \omega_j^2}{(\omega_j^2 - \omega^2 - i\omega\gamma_j)}, \tag{3.11}$$

where f_j and γ_j are the corresponding weighting factor and the bandwidth, respectively. The extended equation (3.11) is referred to as *Drude-Lorenz model*. In the Table 3.1 the model parameters for gold and silver are summarized. For the frequency $\omega = 1.266$ eV ($\hbar = 1$ throughout the thesis unless otherwise indicated) corresponding to the experimental wavelength of $\lambda = 0.98$ µm we obtain $\varepsilon_{\mathrm{Au}} = -40.6890 + i2.629$ and $\varepsilon_{\mathrm{Ag}} = -48.770 + i1.750$ for gold and silver, respectively.

	ε_∞	ω_p (eV)	γ_c (eV)	f_1	ω_1 (eV)	γ_1 (eV)	f_2	ω_2 (eV)	γ_2 (eV)
Au	6.210	8.794	0.066	-1	2.646	0.382	-	-	-
Ag	1.798	8.794	0.057	3.008	5.374	288.227	2.341	25.223	39.875

Table 3.1: Parameters of the Drude-Lorenz model for Au and Ag over the 400-1000 nm wavelength range. Taken from [73, 74]

3.1.3 Surface plasmon polaritons

Having discussed the fundamentals of electromagnetic waves and the optical properties of metals we now come to description of surface plasmon polaritons. SPPs are collective oscillations of the electromagnetic field and the conducting electrons localized at the interface between metal and dielectric. Let us consider such an interface perpendicular to the y-axis so that the upper half-space $y > 0$ is filled with a dielectric with permittivity ε_d and the lower half-space $y \leq 0$ with a metal with ε_m as shown in Fig. 3.1. Without loss of generality we choose the z-axis to be the propagation direction and for the sake of simplicity we assume no spatial field variation along the x-axis. With these assumptions and harmonic time dependence, the electric (as well as magnetic) field of SPPs can be written in a form $\mathbf{E}(\mathbf{r}, t) = \mathcal{E}(y)e^{i\beta z}e^{-i\omega t}$, where β is the propagation constant, i.e. the wave vector component in the propagation direction $\beta = k_z$. Inserting this ansatz into the Helmholtz equation (3.6) yields:

$$\frac{\partial^2 \mathcal{E}(y)}{\partial y^2} + \left(\varepsilon k_0^2 - \beta^2\right)\mathcal{E}(y) = 0. \tag{3.12}$$

An analogous equation obviously holds true for the magnetic field $\mathbf{H}$. In the following we will consider two polarization states: TM (transverse magnetic, i.e. $\mathbf{H} = (H_x, 0, 0)^\mathrm{T}$ and $\mathbf{E} = (0, E_y, E_z)^\mathrm{T}$) and TE (transverse electric, i.e. $\mathbf{H} = (0, H_y, H_z)^\mathrm{T}$ and $\mathbf{E} = (E_x, 0, 0)^\mathrm{T}$) which is sufficient as they form a basis

Figure 3.1: Geometry for the SPP propagation at the interface between dielectric and metal.

in the polarization state space [68].
First, we focus on the case of TM-polarization. Using Eq. (3.12) as well as the curl equations (3.1c) and (3.1d) we obtain the explicit expression for the SPP field:

$$\begin{aligned}\mathbf{H}(\mathbf{r},t) &= (1,0,0)^{\mathrm{T}} A_1 e^{ik_{\mathrm{d}}y} e^{i\beta z} e^{-i\omega t} \\ \mathbf{E}(\mathbf{r},t) &= \left(0, -\frac{\beta}{\omega\varepsilon_0\varepsilon_{\mathrm{d}}}, \frac{k_{\mathrm{d}}}{\omega\varepsilon_0\varepsilon_{\mathrm{d}}}\right)^{\mathrm{T}} A_1 e^{ik_{\mathrm{d}}y} e^{i\beta z} e^{-i\omega t}\end{aligned} \tag{3.13}$$

for $y > 0$ and

$$\begin{aligned}\mathbf{H}(\mathbf{r},t) &= (1,0,0)^{\mathrm{T}} A_2 e^{ik_{\mathrm{m}}y} e^{i\beta z} e^{-i\omega t} \\ \mathbf{E}(\mathbf{r},t) &= \left(0, -\frac{\beta}{\omega\varepsilon_0\varepsilon_{\mathrm{m}}}, \frac{k_{\mathrm{m}}}{\omega\varepsilon_0\varepsilon_{\mathrm{m}}}\right)^{\mathrm{T}} A_2 e^{ik_{\mathrm{m}}y} e^{i\beta z} e^{-i\omega t}\end{aligned} \tag{3.14}$$

for y<0, where

$$k_j^2 = k_0^2\varepsilon_j - \beta^2 \qquad j = \mathrm{d}, \mathrm{m} \tag{3.15}$$

are the wave vector components perpendicular to the interface. According to the boundary conditions (3.4a)-(3.4b), the tangential electric and magnetic field components at the interface must be continuous. Thus, comparing Eqs. (3.13) and (3.14) we find that $A_1 = A_2$ and

$$\frac{k_{\mathrm{d}}}{k_{\mathrm{m}}} = \frac{\varepsilon_{\mathrm{d}}}{\varepsilon_{\mathrm{m}}}. \tag{3.16}$$

This relation in combination with Eqs. (3.15) leads to the central result of this section, namely the dispersion relation of SPPs:

$$\beta = k_0\sqrt{\frac{\varepsilon_{\mathrm{d}}\varepsilon_{\mathrm{m}}}{\varepsilon_{\mathrm{d}} + \varepsilon_{\mathrm{m}}}}. \tag{3.17}$$

With the help of Eq. (3.17) the perpendicular wave vector components can be rewritten as:

$$k_j = \mp k_0\sqrt{\frac{\varepsilon_j^2}{\varepsilon_{\mathrm{d}} + \varepsilon_{\mathrm{m}}}}, \qquad j = \mathrm{d}, \mathrm{m}, \tag{3.18}$$

where according to our sign convention "−" stands for $j = \mathrm{d}$ and "+" for $j = \mathrm{m}$. Having Eqs. (3.17) and (3.18) at hand, we can derive the conditions under which the propagating surface waves can exist. For simplicity, we neglect the imaginary parts of the dielectric functions. First, in order to have propagating waves, β must be real and therefore the radicand in (3.17) positive. Second, localization at the interface demands that both k_{d} and k_{m} are imaginary which holds true only when the denominator in (3.18) is negative. Combining these considerations we arrive at:

$$\begin{aligned}\varepsilon_{\mathrm{d}} + \varepsilon_{\mathrm{m}} &< 0 \\ \varepsilon_{\mathrm{d}} \cdot \varepsilon_{\mathrm{m}} &< 0\end{aligned} \tag{3.19}$$

The conditions (3.19) are satisfied only if one of the dielectric functions is negative and has the larger absolute value. As we have calculated in the previous subsection, the dielectric functions of gold and silver indeed have the large negative real part with the relatively small imaginary part at the frequency of interest. Consequently, the SPPs can exist in this case at the interface between a metal and such

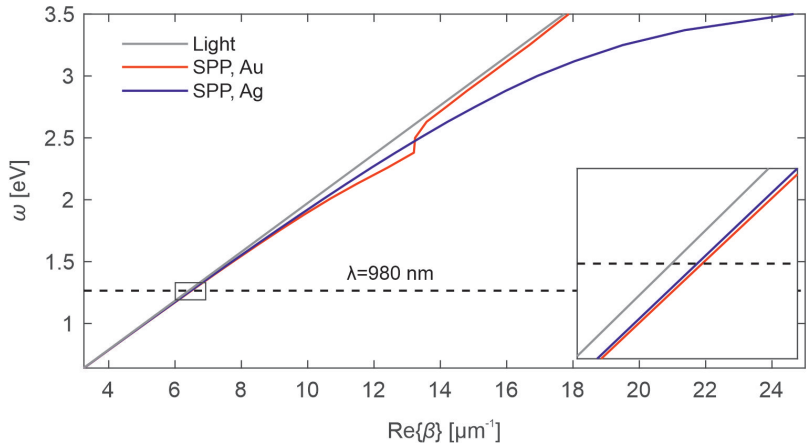

Figure 3.2: Dispersion curve for SPPs propagating at the air-gold (red) and air-silver (blue) interfaces and photons (grey) in the air at the near infrared and visible regime. The black dashed line highlights the experimentally relevant frequency $\omega = 1.266$ eV.

dielectric media as air $\varepsilon_d = 1$ or fused silica $\varepsilon_d = 2.25$.
Before discussing the properties of propagating SPPs, we briefly touch upon the case of TE polarization. Following the same reasoning as for TM polarization, it is easy to show that the continuity of the non-zero tangential field components implies that $k_d = k_m$ [68]. This equality contradicts with the requirement of localization at the interface and hence no SPPs can exist with TE polarization.
Now let us have a closer look at the dispersion relation of SPPs (3.17). In the following we no longer neglect the imaginary part of the SPP propagation constant and denote $\beta = \beta' + i\beta''$. In Fig. 3.2 the real part of the SPP dispersion $\beta'(\omega)$ is plotted for the interface air-metal and compared to the light line in the air. It is seen that at the same frequency ω the propagation constant of an SPP is larger than the wave vector of light in free space, i.e. $\beta' > k_0$. The ratio

$$n_{\text{eff}} = \frac{\beta}{k_0} \tag{3.20}$$

gives the so-called effective refractive index of SPPs and can be regarded as a measure of the momentum difference. For instance, at the free-space wavelength $\lambda = 980$ nm Eq. (3.20) gives $n_{\text{eff}}^{\text{Au}} = 1.0125 + 0.0008i$ and $n_{\text{eff}}^{\text{Ag}} = 1.0105 + 0.0001i$ for gold and silver, respectively.
The imaginary part of the effective refractive index is responsible for the decay of SPPs in propagation direction. The energy dissipation is primarily caused by ohmic losses in a metal and results in a limited propagation length:

$$L = \frac{1}{2\text{Im}\{n_{\text{eff}}\}k_0}, \tag{3.21}$$

which is defined as the distance after which the field intensity drops by the factor of e. The propagation length for gold and silver at $\lambda = 980$ nm is $L^{\text{Au}} = 95\mu$m and $L^{\text{Ag}} = 638\mu$m.
Another important property of SPPs is the strong concentration of the field near the surface in both media. The electromagnetic fields described by (3.13) and (3.14) decay exponentially as $e^{-k_j|y|}$

normal to the interface. The characteristic penetration depth of the SPP field can be defined as follows:

$$\delta_j = \frac{1}{\left|\mathrm{Im}\{k_j\}\right|} \qquad j = \mathrm{d}, \mathrm{m}. \tag{3.22}$$

Applying Eqs. (3.18) and (3.22) to air/gold and air/silver interfaces at $\lambda = 980$ nm we obtain $\delta_{\mathrm{d}}^{\mathrm{Au}} = 984$ nm, and $\delta_{\mathrm{d}}^{\mathrm{Ag}} = 1076$ nm in the air and $\delta_{\mathrm{m}}^{\mathrm{Au}} = 24$ nm and $\delta_{\mathrm{m}}^{\mathrm{Ag}} = 22$ nm in a metal. These values show that the longer propagation length is associated with weaker localization of SPPs in the dielectric media.

3.1.4 Excitation of surface plasmon polaritons

SPPs can be excited either by electrons or photons [75]. In the following we will focus on the latter case as it is more relevant for the experiments described in this thesis. In the previous subsection we have seen that an SPP at the dielectric-metal interface has a larger wave vector (or momentum) than a photon propagating in this dielectric media at the same frequency ω (or energy $\hbar\omega$). Thus, a photon impinging onto the metallic surface from the free space can not excite an SPP due to momentum and energy conservation. The inverse process is likewise forbidden, an SPP does not directly couple to the radiating waves.

There are several ways to overcome the momentum mismatch between SPPs and photons. For example, one can make use of the evanescent field that results from total internal reflection in a coupling medium such as a prism. A prism can be positioned either below the thin metal film in the Kretschmann configuration [76] or very close to a metal surface in the Otto configuration [77]. Alternatively, SPPs can be excited by highly localized light sources placed in the immediate vicinity to the metallic surface, e.g. fluorescent molecules [78] or a tip of a scanning near-field optical microscope [79]. In this thesis we use another method, the so-called grating coupler [68], which is the most suited for our experiments.

The working principle of a grating coupler is sketched in Fig. 3.3. Here, the light with a wave vector $\mathbf{k}_0$ impinges onto a grating of rectangular ridges with a spatial period d at an angle θ. More generally, the grating can be any periodic structure: ridges, grooves, holes etc. When the light hits the grating it gets diffracted. As a result, the wave vector component parallel to the grating $k_{0\|} = k_0 \sin\theta$ can be changed by an integer of the reciprocal lattice vector $\mathbf{g} = \hat{\mathbf{e}}_z 2\pi/d$. SPPs are excited when the phase

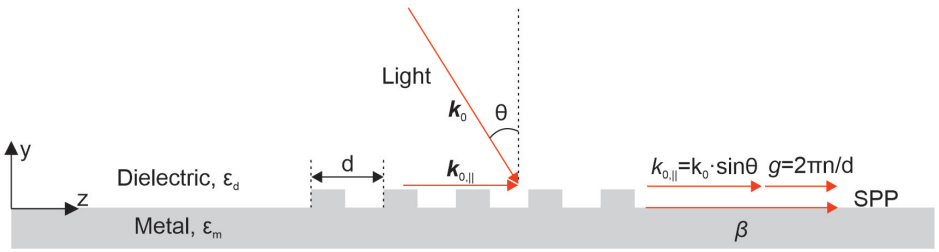

Figure 3.3: Sketch of a grating coupler for excitation of SPPs at the interface between metal and dielectric with ε_{m} and ε_{d}, respectively. The electromagnetic wave the with wave vector $\mathbf{k}_0$ impinges at an angle θ onto the grating with the spatial period d. After diffraction the wave vector component parallel to the grating $\mathbf{k}_{0\|}$ acquires an additional shift $\mathbf{g}$ to match the real part of the SPP wave vector β'.

matching condition is fulfilled:

$$\beta' = k_0 \sin\theta + \frac{2\pi n}{d}, \qquad n \in \mathbb{Z}. \tag{3.23}$$

For normal incidence and the experimentally relevant $\lambda = 980$ nm the required grating period is $d = 968$ nm and $d = 970$ nm for SPPs at air-gold and air-silver interfaces, respectively. We note that SPPs can be also excited by focusing light on the rough metal surface [75], because the random small defects can be thought of as a superposition of gratings with different periods.

3.1.5 Detection of surface plasmon polaritons

Successful optical excitation of SPPs is commonly detected as the reduced intensity of the reflected light [68]. However, for the needs of this thesis, it is highly desirable to access full SPP intensity distribution at the surface as well as SPP momentum distribution. The scanning near field optical microscopy could be the method of choice as it allows to detect not only the amplitude of the SPP field but also its phase [80]. On the downside, scanning a sample line by line can be very time-consuming especially in case of relatively large plasmonic structures as used in our experiments ($\sim$ 100 µm). Therefore, we choose a handier approach, namely leakage radiation microscopy (LRM) [81].
LRM is a far-field technique which enables to obtain full SPP intensity distribution in real or in momentum space with a single measurement. Fig. 3.4 shows the principal scheme of LRM. Here, the metallic film of thickness D is deposited on top pf a glass substrate. SPPs propagate along the air-metal interface so that the momentum mismatch prevents radiation loss into the air ($\beta' > k_0$). However, the SPP mode can leak into the substrate with higher permittivity ($\varepsilon_g = 2.25$) if the metallic film is thin enough for the SPP field to penetrate through. In fact, D must be in the order of the penetration depth of the SPP field in the metal (see Eq. (3.22) and the next subsection). Coupling between SPPs and the radiating mode with a wave vector $\mathbf{k}_{LR}$ occurs when their wave vector components parallel to the surface match, i.e. $k_{LR\parallel} = \beta'$. Denoting by θ_{LR} the emission angle of leakage radiation we come to

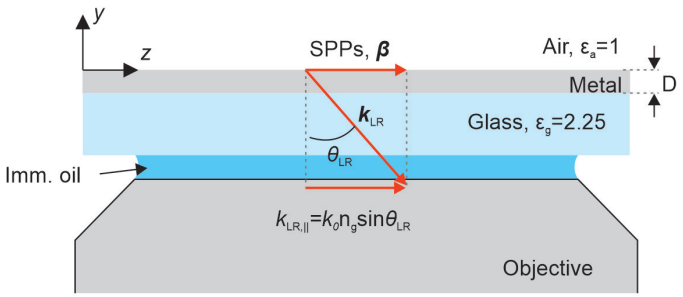

Figure 3.4: Working principal of the leakage radiation microscopy. The glass substrate with permittivity $\varepsilon_g = 2.25$ is covered by a metallic film of thickness D and surrounded by air with $\varepsilon_a = 1$. The SPPs propagate along the air/metal interface with propagation constant β. If the metal layer is thin, the SPP mode becomes leaky and radiates onto the glass substrate at an angle θ_{LR}. The leakage radiation (LR) as well as the transmitted laser beam are collected by the oil immersion objective.

the following phase-matching condition:

$$k_0 n_g \sin\theta_{LR} = \beta', \tag{3.24}$$

where $n_g = \sqrt{\varepsilon_g}$ is the refractive index of the glass substrate ($\theta_{LR} \approx 42^\circ$ for gold and silver at $\lambda = 980$ nm). Note that θ_{LR} is larger than the critical angle of the total internal reflection at glass-air interface. For this reason, leakage radiation must be collected by an oil immersion objective with sufficiently high numerical aperture: NA$> \sqrt{\varepsilon_g}\sin\theta_{LR}$. The collected light can be then imaged onto the camera as described in the chapter "Methods" in Sec. 4.2.1. Looking ahead we note that LRM allows for two options [81]: First, one can image the sample plane and obtain the real-space intensity distribution of SPPs $I(x,z) \propto |E(x,z)|^2$. Second, imaging the back focal plane (BFP) of the oil immersion objective gives an access to the momentum-space intensity distribution which is proportional to the absolute value squared of the 2D Fourier transform of the SPP field:

$$\tilde{I}(k_x, k_z) \propto \left| \iint \mathrm{d}x\mathrm{d}z E(x,z) e^{-ik_x x} e^{-ik_z z} \right|^2. \tag{3.25}$$

Optimal film thickness

After we addressed the basic principle of LRM, we determine the optimal film thickness D. In order to analyse how leakage losses alter the SPP dispersion relation in dependence on D, we consider the system of two interfaces (a/m) air/metal and (m/g) metal/glass coupled via evanescent SPP tunnelling through the metallic layer. The SPP dispersion relation for such a system can only be computed numerically by solving an implicit equation. An elegant way to derive this equation is described in Refs. [75, 81], where authors find zeros of the Fresnel reflectivity for the layered structure (g/m/a). This approach can be understood by noticing that leakage of SPPs through the thin metal slab can be regarded as the reversal of prism coupling in Kretschmann configuration. The Fresnel reflectivity coefficient for the TM wave impinging onto the interface between glass and metal reads:

$$r_{gm} = \frac{k_g/\varepsilon_g - k_m/\varepsilon_m}{k_g/\varepsilon_g + k_m/\varepsilon_m}, \tag{3.26}$$

where $k_g = -\sqrt{k_0^2\varepsilon_g - \beta^2}$ and $k_m = +\sqrt{k_0^2\varepsilon_m - \beta^2}$ are the wave vector components perpendicular to the interface. Likewise, one defines the Fresnel coefficient for the metal-air interface r_{ma} with $k_a = -\sqrt{k_0^2\varepsilon_a - \beta^2}$. The reflectivity of the slab (g/m/a) is given by the sum of the contributions of the primarily reflected wave and those which arise from multiple internal reflections:

$$r_{gma} = r_{gm} + t_{gm} r_{ma} t_{mg} e^{i2k_m D} \sum_{j=1}^{\infty} (r_{mg} r_{ma} e^{i2k_m D})^{j-1} = \frac{r_{gm} + r_{ma} e^{i2k_m D}}{1 + r_{gm} r_{ma} e^{i2k_m D}}, \tag{3.27}$$

where we used the geometric sum and the properties which immediately follow from the corresponding Fresnel coefficients: $t_{gm}t_{mg} = 1 - r_{gm}^2$ and $r_{ij} = -r_{ji}$ (see e.g. [82]). Next, we set the numenator to zero:

$$r_{gm} + r_{ma} e^{i2k_m D} = 0. \tag{3.28}$$

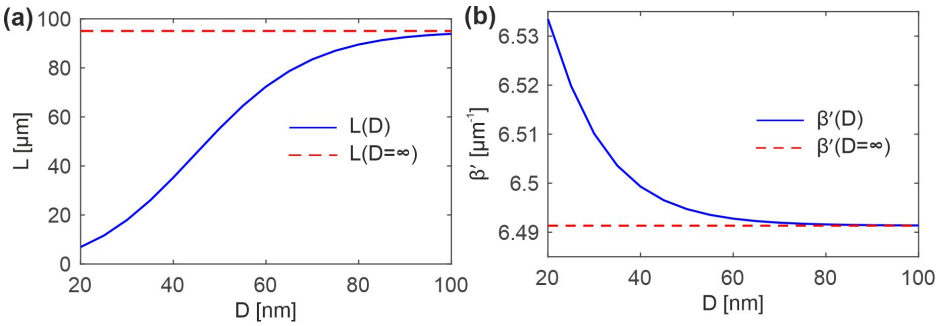

Figure 3.5: Properties of SPPs propagating at the air-gold interface and leaking into the glass in dependence on metal thickness D: (a) Propagation length; (b) Real part of the propagation constant β'.

From the relation above we obtain the desired implicit equation for β:

$$(k_g/\varepsilon_g - k_m/\varepsilon_m)(k_m/\varepsilon_m + k_a/\varepsilon_a) + (k_m/\varepsilon_m - k_a/\varepsilon_a)(k_g/\varepsilon_g + k_m/\varepsilon_m)e^{i2k_m D} = 0. \tag{3.29}$$

Solving Eq. (3.29) numerically we get β' and β'' as a function of the film thickness D.
In Fig. 3.5 we plot the the propagation length and the real part of the propagation constant of SPPs in dependence of D in case of a gold film. If the film is too thick, e.g. $D > 70$ nm, the coupling is so weak that the system behaves almost like disconnected interfaces and leakage radiation can be hardly detected. For smaller thicknesses the coupling enhances, radiation losses increase, hence the propagation length of SPPs shortens (Fig. 3.5 (a)). However, for $D < 50$ nm the coupling is so strong that it also shifts the real part of the propagation constant β' (Fig. 3.5 (b)). Based on the above we can conclude that the optimal thickness lies in between 50 nm and 70 nm because in this region β' remains almost unaffected while at the same time sufficient intensity fraction leaks into the far field. Analogously, one finds that silver behaves in a similar manner.

3.2 Dielectric loaded surface plasmon polariton waveguides

3.2.1 Single DLSPPW

Having discussed the basics of free propagating SPPs we continue with SPP wave-guiding. As we have seen, SPPs are intrinsically tightly bound to an interface between metal and dielectric but are free to propagate in any direction along the surface. It is possible, however, to restrict SPP propagation to a single direction using various waveguide configurations. SPP waveguides range widely: dielectric ridges, metal nano-wires, metal stripes, slots or grooves in a metallic film, chains of metal nanospheres etc [83, 84]. In the following we will focus on the so-called dielectric-loaded surface plasmon polariton waveguides (DLSPPWs) as they are the key components of our quantum simulators.
The key idea of a DLSPPW was borrowed from conventional integrated optics, where the lateral mode confinement is achieved using a high-index dielectric core [85]. Similarly, a dielectric ridge placed on top of a metal film can confine SPPs if the permittivity of the ridge is higher than the permittivity of the surrounding media [86].
Let us consider the DLSPPW geometry sketched in Fig. 3.6. We assume that the metal is gold, the surrounding space is filled with air, and the dielectric stripe consists of poly-methyl-methacrylate

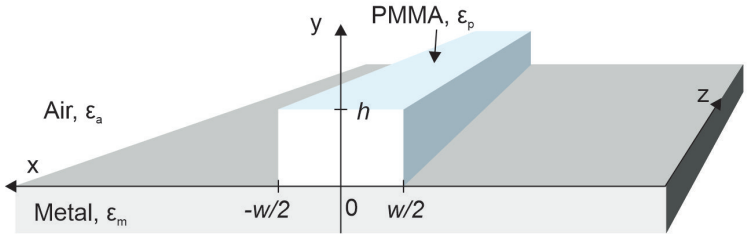

Figure 3.6: Sketch of a DLSPPW. The dielectric ridge made of PMMA with permittivity ε_p lies on a metallic surface (ε_m) surrounded by media (ε_a). h and w denote the height and the width of a DLSPPW respectively.

(PMMA) (refractive index $n = 1.49$). PMMA is a common material for DLSPPWs since it is an electron resist that can be structured at nanoscale using electron beam lithography [86]. The waveguide width and height are set to $w = 250$ nm and $h = 110$ nm, respectively, which is typical for our experiments at the free-space wavelength of $\lambda = 980$ nm. In the z-direction we assume continuous translational symmetry and can therefore limit ourselves to consideration of a cross-section parallel to the xy-plane. The electric field of a guided SPP mode propagating in the z-direction is given by

$$\mathbf{E}(x, y, z, t) = \mathcal{E}(x, y)e^{i(\beta z - \omega t)}. \tag{3.30}$$

Inserting the ansatz (3.30) into the Helmholtz equation (3.6) yields

$$\nabla_\mathrm{t}^2 \mathcal{E} + \left(\varepsilon(x, y)k_0^2 - \beta^2\right)\mathcal{E} = 0, \tag{3.31}$$

where $\nabla_\mathrm{t}^2 = \partial_x^2 + \partial_y^2$ is the Laplacian in the transverse plane and $\varepsilon(x, y)$ is the permittivity, which is homogeneous within each medium:

$$\varepsilon(x, y) = \begin{cases} \varepsilon_\mathrm{p} & \text{if } (-w/2 \le x \le w/2) \text{ and } (0 \le y \le h) \\ \varepsilon_\mathrm{m} & \text{if } y < 0 \\ \varepsilon_\mathrm{a} & \text{elsewhere.} \end{cases} \tag{3.32}$$

At each interface between two different media the usual boundary conditions for the electric and magnetic fields hold (see Eqs. (3.4a)-(3.4d)). This boundary value problem for the partial differential equation (PDE) lacks an analytical solution, but can be solved numerically e.g. using the finite element method (FEM) [85, 87].
In FEM the finite-sized model domain is discretized into small elements, usually triangles in 2D problems or tetrahedrons in the 3D case. Within each element the unknown continuous variable (e.g. electric field) is approximated by a basis function. This function is connected to the ones in the neighboring elements at the nodal points (vertexes of the triangles). The PDE with the corresponding boundary conditions is then replaced by a system of algebraic equations, whose solution gives an approximation of the PDE solution.
In order to access the electromagnetic field distribution and dispersion relation of a guided SPP mode we perform FEM calculations using *COMSOL Multiphysics*. We assume that the field is localized around the dielectric ridge and falls off to almost zero at the boundary of the modelling area Ω. For

that we choose a sufficiently large model domain $\Omega = (-3\ \mu\text{m} \leq x \leq 3\ \mu\text{m}) \cup (-1\ \mu\text{m} \leq y \leq 3\ \mu\text{m})$ and at the exterior boundary $\partial\Omega$ we set the boundary condition of a perfect electric conductor [88]:

$$(\hat{\mathbf{n}} \times \mathbf{E}) = 0. \tag{3.33}$$

Next, we discretize our 2D domain using triangle mesh. Since the accuracy of the FEM calculations depends on the mesh size, we use finer mesh for the regions where we expect faster change of the field. The maximum element size inside the DLSPPW is set to 10 nm while away from the ridge the element size can reach 200 nm.
After finite element analysis we obtain the electric field distribution $\mathcal{E}(x, y)$, $x, y \in \Omega$. In Fig. 3.7 (a) we plot the absolute value of the normal field component $\mathcal{E}_y(x, y)$ in arbitrary units. As expected, the field is concentrated in the PMMA ridge and decays exponentially into air and metal. Due to conservation of the normal component of the dielectric induction, $\mathcal{E}_y$ experiences jumps at every horizontal interface between the media, e.g. air/PMMA and air/gold. The resulting mode index equals $n_{\text{eff}} = 1.038 + 0.0022i$. Here, the real and imaginary parts of n_{eff} are larger than the ones for free propagating SPPs (see Sec. 3.1.3). This is due to the higher index of the PMMA and associated stronger confinement of SPPs to the surface.
In the next step we study how the mode index depends on the geometrical parameters of DLSPPWs. For that we perform FEM calculations for different height values in the range from 90 nm to 190 nm and the widths of $w = 200$ nm, 250 nm, and 300 nm. The real and imaginary parts of n_{eff} are shown in Figs. 3.7 (b) and (c), respectively. It is evident that the larger the cross-section of the PMMA ridge, i.e. the product $h \times w$, the stronger is field confinement to the interface and, consequently, the larger are both the real and the imaginary parts of the mode index. This dependency remains also if the shape of a DLSPPW deviates from a perfect rectangle [89].

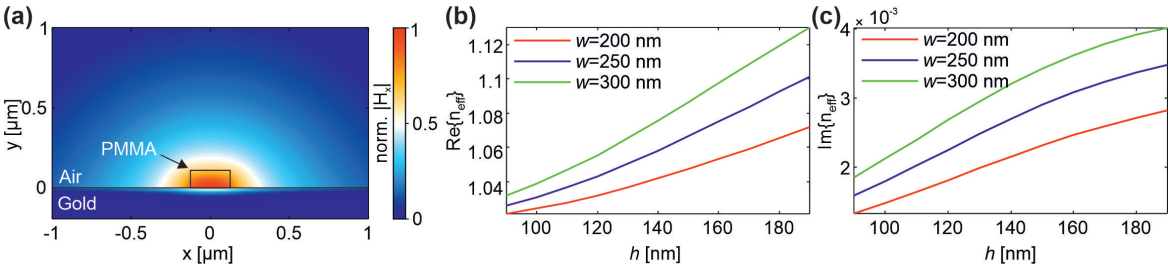

Figure 3.7: (a) Normalized modulus of electric component $\mathcal{E}_y$ in a single-standing DLSPPW calculated by FEM. (b) Real and (c) imaginary part of the guided mode index versus DLSPPW heigh h at constant widths w.

Single-mode condition

Note that at a further increased width, a DLSPPW can also support higher order modes TM_{0n} [86, 88]. At the fixed height value h, the single-mode condition for a DLSPPW is given by the cut-off width w_{cut} for the TM_{01} mode, i.e. the minimum ridge width which supports two modes. As shown in Ref. [88], the cut-off width can be estimated using the effective index method (EIM). This approach is based on the assumption that the variables x and y in the Helmholtz equation (3.31) can be separated. It allows to split the original problem into a system of two 1D Helmholtz equations that can be solved individually using the standard procedure for the planar slab waveguides (e.g. see [85]). As a result,

one comes to the following single-mode condition [88]:

$$w_{\mathrm{cut}} = \frac{\pi}{k_0\sqrt{n'^2_{\mathrm{mpa}}(h) - n'^2_{\mathrm{ma}}}}. \tag{3.34}$$

Here, n'_{ma} is the real part of the effective refractive index of SPPs propagating at an interface metal/air (see Eq. (3.20)), while $n'_{\mathrm{mpa}}(h)$ corresponds to the SPPs on a metallic surface coated with a PMMA layer of thickness h and surrounded by air. One expects that the latter quantity should have the following limits: $\lim_{h\to 0} n'_{\mathrm{mpa}}(h) = n'_{\mathrm{ma}}$ and $\lim_{h\to\infty} n'_{\mathrm{mpa}}(h) = n'_{\mathrm{mp}}$, where n'_{mp} stands for SPPs at a metal/PMMA interface. It was indeed shown that with increasing coating thickness h, the index $n'_{\mathrm{mpa}}(h)$ grows monotonously between these limiting values [75, 88]. Substituting the upper limit n'_{mp} into Eq. (3.34) we obtain $w_{\mathrm{cut}} = 426$ nm. In all our experiments we will always work below this value to ensure the single-mode regime at any DLSPPW height.

3.2.2 Coupling between two DLSPPWs

After we investigated the characteristics of a single DLSPPW, we move on to the case of multiple waveguides. If two or more waveguides are brought into close proximity, so that their mode wave functions overlap, mode coupling occurs leading to power exchange between the waveguides. The wave propagation in a coupled waveguide system can be analysed with the help of the coupled mode theory (CMT). This approach relies on the assumption that if the waveguides are well separated (weak coupling regime) the eigenmodes of a coupled system can be approximated by a linear combination of individual waveguide modes [85]. Nowadays, several CMT formulations exist varying in the application area and accuracy (see [90] and references therein). It is beyond the scope of this thesis to discuss all these formulations. Instead, we will focus on the conventional CMT which assumes that the waveguide modes are orthogonal to each other. Despite a number of simplifications and assumptions, this formulation showed itself well-suited to capture the essential physics behind our experiments with DLSPPWs.

To derive the CMT equations we adapt the approach described in Ref. [91] to TM modes and consider two single-mode DLSPPWs with permittivities $\varepsilon_{1,2}$ spaced at a distance d (see Fig. 3.8). Let $\varepsilon_{\mathrm{ma}}(x, y)$ be the permittivity distribution in the xy plane for a free metal/air interface: $\varepsilon_{\mathrm{ma}}(x, y) = \varepsilon_{\mathrm{m}}$ in metal ($y \leq 0$) and $\varepsilon_{\mathrm{ma}}(x, y) = \varepsilon_{\mathrm{a}}$ in air (y>0). For convenience, we introduce the excess permittivity due to the presence of the waveguides $\Delta\varepsilon_j(x, y)$, which takes the value $\varepsilon_j - \varepsilon_{\mathrm{a}}$ inside the waveguide j

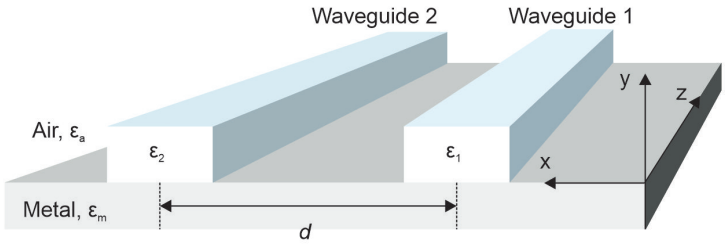

Figure 3.8: Two DLSPPWs with permittivities $\varepsilon_{\mathrm{a}} + \Delta\varepsilon_{1,2}$ separated by a distance d. ε_{a} denotes the permittivity of the surrounding media (air).

($j = 1, 2$) and zero elsewhere. Thus, the permittivity distribution of the composite system can be written as a sum $\varepsilon(x, y) = \varepsilon_{\mathrm{ma}}(x, y) + \Delta\varepsilon_1(x, y) + \Delta\varepsilon_2(x, y)$.
We denote the fields of the individual waveguide modes before coupling by $(\mathbf{E}_1, \mathbf{H}_1)$ and $(\mathbf{E}_2, \mathbf{H}_2)$. With homogeneity in the z direction these fields have the form:

$$\mathbf{E}_j(x, y, t) = \mathcal{E}_j(x, y)e^{i(\beta_j z - \omega t)}, \tag{3.35}$$

$$\mathbf{H}_j(x, y, t) = \mathcal{H}_j(x, y)e^{i(\beta_j z - \omega t)}. \tag{3.36}$$

and therefore satisfy the following Helmholtz equation:

$$\left(\partial_x^2 + \partial_y^2 + k_0^2(\varepsilon_{\mathrm{ma}}(x, y) + \Delta\varepsilon_j(x, y))\right)(\mathcal{E}_j, \mathcal{H}_j) = \beta_j^2(\mathcal{E}_j, \mathcal{H}_j), \quad j = 1, 2, \tag{3.37}$$

where β_j is the propagation constant of the mode j. In the following we neglect the propagation losses and assume $\beta_j'' \approx 0$. This substantially simplifies the derivation, while the losses can be incorporated later to the final result.
The optical power carried by each mode is given by the time average of the normal component of the Poynting vector [85]:

$$P_j = \frac{1}{2}\mathrm{Re}\iint \left(\mathbf{E}_{\mathrm{t}j} \times \mathbf{H}_{\mathrm{t}j}^*\right)_z \mathrm{d}x\mathrm{d}y \tag{3.38}$$

where t denotes the transverse field component. In the absence of losses P_j is conserved. When the waveguides are far apart, the interaction between the modes tends to zero. In this case, the modes obey the orthogonality condition, i.e. the total power flow in the composite system is the sum of the powers carried by each mode individually:

$$P_{\mathrm{sum}} = \frac{1}{2}\mathrm{Re}\iint \left(\mathbf{E}_{\mathrm{t}} \times \mathbf{H}_{\mathrm{t}}^*\right)_z \mathrm{d}x\mathrm{d}y = P_1 + P_2, \tag{3.39}$$

where $\mathbf{E}_{\mathrm{t}} = \mathbf{E}_{\mathrm{t}1} + \mathbf{E}_{\mathrm{t}2}$ and $\mathbf{H}_{\mathrm{t}} = \mathbf{H}_{\mathrm{t}1} + \mathbf{H}_{\mathrm{t}2}$. The mode orthogonality therefore implies that the cross terms in (3.39) must vanish:

$$\frac{1}{2}\mathrm{Re}\iint \left(\mathbf{E}_{\mathrm{t}j'} \times \mathbf{H}_{\mathrm{t}j}^*\right)_z \mathrm{d}x\mathrm{d}y = \delta_{j',j}, \tag{3.40}$$

where $\delta_{j',j}$ is the Kronecker delta and the input power of each mode P_j is normalized to 1 W. We know that plasmonic modes have TM polarization. Since the orthogonality relation is applied to the transversal field components, it is convenient to continue our derivation in terms of the magnetic field. Applying the Maxwell equation (3.1d) to TM modes, Eq. (3.40) reduces to:

$$\frac{\beta_{j'}}{2\omega\varepsilon_0}\iint \frac{\mathcal{H}_{j'} \cdot \mathcal{H}_j^*}{\varepsilon(x, y)}\mathrm{d}x\mathrm{d}y = \delta_{j',j}. \tag{3.41}$$

where we neglect the imaginary part of the permittivity distribution $\varepsilon(x, y)$ because the DLSPPW modes are mostly concentrated in a dielectric structure and decay within a short range inside a metal. If the orthogonality relation holds true, the individual waveguide modes form a complete orthogonal basis and any arbitrary electromagnetic field propagating along the composite waveguide structure

can be expressed as a superposition of the modal fields:

$$\mathbf{H}(x,y,z,t) = a_1(z)\mathcal{H}_1(x,y)e^{i(\beta_1 z-\omega t)} + a_2(z)\mathcal{H}_2(x,y)e^{i(\beta_2 z-\omega t)}, \tag{3.42}$$

where $a_{1,2}(z)$ are the modal expansion coefficients which are to be found. This field obeys the wave equation 3.5, which for our geometry takes the form:

$$\left(\partial_x^2+\partial_y^2+\partial_z^2+k_0^2(\varepsilon_{\text{ma}}(x,y)+\Delta\varepsilon_1(x,y)+\Delta\varepsilon_2(x,y))\right)\mathbf{H}=0. \tag{3.43}$$

Substituting the CMT ansatz (3.42) into (3.43) we assume slow variation of the modal coefficients, i.e. neglect the second order derivatives $\mathrm{d}^2a_j/\mathrm{d}z^2$. With the help of Eq. (3.37) we come to:

$$2i\beta_1\frac{\mathrm{d}a_1}{\mathrm{d}z}\mathcal{H}_1e^{i\beta_1 z}+2i\beta_2\frac{\mathrm{d}a_2}{\mathrm{d}z}\mathcal{H}_2e^{i\beta_2 z}+a_1k_0^2\Delta\varepsilon_2\mathcal{H}_1e^{i\beta_1 z}+a_2k_0^2\Delta\varepsilon_1\mathcal{H}_2e^{i\beta_2 z}=0. \tag{3.44}$$

Next, we multiply Eq. 3.44 by $\mathcal{H}_1^*/\varepsilon(x,y)$ and $\mathcal{H}_2^*/\varepsilon(x,y)$ and integrate over the whole xy plane using the orthonormalization condition 3.41. As a result, we obtain:

$$\begin{aligned}\frac{\mathrm{d}a_1}{\mathrm{d}z}&=iJ_{11}a_1+iJ_{12}a_2e^{i(\beta_2-\beta_1)z}\\ \frac{\mathrm{d}a_2}{\mathrm{d}z}&=iJ_{22}a_2+iJ_{21}a_1e^{i(\beta_1-\beta_2)z},\end{aligned} \tag{3.45}$$

where

$$\begin{aligned}J_{jj}&=\frac{\omega\mu_0}{4}\iint\frac{\mathcal{H}_j^*\Delta\varepsilon_{j'}(x,y)\mathcal{H}_j}{\varepsilon(x,y)}\mathrm{d}x\mathrm{d}y,\\ J_{j'j}&=\frac{\omega\mu_0}{4}\iint\frac{\mathcal{H}_{j'}^*\Delta\varepsilon_{j'}(x,y)\mathcal{H}_j}{\varepsilon(x,y)}\mathrm{d}x\mathrm{d}y,\quad j,j'=1,2.\end{aligned} \tag{3.46}$$

The overlap integrals above are carried out only inside the core of the j'^{th} waveguide, because $\Delta\varepsilon_{j'}(x,y)$ is zero elsewhere. From the previous subsection we know that the mode fields decay exponentially away from the waveguide core. It implies that J_{jj} and $J_{j'j}$ depend as $e^{-\eta d}$ on the separation d, where η is the decay rate, and $J_{jj}\ll J_{j'j}$ since $\mathcal{H}_{j'}(x,y)\ll\mathcal{H}_j(x,y)$ for $(x,y)\in$ waveguide j.
Eqs. (3.45) can be rewritten with the new variables $\tilde{a}_j=a_je^{i\beta_j z}$:

$$\begin{aligned}\frac{\mathrm{d}\tilde{a}_1}{\mathrm{d}z}&=i\tilde{\beta}_1\tilde{a}_1+iJ_{12}\tilde{a}_2\\ \frac{\mathrm{d}\tilde{a}_2}{\mathrm{d}z}&=i\tilde{\beta}_2\tilde{a}_2+iJ_{21}\tilde{a}_1,\end{aligned} \tag{3.47}$$

where $\tilde{\beta}_j=\beta_j+J_{jj}$. Now it becomes evident, that the terms J_{jj} represent a small correction to the propagation constant β_j due to the coupling effect ($J_{jj}\ll\beta_j$), while $J_{j'j}$ are the coupling constants responsible for the power exchange between the waveguides. Due to mode normalization, the total power in the waveguide system is given by $P=\sum_j|\tilde{a}_j|^2$. The power flux conservation implies

$\mathrm{d}P/\mathrm{d}z \equiv 0$ or

$$\frac{\mathrm{d}\sum_j |\tilde{a}_j|^2}{\mathrm{d}z} = \sum_j \left(\tilde{a}_j \frac{\mathrm{d}\tilde{a}_j^*}{\mathrm{d}z} + \tilde{a}_j^* \frac{\mathrm{d}\tilde{a}_j}{\mathrm{d}z} \right) = i \sum_{j'j} \left(J_{j'j} - J_{jj'}^* \right) \tilde{a}_{j'}^* \tilde{a}_j \equiv 0, \tag{3.48}$$

from which we derive the reciprocity relation between the couplings $J_{j'j} = J_{jj'}^*$.
Assume that at $z = 0$ we start with the boundary conditions $\tilde{a}_1(0) = 1$ and $\tilde{a}_2(0) = 0$. Solving the CMT equations (3.47) yields:

$$\begin{aligned} \tilde{a}_1(z) &= (\cos \Omega z + i(\Delta/\Omega) \sin \Omega z) e^{i\phi z}, \\ \tilde{a}_2(z) &= i(J_{21}/\Omega) \sin \Omega z e^{i\phi z}, \end{aligned} \tag{3.49}$$

where $\Delta = (\tilde{\beta}_2 - \tilde{\beta}_1)/2$, $\Omega = \sqrt{\Delta^2 + J_{12}J_{21}}$, and $\phi = (\tilde{\beta}_1 + \tilde{\beta}_2)/2$. In terms of powers in the two waveguides $P_j = |a_j|^2$ the solution is given by

$$\begin{aligned} P_1(z) &= \cos^2 \Omega z + (\Delta/\Omega)^2 \sin^2 \Omega z, \\ P_2(z) &= (J_{21}/\Omega)^2 \sin^2 \Omega z. \end{aligned} \tag{3.50}$$

This result indicates that due to coupling the power flux is periodically exchanged between the waveguides. For identical waveguides, i.e. $\Delta = 0$, the power is completely transferred to the second waveguide after the distance called coupling length

$$L_\mathrm{c} = \frac{\pi}{2|J_{12}|^2}. \tag{3.51}$$

Coupling constants

In real DLSPPWs the energy is not conserved due to propagation losses. Nevertheless, rigorous analysis of the mode coupling in a general case of complex propagation constants and lossy media shows that the system can be still described with the coupled differential equations (3.47) with some modifications to the orthogonality relation and the coupling coefficients [92]. In order to determine the coupling constants in this thesis we will either use the aforementioned mode analysis in COMSOL or measure them experimentally. Both these approaches naturally account for the losses in a plasmonic system and lead to consistent results (see Ref. [93] for details). As an example, in Fig. 3.9 we plot the real part of the coupling constants J obtained with COMSOL against the distance d for three different waveguide heights h = 100 nm, 150 nm, and 200 nm, while the width of the waveguides is kept constant w = 250 nm. The dependency $J(d)$ can be well approximated by an exponential function $\propto e^{-\eta d}$, where the rate η increases with increasing waveguide height. This result is expected since the mode fields become more confined, i.e. decay faster, with increasing waveguide cross-section (see Sec. 3.2.1). The imaginary part of the coupling constant is two orders of magnitude smaller than the imaginary part of the propagation constant and is usually not taken into account.
We note that in the case of non-identical lossy waveguides the coupling constants become in general non-reciprocal, i.e. $J_{jj'} \neq J_{j'j}^*$. The difference between them can be, however, often neglected since it is proportional to the power cross term and gets exponentially small with increasing separation

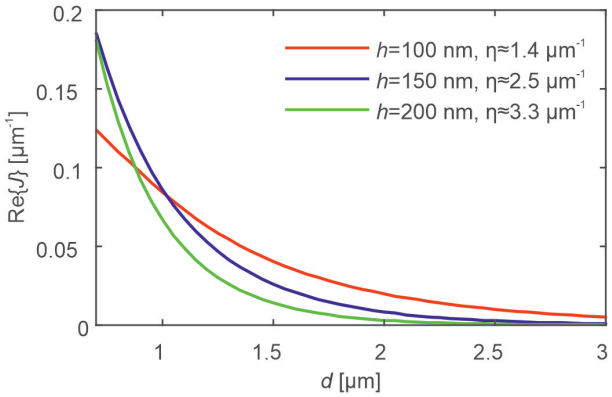

Figure 3.9: Calculated real part of the coupling constant Re$\{J\}$ between two DLSPPWs made of PMMA on gold as a function of distance between the waveguides d at three different waveguide heights h and a constant width $w = 250$ nm. η denotes the exponential factor of the approximating function $\propto e^{-\eta d}$.

d. Finally, it should be emphasized that regardless of the assumptions we make, the CMT is still an approximation which is valid only for the weakly coupled regime. The accuracy of the conventional CMT in dependence on the spacing between the DLSPPWs was analyzed in Ref. [89].

Variation along the propagation direction

Of particular interest for this thesis is the situation when the parameters of a coupled waveguide system (the waveguides' cross-sections or the spacing between them) are periodically modulated along the propagation distance. If the spatial scale of such modulation Λ is much larger than the spatial scale of the field evolution given by the wavelength λ, i.e. $\Lambda/\lambda \gg 1$, the propagating wavepacket is expected to adiabatically follow slow variations of the permittivity profile $\Delta\varepsilon_j = \Delta\varepsilon_j(x, y, z)$ and the system can be described by Eqs. (3.47) where the propagation and coupling constants are replaced by the corresponding functions of z: $\beta_j = \beta_j(z)$ and $J_{jj'} = J_{jj'}(z)$ [94].

3.2.3 Array of N coupled DLSPPWs

The approach discussed above can be readily extended to the case of more than two coupled waveguides. Let us consider an array of N parallel DLSPPWs, where each waveguide is characterized by the propagation constant β_j, $j = 1, ..., N$ (see Fig. 3.10). The mode decomposition of the system wave function becomes:

$$\mathbf{H}(x, y, z) = \sum_{j=1}^{N} \tilde{a}_j(z)\mathcal{H}_j(x, y) \tag{3.52}$$

Next, we follow the same procedure as described in the previous subsection and assume that only the next-nearest neighbour coupling is present. It leads to the system of N coupled differential equations analogous to Eqs. 3.47, where the j^{th} modal amplitude evolves as:

$$\frac{\mathrm{d}\tilde{a}_j}{\mathrm{d}z} = i\left(J_{j-1j}\tilde{a}_{j-1} + \beta_j\tilde{a}_j + J_{jj+1}\tilde{a}_{j+1}\right). \tag{3.53}$$

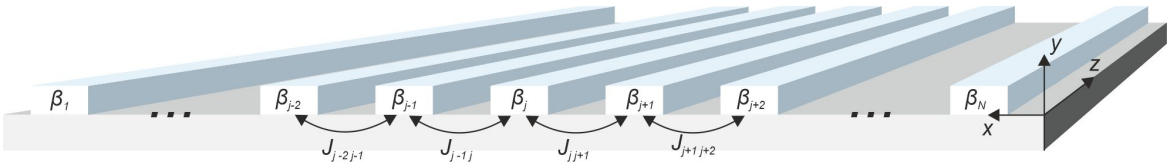

Figure 3.10: An array of N parallel DLSPPWs. β_j is the propagation constant of the j^{th} waveguide and $J_{j,j+1}$ is the coupling between the waveguides j and $j+1$

Here, we neglected the small correction in the propagation constant and assumed that the couplings are real and reciprocal, i.e. $J_{jj\pm1} = J_{j\pm1j}$. The CMT equations (3.53) can be rewritten in a compact matrix form:

$$\frac{\mathrm{d}\mathbf{a}}{\mathrm{d}z} = i\mathbf{M}_{\text{CMT}}\mathbf{a}, \tag{3.54}$$

where

$$\mathbf{a}(z) = \begin{pmatrix} \cdots & \tilde{a}_{j-1} & \tilde{a}_j & \tilde{a}_{j+1} & \cdots \end{pmatrix}^{\text{T}}$$

and

$$\mathbf{M}_{\text{CMT}} = \begin{pmatrix} \ddots & \ddots & & & \\ \ddots & \beta_{j-1} & J_{j-1j} & & \\ & J_{j-1j} & \beta_j & J_{jj+1} & \\ & & J_{jj+1} & \beta_{j+1} & \ddots \\ & & & \ddots & \ddots \end{pmatrix}. \tag{3.55}$$

3.2.4 DLSPPW arrays as quantum simulators

Electromagnetic waves propagating in arrays of coupled waveguides are subject to a spatially periodic refractive index distribution and thus can resemble behaviour of an electron wave function travelling through the periodic potential of a crystal lattice. It is evident, that the time-dependent SE (2.19) in the tight-binding approximation derived in the previous chapter and the CMT equation (3.54) for an array of coupled waveguides have exactly the same mathematical form. In the optical system the propagation distance z plays the role of time t, while the propagation constants β_j and coupling constants $J_{j,j+1}$ stand for the on-site energies E_j and the hopping amplitudes $J_{j,j+1}$, respectively. We on purpose use exactly the same notations for the coupling constants and hopping amplitudes since the physical meaning of both quantities is identical in the scope of this work. The direct comparison yields that the electromagnetic field in the j^{th} waveguide as a function of propagation distance $\tilde{a}_j(z)$ corresponds to the time-dependent probability amplitude of an electron to reside at the j^{th} lattice site, i.e. $p_j(t) = \langle j|\Psi(t)\rangle$. Thus, monitoring the spatial intensity distribution $I(x,z) \propto |\mathbf{E}(x,z)|^2$ in arrays of coupled waveguides one can simulate the temporal evolution of the electron's probability density $|\Psi(x,t)|^2$ in an analogous tight-binding system.
As we have previously discussed in Sec. 3.2, the propagation and coupling constants in a waveguide array can be precisely adjusted by tuning the waveguide geometry. Such a high controllability of the system's parameters and the outstanding ability of direct visualization make waveguide arrays an

attractive platform for quantum simulations. Among the condensed-matter phenomena which have been already realized in this optical setting are Bloch oscillations [25], Zener tunneling [30], Anderson localization [31], dynamic localization [8], and various topological phenomena [98].
An important advantage provided by plasmonic waveguides used in this thesis is a powerful detection technique that is the leakage radiation microscopy introduced in Subsection 3.1.5. It not only captures the full spatial intensity distribution in the array by a single measurement, but also allows for the Fourier imaging. In the quantum-optical analogy the intensity distribution in Fourier space $I(k_x, k_z)$ (see Eq. (3.25)) corresponds to the squared modulus of the 2D Fourier transform of an electron wave function in space and time domains:

$$|\tilde{\Psi}(k,\epsilon)|^2 = \left| \frac{1}{2\pi} \iint \mathrm{d}x\mathrm{d}t \Psi(x,t) e^{-ikx} e^{-i\epsilon t} \right|^2 . \tag{3.56}$$

The above quantity is the momentum and energy resolved probability density which carries information about population and shape of the system's energy bands. In the following chapters the combination of real- and Fourier space imaging will be used to study periodically-driven and topological 1D TB systems.

CHAPTER 4

Experimental methods

In this chapter we touch upon the experimental techniques used to realize and study 1D TB systems with the help of plasmonic waveguide arrays. The chapter is divided into two sections. Section 4.1 is focused on the fabrication of the DLSPPW arrays which mimic the system of interest. Section 4.2 contains the description of optical measurements of SPP propagation in the fabricated arrays that carry information about either the system's temporal evolution in real-space or its momentum-resolved spectrum.

4.1 Sample fabrication

The predictive value of any quantum simulator directly depends on the degree to which one can control the characteristic parameters of the model system. In the case of DLSPPW arrays, it is central to fabricate the waveguides with a precisely adjusted geometry at the nanoscale. In this thesis it is achieved by utilization of electron beam lithography (EBL) [122]. The fabrication process consists of substrate cleaning, evaporation of a metal film, spin coating, and, finally, lithography. Below we discuss them step-by-step along with the methods involved.

4.1.1 Substrate preparation

Substrate cleaning

The fabrication process always starts with the substrate cleaning. As a substrate we use a 22 mm×22 mm microscope cover glass with a thickness of 0.17 mm and a refractive index of $n_g = 1.52$. The cover slips are thoroughly cleaned by wiping them with lens cleaning tissues sequentially soaked in acetone, isopropanol, ethanol, and distilled water. In order to remove residual contamination, the substrates are either immersed in acetone in an ultrasonic bath for 60 min or treated for 10 min at each side in the plasma cleaner *Diener Zepto*. Afterwards, the substrates are ready for the metal film deposition which is done by thermal evaporation.

Thermal evaporation

Thermal evaporation has become the most established deposition method in plasmonics due to its affordability and good performance in creating thin and smooth metallic films [123]. During this process, a material in the high-vacuum chamber (*UNIVEX 250* from *Leybold*) is heated up to its evaporation point by sending an electric current through the tungsten boat in which it is placed. The vaporized material then rises to the substrate which is fixed above the source and homogeneously coats the surface. The evaporation rate and the layer thickness are monitored by a sensor, which detects a change in the resonance oscillation frequency of the quartz crystal driven by the piezo-electric effect. In this thesis we deposit either gold or silver depending on the needs of a particular experiment: While gold films possess lower surface roughness and better chemical stability, silver films enable longer SPP propagation lengths (see Sec. 3.1.3). For both metals the film thickness is chosen to be 60 nm as a good trade-off between the leakage radiation intensity and propagation losses (see Sec. 3.1.5). We note that evaporation conditions for gold and silver substantially differ.
In case of gold, it is sufficient to pump the chamber down to $2 \cdot 10^{-6}$ mbar and use an evaporation rate of 2 $\frac{\text{Å}}{\text{s}}$, which typically consumes 0.25 g of material for 60 nm-thick film. In order to improve adhesion of the film, 5 nm of chromium is deposited prior to gold at a rate of 1 $\frac{\text{Å}}{\text{s}}$. Since the evaporation chamber enables to mount two material sources at once, no the intermediate ventilation between the layers is needed.
In contrast to gold, silver is much more susceptible to residual gases in the chamber such as water vapor and oxygen due to lower adhesion energy and random crystalline orientation of the grains in the film [123]. The effect of residual gases can be minimized by improving vacuum and using higher deposition rates [124]. For our evaporation system the best reachable vacuum is approximately $8 \cdot 10^{-7}$ mbar and the maximum rate which can be stably maintained is 35 $\frac{\text{Å}}{\text{s}}$ [125]. At such a rate, the larger part of the material is lost during the ramp-up of the evaporator. To compensate for these losses, the boat is loaded with approximately 0.75 g of silver. As an adhesion layer we deposit 2 nm of copper below the silver film at a rate of 2 $\frac{\text{Å}}{\text{s}}$.

Spin coating

Before electron beam exposure, an electron resist is spread over the substrate surface via spin coating. As a resist we use polymethylmethacrylate (PMMA) with a molecular weight of 950 k dissolved at 4% in annisole. For spin coating 90 µL of PMMA solution is pipetted onto the metallized side of the substrate. Then the samples are spun in two steps: the first step lasts 3 s at a speed of 500 rpm to distribute the solution over the surface; the second 90 s at 1500 rpm, results in an approximately 200 nm thick polymer film. To remove the residuals of the solvent, the spin-coated samples are annealed on a hot plate for 90 s at 175 °C.

4.1.2 Electron beam lithography

The main principle of EBL is that a focused electron beam scans over the resist that is sensitive to electrons modifying its chemical structure and thereby changing its solubility. It follows by the development step when some parts of the resist get dissolved revealing the transferred pattern. One distinguishes negative- and positive-tone EBL (see Fig. 4.1): In the first case (Fig. 4.1 (a)), the regions exposed to electrons become insoluble in the developer unlike the rest of the resist. This lithography

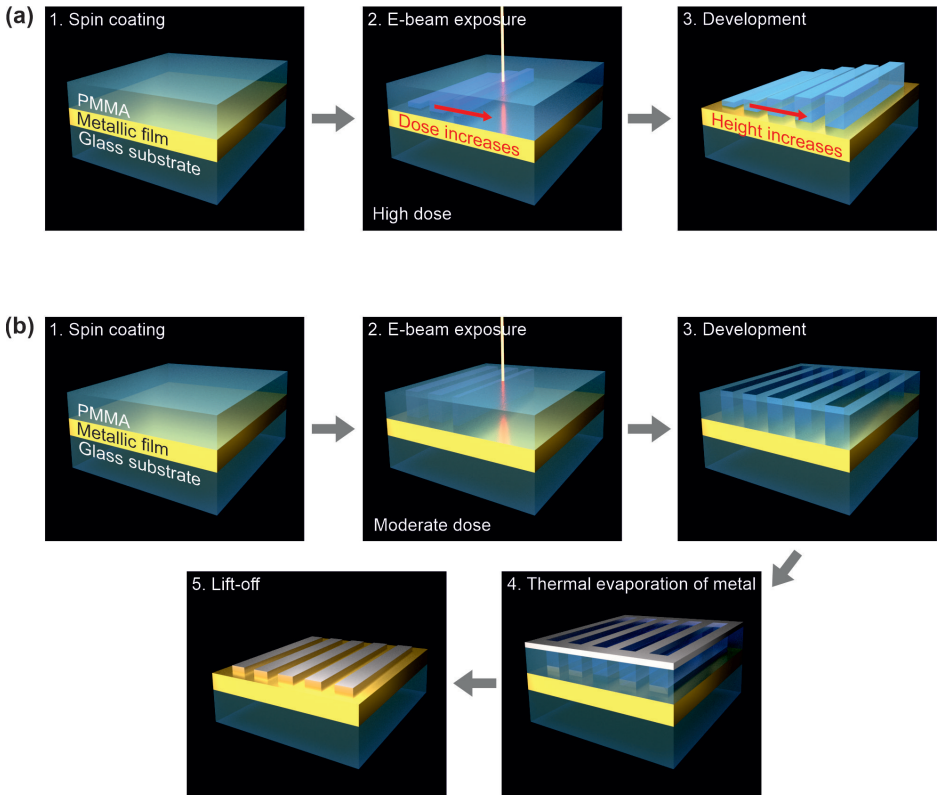

Figure 4.1: The basic steps of the negative- (a) and positive-tone (b) electron beam lithography process.

type, in addition, allows for gray-scale patterning, i.e. the height of the printed structures can be controlled by the applied electron dose. In the second case (Fig. 4.1 (b)), in contrast, the exposed resist is dissolved by a proper solvent thus creating a mask for further processing steps, e.g. metal deposition. Note that depending on the applied electron dose PMMA can act either as a positive- or negative-tone resist [126, 127]: At moderate doses the polymer chains of PMMA are cut into smaller fragments increasing solubility of the resist, while at higher doses these fragments crosslink with each other forming a hard insoluble material.

In order to fabricate DLSPPW arrays, we mostly use gray-scale negative-tone EBL as it is a fast yet high-resolution method to create three-dimensional dielectric nanostructures. However, in chapter 7, positive-tone EBL is utilized as well in order to deposit chromium patches under the waveguides and locally increase propagation losses for SPPs.

Throughout this thesis, the EBL process is carried out inside the *ZEISS Sigma* scanning electron microscope (SEM) equipped with the *Raith ELPHY Plus* EBL system. For electron beam exposure the substrates are mounted onto a mechanical stage and placed inside the vacuum chamber of the SEM which is then pumped. Inside the SEM the electron beam is created by the field-emission gun, accelerated by the acceleration voltage, and focused onto the sample surface by the combination of magnetic and electrostatic lenses and an adjustable aperture. We typically use the acceleration voltage of 10 kV and an aperture diameter of 30 µm.

During the writing process, the beam is deflected by the magnetic scan coils. The maximum beam deflection is determined by the chosen magnification and circumscribes the so-called write field. The

write field containing one array of DLSPPWs has a size of 200 µm×200 µm corresponding to the magnification 300 ×. In order to switch from one write field to another and print several arrays in one EBL process, the substrate is moved relative to the electron beam by the mechanical stage.
In the EBL system the pattern to be written is pixelated. The electron dose assigned to each pixel is related to the beam current I_{beam}, the step size δ_{step} (= pixel size), and the dwell time t_{dwell} (= exposure time per pixel) via:

$$D = \frac{I_{\text{beam}} t_{\text{dwell}}}{\delta_{\text{step}}^2}. \tag{4.1}$$

The step size is fixed and set to 0.0096 µm, while the dwell time required for the given dose is recalculated before every lithography session depending on the magnitude of the electric current. The latter is measured by a Faraday cup integrated into the mechanical stage.

Negative-tone gray-scale EBL

With the chosen SEM settings the negative-tone EBL is performed at electron doses lying between approximately 10 and 35 $\frac{\text{C}}{\text{m}^2}$. Within this range, the height of the printed structure grows with the applied dose from 0 up to the maximum which is defined by the PMMA layer thickness resulting from the spin coating. After electron beam exposure, the unexposed resist is dissolved by development in acetone for 60 s which finalizes the fabrication process (see Fig. 4.1 (a)).
The minimum line width produced by this technique is about 150 nm [126]. The main factor which limits the resolution is the so-called proximity effect, i.e. a smeared-out exposure dose caused by back-scattered and secondary electrons. This effect plays an important role in EBL because in addition to line widening, it strongly affects the structures printed in close vicinity. We discuss this effect in more details below in the subsection "Dose test".

Dose test

Here, we consider the dose test aimed at showing how the geometry of the DLSPPWs produced by negative-tone EBL depends on the exposure dose. In this test the single-standing PMMA ridges are fabricated as described above with different doses in the range of 14 to 28 $\frac{\text{C}}{\text{m}^2}$. Single-standing means that the structures are well separated from each other so that there is no proximity effect from the neighbors. All the ridges are designed to have a width of 350 nm and a length of 180 µm, which are chosen as typical values for the single-mode DLSPPWs. A magnified SEM micrograph of such a waveguide fabricated at a dose of 25.2 $\frac{\text{C}}{\text{m}^2}$ is shown in Fig. 4.2 (a).
The geometrical parameters of these wavegides are measured with atomic force microscopy (AFM) on a *NeaSNOM* microscope. Fig. 4.2 (b) presents a waveguide profile $P(x)$ which results from averaging over 20 AFM scans of a waveguide shown in (a) made with a step of 50 nm along the z-axis. Since the shape of the ridges is asymmetric and evidently deviates from a perfect rectangular due to the proximity effect, we define the characteristic width as $w = \int P(x)\mathrm{d}x/h$, where h is the maximum height of the profile. This definition is motivated by the fact that the propagation constant of a waveguide mainly depends on its cross-section $\int P(x)\mathrm{d}x$ (see Sec. 3.2.1). Therefore, our waveguide can be treated as an effective rectangular with a width w and a height h. We note that our data is slightly influenced by the finite size of an AFM tip, for a detailed analysis see Ref. [93].
In Fig. 4.2 (c) the measured heights h and widths w are plotted against the applied dose D. It is evident that the proximity effect leads to a broadening of the waveguides: The resulting width grows

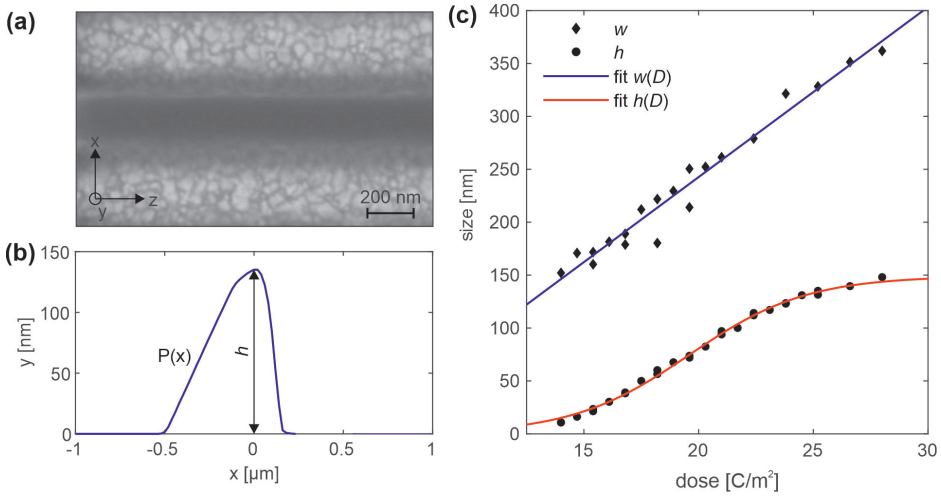

Figure 4.2: (a) Magnified SEM micrograph of a PMMA ridge designed to have a width of 350 nm printed with a dose of 25.2 $\frac{\mathrm{C}}{\mathrm{m}^2}$. (b) The averaged profile of a waveguide shown in (a) obtained from AFM data. Here, h denotes the maximum height of a waveguide. (c) Results of the dose test for single-standing DLSPPWs designed with a constant width of 350 nm. The black diamonds represent the effective widths, while the black circles represent the heights. The fitting functions for measured widths and heights are shown as blue and red lines, respectively.

with the applied dose. This dependency can be fitted by a first-order polynom $w(D) = p \cdot D + q$, where $p = 16.07 \pm 1.52 \frac{\mathrm{nm\,m}^2}{\mathrm{C}}$ and $q = -78.74 \pm 30.16$ nm. The waveguide height as a function of the dose is well described by a sigmoid [93]:

$$h(D) = \frac{a}{e^{-D/b} + c}, \tag{4.2}$$

where the fitting parameters are given by $a = 0.071 \pm 0.033$ nm, $b = 2.56 \pm 0.17 \frac{\mathrm{C}}{\mathrm{m}^2}$, and $c = 4.73 \cdot 10^{-4} \pm 2.14 \cdot 10^{-4}$.
The obtained result is a good starting point for choosing the dose needed to achieve the desired geometrical parameters of PMMA ridges. However, the predictions based on this test are accurate only if separation between the ridges is sufficiently large (> 1.5 µm). It must be taken into account that if waveguides in an array are printed closer to each other, the real exposure dose turns out to be larger than the assigned one due to the proximity effect [128]. This effect can be canceled out by adjusting the exposure dose.

Positive-tone EBL

For the positive-tone EBL in this thesis all the SEM settings other than the exposure dose remain the same as for the negative-tone EBL which enables us to combine both lithography types in one session. The dose of 3 $\frac{\mathrm{C}}{\mathrm{m}^2}$ leads to the fragmentation of long PMMA chains while the crosslinking does not yet occur. At the development stage these low-weight fragments are removed by immersing the samples for 45 s in a developer consisting of a solution 3:1 of isopropanol and methyl isobutylketone (MIBK) with added butanone to 1.5 % of the final volume. The developer is beforehand cooled down to 8 °C in order to increase resolution [129]. As illustrated in Fig. 4.1 (b), it results in a negative mask on top of

which the desired material is deposited by thermal evaporation. At the last lift-off stage, the samples are dipped into 60 °C hot N-Methyl-2-Pyrrolidone (NMP) for 2 hours and then rinsed in acetone and isopropanol. The PMMA mask is dissolved and we obtain the final pattern with sub 10 nm resolution.

4.2 Optical measurements

The fabricated samples are investigated in the optical setup based on leakage radiation microscopy that was introduced in Sec. 3.1.5. In this setup SPPs are excited by a laser beam focused onto the grating deposited on top of one or several DLSPPWs. The excited SPPs then leak into the glass substrate and can be imaged in the real or Fourier space as described below.

4.2.1 Real- and Fourier-space imaging

The operation principal of real- and Fourier-space imaging of leakage radiation is sketched in Fig. 4.3 (a). Here, the first objective (Obj.1) focuses the laser beam onto the sample and excites SPPs. The emitted leakage radiation as well as the transmitted laser beam are collected by a high NA oil immersion objective (Obj. 2). For simplicity, the combination of lenses inside the second objective is substituted by an effective single lens (OL). The colored solid lines display the rays which leave the sample from three different positions in real space at two angles θ_{free} (blue) and θ_{guided} (red) being the leakage radiation angles for free and guided SPPs, respectively. The objective is infinity-corrected so that a ray bundle emitted from one point in the real space becomes collimated after passing through it. As a result, a real-space image cannot be formed without an additional tube

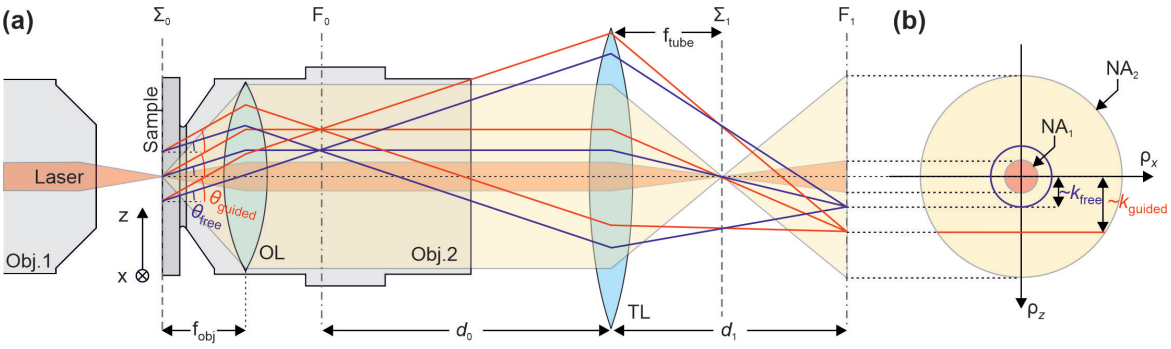

Figure 4.3: (a) Formation of real- and Fourier-space images in leakage radiation microscopy. The laser beam (pale red) is focused by the first objective (Obj.1) onto the sample surface. The transmitted beam and the leakage radiation are collected by the second objective (Obj.2) and imaged with the help of a tube lens (TL). OL denotes the effective objective lens. The cone of light with the maximum opening angle collected by Obj.2 is shown in pale yellow. Different light paths of leakage radiation are displayed as blue and red lines corresponding to the leakage radiation angles of free θ_{free} and guided θ_{guided} SPPs. The focal distances of these lenses are marked as f_{obj} and f_{tube}. Σ_0 and F_0 are the sample plane and the back focal plane of the second objective, respectively. Σ_1 and F_1 are the corresponding image planes produced by the tube lens. d_0 and d_1 are the distances from F_0 to the tube lens and from the tube lens to F_1. (b) Schematic sketch of the light distribution at F_1 in case of excitation of a single DLSPPW. k_{free} and k_{guided} are the wavenumbers of free and guided SPP modes. NA_1 and NA_2 are numerical apertures of the first and the second objectives, respectively.

lens placed behind the objective. The real-image plane (Σ_1) coincides then with the focal plane of this lens. The magnification of a real-space image is given by the ratio between the focal distances of the tube lens and the imaging objective: $M = f_{\text{tube}}/f_{\text{obj}}$. The distance between the objective's lens and the tube lens is called "parallel beam path" or "infinity space". This space is usually utilized to insert additional optical elements into the setup and does not influence the position or magnification of a real-space image. However, note that if the infinity space gets too long it may cause visual artifacts. This happens when the collimated ray bundles deflect from the optical axis so far that a fraction of light cannot be collected by the tube lens due to its finite size.
The Fourier space is accessed by imaging the back focal plane of the second objective (F_0). At this plane all the rays which leave the sample at the same angle (θ_x, θ_z) are focused to one point (ρ_x, ρ_z) no matter where they are emitted from in the real space. For an aplanatic objective the position of this point relative to the optical axis and the emission angle are linked by the Abbe sine condition [130]:

$$\rho_\alpha = f_{\text{obj}} n \sin\theta_\alpha \quad \alpha = x, z, \tag{4.3}$$

where n is the refractive index of immersion oil. Hence, the outmost points of the F_0 are spaced away from the optical axis at a distance $\rho_{\text{max}} = f_{\text{obj}} n \sin\theta_{\text{max}} = f_{\text{obj}}\text{NA}_2$, where NA_2 is the numerical aperture of the second objective.
Now, we recall that the leakage radiation angle of SPPs is related to the SPP wave vector via Eq. (3.24). Denoting by k_x and k_z the corresponding components of the real part of the SPP wave vector and using Eqs. (3.24) and (4.3) we come to

$$\rho_\alpha = f_{\text{obj}} \frac{k_\alpha}{k_0}, \quad \alpha = x, z, \tag{4.4}$$

where k_0 is the vacuum wavenumber. Thus, in the back focal plane we observe the momentum distribution of propagating SPPs (see Eq. (3.25)).
In order to generate an image of F_0 we can utilize the same tube lens (see F_1). The position of F_1, in contrast to Σ_1, directly depends on the length of infinity space and can be estimated using the thin lens approximation:

$$\frac{1}{d_0} + \frac{1}{d_1} = \frac{1}{f_t}, \tag{4.5}$$

where d_0 and d_1 are the distances from F_0 to the lens and from the lens to F_1, respectively. The linear magnification of an image is given by the ratio: $M = -d_1/d_0$, where the minus sign denotes reflection over the optical axis.
Next we consider a simple example of Fourier-space imaging in the case of an isolated single-mode DLSPPW lying parallel to the z-axis. Exciting one guided SPP mode propagating along the z-direction, the laser beam simultaneously gives rise to free SPPs that can propagate in all directions. Then if a camera is placed in F_1, we would observe the image schematically sketched in Fig. 4.3 (b). Here, the transmitted laser beam is projected into the small spot in the center, whose radius is proportional to the numerical aperture of the first objective NA_1. Free SPPs propagating in all directions are manifested by the circle with a radius k_{free}, while the guided mode is seen as a horizontal line $k_z \equiv k_{\text{guided}}$. Now it is clear that the first objective must fulfill $\text{NA}_1 < k_{\text{free}}$. But what are the main criteria for the second objective?
For real-space imaging the higher is the magnification and NA_2, the better is the resolution. For

Fourier-space imaging, in contrast, higher magnification at the same NA leads to the smaller image size because f_{obj} in Eq. 4.3 is in inverse proportion to magnification $f_{\text{obj}} \propto 1/M$. The effect of the NA for Fourier-space imaging is ambiguous. At first sight, higher NA_2 must be advantageous because it allows to detect larger SPP momentum. However, the comparative analysis made in Ref. [131] demonstrated that the objectives with very high NA can result in strongly aberrated Fourier images. The authors find that high-NA plan-corrected apochromat (Plan Apo) objectives with a low magnification (NA = 1.4, 60 ×) are best suited for Fourier-space imaging. Since the typical size of our DLSPPW array is on the order of 100 µm, such objectives provide sufficient resolution for real-space imaging as well.

4.2.2 Optical setup

A schematic of the LRM setup utilized in this thesis for optical measurements is given in Fig. 4.4. As a light source we use a laser diode with central wavelength of 980 nm and maximum output power of 30 mW. Since the beam directly emitted from the diode has a poorly shaped profile, the laser light is coupled into a single-mode fiber via a fiber coupler. Passing the fiber, the beam acquires a perfect Gaussian profile that guarantees the smallest possible focal spot. At the output port of the fiber the beam is collimated by a fiber collimator and directed to a polarizing beamsplitter (PBS). Here, the PBS not only provides a TM-polarization needed for SPP excitation but also allows to introduce an additional white light source that serves for sample illuminating. The laser beam as well as the white light are focused onto the sample by the first objective (Obj.1: magnification 20× and $\text{NA}_1 = 0.4$). The sample can be moved relative to the laser spot by making use of a 3D translation stage to which it is attached. Light emitted from the backside of the sample is collected by an infinity-corrected oil immersion objective (Obj.2: Plan Apo 60×, $\text{NA}_2 = 1.4$).
Next, the beam passes through a system of lenses $\{L_1, L_2, L_3/ L_4\}$ that helps to focus the desired image onto a scientific complementary metal–oxide–semiconductor (sCMOS) camera (*Marana Andor*). The first two lenses generate the intermediate real and Fourier images. At the intermediate BFP a knife edge is placed (between L_2 and L_3) in order to filter out the laser beam while keeping the leakage radiation from guided SPPs. Note that this can be always done since $\text{NA}_1 < k_{\text{free}}$, i.e. at the BFP the transmitted beam and the leakage radiation are spatially separated (see Fig. 4.3 (b)). In our setup

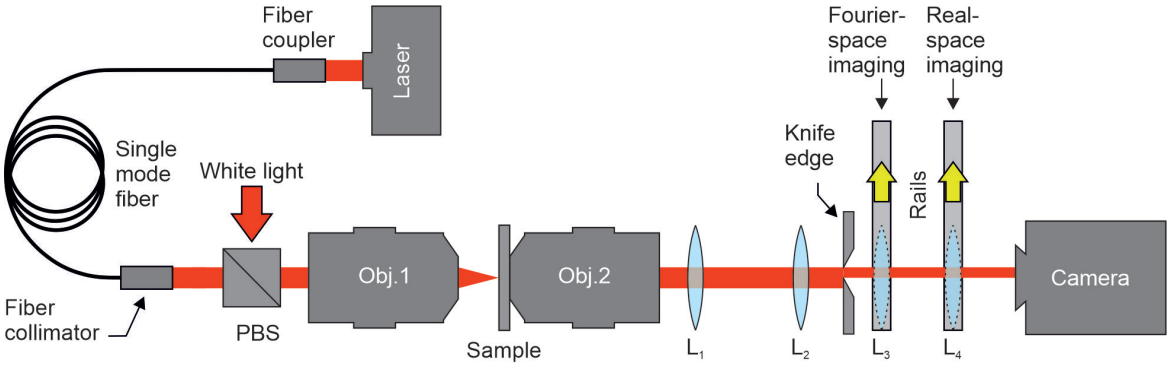

Figure 4.4: Sketch of the optical setup used for real- and Fourier-space imaging of excited DLSPPWs. PBS denotes polarizing beamsplitter. The dashed contour of the lenses L_3 and L_4 indicates that they can move along the rails in the direction of the yellow arrows and only one of them is involved at any one time. In case of Fourier-space imaging it is L_3, for real-space imaging it is L_4.

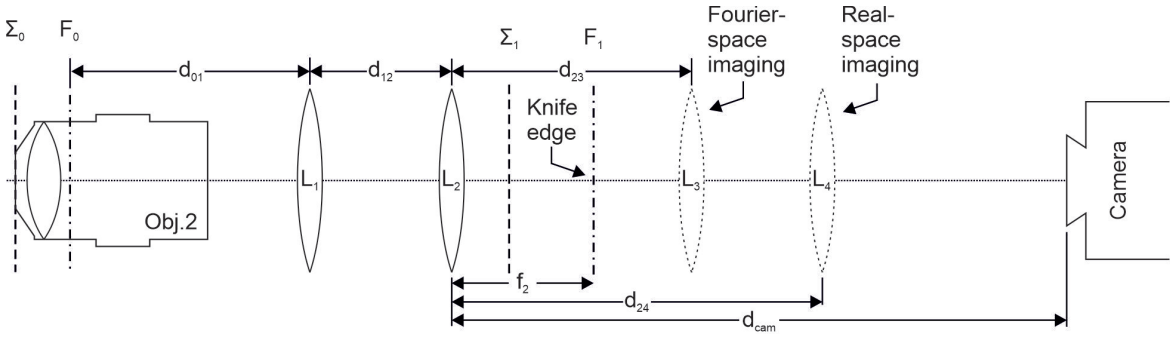

Figure 4.5: Part of the optical setup from Fig. 4.4 containing the system of four lenses $\{L_1, L_2, L_3/ L_4\}$ with all the distances marked. Σ_0 and F_0 denote the sample plane and the back focal plane of the second objective, respectively, while Σ_1 and F_1 are the corresponding intermediate images. The dashed contour of the lenses L_3 and L_4 indicates that they are not involved both simultaneously but only one of them is used depending on the imaging type.

L_1 and L_2 are thoroughly fixed, while L_3 and L_4 are mounted onto the carriages that can slide along the rails whereby these lenses can be easily removed from the beam path and then placed back with no need for alignment. These lenses are not used simultaneously: Depending on whether L_3 or L_4 is inserted into the light path the Fourier or real-space image can be focused onto the camera. The camera's position in turn does not change. Such a configuration is more preferable than having all lenses fixed because the bulky cooling system makes a displacement of the camera difficult. The exact arrangement of the lenses in our setup is elaborated below.

Lens system

In order to perform real- and Fourier space imaging without moving the camera the lens system has to fulfill the following requirements: First, it must focus the BFP and the real-space plane to the same position in space and switching between them should be fast and convenient. Second, both images should cover most of the camera sensor but not exceed it. Note that our camera has a relatively large 22.5 mm×22.5 mm sensor. Finally, one should keep the setup as compact as possible and use minimum optical elements.
To meet these requirements we employ the lens system sketched in Fig. 4.5. Here, L_1 is a tube lens compatible with our imaging objective with a focal length of $f_1 = 200$ mm. The lenses L_2, L_3, and L_4 have the corresponding focal lengths of $f_2 = f_3 = 75$ mm, and $f_4 = 150$ mm. The distances d_{01} and d_{12} are chosen to be equal to f_1 and f_2, respectively. As a result, the sample plane Σ_0 and the back focal plane F_0 are projected behind L_2 at a distance of $f_2 - f_2^2/f_1$ and f_2, respectively (see Σ_1 and F_1). More importantly, both intermediate images are comparably sized, and due to the relatively short f_2, Σ_1 and F_1 are found close to each other which allows us to magnify and project them onto the sCMOS camera with the help of either L_3 or L_4. During the setup alignment, one first sets the distance d_{23} so that the Fourier-space image is properly sized and, next, finds d_{24} to focus the real-space image at the same position. Let us demonstrate that it is possible for a certain range of distances by a simple calculation.
If we assume that a DLSPPW array has a length of 180 µm, the objective and the tube lens give a magnification of 60×, and the lens L_2 adds a factor of f_2/f_1, we end up with the characteristic image

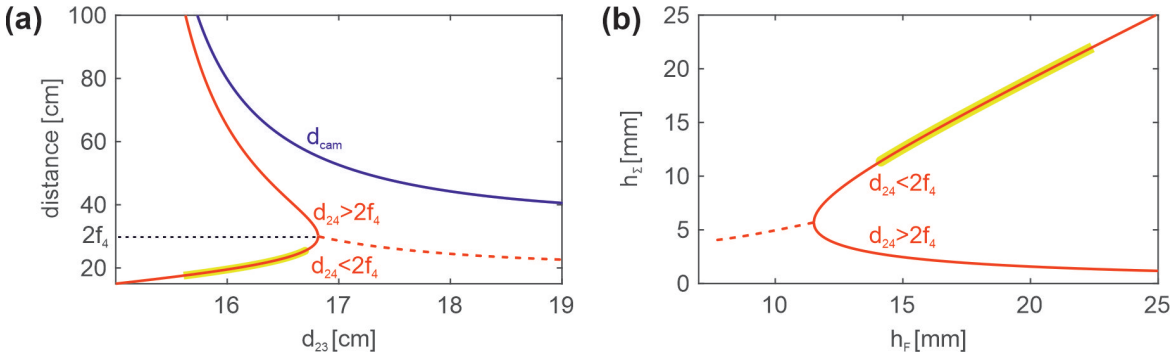

Figure 4.6: (a) Distances d_{24} (red line) and d_{cam} (blue line) as a function d_{23} (all notations correspond to the ones in Fig. 4.5). The dashed red line shows the real part of the complex solutions for d_{24}. The yellow marker shows the suitable distance range. (b) Size of the real-space image h_Σ versus the Fourier image size h_F when they are projected onto the camera at d_{23}, d_{24}, and d_{cam} taken from (a). The yellow marker indicates the suitable size range.

size of $h_{\Sigma_1} = 4.05$ mm. The size of the Fourier image F_1 is a product of the BFP diameter and the magnification factor: $h_{\text{F}_1} = 2f_{\text{obj}}\text{NA}_2 f_2/f_1 = 3.5$ mm.
Once the sizes of the intermediate images are found, the distances d_{23}, d_{24}, and d_{cam} can be determined as follows: we use d_{23} as a variable and for each value calculate the position of the camera $d_{\text{cam}}(d_{23})$. Then knowing that the distances d_{24} and $d_{\text{cam}}(d_{23}) - d_{24}$ are linked by the thin lens formula (4.5), we obtain a quadratic equation for d_{24}. The solutions of this equation are plotted in Fig. 4.6 (a). For $d_{23} \lessapprox 16.8$ cm we have two branches of real solutions corresponding to $d_{24} < 2f_4$ and $d_{24} > 2f_4$. Now we can compute the corresponding magnifications and hence the final image sizes that are seen by the camera (see Fig. 4.6 (b)). As expected, for $d_{24} > 2f_4$ both images get magnified. With a yellow marker the suitable size range is shown based on the criteria that both images must be larger than half of the sensor width but smaller than the full width. From this we finally determine the optimal values for d_{23} and d_{24} (see yellow marker in Fig. 4.6 (a)).
The above calculations can be used as a starting point when the setup is built. In practice, these distances are found manually by shifting the corresponding lenses. Therefore, after each realignment of the setup, the image sizes can slightly differ and a proper calibration of the real- and Fourier space images is needed. The calibration procedure was explained in details in Ref. [93] and will not be discussed here.
As a final remark, let us note that another solution for the lens system in the LRM setup with a fixed camera was presented in Ref. [132]. However, such a configuration would not provide a sufficient image magnification for our camera.

CHAPTER 5

Limits of topological protection under local periodic driving

A fundamental consequence of non-zero topological invariants are midgap edge states supported by the interface between two topologically distinct insulators. Despite localization at the boundary, the existence of these states is determined by a property defined for a bulk Hamiltonian, i.e. for a fully periodic system. As a result of this bulk-boundary correspondence principle, such states are intrinsically insensitive to static deformation as long as the band gap remains open and the relevant symmetries are preserved [103, 116]. This intriguing phenomenon has been observed in a number of solid state [133, 134], photonic [24] and cold atom systems [135]. Whereas in the static case, the coupling of the edge state to the bulk states is energetically forbidden, dynamic perturbations of the system might result in hybridization of the modes and drastically change their character.
In this chapter we explore the effect of local time-periodic perturbations on a topologically protected edge state. This problem is comprehensively studied experimentally, by means of the arrays of coupled plasmonic waveguides, as well as theoretically, by means of Floquet theory. As a toy model we use a paradigmatic model describing a 1D topological insulator named after Su, Schriefer and Heeger (SSH). Periodic perturbations are applied locally to the edge, while the bulk is kept static. This allows us to study topological protection for a special kind of Floquet systems. The fact that we do not drive the bulk distinguishes our work from previous studies [136, 137] and guarantees that the topological invariants stay unchanged and the bulk gap stays open. In theory we consider two different polarizations of the perturbing field: longitudinal and transverse polarization with respect to the lattice. Due to specific properties of our experimental platform, the plasmonic waveguide system is only suited to realize longitudinal modulation of the edge. The transverse polarization in turn was realized by C. Jörg under the supervision of G. von Freymann from the Technical University of Kaiserslautern (TU Kaiserslautern) in an independent experiment with dielectric waveguide arrays. The Floquet analysis was done in close cooperation with C. Dauer and F. Letscher under the supervision of S. Eggert and M. Fleischhauer, respectively, from the TU Kaiserslautern.
The chapter is organised as follows: The static SSH model and its toplogical properties are introduced in Section 5.1. In Section 5.2 we analyse the perturbed SSH model using the Floquet theory with an eye on our experimental realizations. In Section 5.3 we describe the plasmonic implementation of the perturbed SSH model, present the results of our optical measurements, and compare them with theoretical predictions. This chapter closely follows Ref. [138].

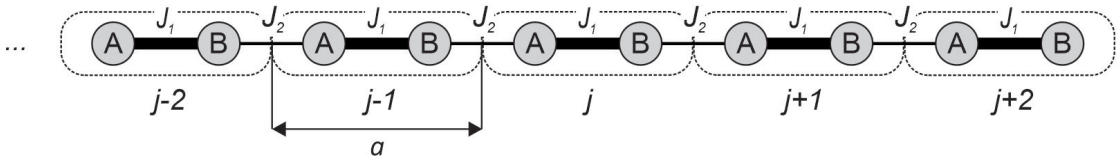

Figure 5.1: Schematic representation of the SSH model. Here, the thickness of the line connecting the lattice sites reflects the strength of the bond. J_1 and J_2 denote the intracell and intercell hopping amplitudes, respectively. The index j labels the unit cells that are encircled by the dotted lines. a is the lattice constant.

5.1 Su-Schrieffer-Heeger model

The SSH model is known as the simplest system with non-trivial topology. Therefore, it is commonly encountered in literature as a toy model to illustrate basic topological phenomena. This model was first introduced by Su, Schrieffer, and Heeger in order to explain conducting properties of poly-acetylene $(C_2H_2)_n$ [139] and describes a 1D tight-binding chain with alternating strong and weak hopping amplitudes (see Fig. 5.1). In contrast to the lattice model discussed in Sec. 2.1.1, where we had a single-site unit cell, the SSH model has two sites per unit cell labeled as A and B. The TB Hamiltonian for such a chain consisting of N unit cells reads [106]

$$\hat{H} = -J_1 \sum_{j=1}^{N} \left(|j, B\rangle\langle j, A| + h.c. \right) - J_2 \sum_{j=1}^{N-1} \left(|j+1, A\rangle\langle j, B| + h.c. \right), \tag{5.1}$$

where J_1 and J_2 are the intracell and intercell hopping amplitudes, respectively. Without loss of generality the on-site energies are set to zero. Here, $|j, A \text{ (or } B)\rangle$ denotes the state of the system when the electron resides on sublattice A (or B) in unit cell $j \in \{1, 2, ..., N\}$. It is important to note that the basis states in the Hamiltonian (5.1) can be also written as the tensor product $|j, A \text{ (or } B)\rangle = |j\rangle \otimes |A \text{ (or } B)\rangle$. This representation illustrates the fact that the full Hilbert space can be divided into two subspaces $\mathcal{H}_{\text{external}} \otimes \mathcal{H}_{\text{internal}}$, where the external Hilbert space accounts for the unit cell index, while the internal Hilbert space is the space of the sublattice indices A and B.

5.1.1 Bulk Hamiltonian

We begin with analyzing the bulk part of the SSH model. For that we impose periodic boundary conditions by closing the SSH chain into the ring as shown in Fig. 5.2. Mathematically it corresponds to adding of the coupling term between the first and the last lattice sites to the Hamiltonian $\hat{H}$ given by Eq. (5.1):

$$\hat{H}_{\text{bulk}} = \hat{H} - J_2(|1, A\rangle\langle N, B| + |N, B\rangle\langle 1, A|). \tag{5.2}$$

The resulting periodicity allows us to apply the Bloch theorem similar to how we did it in Sec. 2.1.1. The only difference is that now we use the plane wave basis states (2.15) that belong not to the full Hilbert space but only to the external subspace $\mathcal{H}_{\text{external}}$:

$$|j\rangle \otimes |A \text{ (or } B)\rangle = \frac{1}{\sqrt{N}} \sum_k e^{-ikj} |k\rangle \otimes |A \text{ (or } B)\rangle, \quad k \in 1^{\text{st}}\text{BZ} \tag{5.3}$$

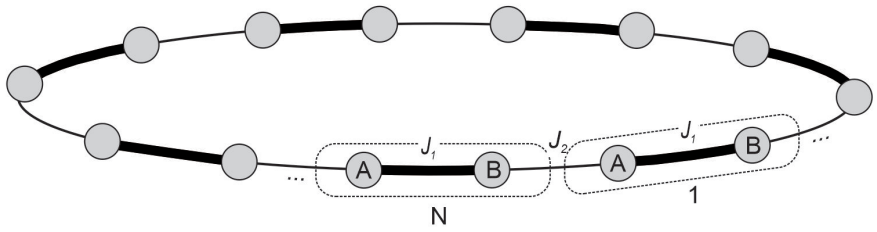

Figure 5.2: SSH model under periodic boundary conditions, where the unit cells 1 and N are connected via the intercell coupling J_2.

Here and subsequently we set the lattice constant to $a = 1$. Substituting Eq. (5.3) into Eq. (5.2) we come to

$$\hat{H}_{\text{bulk}} = -\sum_k (J_1 + J_2 e^{ik})|k, B\rangle\langle k, A| + (J_1 + J_2 e^{-ik})|k, A\rangle\langle k, B|. \tag{5.4}$$

Separation of the external and internal degrees of freedom in Eq. (5.4) results into

$$\hat{H}_{\text{bulk}} = -\sum_k |k\rangle\langle k| \otimes \left\{(J_1 + J_2 e^{ik})|B\rangle\langle A| + (J_1 + J_2 e^{-ik})|A\rangle\langle B|\right\}. \tag{5.5}$$

The expression above can be also rewritten as

$$\hat{H}_{\text{bulk}} = \sum_k |k\rangle \hat{H}_k \langle k| \tag{5.6}$$

with $\hat{H}_k$ being the Bloch Hamiltonian of the SSH model. Note that $\hat{H}_k$ acts in the internal Hilbert space $\mathcal{H}_{\text{internal}}$ and its matrix representation reads

$$\hat{H}_k = -\begin{pmatrix} 0 & \rho(k) \\ \rho^*(k) & 0 \end{pmatrix}, \tag{5.7}$$

where $\rho(k) = J_1 + J_2 e^{-ik}$. Solving the stationary SE (2.5) for the Bloch Hamiltonian (5.7) we find the k-dependent eigenvalues

$$E_\pm = \pm|\rho(k)| = \pm\sqrt{J_1^2 + J_2^2 + 2J_1 J_2 \cos k} \tag{5.8}$$

that form two energy bands of the SSH model. This dispersion relation is exemplified in Fig. 5.3 in the first Brillouin zone for different values of the hopping amplitudes J_1 and J_2. The total bandwidth of the SSH model is given by $2(J_1 + J_2)$ while the width of the gap separating the two bands equals to $2|J_1 - J_2|$. Like in Sec. 2.1.1 we can assume the Fermi energy to lie in the middle of the band structure ($E_F = 0$). Thus if $J_1 \neq J_2$ the Fermi energy lies inside the band gap and the system must be an insulator (Fig. 5.3 (a) and (c)), while at $J_1 = J_2$ the band gap closes and the system becomes a conductor (Fig. 5.3 (b)).
It is evident that swapping J_1 and J_2 in Eq. (5.8) does not change the dispersion relation of the SSH model (compare Figs. 5.3 (a) and (c)). However, as we will see later, despite the same bulk spectrum, the cases $J_1 > J_2$ and $J_1 < J_2$ correspond to different topological phases which leads to interesting

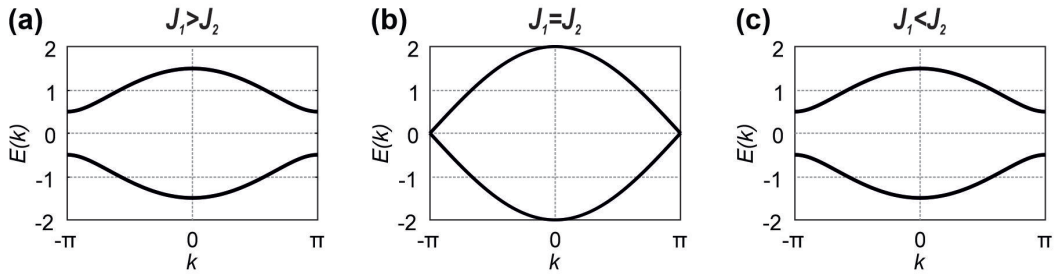

Figure 5.3: Dispersion relation of the SSH model with periodic boundary conditions for different parameter sets: (a) $J_1 = 1$, $J_2 = 0.5$; (b) $J_1 = 1$, $J_2 = 1$; (c) $J_1 = 0.5$, $J_2 = 1$. The Fermi energy is assumed to be zero.

physical consequences.

5.1.2 Topological properties

We recall that in Sec. 2.3.1 the Berry phase has been introduced as a quantity that characterizes topological properties of Bloch Hamiltonians. The bulk of the SSH model has a 1D parameter space due to the quasimomentum k that makes a loop when it runs through the first Brillioun zone. In 1D case the Berry phase reduces to the Zak phase that is given by Eq. (2.48). But before we calculate it for the SSH model, let us introduce some useful notations.
Since the Bloch Hamiltonian of the SSH model formally describes a two-level system, it can be written with the help of the Pauli matrices $\hat{\sigma} = (\hat{\sigma}_x, \hat{\sigma}_y, \hat{\sigma}_z)^{\mathrm{T}}$ as follows:

$$\hat{H}_k = -\mathbf{h}(k) \cdot \hat{\sigma}, \tag{5.9}$$

where the components of the vector $\mathbf{h}(k)$ are given by [108]

$$\begin{aligned} h_x &= \mathrm{Re}(\rho(k)) = J_1 + J_2 \cos k; \\ h_y &= -\mathrm{Im}(\rho(k)) = J_2 \sin k; \\ h_z &= 0. \end{aligned} \tag{5.10}$$

As k varies across the 1$^{\mathrm{st}}$ BZ the endpoint of the vector $\mathbf{h}(k)$ traces out a circle of a radius J_2 centered at a point $(J_1, 0)$. This is illustrated in Fig. 5.4 for different values of J_1 and J_2. Comparing Figs. 5.4 (a) and (c) one notices that depending on the ratio between J_1 and J_2 the circle either winds around the origin $(0, 0)$ or not. It turns out that this behaviour is directly related to the value of the Zak phase.
As we have learnt from the Sec. 2.3.1, computation of the Zak phase requires knowing the eigenvectors of the Bloch Hamiltonian. For the SSH model we get

$$|u_{\pm}\rangle = \frac{1}{\sqrt{2}} \begin{pmatrix} e^{-i\phi(k)} \\ \pm 1 \end{pmatrix} \tag{5.11}$$

where the phase $\phi(k)$ is defined as

$$\rho(k) = |\rho(k)| e^{-i\phi(k)}. \tag{5.12}$$

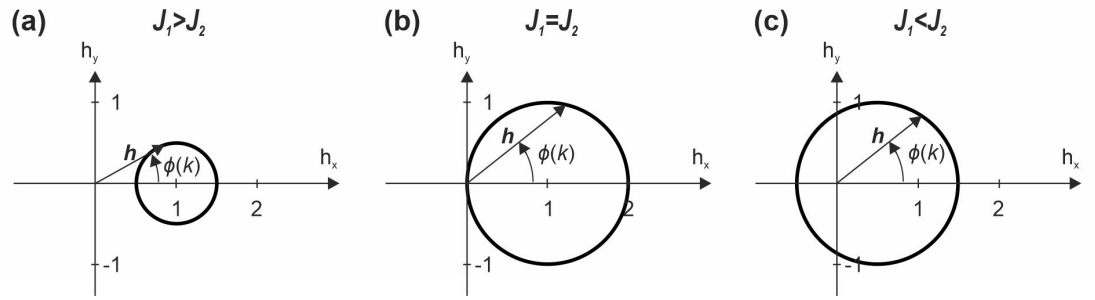

Figure 5.4: Trajectories of $\mathbf{h}(k)$ as k runs through the 1st BZ in the $h_x - h_y$ plane for different parameter sets: (a) $J_1 = 1$, $J_2 = 0.5$; (b) $J_1 = 1$, $J_2 = 1$; (c) $J_1 = 0.5$, $J_2 = 1$.

This phase can be also understood as an angle between the vector $\mathbf{h}(k)$ and the positive h_x axis as shown in Fig. 5.4. The Berry connection of the ground state $|-\rangle$ reads

$$A_- = i\langle u_-|\frac{\mathrm{d}}{\mathrm{d}k}|u_-\rangle = \frac{1}{2}\frac{\mathrm{d}\phi}{\mathrm{d}k}. \tag{5.13}$$

Thus, the Zak phase is

$$\gamma_Z = \oint_{-\pi}^{\pi} \mathrm{d}k \frac{\mathrm{d}\phi}{\mathrm{d}k} = \frac{\Delta\phi}{2}, \tag{5.14}$$

where $\Delta\phi$ is the variation of the phase $\phi(k)$ as k runs though the 1st BZ. From the plots in Fig. 5.4 it immediately follows that

$$\gamma_Z = \begin{cases} 0 & \text{if } J_1 > J_2 \\ \pi & \text{if } J_1 < J_2 \\ \text{undefined} & \text{if } J_1 = J_2 \end{cases}. \tag{5.15}$$

Eq. (5.15) demonstrates that the Zak phase in the SSH model is quantized, i.e. it can be either 0 or π. The fact that the value of γ_Z only depends on whether the trajectory traced by $\mathbf{h}(k)$ encloses the origin or not, makes it insensitive to small changes in the Hamiltonian. Importantly, the state of the chain characterized by $\gamma_Z = 0$ cannot be continuously deformed into the state $\gamma_Z = \pi$ and vice versa without crossing the origin, i.e., closing the band gap. Therefore, the Zak phase plays a role of a topological invariant for the SSH model and distinguishes two topologically distinct phases or dimerisations. The point where the Zak phase is undefined corresponds to the topological phase transition. In the following, we will refer to the phase with $\gamma_Z = 0$ as "trivial" and to the phase with $\gamma_Z = \pi$ as "non-trivial" or topological. Note that in literature one can also encounter a topological invariant of the SSH model called the winding number [106]. Being simply the Zak phase divided by π, it takes the values 0 or 1.

5.1.3 Edge states and bulk-boundary correspondence principle

In order to see the physical consequences of different values of the Zak phase we have to look at the SSH chain with open boundaries. Note that we cut the periodic system so that the breaking point lies in between the unit cells and not inside a unit cell. As a result, in the trivial phase the edge sites are

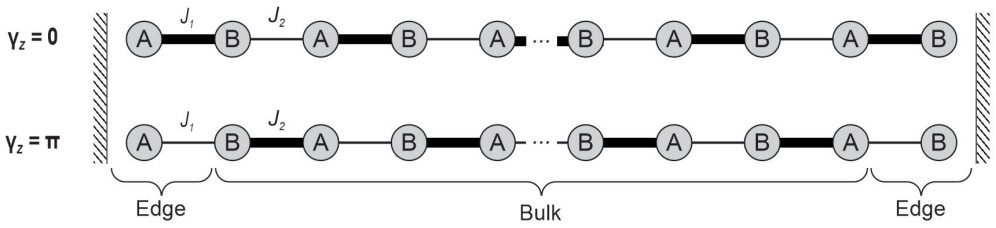

Figure 5.5: The SSH chain with open boundaries in the trivial phase $J_1 > J_2$ (top) and in the topological phase $J_1 < J_2$ (bottom).

connected to the neighboring sites via the strong bond, while in the topological phase the outermost couplings are weak as sketched in Fig. 5.5.
The effect of open boundaries becomes most evident in the so-called fully dimerized limit. In this limit the weak hopping amplitude (J_2 in the trivial phase and J_1 in the topological phase) tends to zero which ultimately breaks the chain into disconnected dimers. The energy eigenvalues of the resulting Hamiltonian can be found without performing any calculations. Indeed, we know that each dimer contributes two solutions given by the superposition of the sites A and B. Thus we have

$$\hat{H}(|j,A\rangle \pm |j,B\rangle) = E_{\pm}(|j,A\rangle \pm |j,B\rangle) \quad j = 1,2,...,N \tag{5.16}$$

with $E_{\pm} = \pm J_1$ and

$$\hat{H}(|j,B\rangle \pm |j+1,A\rangle) = E_{\pm}(|j,B\rangle \pm |j+1,A\rangle) \quad j = 1,2,...,N-1 \tag{5.17}$$

with $E_{\pm} = \pm J_2$ for the trivial and non-trivial dimerisations, respectively. As a result, the eigenvalues no longer depend on k, the two bands become flat, and the group velocity vanishes. It is clearly an anticipated result for the chain consisting of disconnected dimers. However, in the topological phase in addition to the above there are two single-standing sites at each boundary that support zero-energy eigenvalues:

$$\hat{H}|1,A\rangle = \hat{H}|N,B\rangle = 0. \tag{5.18}$$

These are the edge states that naturally cannot appear in the trivial phase.
But what happens if we go away from the fully dimerized limit by allowing the finite hopping amplitude J_1 in the topological SSH chain? Solving the eigenvalue problem for the Hamiltonian (5.1) numerically we find that with increasing J_1 the previously degenerate bulk states split and start to form the bands (see Fig. 5.6 (a)). Meanwhile, the zero-energy eigenvalues persist as long as $J_1 < J_2$. Strictly speaking, there is a negligible deviation from zero which is caused by the finite length of the chain but we will comment on it later. When approaching the point of the topological phase transition ($J_1 = J_2$) the band gap shrinks while the states in the middle of the spectrum start to deflect from zero. By increasing J_1 even further we reopen the gap and turn the system into the trivial phase, where there are no states at zero energy.
Next, we draw our attention to the corresponding wave functions. Fig. 5.6 (b) exemplifies the wave function amplitudes at each lattice site for three different states at the point when $J_1 = 0.5J_2$. The plots (1) and (2) show that two almost-zero-energy eigenstates have symmetric and anti-symmetric wave functions, respectively, that decay exponentially as we move away from the edges. It is evident

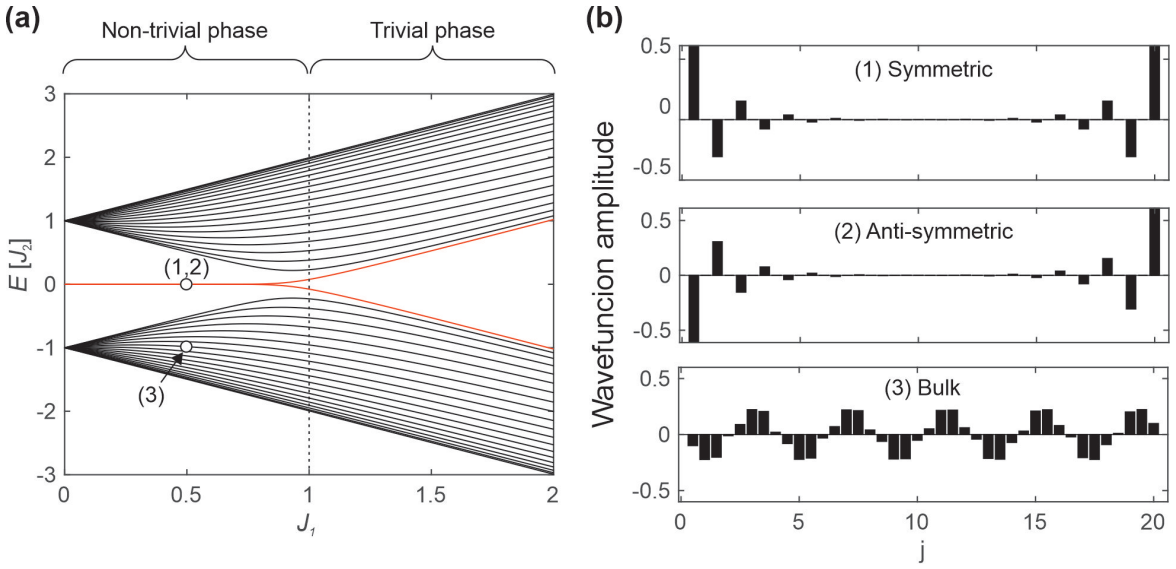

Figure 5.6: (a) Energy eigenvalues of the SSH chain consisting of $N = 20$ unit cells in dependence on the hopping amplitude J_1. The edge states in the non-trivial phase are highlighted by red color. In the trivial phase these states become a part of the bands. (b) The wave function amplitude at each lattice site for the two edge states (1), (2) and for the bulk state (3). These states are marked in (a) and correspond to the situation when $J_1 = 0.5J_2$. Adopted from Ref. [106].

that they result from even and odd superpositions of the wave functions completely localized at each boundary. If the two edges are infinitely far apart (thermodynamic limit), the edge states can not overlap and the corresponding eigenvalues are exactly zero. In contrast, when these states overlap, they hybridize and split in energy which causes the aforementioned deviation from zero. The splitting in the vicinity of the phase transition becomes larger. It indicates that the localization length of the edge states also increases. In fact, one can show that the the localization length is given by [106]

$$\xi^{-1} = \log\left|\frac{J_2}{J_1}\right|. \tag{5.19}$$

As a comparison, in plot (3) we present an example of a bulk state. In contrast to the edge states, it is totally delocalized throughout the chain. In Fig. 5.6 one can notice another important difference between bulk and edge states of the SSH model. Whereas the bulk states have equal support on both sublattices A and B, the edge states have vanishing amplitude on every second site. This property is due to the presence of chiral symmetry that will be explained in the next subsection.
Now it is reasonable to ask ourselves what is the origin of these edge states and how is it related to the value of the Zak phase? It turns out that when we cut the SSH chain we thereby connect it to the outside world (vacuum) which is, by definition, always topologically trivial. Therefore, if the SSH chain features a non-zero Zak phase there is a jump in the topological invariant at the interface which implies the closing of the band gap. And the band gap closes by means of the zero-energy states. Clearly, an edge state can occur not only at an open end of the SSH chain but also at an interface between two chains with different topologies as realized, for instance, in [28].
Although a topological edge state is exponentially localized at the interface between two phases, we

remember that the Zak phase was obtained using the bulk Hamiltonian. This is the manifestation of the so-called bulk-boundary correspondence principle. Due to this principle, the topological edge states cannot be destroyed even by strong static deformations as long as the topological property of the bulk is unaltered. It is important to emphasize that the bulk-boundary correspondence principle and the ensuing topological protection are in general valid only for the case of static deformations [34]. This is due to the fact that in the static case the coupling of the edge state to the bulk states is prevented by the band gap, while dynamic perturbations can in principle induce hybridization of these states. Hence, it is important to understand under which conditions such a hybridization becomes relevant and when not.

5.1.4 Symmetries

The SSH model obeys chiral symmetry (see Sec. 2.3.2) because the operator

$$U_{\mathrm{S}} = P_A - P_B, \tag{5.20}$$

where

$$P_A = \sum_j |A, j\rangle\langle A, j| \qquad \text{and} \qquad P_B = \sum_j |B, j\rangle\langle B, j| \tag{5.21}$$

is unitary, Hermitian, and local (within each unit cell) and it satisfies:

$$U_{\mathrm{S}}^{\dagger} \hat{H} U_{\mathrm{S}} = -\hat{H}. \tag{5.22}$$

We note that operators P_A and P_B from Eq. (5.21) act as projectors on sublattices A and B, respectively, and that they can be alternatively expressed as

$$P_A = \frac{1}{2}(\mathbb{I} + U_{\mathrm{S}}) \qquad \text{and} \qquad P_B = \frac{1}{2}(\mathbb{I} - U_{\mathrm{S}}). \tag{5.23}$$

Due to chiral symmetry, the spectrum of the SSH model is symmetric with respect to zero energy. Indeed, if $|\Psi_j\rangle$ is an eigenstate of $\hat{H}$ with energy E_j, then $U_{\mathrm{S}}|\Psi_j\rangle$ is also an eigenstate with energy

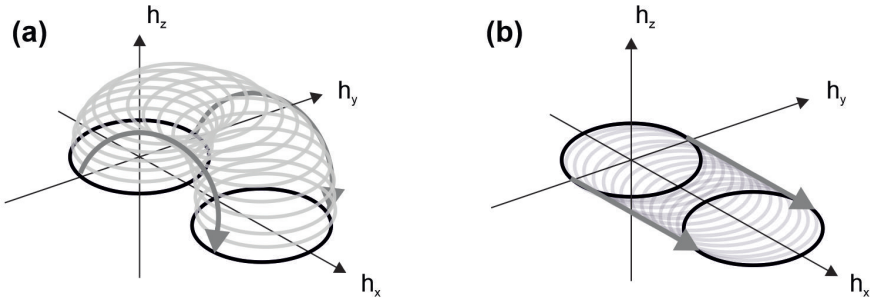

Figure 5.7: (a) An example of a trajectory that adiabatically connects two dimerisations without crossing the origin in the case when $h_z \neq 0$ is allowed. (b) If the constraint $h_z = 0$ is imposed, the trajectory that connects two dimerizations strictly lies on the plane (h_x, h_y) and has to cross the origin. Adopted from Ref. [106].

$-E_j$, i.e.

$$\hat{H}|\Psi_j\rangle = E_j|\Psi_j\rangle \implies \hat{H}U_S|\Psi_j\rangle = -U_S\hat{H}|\Psi_j\rangle = -U_S E_j|\Psi_j\rangle = -E_j U_S|\Psi_j\rangle. \tag{5.24}$$

This leads to important consequences for bulk and edge states. If $E_j \neq 0$ (bulk states), then $|\Psi_j\rangle$ and $U_S|\Psi_j\rangle$ have different energies and must be orthogonal

$$0 = \langle\Psi_j|U_S|\Psi_j\rangle = \langle\Psi_j|P_A|\Psi_j\rangle - \langle\Psi_j|P_B|\Psi_j\rangle. \tag{5.25}$$

Since P_A and P_B are the lattice projectors, Eq. (5.25) means that the bulk states have equal support on both sublattices. The edge states, in contrast, can be chosen to have support only on one sublattice. If $E_j = 0$, the corresponding states $|\Psi_j\rangle$ and $U_S|\Psi_j\rangle$ are degenerate and thus can be rearranged as $(|\Psi_j\rangle \pm U_S|\Psi_j\rangle)/\sqrt{2}$. Taking into account Eq. (5.23), it becomes obvious that these states have vanishing amplitude on one of the sublattices

$$\hat{H}|\Psi_j\rangle = 0 \implies \hat{H}(|\Psi_j\rangle \pm U_S|\Psi_j\rangle)/\sqrt{2} = \hat{H}\sqrt{2}P_{A,B}|\Psi_j\rangle = 0 \tag{5.26}$$

In momentum space the condition providing chiral symmetry reads

$$\hat{\sigma}_z\hat{H}_k\hat{\sigma}_z = -\hat{H}_k, \tag{5.27}$$

that can only hold true if $h_z = 0$ which is indeed the case for the SSH model (see Eq. (5.10)). Importantly, if we allow $h_z \neq 0$ and break chiral symmetry, then it is possible to adiabatically connect two different dimerisations of the SSH model without crossing the origin as exemplified in Fig. 5.7 (a). Chiral symmetry restricts us to the surface (h_x, h_y) so that the gap closure can not be avoided in the transition from one dimerisation to another (Fig. 5.7 (b)). Therefore, the quantized value of the Zak phase is, in fact, a consequence of chiral symmetry. For this reason, the SSH model is an example of the so-called symmetry-protected topology [140].
Note that presence of chiral symmetry automatically implies time-reversal and charge conjugation symmetries. Since $\mathcal{T}^2$ is always +1 for spinless particles and, in our case, U_C can be chosen equal to U_S, hence $C^2 = +1$ as well. Consequently, the SSH model belongs to the BDI symmetry class of the Altland-Zirnbauer classification scheme (see Table 2.1).

5.2 Perturbed SSH model

We are interested in what happens if an edge between two topologically distinct phases of the SSH model is subject to an external periodic field, while the bulk stays intact. The corresponding model is sketched in Fig. 5.8 for two different polarization states of the perturbing field that can oscillate either parallel (a) or perpendicular (b) to the chain. Here, unlike in the previous sections, J_1 and J_2 denote the strong and the weak bonds, respectively, regardless whether these bonds connect the atoms within one unit cell or the atoms from the neighboring unit cells. As explained in Sec. 5.1.3, the topological edge state emerges at every interface between two topologically distinct phases. By repeating the weak bonds twice we attach the two SSH chains with different dimerisations and thereby create such an interface. We apply local time-periodic perturbations with the frequency ω associated with a single

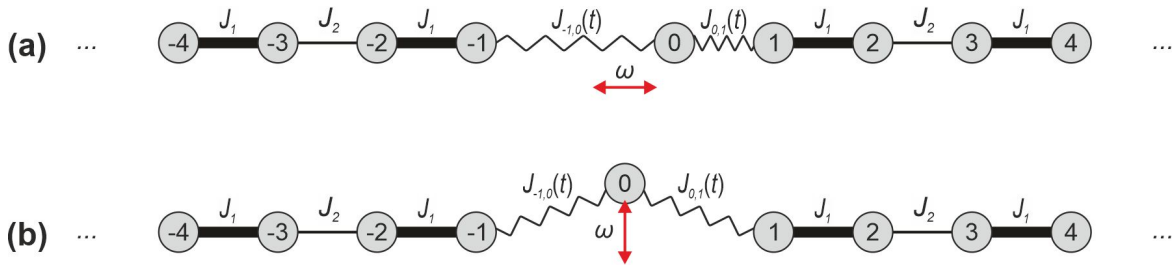

Figure 5.8: Sketches of the SSH chains with time-periodic perturbations of a single lattice site at the interface between two distinct dimerization. (a) The perturbing field is polarized along the chain. (b) The perturbing field is polarized perpendicular with respect to the chain. Here, J_1 (J_2) denotes the large (small) hopping amplitude in the bulk, $J_{0,1}(t)$ ($J_{-1,0}(t)$) is the periodically modulated hopping amplitude between the 0^{th} and 1^{st} lattice sites (0^{th} and -1^{st} lattice sites), ω is the driving frequency.

lattice site at the interface (site 0 in Fig. 5.8). In particular, we harmonically modulate the hopping amplitudes between the 0^{th} site and its nearest neighbours (site 1 and -1):

$$\begin{aligned} J_{-1,0}(t) &= J_2 + \Delta J \sin(\omega t + \phi_1), \\ J_{0,1}(t) &= J_2 + \Delta J \sin(\omega t + \phi_2) \end{aligned} \tag{5.28}$$

and the local on-site potential

$$V_0(t) = -\Delta V + \Delta V \cos(\omega t). \tag{5.29}$$

The phase factors are $\phi_1 = 0$, $\phi_2 = \pi$ for the longitudinal modulation and $\phi_1 = \phi_2 = \pi/2$ for the transverse modulation, respectively. Due to the specific character of each experimental realization we can set $\Delta V = 0$ for the plasmonic waveguide model, while for the dielectric waveguides $\Delta V \neq 0$ holds (see Sec. 5.3 for details). Assuming $N = 4M + 1$ lattice sites (M dimers to either side of the topological defect and one unpaired site in the middle), the corresponding Hamiltonian can be written as a sum of a time-independent and time-periodic part

$$\mathrm{H}(t) = \mathrm{H}_0 + \mathrm{H}_\mathrm{T}(t), \tag{5.30}$$

given by

$$\begin{aligned} \mathrm{H}_0 = &\sum_{s=-M+1}^{0} (J_1 |2s-1\rangle\langle 2s-2| + J_2 |2s\rangle\langle 2s-1|) \\ &+ \sum_{s=0}^{M-1} (J_2 |2s+1\rangle\langle 2s| + J_1 |2s+2\rangle\langle 2s+1|) \\ &+ \text{h.c.} - \Delta V \, |0\rangle\langle 0| \end{aligned} \tag{5.31}$$

and

$$\begin{aligned} \mathrm{H}_\mathrm{T}(t) = &\Delta J \sin(\omega t + \phi_1) |-1\rangle\langle 0| + \Delta J \sin(\omega t + \phi_2) |0\rangle\langle 1| \\ &+ \text{h.c.} + \Delta V \cos(\omega t) \, |0\rangle\langle 0|, \end{aligned} \tag{5.32}$$

where s labels the lattice sites.
The Hamiltonian of the perturbed SSH model (5.30) is periodic in time, hence the Floquet theory

applies (see Sec. 2.2). Before we come to the Floquet analysis, let us briefly comment on the topological properties of our model. We know that topological invariants are global characteristics of bulk Hamiltonians and, therefore, topological invariants of time-periodic systems must be obtained using the Floquet Hamiltonian if the bulk is periodically driven. However, in our case, the bulk is static. The topological invariant, i.e., in our case, the Zak phase, must not depend on the representation of our system; whether we use the Floquet picture or not it stays the same as in the static SSH model. Another important property of our model is that in the absence of the on-site potential offset ($\Delta V = 0$) the local time-periodic perturbations preserve chiral symmetry. Indeed, if $\Delta V = 0$ the unitary, Hermitian, and local operator

$$U_{\mathrm{S}} = \sum_{s=-M}^{M} |2s\rangle\langle 2s| - \sum_{s=-M-1}^{M-1} |2s+1\rangle\langle 2s+1| \tag{5.33}$$

fulfills the relation $U_{\mathrm{S}}^{\dagger}\mathrm{H}_0 U_{\mathrm{S}} = -\mathrm{H}_0$ for the static Hamiltonian (5.31). For the time-periodic part (5.32) it holds

$$U_{\mathrm{S}}^{\dagger}\mathrm{H}_{\mathrm{T}}(t+t_0)U_{\mathrm{S}} = -\mathrm{H}_{\mathrm{T}}(-t+t_0), \tag{5.34}$$

where $t_0 = T/4$ for the longitudinal and $t_0 = 0$ for the transverse modulation, which implies chiral symmetry for Floquet systems (see Sec. 2.3.2). Being chirally symmetric our system possesses a zero-energy Floquet mode which exhibits a vanishing amplitude on every second lattice site [35, 137]. Adding a harmonic time-dependent on-site potential variation ($\Delta V \neq 0$) breaks chiral symmetry. Nevertheless, as was shown in [35], it does not affect the topological robustness of the system.

5.2.1 Floquet analysis

We apply the Floquet theory that was outlined in Sec. 2.2 to the Hamiltonian (5.30). In our further calculations, it is convenient to express H_0 and $\mathrm{H}_{\mathrm{T}}(t)$ as $(4M+1)\times(4M+1)$ matrices

$$\mathrm{H}_0 = \begin{pmatrix} \ddots & & & & & & & & \\ & & J_2 & & & & & & \\ & J_2 & 0 & J_1 & & & & & \\ & & J_1 & \boxed{\begin{matrix} 0 & J_2 & 0 \\ J_2 & -\Delta V & J_2 \\ 0 & J_2 & 0 \end{matrix}} & & & & \\ & & & & J_1 & & & \\ & & & & 0 & J_2 & & \\ & & & & J_2 & & & \\ & & & & & & \ddots & \end{pmatrix}, \tag{5.35}$$

and

$$\mathrm{H}_{\mathrm{T}}(t) = \mathrm{H}_1 \mathrm{e}^{-\mathrm{i}\omega t} + \mathrm{H}_{-1}\mathrm{e}^{\mathrm{i}\omega t}, \tag{5.36}$$

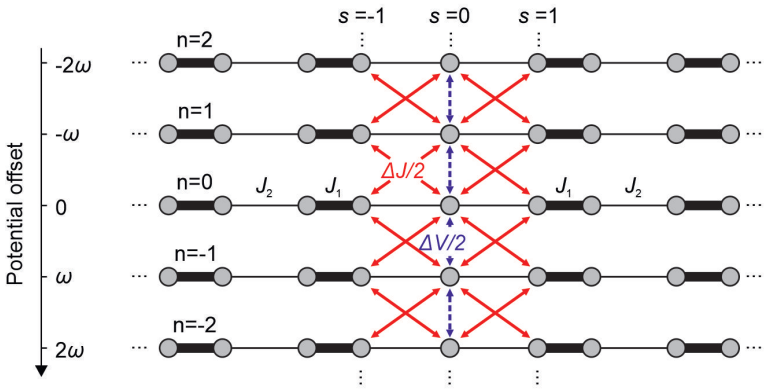

Figure 5.9: (1+1)D time-independent analogue of the SSH model with local periodic perturbations at the interface and J_1 (J_2) being the large (small) hopping amplitude. The Floquet index n enumerates coupled SSH chains, each with the overall potential $-n\omega$. Red and blue arrows denote the coupling between Floquet replicas (n) and sites (s) created by the harmonic driving of local couplings with amplitude ΔJ and on-site potential with ΔV (compare with Eq. (5.37)).

where the Fourier components $\mathrm{H}_{\pm 1}$ according to Eq. (2.33) are

$$\mathrm{H}_{\pm 1} = \mp\frac{1}{2}\cdot\begin{pmatrix} \ddots & & & & & & \\ & 0 & & & & & \\ & & \boxed{\begin{matrix} 0 & \mathrm{i}\Delta J\mathrm{e}^{\mp\mathrm{i}\phi_1} & 0 \\ \mathrm{i}\Delta J\mathrm{e}^{\mp\mathrm{i}\phi_1} & \mp\Delta V & \mathrm{i}\Delta J\mathrm{e}^{\mp\mathrm{i}\phi_2} \\ 0 & \mathrm{i}\Delta J\mathrm{e}^{\mp\mathrm{i}\phi_2} & 0 \end{matrix}} & & & \\ & & & 0 & & \\ & & & & \ddots \end{pmatrix}. \tag{5.37}$$

The boxes in (5.35) and (5.37) highlight the central parts of the matrices which are associated with the defect (0^{th} lattice site in Fig. 5.8). Due to the spatially local character of perturbations of our model, all the elements outside of the box in the time-dependent part $\mathrm{H}_{\mathrm{T}}(t)$ are zero.
Now we have everything at hand to compose the time-independent Floquet equation (2.34) that in the matrix form reads

$$\begin{pmatrix} \ddots & & & & & \\ \mathrm{H}_1 & \mathrm{H}_0+\omega\mathbb{I} & \mathrm{H}_{-1} & & & \\ & \mathrm{H}_1 & \mathrm{H}_0 & \mathrm{H}_{-1} & & \\ & & \mathrm{H}_1 & \mathrm{H}_0-\omega\mathbb{I} & \mathrm{H}_{-1} & \\ & & & & \ddots \end{pmatrix}\begin{pmatrix} \vdots \\ |\Phi_j^{n-1}\rangle \\ |\Phi_j^{n}\rangle \\ |\Phi_j^{n+1}\rangle \\ \vdots \end{pmatrix} = \varepsilon_j \begin{pmatrix} \vdots \\ |\Phi_j^{n-1}\rangle \\ |\Phi_j^{n}\rangle \\ |\Phi_j^{n+1}\rangle \\ \vdots \end{pmatrix}. \tag{5.38}$$

Here, the index of the operator elements runs over the lattice sites. This equation transforms our 1-dimensional time-periodic system into a (1+1)-dimensional time-independent system that is displayed in Fig. 5.9. The resulting (1+1)D lattice consists of an infinite number of SSH chains labeled by the Floquet index n with the overall potential shifted by $-n\omega$. Each lattice site can now be identified by

two numbers $[n, s]$, where s is the site index within each chain and n labels the Floquet replicas of the system. Due to local perturbations the chains are coupled to each other only through the sites in the vicinity of the topological defect ($s = -1, 0, 1$). The harmonic variation of the hoppings $J_{-1,0}(t)$ and $J_{0,1}(t)$ thus induces the bonds between the sites $[n, 0]$ and $[n \pm 1, \pm 1]$, $\forall n$ with the hopping amplitude $\Delta J/2$. Likewise, a harmonic on-site potential variation at the 0^{th} lattice site with the amplitude ΔV creates bonds between the central sites $[n, 0]$ and $[n \pm 1, 0]$ $\forall n$ with the hopping term $\Delta V/2$. Hence, we anticipate that by applying a local perturbation to the interface, we selectively populate the Floquet replicas of the topological edge state while the bulk states should stay almost unaffected.
In order to see how local perturbation affect the topological edge state we have to solve the eigenvalue problem which involves the infinite matrix (5.38). Numerically, it is realized by introducing a cutoff Floquet index n_{cutoff} such that $|\Phi_j^n\rangle = 0$ for any $n > n_{\text{cutoff}}$. A sufficiently large n_{cutoff} yields eigenvectors and eigenvalues that converge well. Note, that at constant driving amplitude the value of a cutoff depends on the driving frequency ω because the lower is ω, the more Floquet replicas must be taken into account and hence the larger is n_{cutoff}. We restrict ourselves to the quasienergies from the first Floquet Brillouin zone $\varepsilon \in [-\omega/2, \omega/2)$. The corresponding eigenvectors contain the Fourier components of the Floquet modes $|\Phi_j^n\rangle$ where each of them is associated with the energy $\varepsilon_j^n = \varepsilon_j + n\omega$. The complete solution of the Schrödinger equation is given by

$$|\Psi(t)\rangle = \sum_j c_j \sum_n e^{(-i\varepsilon_j^n t)} |\Phi_j^n\rangle, \tag{5.39}$$

where the constants c_j are found from the initial conditions $|\Psi(0)\rangle$ as follows

$$c_j = \langle \Phi_j(0)|\Psi(0)\rangle, \quad |\Phi_j(0)\rangle = \sum_n |\Phi_j^n\rangle. \tag{5.40}$$

As an initial condition we solely excite the central lattice site $s = 0$ in accordance with our experiments (see Sec. 5.3). Note that $|\Psi(t)\rangle$ is a time-dependent vector whose components, corresponding to different lattice sites s, take the value of a wave function $\Psi(s, t)$. The 2D Fourier transform $\tilde{\Psi}(k, E)$ yields the momentum representation of the wave function $\Psi(s, t)$.
A useful quantity for our analysis is the spectral weight of a Floquet state at a given energy. The temporal Fourier transform of the wave function (5.39) reads $|\Psi(E)\rangle = \sum_{j,n} c_j |\Phi_j^n\rangle \delta(E - \varepsilon_j^n)$ and motivates to define the spectral weight at energy $E = \varepsilon_j^n$ by

$$w(\varepsilon_j^n) = |c_j|^2 \langle \Phi_j^n | \Phi_j^n \rangle. \tag{5.41}$$

The sum over all weights is normalized to one $\sum_\varepsilon w(\varepsilon) \equiv 1$.
In the following we present results of the numerical calculations for the model with the longitudinal modulation of the topological defect (Fig. 5.8 (a)). In this case, the couplings to the left $J_{-1,0}(t)$ and right $J_{0,1}(t)$ nearest neighbors of the 0^{th} site change with a phase shift of π. We choose $J_{-1,0}(t) = J_2 + \Delta J \sin \omega t$, $J_{0,1}(t) = J_2 - \Delta J \sin \omega t$ and $V_0(t) \equiv 0$. In all our calculations we set $J_1 = 1$, $J_2/J_1 = 0.5$, $\Delta J = 0.3 J_1$, and $2M = 100$ dimers. The corresponding quasienergy spectrum in dependence on the driving frequency ω is presented in Fig. 5.10. Here, color coding indicates the spectral weight of each Floquet state calculated using Eq. (5.41). As we have expected, local time-periodic perturbations split the topological edge state into the Floquet copies that are seen as

bright diverging lines, whereas no significant change of the bulk states is observed. Importantly, if the energy of such a Floquet replica of the edge state ($n\omega$) has the same value as that of a bulk state ($|J_1 - J_2| \leq \varepsilon \leq |J_1 + J_2|$), then the edge and bulk states hybridise. As a consequence, the edge state depopulates into the bulk due to the local time-periodic coupling. Due to relatively small driving amplitude, the first-order Floquet replica of the topological edge state becomes predominantly populated and thus plays the principle role in this effect. Depending on its spectral position, we can distinguish three frequency regimes: low-frequency $\omega < |J_1 - J_2|$, intermediate frequency $|J_1 - J_2| \leq \omega \leq |J_1 + J_2|$, and high frequency $\omega > |J_1 + J_2|$.

Before we discuss each frequency regime separately, as reference, we consider the static system ($\Delta J = 0$) which can be thought as the limit $\omega \to 0$. In Fig. 5.11 (a) we plot the corresponding temporal evolution of the probability density $|\Psi(s,t)|^2$ (see Eq. (5.39), where $\Psi(s,t)$ is the projection of $|\Psi(t)\rangle$ on the lattice sites s) for the single-site input at the 0^{th} lattice site. Here, the excited bulk modes are spreading ballistically while the topological edge state shows itself as a fraction of the probability density localized at the interface. The momentum distribution of the probability density $|\tilde{\Psi}(k,E)|^2$ (see Fig. 5.11 (b)) features two cosine-shaped bands (compare with Fig. 5.3) and a horizontal line in the middle of the band gap, a manifestation of the topological edge state.

In the low frequency regime ($\omega < |J_1 - J_2|$), the first ($n = \pm 1$) replicas of the zero-energy mode lie inside the band gap (see green arrows in Fig. 5.11 (d)). Additionally, one observes higher replicas ($n > 1$) that overlap with the bulk states in the frequency interval $\omega_n \in [\frac{|J_1-J_2|}{n}, \frac{|J_1+J_2|}{n}]$ and thereby induce higher-order transitions. However, for all the modulation amplitudes accessible in the experiments the effect of higher replicas is negligible which is confirmed by the calculation of the decay rates that will be addressed later. Fig. 5.11 (c) shows that $|\Psi(s,t)|^2$ stays localized at the 0^{th}

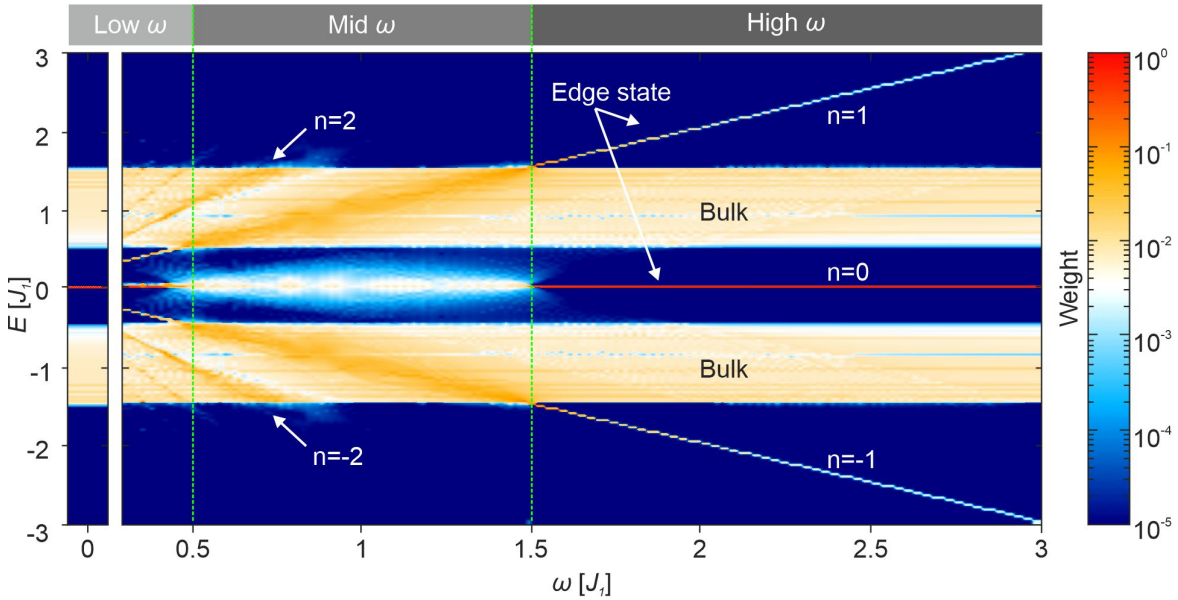

Figure 5.10: Frequency-dependent quasienergy spectrum with assigned weights in the case of the longitudinal perturbations at the interface. In the left column the spectrum of a static system is shown which can thought as a limit $\omega \to 0$. In the calculations we assumed $2M = 100$ dimers, $J_1 = 1$, $J_2/J_1 = 0.5$, and $\Delta J = 0.3J_1$. As initial conditions we solely excited the 0^{th} lattice site.

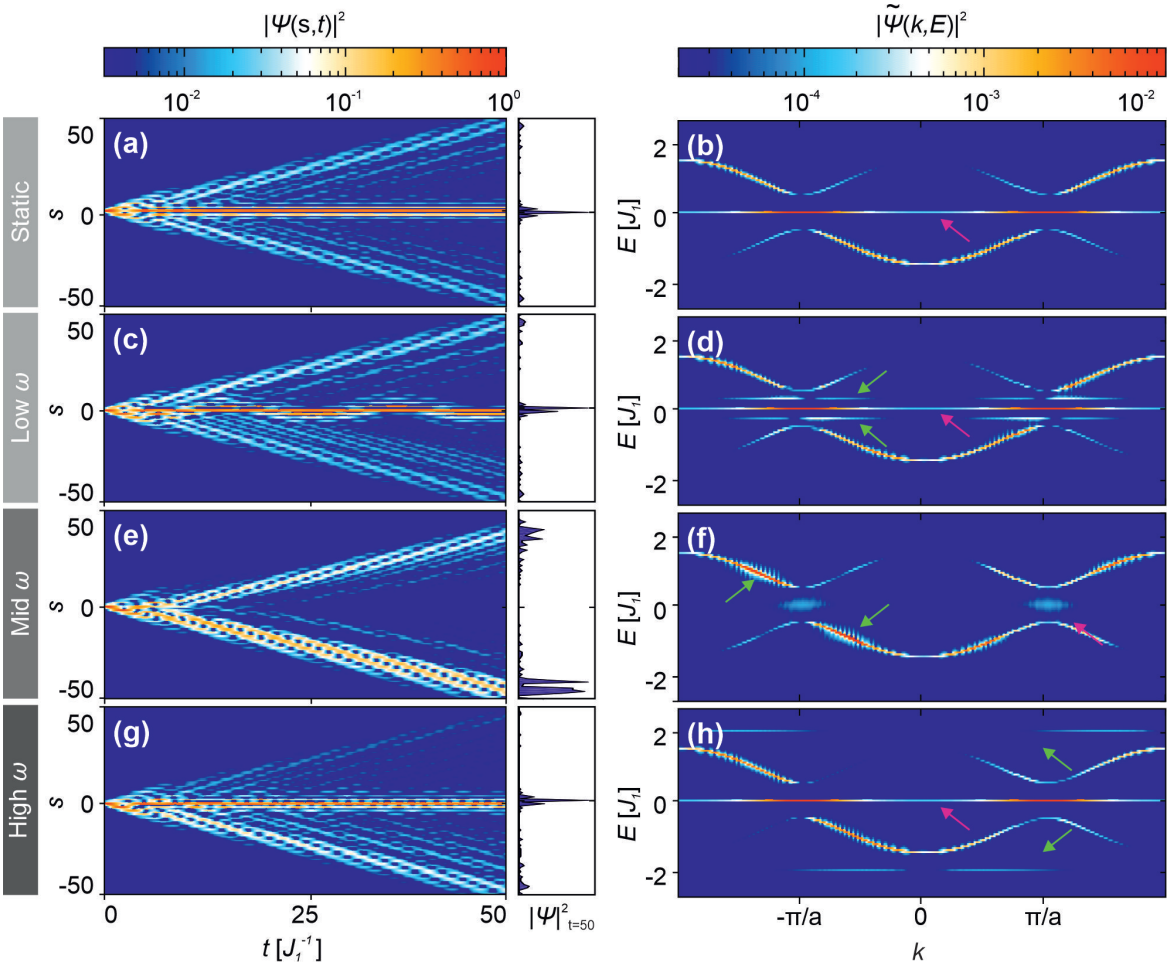

Figure 5.11: Temporal evolution of the probability density (left) and corresponding momentum-resolved spectra (right) for: (a, b) undriven case, (c, d) low frequency ($\omega = 0.3J_1$), (e, f) intermediate frequency ($\omega = J_1$), (g, h) high frequency ($\omega = 2J_1$). The histograms at the right side from (a), (c), (e), and (g) show the distribution of the probability density at $t = 50J_1^{-1}$. In the spectra, magenta arrows point to the 0^{th} Floquet replica of the edge state, while green arrows indicate the location of its 1^{st} Floquet replicas. All calculations were performed for the longitudinally modulated SSH model with $2M = 100$ dimers, $J_1 = 1$, $J_2/J_1 = 0.5$, and $\Delta J = 0.3J_1$. As initial conditions we solely excited the 0^{th} lattice site.

lattice site.

This picture completely changes in the intermediate frequency regime ($|J_1 - J_2| \leq \omega \leq |J_1 + J_2|$), when the first replicas of the topological edge state enter the energy interval of the static bulk states inducing the aforementioned hybridization of bulk and edge states. As a result, the probability density delocalizes (Fig. 5.11 (e)) and the momentum distribution also shows the pronounced coupling, i.e. the population of the zero-energy state drops drastically despite the non-trivial topological invariants (see magenta arrow, Fig. 5.11 (f)), while the bulk bands gain more weight (green arrows in Fig. 5.11 (f)). No such coupling has been observed when driving the whole bulk of the system, as in [136]. There, the driving induces gaps to open when two Floquet replicas overlap, such that edge states are

protected by the gaps from coupling to bulk states. Here, however, due to the spatially local driving no such gaps are opened, and coupling can occur.
Finally, in the high frequency regime ($\omega > |J_1 + J_2|$) the 1st Floquet replicas of the zero energy mode lie outside of the band and no hybridization of bulk and edge states takes place. Consequently, the probability density is again localized and the population of the topological edge state is restored (Figs. 5.11 (g), 5.11 (h)).
We note, that in our system no anomalous edge states [114] are created for any driving frequency since there is no periodic drive of the bulk. The periodic intensity modulation at the interface in Figs. 5.11 (c) and (g) results from beating of the topological edge state and its Floquet replicas. The asymmetry of the probability density distribution $|\Psi(s,t)|^2$ with respect to the interface in Figs. 5.11 (c), (e), and (g) results from the π phase shift of the longitudinal coupling modulation.
Analogous calculations for the transverse perturbations (couplings are modulated in phase) show qualitatively the same behavior. This case fulfills parity, which leads to a symmetric distribution of $|\Psi(s,t)|^2$ around the 0th site. Adding a periodic local on-site potential variation for the 0th site violates chiral symmetry by shifting the energy of the edge mode by the amount of ΔV. However, this does not have a strong influence on the overall picture if the corresponding amplitude ΔV is smaller or in the order of ΔJ.

Decay rate of a topological edge state

An insightful quantitative analysis of the perturbed SSH model was provided by C. Dauer from the TU Kaiserslautern. For the same model parameters he evaluated how fast the topological edge state decays due to coupling to the bulk states. We briefly discuss his results as they are important for completeness of the theoretical analysis.
The first finding was that the decay rates due to $n > 1$-order transitions are very low for the experimentally observable time scales. For example, the maximum 2nd-order transition rate for our driving scheme was estimated to be two orders of magnitude smaller than the rate of the 1st-order transition. Hence, it is indeed reasonable to restrict ourselves to consideration of the 1st-order Floquet replicas only.
The 1st-order transition rate Γ in dependence on the driving frequency ω was calculated using two different approaches. First, it was extracted by fitting the squared overlap between the zero-energy eigenstate of the undriven SSH model $|\varepsilon = 0\rangle$ and the time-dependent solution of the perturbed problem $|\Psi(t)\rangle$ with an exponentially decaying function:

$$|\langle \varepsilon = 0 | \Psi(t) \rangle\rangle|^2 \approx (1-c)e^{-\Gamma t} + c, \tag{5.42}$$

where the parameter c was zero at the intermediate frequency interval $\omega \in [|J_1 - J_2|, |J_1 + J_2|]$ (see Fig. 5.12 (a)). Second, the decay rate Γ_{FGR} was evaluated using Fermi's golden rule. Both methods showed qualitatively the same behaviour (see Fig. 5.12 (b)): The decay rate reached the maximum of $\Gamma \approx 0.2 J_1$ inside the intermediate frequency interval and dropped to zero at $\omega = |J_1 - J_2|$ and $\omega = |J_1 + J_2|$. Fig. 5.12 (c) proves that at small driving amplitudes ΔJ the decay rates defined in these two different ways converge.

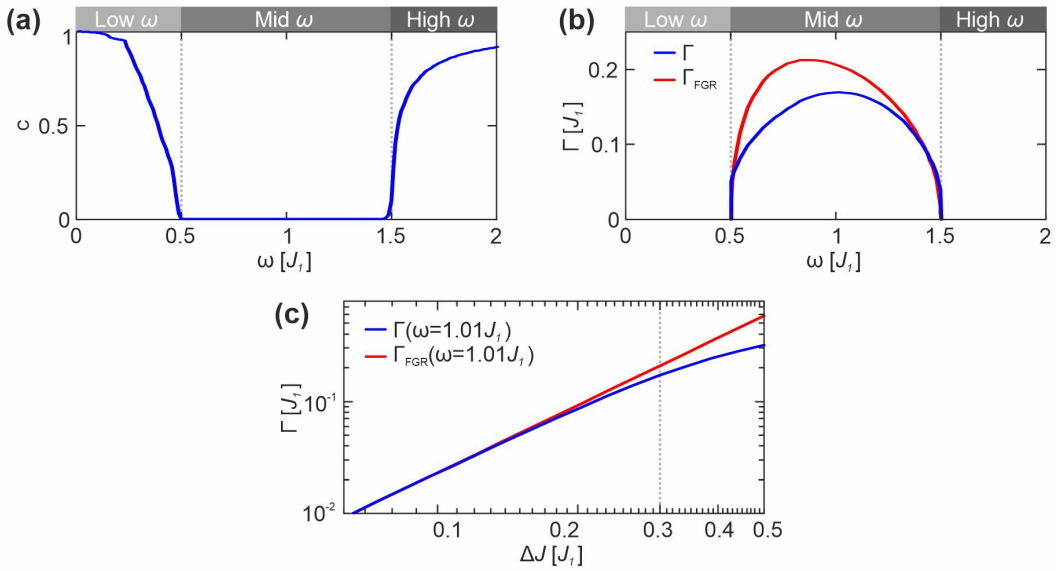

Figure 5.12: Results of the decay rates calculations of the topological edge state in the perturbed SSH model obtained by C. Dauer from TU Kaiserslautern. (a) Fitting parameter c from Eq. (5.42) versus driving frequency ω. (b) The decay rates of the topological edge mode in dependence on driving frequency in the intermediate frequency regime, obtained by two different methods: from Eq. (5.42) (blue line) and Fermi's golden rule (red line) at the driving amplitude $\Delta J = 0.3J_1$. (c) The decay rate Γ sampled at $\omega = 1.01J_1$ in dependence on driving amplitude ΔJ. The dashed line marks $\Delta J = 0.3J_1$ which was used in the previous numerical calculations.

5.3 Experiments

Our theoretical predictions are verified by the experiments based on arrays of coupled DLSPPWs. The experimental realization of the perturbed SSH model described by Eqs. (5.30), (5.31), and (5.32) is based on the mathematical equivalence between the time-dependent TB Schrödinger equation and equations of the coupled mode theory as justified in Sec. 3.2.4. Fig. 5.13 (a) illustrates the plasmonic implementation of the SSH model with longitudinal time-periodic perturbations of the topological defect. The strong and weak bonds J_1 and J_2 are modeled by alternating short d_1 and long d_2 distances between adjacent waveguides, respectively. The central unpaired waveguide represents an interface between two distinct dimerizations of the SSH model. Since in the waveguide model the propagation distance z plays the role of time [4], bending the 0^{th} waveguide sinusoidally with amplitude A, we implement longitudinal perturbations at the interface. Different frequency regimes are realized by varying the period T while A is always kept constant.

Whereas localization of SPPs to a surface allows to realize only longitudinal perturbations, dielectric waveguides fabricated with direct laser writing have an additional dimensional degree of freedom thereby allowing for transverse bending of a waveguide. In contrast to DLSPPWs, dielectric waveguides are designed to guide light. However, by monitoring light intensity in arrays of coupled dielectric waveguides, one can simulate TB systems by means of the same quantum-optical analogy which was discussed in the context of a plasmonic system. Transverse perturbations of the topological defect in the SSH model were implemented in dielectric waveguide arrays by C. Jörg from the TU Kaiserslautern as shown in Fig. 5.13 (b).

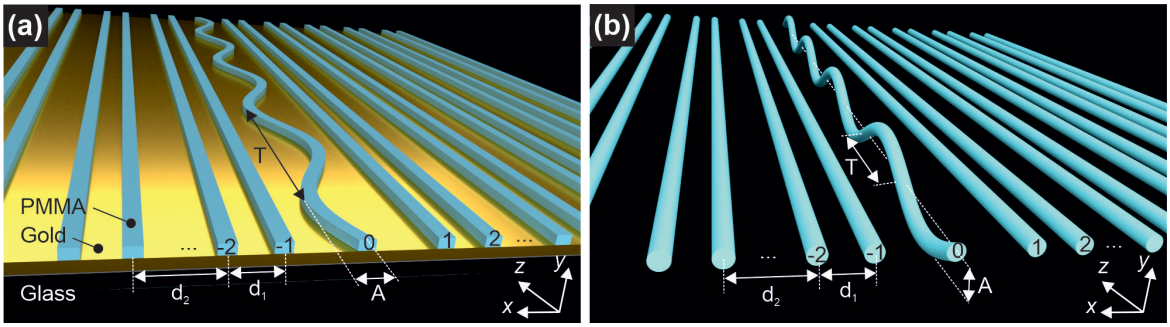

Figure 5.13: Sketches of the experimental realizations of the SSH chain with time-periodic perturbations of a single lattice site at the interface between two distinct dimerizations. (a) Longitudinal modulation of the boundary implemented in a plasmonic waveguide array. (b) Transverse modulation of the boundary implemented in a dielectric waveguide array. Here, d_1 (d_2) is the short (long) center-to-center distance, A is the maximum deflection of the 0^{th} waveguide from the center, and T is the period of driving. Note that in the waveguide system the propagation distance z corresponds to time t in the Schrödinger equation.

5.3.1 Fabricated samples

The DLSPPW arrays are fabricated by negative-tone gray-scale electron beam lithography (see Sec. 4.1 for details). Fig. 5.14 (a) depicts an electron micrograph of a typical sample. In the following, propagation and coupling constants are calculated numerically using the finite element method which was introduced in Sec. 3.2.1. The width and the height of each waveguide are designed to be 250 nm and 110 nm, respectively, to guarantee single-mode operation at the working light wavelength of $\lambda = 980$ nm. This results in a propagation constant of a single DLSPPW of $\beta = 6.65\ \mu\text{m}^{-1}$. In all the samples the short distance is $d_1 = 0.7\ \mu$m and the long distance is $d_2 = 1.1\ \mu$m. These separations correspond to coupling constants $J_1 = 0.16\ \mu\text{m}^{-1}$ and $J_2 = 0.08\ \mu\text{m}^{-1}$, respectively. These parameters are chosen to ensure sufficient coupling between the adjacent waveguides and to create a large enough band gap to see topological effects. The position of the central waveguide is modulated sinusoidally resulting in

$$J_{0,1}(t) = J_1 \cdot p_1 e^{\left(-p_2 \cdot A \sin(\omega t)\right)}, \tag{5.43}$$

where $p_1 = 0.49$ and $p_2 = 1.75\ \mu\text{m}^{-1}$ are fitting parameters and ω is the modulation frequency. For all the samples the maximum deflection of the central waveguide is chosen to be $A = 0.3\ \mu$m, being a good trade-off between bending losses and the strength of dynamic effects. It corresponds to the coupling variation of $\Delta J \approx 0.25 J_1$ (for linear approximation of the exponent in Eq. (5.43)). Varying the period T from 8 µm up to 80 µm we realize different frequency regimes. In the static case, the 0^{th} waveguide is kept straight.

In Sec. 4.1 we have already mentioned the proximity effect which inevitably arises in lithographic processes. If we fabricate all the waveguides with equal electron dose, then, due to this effect, every first waveguide in a dimer (in the order of fabrication) acquires an additional dose from the second waveguide, and thereby its height turns to be larger. Moreover, the central curved waveguide, due to periodic modulation of the distance to the subsequently fabricated nearest neighbor, features periodic height variation. It leads to unwanted on-site potential variation which breaks chiral symmetry and thus can influence the topological properties of the system. These effects were revealed by atomic

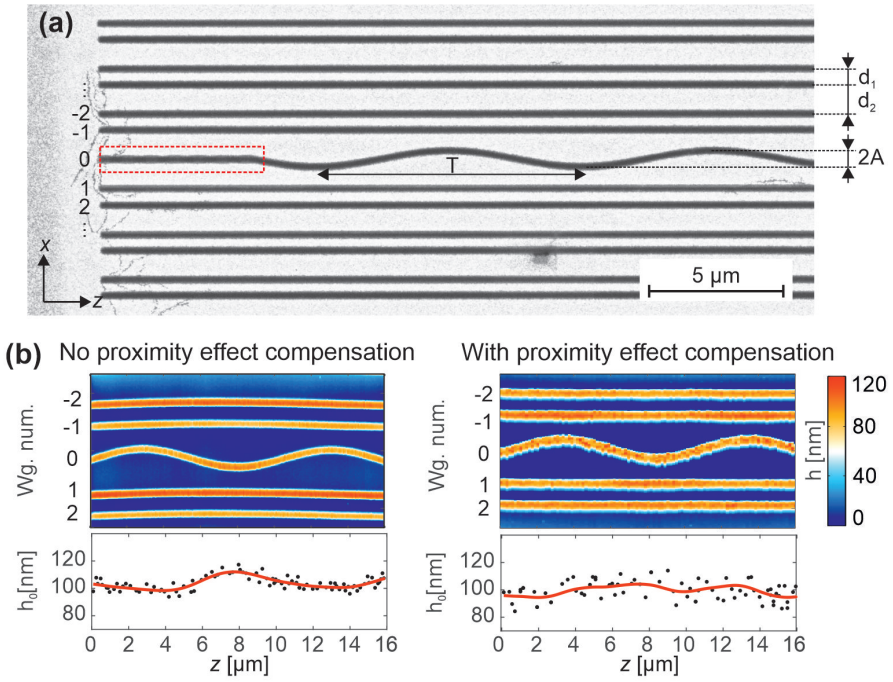

Figure 5.14: (a) Scanning electron micrograph of the plasmonic waveguide sample with the period $T = 10$ µm. The red dotted box highlights the grating coupler. (b) The AFM scans of two DLSPPW arrays with $T = 10$ µm fabricated with different SEM settings. Plots in the bottom show the height of the 0^{th} waveguide taken correspondingly from the AFM scans on top. Here, the black dots are the sampling points while the red lines are smoothing splines. The waveguides are first fabricated with equal dose (left) demonstrating that the heights of the waveguides from one dimer are different (compare waveguides 1 and 2) and the height of the 0^{th} waveguide varies periodically. Then the electron dose was adjusted so that all the waveguide heights are equal and there is no periodic height variation of the wobbling waveguide (right). Note that the random height variation seen in the bottom plots comes from the measurement error.

force microscopy (see Fig. 5.14 (b)). In order to keep the heights of the waveguides constant, the proximity effect in the lithographic process was compensated by equalizing the background dose. It was achieved by reducing the dose for every first waveguide in a dimer. In addition to that, the curved waveguide was fabricated with slightly increased dose as the last element, i.e. after all the straight waveguides are written. The resulting geometry was again controlled after fabrication by atomic force microscopy to ensure that all the waveguides are of the same height.

Periodic bending of the central waveguide can cause local on-site potential variation. Using the approach described in Ref. [141], where a curved waveguide is considered as a straight waveguide with modified propagation constant, we can approximate the periodic modulation of the real part of the propagation constant due to sinusoidal bending as

$$\tilde{\beta}(z) \approx \beta - \Delta V(T)(1 - \sin 4\pi z/T), \tag{5.44}$$

with β being the propagation constant in the absence of modulation and $\Delta V > 0$ is an amplitude that depends on T. Note the factor of 4π in the argument of the sine in Eq. (5.44), it comes from the fact that the change in propagation constant does not depend on whether the waveguide core deflects to the

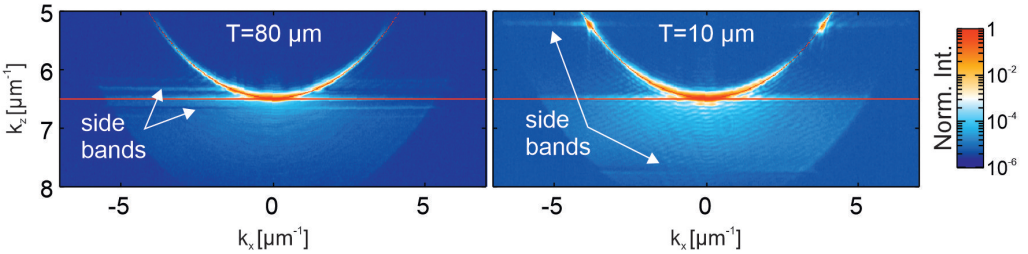

Figure 5.15: Fourier-space LRM micrographs recorded for isolated sinusoidally bent DLSPPWs at $T = 80$ µm (left) and $T = 10$ µm (right). The horizontal red line indicates the position of the prime mode. No shift is observed.

right or to the left, thus, $\tilde{\beta}(z)$ varies with half the waveguide period. In order to estimate ΔV for our experiments, single-standing sinusoidally-bent waveguides at different periods T were fabricated and measured using Fourier-space LRM (see Sec. 4.2). Next, the spectral positions of the prime waveguide mode at different periods were compared (see Fig. 5.15). We use the term "prime" to distinguish this mode from the side bands that result from modulation. We expected that, due to increased radius of curvature, the shift $\Delta V(T)$ of the prime mode would be larger for lower T. However, no visible difference was observed in our experiments, the position of the prime mode at all T was approximately the same as for the straight waveguide that is $\beta = 6.65$ µm^{-1}. Therefore, we can estimate the maximum ΔV to be smaller than the resolution of the Fourier measurements, i.e. $\Delta V < 0.02$ µm^{-1}. This is already more than four times smaller than the variation of the coupling constant $\Delta J = 0.086$ µm^{-1}. These results justify that, due to strong confinement of the SPPs, we can neglect the variation of the effective refractive index due to the curvature of the waveguide, i.e. we can set the on-site potential $V_0(t) \approx 0$.

5.3.2 Optical measurements

In the resulting arrays SPPs are excited by focusing a TM-polarized laser beam onto the grating coupler (see red dotted box in Fig. 5.14 (a)), which was fabricated on top of the 0$^{\text{th}}$ waveguide. The propagation of SPPs in each array is monitored by real- and Fourier-space leakage radiation microscopy as described in details in Sec. 4.2.
We first consider the intensity distribution of SPPs in the real-space $I(x, z)$, that corresponds to the probability density distribution $|\Psi(s, t)|^2$. Fig. 5.16 presents the real-space LRM measurements for the static case as well as for three different frequency regimes. For our experimental parameters $J_2/J_1 = 0.5$, thus low, intermediate, and high frequency regimes are realized at the periods of $T = 80$ µm, $T = 50$ µm, and $T = 8$ µm, respectively, corresponding to $\omega = 0.49J_1$, $\omega = 0.8J_1$, and $\omega = 4.9J_1$. In all plots, $x = 0$ indicates the position of the 0$^{\text{th}}$ waveguide which represents an interface between two SSH chains with topologically distinct dimerisations, while the origin of the z axis is placed immediately after the grating coupler. The case of the static SSH model is shown in Fig. 5.16 (a). Similar to numerical simulations from Fig. 5.11 (a), the excitation of the topologically protected mode results in localization of SPPs at the interface. The decaying intensity along the z-axis is due to radiation losses and absorption. However, this does not affect the topological properties of the system [28]. As predicted by Floquet theory, SPP localization at the interface in real space is also observed for modulation at low (Fig. 5.16 (b)) and high (Fig. 5.16 (d)) frequencies (compare to

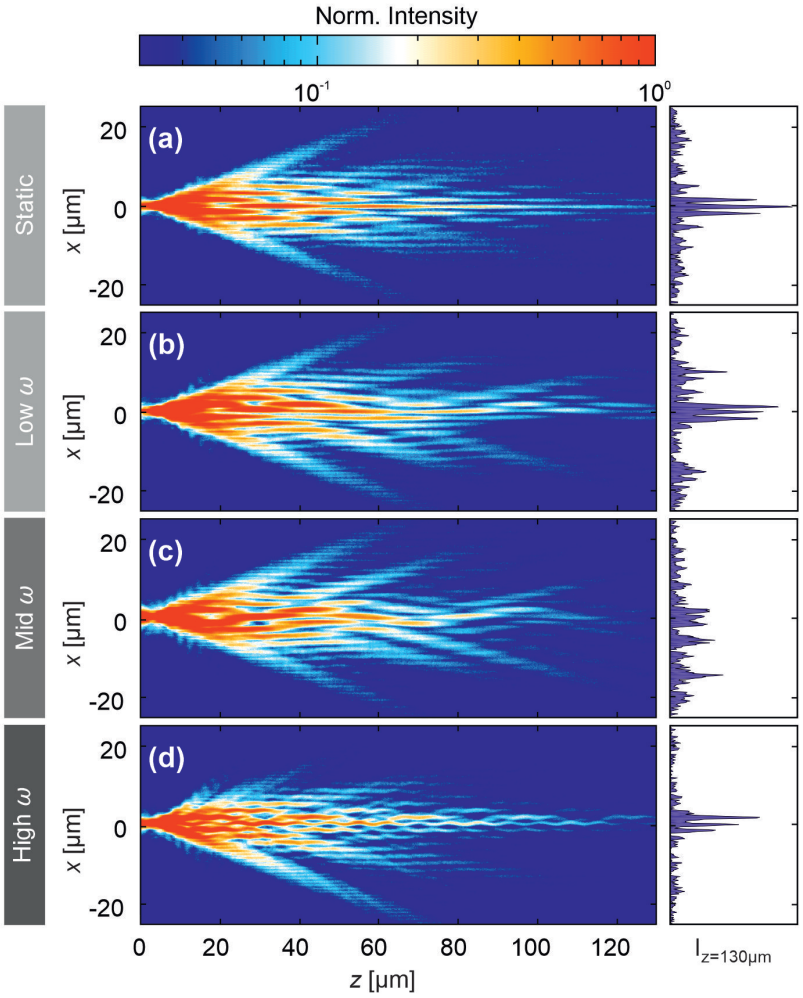

Figure 5.16: Real-space leakage radiation micrographs of the DLSPPW arrays, analogous to the SSH model with a topological defect at $x = 0$. The geometric parameters of all arrays are chosen such that $J_2/J_1 = 0.5$. (a) Corresponds to the static case. In (b-d) the defect is modulated in the longitudinal direction ($\Delta J \approx 0.25 J_1$) with different frequencies: (b) low frequency regime ($\omega = 0.49 J_1$ corresponding to $T = 80$ µm), (c) intermediate frequency regime ($\omega = 0.8 J_1$ corresponding to $T = 50$ µm), (d) high frequency regime ($\omega = 4.9 J_1$ corresponding to $T = 8$ µm). The histograms at the right side show the intensity distribution after the propagation distance of $z = 130$ µm.

Figs. 5.11 (c) and (g)). In contrast, in the intermediate frequency regime (Fig. 5.16 (c)), delocalization of SPPs into the bulk is observed (see histogram at the right side of Fig. 5.16 (c)). Hence, we see clear experimental evidence of the depopulation of a topologically protected edge mode by local driving in agreement with the results of our Floquet analysis (see Fig. 5.11 (e)).
Next, we come to the Fourier-space measurements which were performed for the same DLSPPW arrays (see Fig. 5.17). As we have learnt from the quantum-optical analogy, these momentum resolved spectra $I(k_x, k_z)$ can be directly related to the Fourier-transformed probability density $|\tilde{\Psi}(k, E)|^2$. The static SSH model shown in Fig. 5.17 (a) features the midgap position of the topologically protected edge mode. We note that the asymmetry of the bulk bands arises from non-vanishing next-nearest

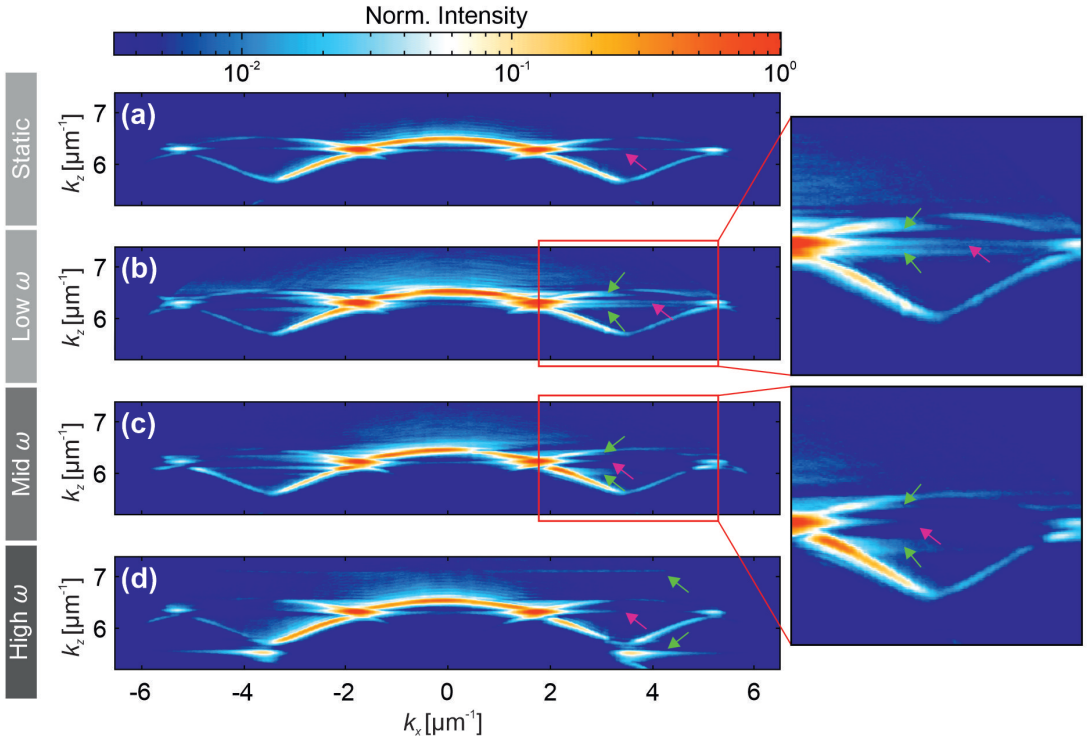

Figure 5.17: The Fourier-space leakage radiation micrographs of the DLSPPW arrays corresponding to the real-space measurements from Fig. 5.16. All the parameters of the samples are the same as in Fig. 5.16. Again, (a) is the static case, while in (b), (c), and (d) the topological defect is longitudinally modulated with low, intermediate, and high frequency, respectively. The magenta arrows highlight the 0^{th} Floquet replica of the edge state, while green ones point to the location of its first Floquet replicas.

neighbor coupling [28]. In the low and high frequency regimes, the Fourier-space measurements reveal that the 1^{st} Floquet replicas do not overlap with the bulk bands: they either reside inside the band gap (Fig. 5.17 (b)) or outside of the bands (Fig. 5.17 (d)), respectively. Finally, the energy of the 1^{st} Floquet replicas coincides with the static bulk states in the intermediate frequency regime and the edge mode becomes fainter due to coupling to the bulk states induced by time-periodic perturbations (Fig. 5.17 (c)). These results confirm the numerically predicted behaviour in Figs 5.11 (b), (d), (f), and (h).

Experiments with 3D-printed dielectric waveguides performed by C. Jörg from TU Kaiserslautern showed that transverse periodic perturbations of the topological defect also led to depopulation of the topologically-protected edge state in the intermediate frequency regime. The obtained results agreed well with the corresponding Floquet analysis. The detailed description of these experiments can be found in [138].

Summary

In conclusion, in this chapter we got familiar with the simplest model for a topological insulator, the Su-Schrieffer-Heeger model. On its example we have shown that if an edge of a topologically

non-trivial material is locally subject to an external periodic field, it can result into the depopulation of an edge state for a certain frequency range. In the case when the perturbation respects the chiral symmetry, the topological edge state remains in the middle of the band gap. Local driving splits this midgap state into the Floquet copies but keeps the bulk spectrum almost unaltered. The depopulation happens once the Floquet replicas of the edge state intersect the bulk energies. For the examined driving scheme, where the amplitude of the driving is relatively small, this effect is predominantly governed by the first-order replica. This phenomenon was analysed theoretically with the help of the Floquet theory and demonstrated experimentally in arrays of plamonic waveguides for longitudinal polarization of the perturbing field. Independent experiments based on dielectric waveguides showed qualitatively the same behaviour for transverse polarization.

CHAPTER 6

Observation of topological transport quantization by dissipation in fast Thouless pumps

The focus of this chapter is the topological transport quantization in slowly varying one-dimensional potentials known as the Thouless pumping [36]. The standard model for realizing of the Thouless pumping is the periodically driven Rice-Mele (RM) model [41, 142]. It describes a dimerized tight-binding chain whose system parameters change cyclically along a closed loop in the Hamiltonian parameter space. In the adiabatic regime, for a homogeneously filled band the net particle transfer per pumping cycle is an integer given by the Chern number, a topological invariant, and thus is robust against topology-preserving perturbations. Periodicity in time naturally suggests to consider Thouless pumping within the Floquet formalism. From this perspective, a nontrivial Chern number manifests itself in the continuous winding of the quasienergy band around the two-dimensional Floquet-Bloch Brilliouin zone.

Since its discovery, Thouless pumping has been believed to be restricted only to the limit of adiabatically slow driving. The reason is that at finite driving frequencies, the system becomes topologically trivial due to non-adiabatic transitions between the bands [15, 39]. In Floquet picture, these transitions show themselves as gap opening at the avoided crossings of the quasienergy bands propagating in the opposite directions. As a result, the winding number becomes trivial and particle transport deviates from perfect quantization. The adiabaticity requirement is one of the major limitations for the experimental observation of the Thouless pumping.

In this chapter, we introduce a time-periodic modulation of the dissipation as a new concept to overcome this limitation. In particular, we show that a topological band structure and the associated quantized transport in the driven RM model can be restored even at driving frequencies as large as the system's band gap. The basic idea is to suppress non-adiabatic transitions by tailored, time-periodic losses. In order to analyse systems of this kind, we generalize the Floquet-Bloch theory using elements of non-Hermitian quantum mechanics. Theoretical results presented in this chapter were performed in close cooperation with H. Qiu and J. Kroha from the University of Bonn. Our theoretical predictions are then confirmed by an experimental observation of the topological transport quantization in DLSPPW arrays.

The chapter is organized as follows: In Section 6.1 we introduce the Rice-Mele model and on its basis explain the mechanism of topological transport quantization upon slow periodic variation of the system's parameters. We thereafter consider the Thouless pumping in the Floquet picture and

show that at finite driving frequencies it breaks down. Next, in Section 6.2 we add time-periodic losses to the driven RM model, develop a suitable non-Hermitian Floquet-Bloch theory and designate conditions for dissipative transport quantization. In the end of the section we present the results of our theoretical analysis. Finally, in Section 6.3 we implement the driven RM model with periodic losses to DLSPPW arrays and show the resulting optical measurements. The chapter closely follows Ref. [143].

6.1 Thouless pumping in the driven Rice-Mele model

6.1.1 Static Rice-Mele model

Our starting point is the static Rice-Mele model (see sketch in Fig. 6.1). It was originally developed to study soliton excitations in linearly conjugated diatomic polymers with alternating single and double bonds such as poly-carbonitrile $(CH=N)_n$ [144]. The Hamiltonian of the RM model with N unit cells can be obtained from the SSH Hamiltonian (5.1), that was analysed in the previous chapter, by adding extra onsite potential offsets u_a and u_b to the sublattices A and B, respectively

$$\begin{aligned}\hat{H} = &- J_1 \sum_{j=1}^{N} (|j,B\rangle\langle j,A| + h.c.) - J_2 \sum_{j=1}^{N-1} (|j+1,A\rangle\langle j,B| + h.c.) \\ &- u_a \sum_{j}^{N} |j,A\rangle\langle j,A| - u_b \sum_{j}^{N} |j,B\rangle\langle j,B|.\end{aligned} \tag{6.1}$$

We impose periodic boundary conditions analogously to how it was done for the SSH model (see Sec. 5.1.1 for details). As a consequence, the solutions of the time-independent SE are the Bloch states

$$|\psi_{\alpha,k}\rangle = |k\rangle \otimes |u_{\alpha,k}\rangle, \quad \alpha \in \{-,+\}, \tag{6.2}$$

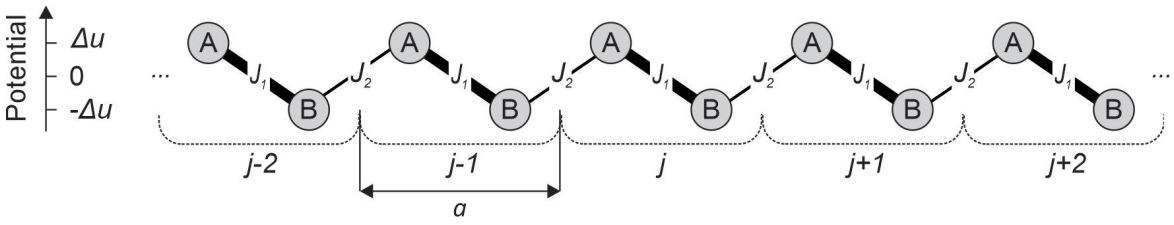

Figure 6.1: Schematic representation of the RM model. Here, the thickness of the line connecting the lattice sites reflects the strength of the bond. J_1 and J_2 denote the intercell and intracell hopping amplitudes, respectively. The sites A and B have an extra onsite potential shifted by $+\Delta u$ and $-\Delta u$, respectively. The index j labels the unit cells. a is the lattice constant.

comprised of the plane wave basis states $|k\rangle \in \mathcal{H}_{\text{external}}$ (see Eq. (2.15)) and the Bloch modes $|u_{\alpha,k}\rangle \in \mathcal{H}_{\text{internal}}$. The Bloch modes are the eigenstates of the Bloch Hamiltonian

$$\hat{H}_k = -\begin{pmatrix} h_0 + h_z & h_x - ih_y \\ h_x + ih_y & h_0 - h_z \end{pmatrix} = -h_x\hat{\sigma}_x - h_y\hat{\sigma}_y - h_z\hat{\sigma}_z - h_0\hat{\sigma}_0, \tag{6.3}$$

where $\{\hat{\sigma}_x, \hat{\sigma}_y, \hat{\sigma}_z\}$ are the Pauli matrices, $\hat{\sigma}_0$ is the identity matrix and

$$\begin{aligned} h_x &= J_1 + J_2 \cos k; \\ h_y &= J_2 \sin k; \\ h_z &= (u_a + u_b)/2 = \bar{u}; \\ h_0 &= (u_a - u_b)/2 = \Delta u; \end{aligned} \tag{6.4}$$

Here and elsewhere, the lattice constant is set to one $a = 1$. The corresponding eigenvalues read

$$E_{\pm}(k) = \bar{u} \pm \sqrt{\Delta u^2 + J_1^2 + J_2^2 + 2J_1J_2\cos k}, \quad \alpha \in \{1, 2\}. \tag{6.5}$$

Eq. (6.5) shows that, if we set the Fermi energy $E_{\text{F}} = \bar{u}$, the RM model describes an insulator whose spectrum consists of the two bands separated by a band gap of $2\sqrt{\Delta u^2 + \Delta J^2}$, where we denoted $\Delta J = J_1 - J_2$. This gap closes and the system becomes a metal only simultaneously when $\Delta u = 0$ and $\Delta J = 0$.

Since in this chapter we will inquire about the transport phenomena, it is necessary to know where a particle is localized in the lattice. We go back from momentum space to position space by making use of the Wannier states

$$|w_{\alpha,j}\rangle = \frac{1}{\sqrt{N}} \sum_k e^{-ijk} |\psi_{\alpha,k}\rangle, \quad k \in 1^{\text{st}}\text{BZ} \tag{6.6}$$

which form an orthonormal set in $\mathcal{H}_{\text{external}} \otimes \mathcal{H}_{\text{internal}}$ (see Sec. 2.1.1). At this point it is important to note, that the Bloch states are unique only up to a phase factor, i.e. a gauge transformation $|\psi_{\alpha,k}\rangle \to |\psi_{\alpha,k}\rangle e^{i\chi(k)}$, where $\chi(k)$ is an arbitrary chosen real phase, gives rise to an equally good set of Bloch states. In contrast, this phase can significantly alter the localization properties of the Wannier states. Luckily, in 1D one we can always find a gauge such that $|w_{\alpha,j}\rangle$ is localized around x_j and decays rapidly away from x_j [145]. In the following, we assume that such a gauge is found and that the Bloch states in Eq. (6.6) already incorporate the proper phase factor.

6.1.2 Connection between the Wannier center and the Zak phase

Using the position operator

$$\hat{x} = \sum_j^N j \left(|j, A\rangle\langle j, A| + |j, B\rangle\langle j, B|\right), \quad j \in \{1, 2, ..., N\} \tag{6.7}$$

we define the Wannier center with respect to a unit cell as [106]

$$\bar{X}_j^{\alpha} = \langle w_{\alpha,j}|\hat{x}|w_{\alpha,j}\rangle. \tag{6.8}$$

Inserting Eqs. (2.15) and (6.2) into Eq. (6.6) and taking into account Eq. (6.7) we get

$$\begin{aligned}\hat{x}|w_{\alpha,j}\rangle &= \hat{x}\frac{1}{\sqrt{N}}\sum_k e^{-ijk}\frac{1}{\sqrt{N}}\sum_{l=1}^{N} e^{ilk}|l\rangle\otimes|u_{\alpha,k}\rangle \\ &= \frac{1}{N}\sum_k e^{-ijk}\sum_{l=1}^{N} l e^{ilk}|l\rangle\otimes|u_{\alpha,k}\rangle.\end{aligned} \tag{6.9}$$

Since N is assumed to be large, we can replace the sum by an integral over the Brillouin zone $\sum_k \to \frac{N}{2\pi}\int_{\mathrm{BZ}}\mathrm{d}k$ and transform it using partial integration

$$\begin{aligned}\hat{x}|w_{\alpha,j}\rangle &= \frac{1}{2\pi}\int_{\mathrm{BZ}}\mathrm{d}k\sum_l l e^{-i(j-l)k}|l\rangle\otimes|u_{\alpha,k}\rangle \\ &= \frac{-i}{2\pi}\int_{\mathrm{BZ}}\mathrm{d}k\frac{\partial}{\partial k}\sum_l e^{-i(j-l)k}|l\rangle\otimes|u_{\alpha,k}\rangle \\ &+ \frac{j}{2\pi}\int_{\mathrm{BZ}}\mathrm{d}k\sum_l e^{-i(j-l)k}|l\rangle\otimes|u_{\alpha,k}\rangle \\ &+ \frac{i}{2\pi}\int_{\mathrm{BZ}}\mathrm{d}k\sum_l e^{-i(j-l)k}|l\rangle\otimes\frac{\partial}{\partial k}|u_{\alpha,k}\rangle.\end{aligned} \tag{6.10}$$

Eq. (6.10) can be simplified by noticing that the first term is a periodic function of k, hence, integration over the 1$^{\mathrm{st}}$ BZ gives zero

$$\left(\frac{-i}{2\pi}\sum_l e^{-i(j-l)k}|l\rangle\otimes|u_{\alpha,k}\rangle\right)\Bigg|_{-\pi}^{\pi} = 0, \tag{6.11}$$

while the second term recovers the original Wannier function multiplied by j

$$\frac{j}{2\pi}\int_{\mathrm{BZ}}\mathrm{d}k\sum_l e^{-i(j-l)k}|l\rangle\otimes|u_{\alpha,k}\rangle = j|w_{\alpha,j}\rangle. \tag{6.12}$$

It brings us to the central result of this subsection

$$\bar{X}_j^{\alpha} = j + \frac{i}{2\pi}\int_{\mathrm{BZ}}\mathrm{d}k\langle u_{\alpha,k}|\frac{\partial}{\partial k}|u_{\alpha,k}\rangle, \tag{6.13}$$

where the first term simply tells us that the Wannier functions are equally spaced from each other by a distance of one unit cell, while the second term is exactly given by the Zak phase $\gamma_{\mathrm{Z}}^{\alpha}$ divided by 2π (compare to Eq. (2.48)).

Recall that in the SSH model the Zak phase served as a topological invariant and was quantized (see Sec. 5.1.2 for details). In particular, for the filled band it took two different values, $\gamma_{\mathrm{Z}}^{-} = 0$ or $\gamma_{\mathrm{Z}}^{-} = \pi$, depending on the dimerization, i.e. on whether $J_1/J_2 > 1$ or $J_1/J_2 < 1$. However, the SSH model is just a special case of the RM model for $\Delta u = 0$. Computation of the Zak phase for the RM model at different values of ΔJ and Δu reveals that it is not quantized, in contrast, it can take any value from $-\pi$ to π (see Fig. 6.1).

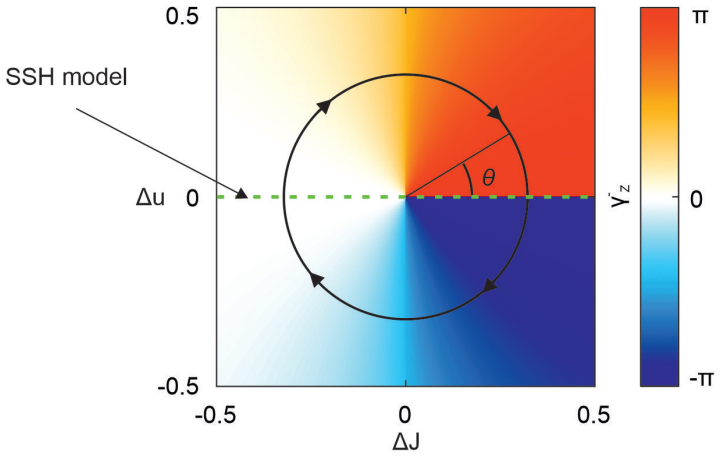

Figure 6.2: Zak phase γ_Z^- of the lower band computed for the RM model in dependence on ΔJ and Δu. In the calculations we assumed $J_1 = 1 + \Delta J/2$, $J_2 = 1 - \Delta J/2$, $\Delta J \in [-0.5, 0.5]$ and $\Delta u \in [-0.5, 0.5]$. The black circle exemplifies a closed loop in $(\Delta J, \Delta u)$ parametrized by an angle θ. The dashed green line shows the case of the SSH model.

Eq. (6.13) allows to look at the Zak phase from a different perspective. Now, we can interpret γ_Z as a relative shift of an electron from the filled band within a unit cell. That is why the Zak phase is commonly used as a measure of the electric polarization in one-dimensional solids [119, 146]. Let us consider the SSH model as an example. The Zak phase can be either 0 or π. In terms of the position operator, it means that the charge center of the band is localized either on a lattice site, or in the middle of the intercell bond and the difference between these two situations is half the lattice constant $a/2$. Hence, if we go from one dimerisation to another, there is a change in polarization of $\Delta P = ea/2$, where e is the elementary charge.

6.1.3 Symmetries

It is easy to check that the RM model satisfies time-reversal symmetry and $\mathcal{T} = +1$. However, due the extra onsite potential Δu, it violates charge conjugation and chiral (or sublattice) symmetries, i.e. $C = 0$ and $\mathcal{S} = 0$. Indeed, if we add an onsite energy of $-\Delta u$ to sites A and $+\Delta u$ to sites B, we will not end up with the same situation upon exchanging A and B sites. Going back to the periodic Table 2.1, we find that the RM model belongs to the AI symmetry class of the Altland-Zirnbauer classification scheme and thus cannot be topological in 1D.
However, one can "reinstall" topology by introducing adiabatic periodic variation of the parameters

$$\begin{aligned} \Delta J &\to \Delta J(t) = \Delta J(t+T) \\ \Delta u &\to \Delta u(t) = \Delta u(t+T). \end{aligned} \tag{6.14}$$

We can thereby break time-reversal symmetry and create an extra dimension in the parameter space by means of the time-dependent parameter $\mathbf{R}(t) = (\Delta J(t), \Delta u(t))$. As a result, we jump to the A symmetry class, which in 2D allows for a non-trivial topology. As we will see later, the relevant topological invariant in this case is the Chern number.

6.1.4 Adiabatic charge pumping

Now, we have everything at hand to construct a topological quantum pump. It is clear that in order to pump particles through the chain, one has to shift the Wannier centers, which implies changing the Zak phase. We can now return to Fig. 6.2 and consider a closed loop in parameter space $(\Delta J, \Delta u)$. If we parametrize the parametric path by an angle θ and change it adiabatically from 0 to 2π, then after a full cycle the Wannier centers will be shifted by

$$\Delta X^{\alpha} = \frac{1}{2\pi} \oint \mathrm{d}\theta \frac{\partial \gamma_{\mathrm{Z}}^{\alpha}}{\partial \theta}. \tag{6.15}$$

Without performing any calculations we can already guess from Fig. 6.2 that if such a loop encloses the metallic point $(\Delta J, \Delta u) = (0, 0)$, then the total Zak phase accumulated during the cycle is 2π, thus the Wannier centers of the lower band get shifted by one unit cell $\Delta X^{-} = 1$. If not, then $\Delta X^{-} = 0$. Note, that for the upper band the Zak phase has the inverse sign. Hence, if filled, it pumps a charge in the opposite direction $\Delta X^{+} = -1$.
We can rewrite Eq. (6.15) as

$$\begin{aligned} \Delta X^{\alpha} &= \frac{i}{2\pi} \int_{\mathrm{BZ}} \mathrm{d}k \int_{0}^{2\pi} \mathrm{d}\theta \frac{\partial}{\partial \theta} \langle u_{\alpha,k} | \frac{\partial}{\partial k} | u_{\alpha,k} \rangle \\ &= \frac{1}{2\pi} \int_{\mathrm{BZ}} \mathrm{d}k \int_{0}^{2\pi} \mathrm{d}\theta i \left[\langle \partial_{\theta} u_{\alpha,k} | \partial_{k} u_{\alpha,k} \rangle - \langle \partial_{k} u_{\alpha,k} | \partial_{\theta} u_{\alpha,k} \rangle \right] = \mathscr{C}. \end{aligned} \tag{6.16}$$

One immediately notices that the shift of the Wannier centers in a closed loop is an integral over the Berry curvature and, hence, must be an integer. From Sec. 2.3.1 we have learnt that this integer is a topological invariant called the Chern number. Indeed, the value of $\mathscr{C}$ is robust against deformations of the parametric loop. As long as we do not cross the origin and thereby close the band gap, the particle will be always pumped exactly by one unit cell after each cycle giving rise to quantized current. To sum up, we have found that a nontrivial Chern number leads to quantized particle transfer in the bulk. This phenomenon is known as Thouless pumping. Although Thouless pumping was theoretically predicted long ago, the first experimental realizations were reported only recently [37, 38].
For a better understanding of the transport mechanism in the Thouless pump let us follow a full pumping cycle step by step. The problem becomes particularly simple in the fully dimerized limit. In this limit, the couplings J_1 and J_2 are periodically turned on and off such that at every instant time point the chain falls apart into disconnected dimers. For instance, we can choose the following driving protocol, where one driving period $t \in [0, T)$ reads

$$\begin{aligned} J_1(t) &= \begin{cases} \sin\theta(t) & \text{if } t \in [0, T/2) \\ 0 & \text{if } t \in [T/2, T) \end{cases}, \\ J_2(t) &= \begin{cases} 0 & \text{if } t \in [0, T/2) \\ -\sin\theta(t) & \text{if } t \in [T/2, T) \end{cases}, \\ u_a(t) &= \cos\theta(t), \\ u_b(t) &= u_a(t - T/2) \end{aligned} \tag{6.17}$$

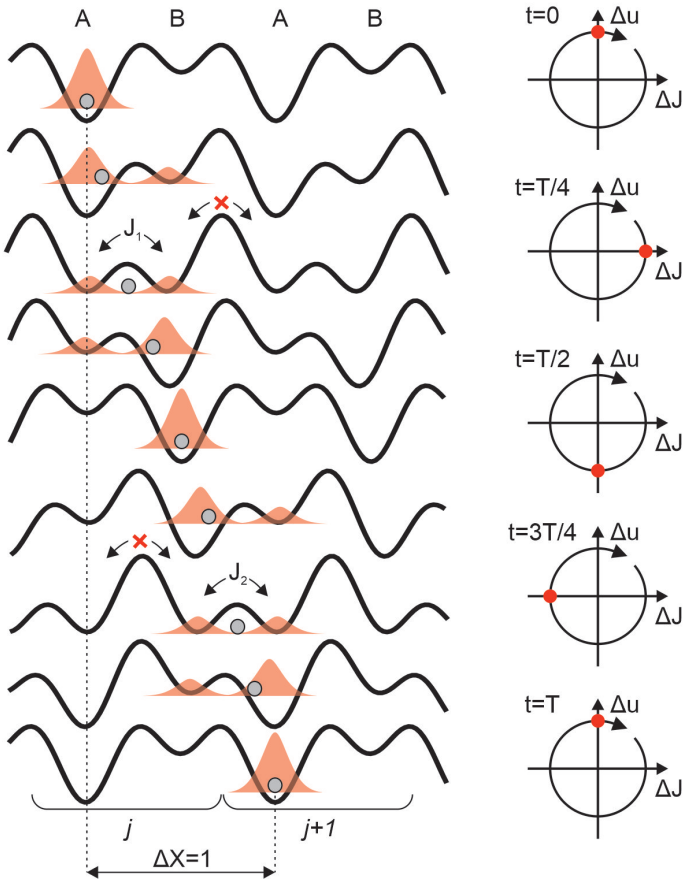

Figure 6.3: Sketch of the full pumping cycle of the driven Rice-Mele model. Here, the lattice is represented by a continuous potential profile, where the potential minima correspond to lattice sites. The lower is the barrier between the wells the higher is the probability to hop to the neighboring site and hence, the higher is the coupling. In the fully dimerized limit, we assume that high barrier means zero coupling. Evolution of the wave function probability density is schematically shown in red. The position of the Wannier center is indicated by grey circles. It is localized at site A at $t = 0$ and gets shifted by one unit cell by the end of the period. At the right side of the figure the red circles highlight the points in the parametric cycle $(\Delta J, \Delta u)$.

with $\theta(t) = \frac{2\pi t}{T}$. During such a period the system traces out a circle in the parameter space $(\Delta J, \Delta u)$ centered in the origin. Hence, the band gap always remains open. At $t = 0$ the atoms in the chain are totally disconnected and the eigenstates are localized atomic orbitals. Assume that the particle is situated in site A of the j^{th} unit cell at the initial time point, i.e. $|\Psi(0)\rangle = |j, A\rangle$. Within the first half of the period acts only the intracell hopping amplitude J_1, the onsite potential at site A rises while the onsite potential at site B gets lower. Since $J_2 = 0$, we can restrict ourselves to a two-site problem with the Hamiltonian

$$\hat{H}_{T/2} = -\begin{pmatrix} \cos\theta(t) & \sin\theta(t) \\ \sin\theta(t) & -\cos\theta(t). \end{pmatrix} \tag{6.18}$$

Using Eq. (2.39) we find the instantaneous eigenstates of this Hamiltonian

$$\begin{aligned} |E=-1\rangle &= \cos\frac{\theta(t)}{2}|A\rangle - \sin\frac{\theta(t)}{2}|B\rangle, \\ |E=+1\rangle &= \sin\frac{\theta(t)}{2}|A\rangle + \cos\frac{\theta(t)}{2}|B\rangle. \end{aligned} \tag{6.19}$$

If at $t=0$ the system was in the ground state $|E=-1\rangle$, then, according to the adiabatic theorem, it will remain in this state over the time up to a phase factor (see Eq. (2.40)). However, this phase factor can be eliminated if we only consider populations on sites A and B of unit cell j, i.e. $\mathcal{P}_A(t) = |\langle\Psi(t)|j,A\rangle|^2$ and $\mathcal{P}_B(t) = |\langle\Psi(t)|j,B\rangle|^2$. One finds that the populations evolve as $\mathcal{P}_A(t) = \cos^2\frac{\theta(t)}{2}$ and $\mathcal{P}_B(t) = \sin^2\frac{\theta(t)}{2}$. Thus, at $t=T/2$ we have $\mathcal{P}_A(T/2)=0$ and $\mathcal{P}_B(T/2)=1$, meaning that the particle is totally transferred to site B. In the next half of the period we repeat the same procedure with site B from unit cell j and site A from unit cell $j+1$. These ideas are sketched pictorially in Fig. 6.3. Through this process by the end of the period the particle is shifted by one lattice constant to the right.

6.1.5 Thouless pump in the Floquet picture

The driven Rice-Mele model is translational invariant in both space and time. Thus, it is natural to apply the Floquet-Bloch theory introduced in Sec. 2.2.2. As a result, the eigenstates of the time-periodic RM Hamiltonian can be written in the form of the Floquet-Bloch states $|\psi^F_{\alpha,k}\rangle$ given by Eq. (2.37) with the corresponding quasienergies $\epsilon_\alpha(k)$ belonging to the 1st Floquet-Bloch BZ $\{-\omega/2 \le \epsilon < \omega/2; -\pi \le k < \pi\}$ with $\omega = 2\pi/T$. The velocity operator reads $\hat{v} = \partial\hat{H}_k/\partial k$, hence for each Floquet-Bloch state $|\psi^F_{\alpha,k}\rangle$ its eigenvalue is the group velocity [147]

$$\langle v_{\alpha,k}\rangle = \frac{\partial\epsilon_\alpha(k)}{\partial k}. \tag{6.20}$$

Multiplying it by T we get a shift after one period $\Delta X^\alpha_k = T\langle v_{\alpha,k}\rangle$. Integration over the BZ thus yields the shift of a charge by a completely filled band within one period

$$\Delta X^\alpha = \frac{1}{\omega}\int_{\mathrm{BZ}} \mathrm{d}k \frac{\partial\epsilon_\alpha(k)}{\partial k}. \tag{6.21}$$

It is intutively clear that Eqs. (6.21) and (6.16) must give us the same result. This can be actually proved by establishing a connection between the adiabatic treatment and Floquet picture. Solving the stationary SE for the time-dependent RM Bloch Hamiltonian $\hat{H}_k(t)$ at every fixed time point t, one obtains the instantaneous eigenvalues $E_\alpha(k,t)$ and instantaneous Bloch modes $|u_{\alpha,k}(t)\rangle$. In Ref. [39] it was shown that in the adiabatic limit the quasienergy of the band α equals to

$$\epsilon_\alpha(k) = \frac{\zeta_{\alpha,k} + \gamma_{\alpha,k}}{T}, \tag{6.22}$$

where $\zeta_{\alpha,k} = -\int_0^T \mathrm{d}t E_\alpha(k,t)$ and $\gamma_{\alpha,k} = i\int_0^T \mathrm{d}t\langle u_{\alpha,k}(t)|\partial_t u_{\alpha,k}(t)\rangle$ are the dynamic and geometric phases, respectively. Recall that in Sec. 2.3.1 we have already encountered these phases in the context of adiabatic evolution of instantaneous states. Eq. (6.22) provides us the sought connection. Indeed,

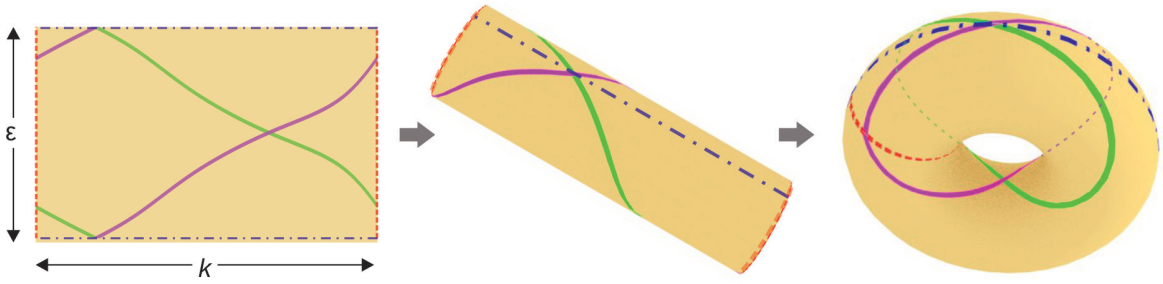

Figure 6.4: The first FBBZ which evolves into a 2D torus due to the periodicity along the ϵ-axis (coincidence of blue dashed-dotted lines), as well as the k axis (coinciding red dashed lines). The magenta and green lines are the schematic counter-propagating quasienergy bands. They wind around the torus with winding numbers $\nu = \pm 1$.

plugging it into Eq. (6.21), the dynamic phase vanishes and we end up with Eq. (6.16), where the Wannier center displacement was expressed as an integral of the Berry curvature.
Eq. (6.21) brings us to an important consequence for the quasienergy spectrum of the driven RM model. Note, that it identifies the charge pumped within one period with a winding number of the quasienergy bands ν. It is clear, that in order to have a quantized displacement of a charge, i.e. $\Delta X^{\alpha} = \pm 1$, the filled quasienergy band $\epsilon_{\alpha}(k)$ has to obey

$$\epsilon_{\alpha}(\pi) - \epsilon_{\alpha}(-\pi) = \pm\omega. \tag{6.23}$$

This has an elegant geometric interpretation. Due to the periodicity in energy and momentum, we can glue the corresponding edges of the FBBZ and represent it as a 2D torus. Then the quantized transport is present if and only if the quasienergy bands wind around this torus. This is illustrated in Fig. 6.4, where the magenta and green lines schematically show the two counter-propagating Floquet-Bloch bands that wind around the FBBZ with winding numbers $\nu = \pm 1$.

6.1.6 Non-adiabatic breaking of Thouless pump

Up to now, we have always relied on the fact that the RM model is driven adiabatically. However, in view of experimental realization of Thouless pumping in a plasmonic waveguide system, it is impossible to achieve adiabatic conditions due to losses, inherent for plasmons. In the previous chapter we have seen that experimentally achievable frequency range is the order of the band gap, which is clearly very far from adiabaticity.
The question naturally arises what happens with Thouless pumping if the RM model is driven at a finite frequency ω, away from the adiabatic limit? This problem was comprehensively studied in Refs. [15, 39, 41] and it was found out that, despite the topological nature of this effect, Thouless pumping is not robust against non-adiabatic effects. More specifically, non-zero driving frequencies lead to hybridization of the forward-propagating and backward-propagating states. In the Floquet picture it manifests itself in the gap opening at the avoided crossings of the quasienergy bands as sketched in Fig. 6.5 (a). As a result, the bands no longer wind around the FBBZ so that the Chern number, or winding number around the FBBZ, becomes trivial. This implies deviation of particle

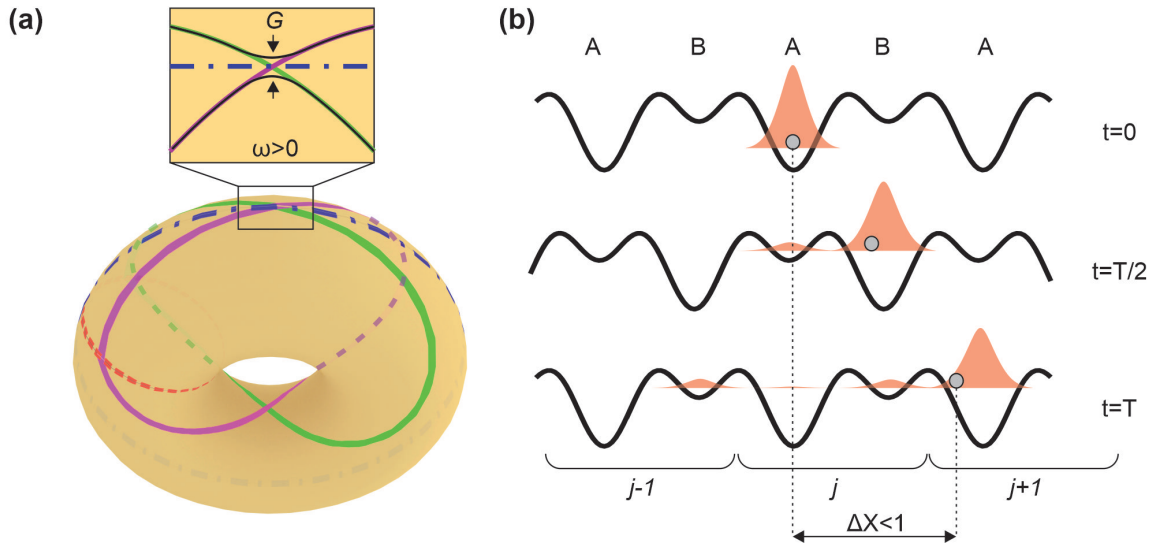

Figure 6.5: (a) Non-adiabatic breaking of Thouless pumping in the Floquet picture. The magenta and green lines depict forward- and backward propagating bands which, in the non-adiabatic regime, hybridize resulting in the gap G opening at the avoided crossings. Therefore, the winding number becomes trivial. (b) Non-adiabatic breaking of Thouless pumping in the fully dimerized RM model. Probability density distribution is schematically shown in red, the grey circles indicate the position of the Wannier center. At $t = 0$ the particle is localized at site A. At $t = T/2$ the particle is partially transferred to site B, however, the population on site A remains non-zero. At $t = T$ the wave function delocalizes even further shifting the Wannier center to the left in comparison to adiabatic limit shown in Fig. 6.3.

transport from perfect quantization.

To have a simple picture in mind of how transport quantization breaks down at fast driving, we refer to the fully dimerized limit that was introduced in Sec. 6.1.4. Consider the non-adiabatically driven RM model with pumping protocol given by Eq. (6.17) and assume that the system is initiated at site A. At sufficiently high ω the adiabatic theorem is no longer valid, hence, the transitions between the instantaneous states are allowed. Due to these transitions, at half period the particle is only partially transferred to the site B with non-zero probability to stay at site A. Through this process, instead of being shifted by one unit cell at the end of the period, the wave function smears in real space giving rise to deviation from quantized transport predicted for adiabatic limit. This situation is illustrated in Fig. 6.5 (b).

Summarizing the above, quantized transport in the simplified version of the RM model breaks down when full population transfer between the neighboring lattice sites cannot be completed within a half period. Interestingly, there exist several techniques that allow to accelerate population transfer in two-level quantum systems compared to the adiabatic evolution. One approach is to create a "shortcut to adiabaticity" utilizing time-dependent gain or loss [50–52]. It was shown that additional complex time-dependent diagonal terms in the Hamiltonian representing gain or loss (depending on the sign) of population in the two bare states can be chosen such that they totally cancel nonadiabatic coupling. These ideas inspired the non-Hermitian modification of the RM model presented below, where engineered time-periodic losses are aimed to suppress non-adiabatic transitions and thereby restore topological transport quantization for the experimentally relevant driving frequencies. Although, due

to losses, the norm of the state vector is not conserved during time evolution, the great advantage of our model is that it can be easily implemented to arrays of DLSPPWs (see Sec. 6.3).

6.2 Non-Hermitian RM model

Consider a periodically driven RM model with additional on-site, periodic dissipation (see Fig. 6.6)

$$\begin{aligned}\hat{H}_{\mathrm{NH}}(t) = &- J_1(t) \sum_{j=1}^{N} \left(|j,B\rangle\langle j,A| + h.c.\right) - J_2(t) \sum_{j=1}^{N-1} \left(|j+1,A\rangle\langle j,B| + h.c.\right) \\ &- \sum_{j}^{N} \left[\left(u_a(t) + i\gamma_a(t)\right)|j,A\rangle\langle j,A| + \left(u_b(t) + i\gamma_b(t)\right)|j,B\rangle\langle j,B|\right],\end{aligned} \tag{6.24}$$

where $J_{1/2}(t)$, $u_a(t)$ and $u_b(t)$, are all real-valued, periodic functions of time given by

$$\begin{aligned} u_a(t) &= u_0 \cos(\omega t + \varphi), & u_b(t) &= u_a(t - T/2), \\ J_1(t) &= J_0 e^{-\lambda(1-\sin\omega t)}, & J_2(t) &= J_1(t - T/2), \end{aligned}$$

with u_0, J_0, $\lambda > 0$, and $\varphi = 0$ (unless otherwise specified). The choice of the hopping amplitudes is motivated by the exponential dependence of the wave-function overlaps on the spacing $\lambda(1 - \sin\omega t)$ between neighboring sites, as in the coupled waveguide system. In our NH modification of the RM model, the time-periodic decay rates $\gamma_a(t) \geq 0$ and $\gamma_b(t) \geq 0$ are nonzero once the on-site potential exceeds the mean value $\bar{u} = 0$. This resembles, for instance, a realistic situation where particles in a trapping potential are lost from the trap once the trapping potential is not sufficiently deep. Thus, we choose

$$\gamma_a(t) = \gamma_0\, \Theta(u_a(t))\, \cos(\omega t + \varphi), \qquad \gamma_b(t) = \gamma_a(t - T/2),$$

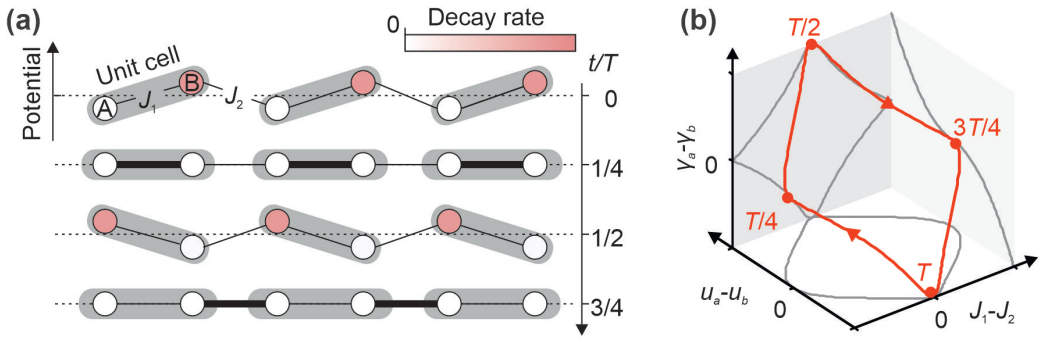

Figure 6.6: (a) Schematic of the periodically driven, NH RM lattice for four equidistant times during a pumping cycle. Lossy sites are depicted by a red color, and the large (small) hopping amplitudes $J_{1,2}$ by thick (thin) lines connecting the sites. (b) Pumping cycle in the parameter space $(J_1 - J_2, u_a - u_b, \gamma_a - \gamma_b)$.

where $\Theta(x)$ is the Heaviside step function.

6.2.1 Non-Hermitian Floquet-Bloch theory

In momentum space the Hamiltonian (6.24) reads

$$\hat{K}_k(t) = \hat{H}_k(t) - i\hat{\Gamma}(t), \tag{6.25}$$

where $\hat{H}_k(t)$ is given by Eq. (6.3) with all parameters being periodic in time and

$$\hat{\Gamma}(t) = \begin{pmatrix} \gamma_a(t) & 0 \\ 0 & \gamma_b(t) \end{pmatrix}. \tag{6.26}$$

While the time evolution of Hermitian systems can be always described by an effective time-independent Hamiltonian, the Floquet representation for lossy systems does not always exist and remains a matter of intensive ongoing research [148]. However, for a specific case of Hamiltonians like (6.25), where both terms separately are Hermitian, i.e. $\hat{H}_k = \hat{H}_k^\dagger$ and $\hat{\Gamma} = \hat{\Gamma}^\dagger$, we can extend conventional Floquet-Bloch theory outlined in Sec. 2.2.2 using elements of the so-called biorthogonal quantum mechanics (see e.g. Ref. [149]). This formalism generalizes the notion of orthogonality in standard Hermitian quantum mechanics and is perfectly suited for analysis of such complex Hamiltonians.
Due to periodicity in time, we look for the eigenstates of $\hat{K}_k$ in the form

$$|u^F_{\alpha,k}\rangle = e^{i\epsilon_\alpha(k)t}|\phi_{\alpha,k}(t)\rangle, \tag{6.27}$$

where $|\phi_{k,\alpha}(t)\rangle = |\phi_{k,\alpha}(t+T)\rangle$ are time-periodic Floquet-Bloch modes which, by construction, satisfy the Floquet equation

$$\hat{\mathcal{K}}_k(t)|\phi_{\alpha,k}(t)\rangle = \epsilon_\alpha(k)|\phi_{\alpha,k}(t)\rangle, \tag{6.28}$$

with $\hat{\mathcal{K}}_k(t) \equiv [\hat{K}_k(t) - \mathrm{i}\partial_t]$. Note, that we distinguish the eigenstates of the Hamiltonian in momentum-space (6.25) and real-space (6.24) representations denoting them by $|u^F_{\alpha,k}\rangle$ and $|\psi^F_{\alpha,k}\rangle$, respectively. They are linked via $|\psi^F_{\alpha,k}\rangle = |k\rangle \otimes |u^F_{\alpha,k}\rangle$. Just like we did it previously, using the Fourier expansion

$$|\phi_{\alpha,k}(t)\rangle = \sum_n e^{-in\omega t}|\phi_{\alpha,k,n}\rangle \tag{6.29}$$

$$\hat{K}_k(t) = \sum_n e^{-in\omega t}K^n_k \tag{6.30}$$

we obtain the time-independent Floquet equation

$$\sum_l \left(K^{(n-l)}_k - n\omega\delta_{n,l}\right)|\phi^{(l)}_{\alpha,k,m}\rangle = \epsilon_{\alpha,m}(k)|\phi^{(n)}_{\alpha,k,m}\rangle, \tag{6.31}$$

that can be solved numerically upon reasonable truncation in Floquet space.
The found quasienergies $\epsilon_\alpha(k)$ taken from the first FBBZ are complex numbers, whose imaginary parts account for decay. In the next step we want to expand the arbitrary quantum state $|\Psi(t)\rangle$, prepared

at the initial time moment at $|\Psi(0)\rangle$, in terms of the eigenstates of the complex Floquet equation, i.e.

$$|\Psi(t)\rangle = \sum_{\alpha,k,n} C_{\alpha,k} e^{-i(\epsilon_\alpha(k)+n\omega)t} |k\rangle \otimes |\phi_{\alpha,k,n}\rangle \tag{6.32}$$

Commonly, the expansion coefficients $C_{\alpha,k}$ are found by projecting the corresponding Floquet state at $t = 0$ given by $|\psi^F_{\alpha,k}(0)\rangle = |k\rangle \otimes \sum_n |\phi_{\alpha,k,n}\rangle$ onto the initial conditions $|\Psi(0)\rangle$. However, this technique fails when dealing with eigenvectors of complex Hamiltonians. The reason is that such eigenvectors are in general not orthogonal to each other [51, 149]. In our numerical calculations, we indeed find that at nonzero decay rate $\gamma_0 > 0$ the Floquet-Bloch modes with different band indices become nonorthogonal $\langle\phi_{\beta,k}(0)|\phi_{\alpha,k}(0)\rangle \neq 0$ for any α, β.
This problem can be handled with the aid of the adjoint Floquet-Bloch modes $|\tilde{\phi}_{\alpha,k}(t)\rangle$ constructed in the following way. When $|\phi_{\alpha,k}(t)\rangle$ is an eigenstate of Eq. (6.28) then there exists the so-called biorthogonal partner $|\tilde{\phi}_{\alpha,k}(t)\rangle$ defined as

$$\hat{\mathcal{K}}^\dagger_k |\tilde{\phi}(t)_{\alpha,k}\rangle = \epsilon^*_\alpha(k) |\tilde{\phi}_{\alpha,k}(t)\rangle. \tag{6.33}$$

Using Eq. (6.28) and the Hermitian adjoint of Eq. (6.33) it is easy to show that for non-degenerate $\epsilon_\alpha(k) \neq \epsilon_\beta(k')$ they satisfy

$$\langle\tilde{\phi}_{\alpha,k}(0)|\phi_{\beta,k'}(0)\rangle = 0. \tag{6.34}$$

The scalar product in the generalized Floquet theory reads

$$\langle\langle\tilde{a}|b\rangle\rangle = \frac{1}{T}\int_0^T \mathrm{d}t \langle\langle\tilde{a}|b\rangle\rangle, \tag{6.35}$$

where $|\tilde{a}\rangle$ is the biorthogonal partner of $|a\rangle$ (c.f. Eq. (2.30)). For further calculations it is useful to normalize the two bases

$$\begin{aligned} |\phi_{\alpha,k}\rangle &\to \frac{|\phi_{\alpha,k}\rangle}{\sqrt{\langle\tilde{\phi}_{\alpha,k}|\phi_{\alpha,k}\rangle}} \\ |\tilde{\phi}_{\alpha,k}\rangle &\to \frac{|\tilde{\phi}_{\alpha,k}\rangle}{\sqrt{\langle\tilde{\phi}_{\alpha,k}|\phi_{\alpha,k}\rangle}} \end{aligned} \tag{6.36}$$

such that the Floquet-Bloch modes and their biorthogonal partners obey the biorthonormality relation

$$\langle\langle\tilde{\phi}_{\alpha,k}|\phi_{\beta,k'}\rangle\rangle = \delta_{k,k'}\delta_{\alpha,\beta}. \tag{6.37}$$

As a consequence, the Floquet-Bloch modes by themselves are no longer normalized, i.e. $\langle\phi_{\alpha,k}(0)|\phi_{\alpha,k}(0)\rangle \neq 1$. The advantage of this convention becomes evident by noting that the dynamics of the two adjoint Floquet states, $|\psi^F_{\alpha,k}(t)\rangle$ and $|\tilde{\psi}^F_{\alpha,k}(t)\rangle$, is governed by quasienergies $\epsilon_\alpha(k)$ and $\epsilon^*_\alpha(k)$, respectively. This means, that whenever the probability density of the dissipative Floquet state exponentially decays in time $\langle\psi^F_{\alpha,k}(t)|\psi^F_{\alpha,k}(t)\rangle \propto e^{-2\mathrm{Im}\{\epsilon_\alpha(k)\}t}$, the density of the adjoint state grows as $\langle\tilde{\psi}^F_{\alpha,k}(t)|\tilde{\psi}^F_{\alpha,k}(t)\rangle \propto e^{2\mathrm{Im}\{\epsilon_\alpha(k)\}t}$. Thus, the scalar product (6.35) is aimed to preserve the norm in time which simplifies various calculations. For instance, the period-averaged expectation value of a

generic observable $\hat{A}$ in a pure dissipative Floquet state $|\psi^F_{\alpha,k}\rangle$ reads

$$\langle A\rangle_T = \langle\langle\tilde{\psi}^F_{\alpha,k}|\hat{A}|\psi^F_{\alpha,k}\rangle\rangle. \tag{6.38}$$

The desired expansion coefficients are ultimately found by projecting the biorthogonal partner of the corresponding Floquet state onto the initial condition

$$C_{\alpha,k} = \langle\tilde{\psi}^F_{\alpha,k}(0)|\Psi(0)\rangle. \tag{6.39}$$

In our DLSPPW experiments we commonly measure real- and Fourier space intensity distributions of propagating SPPs in properly designed arrays as described in Sec. 4.2. The time evolution of probability density that corresponds to our real-space measurements can be calculated using Eqs. (6.32) and (6.39), in a straightforward way as $|\Psi(s,t)|^2$, where $\Psi(s,t)$ is the projection of $|\Psi(t)\rangle$ onto the lattice sites labeled by the index s. The momentum- and energy-resolved spectra that we measure in Fourier space are calculated as intensity of the Fourier transform $\Psi(k,E)$ using

$$I(E,k) = |\Psi(k,E)|^2 \propto \sum_{\alpha,\beta,n} \frac{C^*_{k\beta}C_{k\alpha}\,\langle\phi_{k,\beta,n}|\phi_{k,\alpha,n}\rangle}{(E-\epsilon^*_\beta(k)-n\omega-i0)(E-\epsilon_\alpha(k)-n\omega+i0)}. \tag{6.40}$$

Note, that, due to the non-orthogonality of the Floquet-Bloch modes, Eq. (6.40) involves the mixing of the two bands α,β. However, as we will see later, in our model it is possible to effectively populate only one band α by exciting the system at a single site on the initially non-lossy sublattice. In this case, the cross terms vanish and Eq. (6.40) simplifies to

$$I_\alpha(E,k) \propto \sum_n \frac{C^*_{k\alpha}C_{k\alpha}\,\langle\phi_{k,\alpha,n}|\phi_{k,\alpha,n}\rangle}{|E-\epsilon^*_\alpha(k)-n\omega-i0|^2}. \tag{6.41}$$

Strictly speaking, due to non-Hermiticity, the quantity above is not the "true spectral density" because the Floquet-Bloch modes are not normalized. The spectral density which accounts for the normalization condition necessarily involves the biorthogonal partner states and reads

$$S_\alpha(E,k) = \sum_n \frac{\tilde{C}^*_{\alpha,k}C_{\alpha,k}\langle\tilde{\phi}_{k,\alpha,n}|\phi_{k,\alpha,n}\rangle}{|E-\epsilon^*_\alpha(k)-n\omega-i0|^2}, \tag{6.42}$$

where $\tilde{C}_{\alpha,k} = \langle\psi^F_{\alpha,k}(0)|\Psi(0)\rangle$. An analogue of Eq. (6.42) was derived by J. Kroha from the University of Bonn from the imaginary part of the Green's function (see Ref. [143] for details). Nevertheless, our calculations show that, despite a slight deviation, Eqs. (6.40) and (6.42) lead to very similar results. It justifies that our Fourier measurements provide detailed information about the relative occupation of the quasienergy bands.

6.2.2 Dissipative transport quantization

Here, we heavily rely on the derivations of J. Kroha from the University of Bonn. In Sec. 6.1.4 we have seen that in the adiabatic Thouless pump the particle gets shifted by one lattice constant per cycle given by the Berry phase accumulated in the closed loop in the Hamiltonian parameter space. However, the concept of Berry phase intrinsically leans on the adiabatic theorem and thus fails at

finite driving frequencies. Therefore, if we want to study a fast pumped, dissipative situation, it is better to use the Floquet picture, where the transport quantization is associated with the quasienergy winding around the 2D FBBZ as explained in Sec. 6.1.5.
In the non-Hermitian case, the velocity operator reads $\hat{v} = \partial \mathrm{Re}\{\hat{K}_k\}/\partial k = \partial \hat{H}_k/\partial k$, hence, the displacement of the particle during one pumping cycle carried by a dissipative Floquet-Bloch state $|\psi^F_{\alpha,k}\rangle = |k\rangle \otimes |u^F_{\alpha,k}\rangle$ is

$$\Delta X^\alpha_k = \langle\langle \tilde{u}^F_{\alpha,k} | \hat{v} | u^F_{\alpha,k} \rangle\rangle T = \frac{\mathrm{dRe}\{\epsilon_\alpha(k)\}}{\mathrm{d}k} T. \tag{6.43}$$

Note that, in contrast to Eq. (15) from Ref. [143], in the expression above we have used the NH definition of the expectation value (6.38). This prevents the emergence of the exponential decay factor $e^{-2\mathrm{Im}\{\epsilon_\alpha(k)\}T}$. The shift per cycle carried by a homogeneously filled band α is obtained by integration over all k-states

$$\Delta X^\alpha = \int_{-\pi}^{\pi} \frac{\mathrm{d}k}{2\pi} \frac{\mathrm{dRe}\{\epsilon_\alpha(k)\}}{\mathrm{d}k} T = \nu_\alpha, \tag{6.44}$$

where ν_α is the winding number of the real part of the quasienergies. To sum up, we have found that the winding of the real part of the quasienergy bands indicates the transport quantization in our lossy RM model.

6.2.3 Results of NH Floquet analysis

We apply the non-Hermitian Floquet formalism to the dissipative RM model (6.24) driven at the frequencies relevant for the DLSPPW-based experiments. In our numerical calculations we set $u_0 = J_0 = 1$, $\lambda = 1.75$ and all energies are given in units of J_0. In what follows we consider the time-evolution of the states $|\Psi_A(t)\rangle$ and $|\Psi_B(t)\rangle$ that have been initiated at $t = 0$ with non-zero amplitude at a single site on sublattices A and B, respectively. This corresponds to the typical situation in our experiments, when we excite SPPs in a single waveguide in the array (see Sec. 6.3).
To begin with, we analyze the Hermitian case ($\gamma_0 = 0$, $\omega = 1.1J_0$) shown in Fig. 6.7 (a). Evidently, the counterpropagating bands hybridize, accompanied by avoided crossings and gaps with a width G opening at the FBBZ boundaries, such that the bands become topologically trivial. As a result, the charge pumped per period deviates from the quantized value. This indicates the generic breakdown of quantized Thouless pumping at any finite pumping frequncy ω (see Sec. 6.1.6). Note, that in the absence of losses the spectral density $|\Psi_B(k,E)|^2$ is just a reflection of $|\Psi_A(k,E)|^2$ about $E = 0$, i.e. $|\Psi_B(k,E)|^2 = |\Psi_A(k,-E)|^2$.
Now we add time-periodic losses with the amplitude of $\gamma = 0.4J_0$ (see Figs. 6.7 (b-d)). As a result, for the parametric cycle configuration shown in Fig. 6.6 (b) at the initial time moment, the decay rate on sublattice A is zero, while on sublattice B is γ_0. Our calculations reveal several profound effects of non-Hermiticty. First, the quasienergies become complex, whereby the right-moving and left-moving bands acquire considerably different dampings shown in Fig. 6.7 (d) and seen as different broadenings of the spectral band occupations in Fig. 6.7 (b) and (c). Second, the two inputs are no longer equivalent in respect to the relative populations of the two bands. In particular, for the input A we almost exclusively excite right-moving states, while for the input B in addition to the lossy left-moving states, we partially populate right moving-states. Remarkably, in the case of input A the right-moving band is populated almost homogeneously. Thus, it is a way to create the topologically

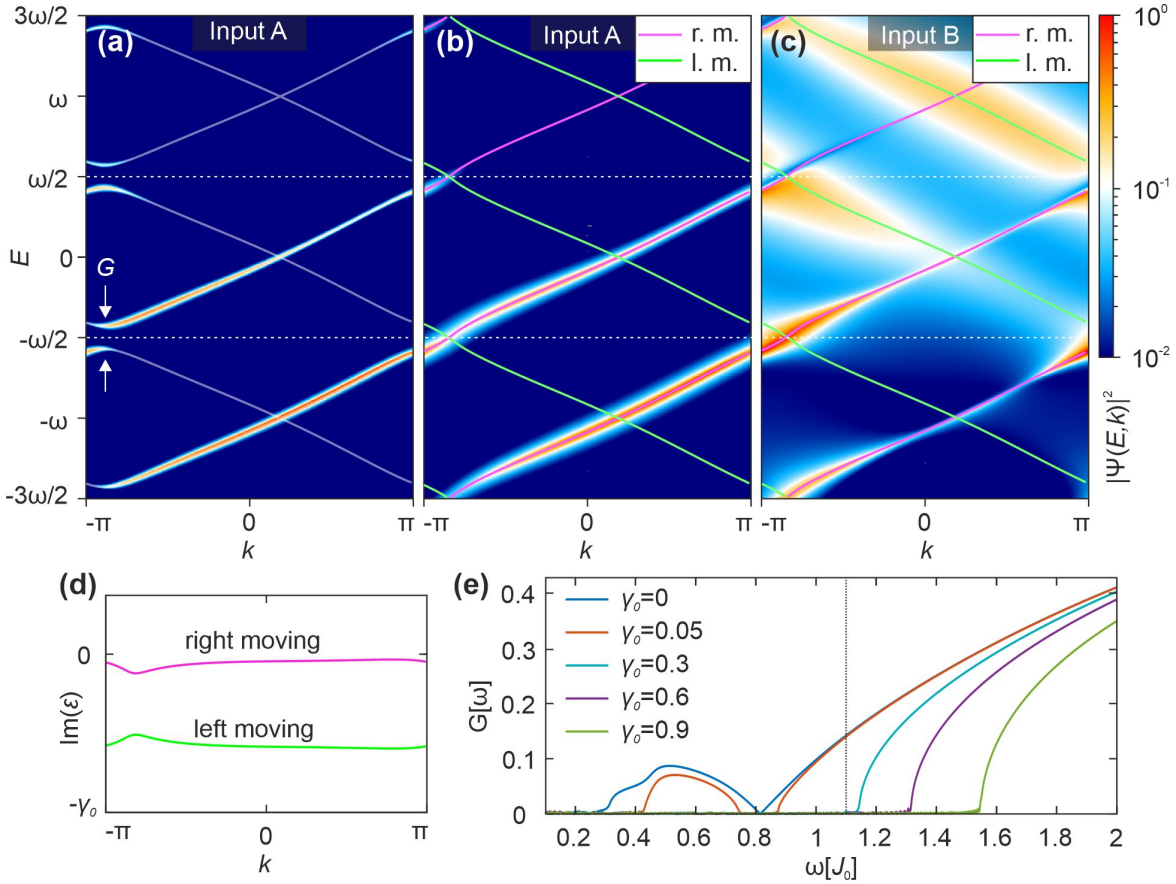

Figure 6.7: (a-c) Band structures of the RM model driven at non-adiabatic frequency $\omega = 1.1J_0$. Thin lines highlight the Floquet quasienergy bands (real parts), color code shows normalized spectral density calculated using Eq. (6.40). (a) Input A in Hermitian case ($\gamma_0 = 0$). The band gaps at $E = \pm\omega/2$ indicate a topologically trivial band structure, i.e., the breakdown of transport quantization. (b) Same as in (a) but for the NH RM model with $\gamma_0 = 0.4J_0$ when the system is excited at a single site of the initially nonlossy sublattice A. Almost no mixing of Floquet modes occurs. The gap at the FBBZ boundary closes, restoring transport quantization. Right- and left- moving bands are distinguished by magenta and green color, respectively. (c) Same as in (b), but for a state injected at a site of the initially lossy sublattice B. Left-moving bands are predominantly populated with a broad distribution, indicating high losses. (d) Imaginary part of the quasienergy bands presented in (b, c), showing low dissipation in the right-moving band. (e) The size of the band gap G in dependence on the driving frequency at different loss amplitudes γ_0. The black dashed line shows $\omega = 1.1J_0$.

important complete band filling, which would otherwise be possible only in fermionic systems at low temperature. Finally, and most importantly, the gap G closes and, hence, the bands wind around the entire 2D FBBZ. Quasienergy winding together with complete band filling restores transport quantization according to Eq. (6.44).

Furthermore, we find, that the gaps close once γ_0 is larger than some threshold value. In order to study this threshold behaviour we numerically evaluated the gap size G at various driving frequencies and loss amplitudes (see Fig. 6.7 (e)). In the Hermitian case ($\gamma_0 = 0$) the gap size has a complex oscillatory behaviour as a function of the driving frequency as also noted by [150]. Our analysis shows that a

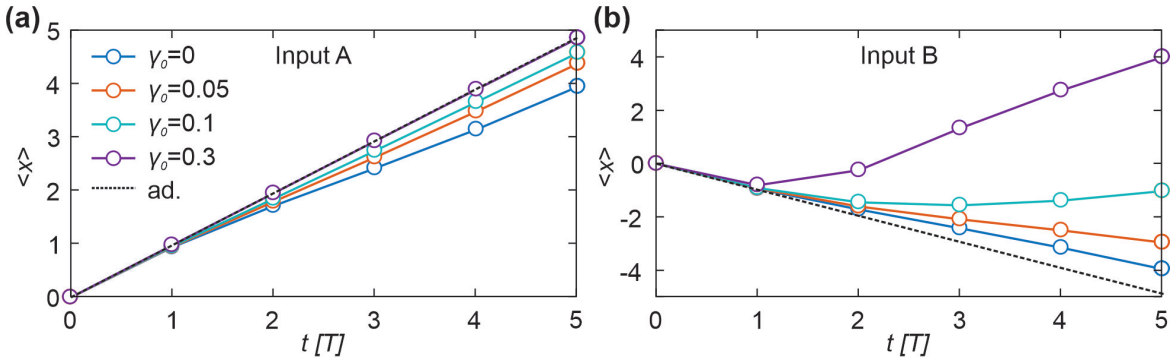

Figure 6.8: The center-of-mass position in the NH RM model of the injected wavepacket after up to 5 full pumping cycles ($\omega = 1.1J_0$) at different loss amplitudes γ_0 for a single-site input on (a) sublattice A and (b) sublattice B. The black dashed line show the adiabatic limit in the Hermitian case $\gamma_0 = 0$.

larger gap size requires stronger damping in order to close it. For instance, at the previously analyzed driving frequency $\omega_0 = 1.1J_0$ the loss amplitude γ_0 should be larger than $0.3J_0$ to close the gap.
Next, we investigate the transport properties of the NH RM model in real space characterized by the position of the center of mass (CoM) of the wave-packet

$$\langle x(t)\rangle = \frac{\langle\Psi(t)|\hat{x}|\Psi(t)\rangle}{\langle\Psi(t)|\Psi(t)\rangle}. \tag{6.45}$$

We choose this quantity because it can be also extracted from the measured real-space SPP distributions and thus enables the direct comparison between numerical and experimental results. In Fig. 6.8 (a,b) we plot CoM after up to 5 completed driving cycles at various losses and a fixed driving frequency $\omega = 1.1J_0$ for different initial conditions, input A or B. In the adiabatic case the mean displacement is almost +1 (-1) unit cell per cycle for delta-like excitations on sublattice A (B). Small deviations from unity result from slight inhomogeneity of the band population. At the driving frequency $\omega = 1.1J_0$ the displacement per cycle is considerably smaller in the Hermitian case ($\gamma = 0$) indicating deviation from the quantized transport. With increasing the losses this deviation becomes smaller and smaller for input A and for $\gamma \geq 0.3$ the displacement cannot be distinguished from the adiabatic case. Surprisingly, for the input B we observe that the CoM position switches direction with time. This is a signature of the chirality of the Floquet bands and is due to the fact that the propagation of even poorly populated low-loss states in positive x-direction starts to dominate after the first few periods, while the states propagating in negative x-direction are quickly damped due to the phase relation of the periodic losses with respect to the hopping amplitude.

6.3 Experiments

In order to test our theoretical predictions we perform experiments based on DLSPPWs. The experimental realization of the model described by Eq. (6.24), is based on the mathematical equivalence between the time-dependent Schrödinger equation in the tight-binding approximation and the paraxial Helmholtz equation which describes propagation of light in coupled waveguide arrays. Fig. 6.9 shows

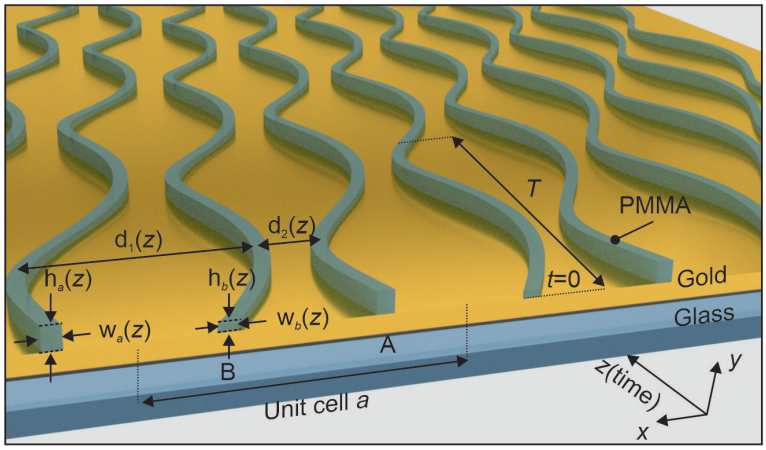

Figure 6.9: Sketch of the plasmonic implementation of the NH RM model.

a scheme of a DLSPPW array. The waveguide array represents a dimerized 1D lattice, where each unit cell contains two waveguides, A and B. Here, the propagation direction z plays the role of time. Periodic modulation of the effective hopping amplitudes is reached by sinusoidally varying the spacing between the adjacent waveguides $\mathrm{d}_{1,2}(z)$ while the on-site potential variation is realized by changing the waveguides' cross-sections (heights $\mathrm{h}_{a,b}(z)$ and widths $\mathrm{w}_{a,b}(z)$). In addition, the variation of the waveguides' cross-section affects the instantaneous losses $\gamma_{a,b}(z)$. When the cross-section decreases, the confinement of the guided mode weakens. As a result, the modes can couple to free-propagating surface plasmon polaritons (SPPs) and scatter out from the array. We employ this effect to introduce time-dependent losses $\gamma_{a,b}(z)$.

6.3.1 Fabricated samples

The DLSPPW arrays are fabricated by negative-tone gray-scale electron beam lithography as described in Sec. 4.1. A scanning electron micrograph and an AFM scan of a typical sample are shown in Fig. 6.10. The waveguides consist of PMMA ridges deposited on top of a 60 nm thick gold film evaporated on a glass substrate. The modulated part of the array is preceded by a short straight interval of the length 7.5 µm. This region contains the grating couplers (red boxes) which are used for SPP excitation. The grating is deposited only onto the two waveguides (inputs A and B), while the extension of others to this region is needed to prevent fire-end excitation of the adjacent waveguides. In order to ensure equal excitation conditions all the waveguides start with the same height which then smoothly approaches the initial conditions at $z = 0$ (blue dotted line). The mean center-to-center distance between the ridges is 1.7 µm and the maximum deflection from the center is 0.5 µm. The resulting variation of coupling constants is

$$\begin{aligned} J_1(z) &= J_0 \mathrm{e}^{-\lambda(1-\sin\Omega z)} \\ J_2(z) &= J_1(z - T/2) \end{aligned} \tag{6.46}$$

with $J_0 = 0.144\ \mu\mathrm{m}^{-1}$ and $\lambda = 1.75$. The cross-section of each waveguide is controlled by the applied electron dose during the lithographic process. By varying the electron dose sinusoidally along the z-axis we modulate the waveguides' cross-sections. The resulting geometry is measured by AFM

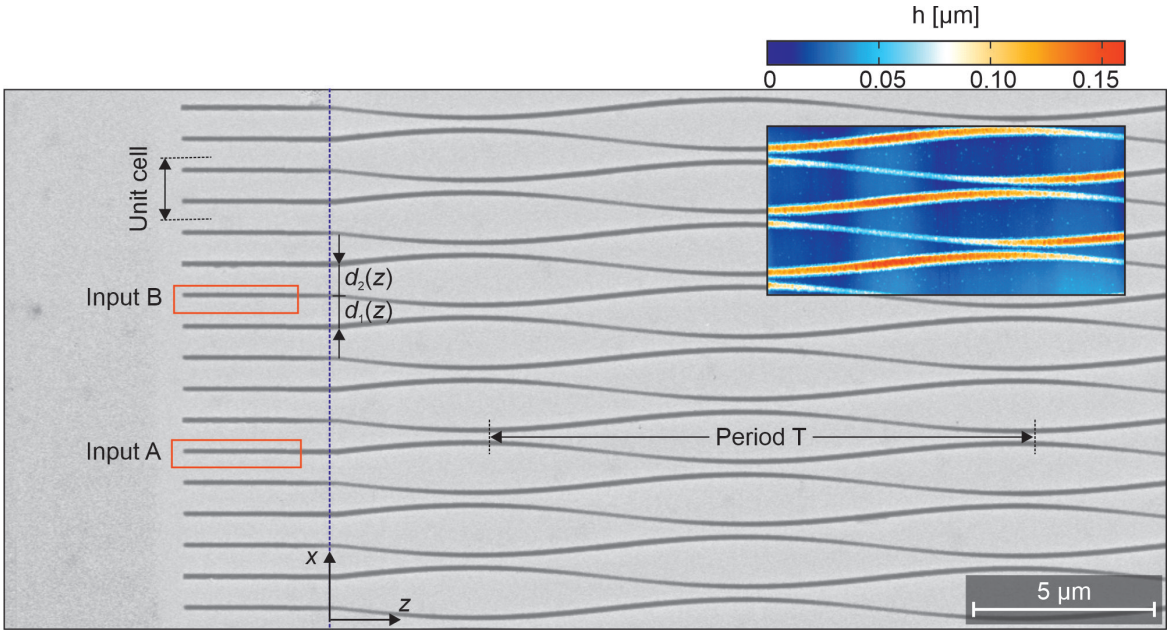

Figure 6.10: Scanning electron micrograph of a typical sample with $J_0 = 0.144\ \mu\text{m}^{-1}$, $\omega = 1.45 J_0$, $u_0 = 1.1\, J_0$, $\gamma_0 = 0.8\, J_0$. The red boxes highlight the grating couplers deposited onto the input waveguide A and B. Blue dashed line corresponds to $z = 0$ and separates the excitation region from the modulated part of the array. The AFM scan at the top right corner shows the waveguide height variation.

and the corresponding real parts of the propagation constants are calculated numerically using the finite element method (see Sec. 3.2.1). For the waveguides from sublattices A and B the real parts of propagation constants are modulated according to

$$\begin{aligned} \beta'_a(z) &\approx \bar{\beta}' + u_0 \cos(\Omega z + \varphi), \\ \beta'_b(z) &= \beta'_a(z - T/2), \end{aligned} \tag{6.47}$$

where $\bar{\beta}' = 6.62\ \mu\text{m}^{-1}$ corresponds to the mean height $h = 95$ nm and the mean width $w = 250$ nm of a waveguide. The amplitude of modulation u_0 is determined by the maximum electron dose variation in EBL and can be adjusted within the accessible range limited by the thickness of the PMMA layer.

Implementation of periodic losses

In addition to the real part of the propagation constant, variation of the waveguide's cross-section modulates the instantaneous losses $\gamma_{a,b}(z)$. The finite element method predicts: With decreasing cross-section of a DLSPPW the losses steadily decrease approaching the limit of free-propagating SPPs for a vanishing waveguide core (see Fig. 3.7). But in the experiment we observe the inverse situation, namely, when the waveguide's cross-section gets smaller than the mean value ($h = 95$ nm, $w = 250$ nm), the losses rapidly increase. It is shown in Fig. 6.11, where we compare the SPP propagation in single-standing straight waveguides printed with different electron doses that cover the range used for fabrication of the sample in Fig. 6.10. At a first glance it seems to contradict with the FEM calculations. However, this contradiction can be easily resolved by looking carefully at this

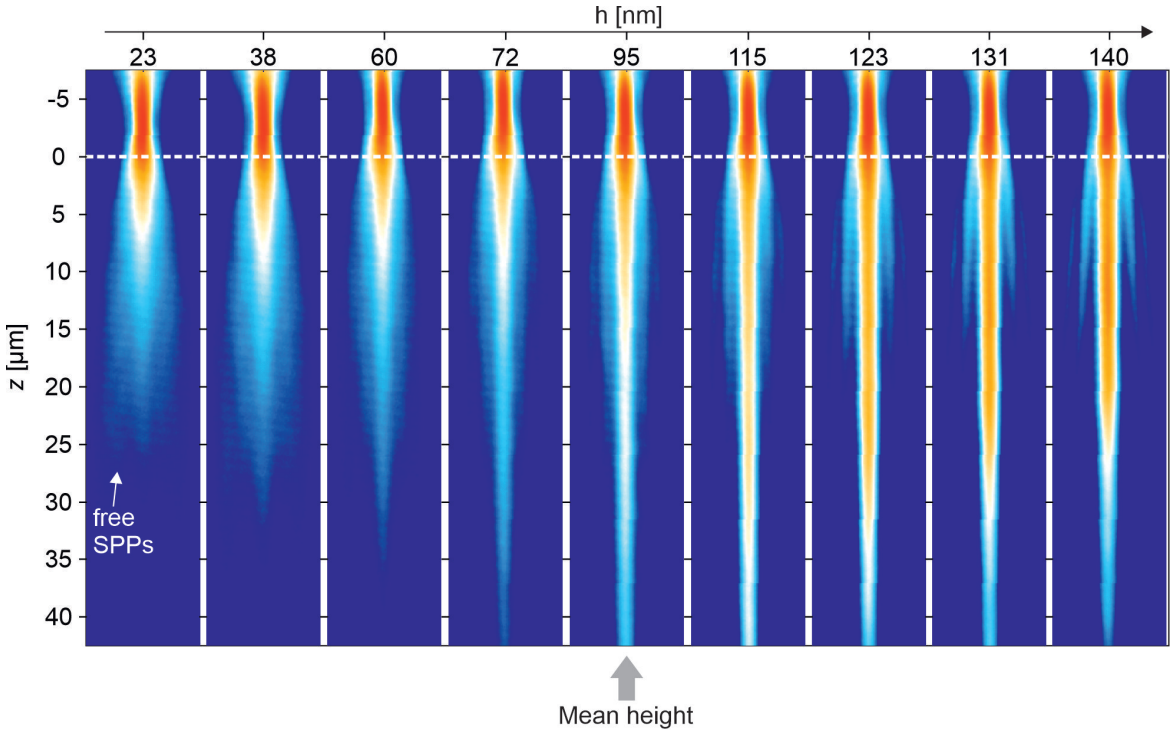

Figure 6.11: Real-space intensity distributions of SPPs propagating in single-standing straight DLSPPWs of different cross-sections. These DLSPPWs are printed with electron doses that cover the range used for fabrication of the sample in Fig. 6.10. The resulting waveguide heights h are shown on top. White dashed line indicates where the excitation region ends. The data demonstrates strong losses in the waveguides of heights below average.

problem. When the waveguide core gets smaller, the confinement of the guided mode weakens and its propagation constant tends to the value of free propagating SPPs. As a result, the guided mode couples to a continuum of free propagating SPPs and scatters out from a DLSPPW. The FEM calculations in turn only determine how much of the optical power is absorbed by metal. With decreasing waveguide cross-section, the optical power is obviously not absorbed more intensively, but, nevertheless, it is effectively lost from the waveguide system.
Experimental data shown in Fig. 6.11 confirms that coupling to free-propagating SPPs is the dominant source of z-dependent losses in our plasmonic implementation of the driven NH RM model. Therefore, we approximate the periodic decay function by

$$\begin{aligned} \gamma_a(z) &\approx \bar{\gamma} + \gamma_0 \Theta(u_a(z)) \cos(\Omega z + \varphi), \\ \gamma_b(z) &= \gamma_a(z - T/2), \end{aligned} \tag{6.48}$$

where γ_0 denotes the maximum decay rate induced by coupling to free SPPs, while $\bar{\gamma} = 0.015\ \mu\text{m}^{-1}$ accounts for other losses that are assumed to be independent of z. Note, that in our experimental model the parameters u_0 and γ_0 are always linked to each other, we cannot change the amplitude of the "potential" u_0 without changing the amplitude of losses γ_0.
.

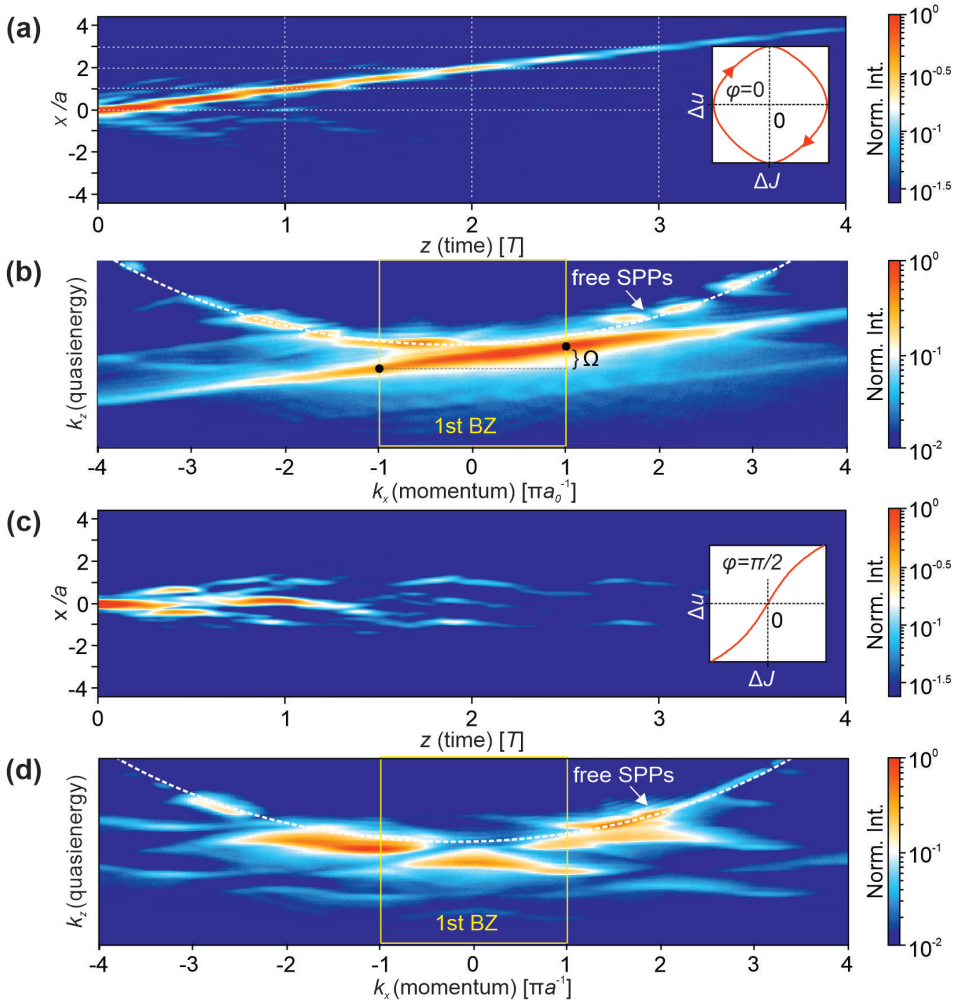

Figure 6.12: (a) Real-space SPP intensity distribution for $u_0 = 1.1J_0$, $\gamma_0 = 0.8J_0$, and $\varphi = 0$. Plot on the right shows the projection of the corresponding pumping cycle onto the plane $(J_1 - J_2, u_a - u_b)$. (b) Fourier-space SPP intensity distribution corresponding to (a). (c) Real-space SPP intensity distribution for $u_0 = 1.1J_0$, $\gamma_0 = 0.8J_0$, and $\varphi = \pi/2$. Plot on the right again shows the corresponding cycle in parameter space. (d) Fourier-space SPP intensity distribution corresponding to (c).

6.3.2 Optical measurements

In our optical experiments SPPs are excited by focusing a TM-polarized laser beam onto the grating coupler deposited on top of the input waveguide (either sublattice A or B). The propagation of SPPs in an array is monitored by real- and Fourier-space leakage radiation microscopy as described in Sec. 4.2. We first consider a pumping cycle that encloses the critical point. For this purpose we choose the geometrical parameters of the DLSPPW array such that $u_0 = 1.1J_0$ and $\omega = 1.45J_0$. By comparing the real-space intensity distribution to numerical calculations we estimate the loss amplitude to be $\gamma_0 = 0.8J_0$. The real-space SPP intensity distribution $I(x, z)$ recorded by leakage radiation microscopy for single site excitation at site A is shown in Fig. 6.12 (a). According to the aforementioned quantum

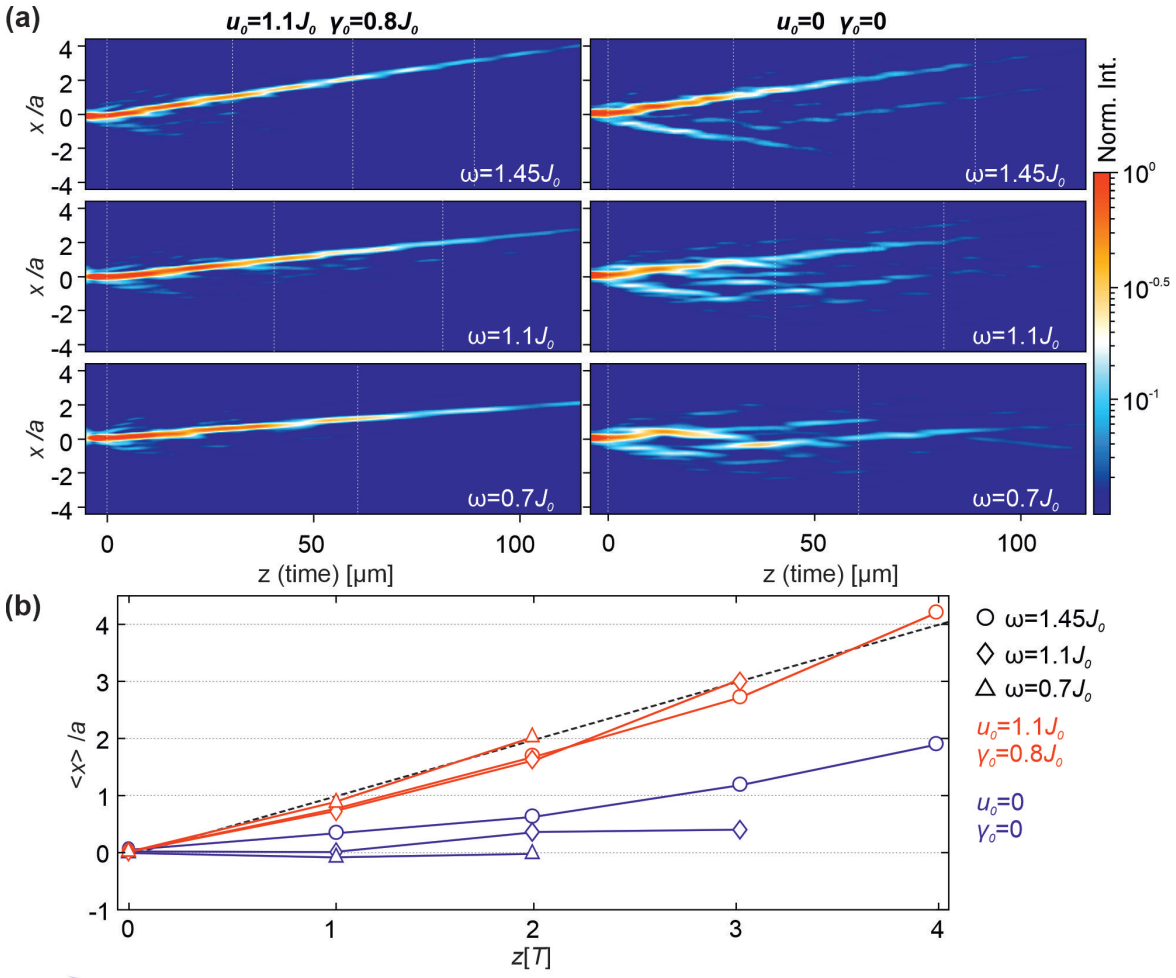

Figure 6.13: (a) Real-space SPP intensity distributions for different driving frequencies and single-site excitation at waveguide A. The left and right column correspond to arrays with cross-section modulation ($u_0 = 1.1J_0, \gamma_0 = 0.8$) and without cross-section modulation ($u_0 = 0$, $\gamma_0 = 0$), respectively. (b) The CoM position of the SPP intensity in dependence on propagation distance z calculated from the experimental results shown in (a). Note that the z-axis here is normalized to the period T. Red markers correspond to arrays with cross-section modulation and blue markers correspond to no modulation. The black dashed line shows the anticipated adiabatic behavior.

optical analogy this corresponds to the probability density $I(x,t) = |\Psi(x,t)|^2$. We observe for all z a strongly localized wave packet, whose CoM is transported in positive x-direction in a quantized manner, i.e., by one unit cell per driving period (see dotted lines), even though the driving frequency ω is larger than the modulation amplitudes of all relevant parameters.
The corresponding momentum resolved spectrum $I(k_x, k_z)$ is obtained by Fourier-space leakage radiation microscopy and is shown in Fig. 6.12 (b). This intensity distribution is analogous to the spectral energy density presented in Fig. 6.7. We note that this technique provides the full decomposition in momentum components in the higher Brillouin zones. The main feature of the spectrum is a continuous band with average slope a/T. The absence of gaps in the band indicates that

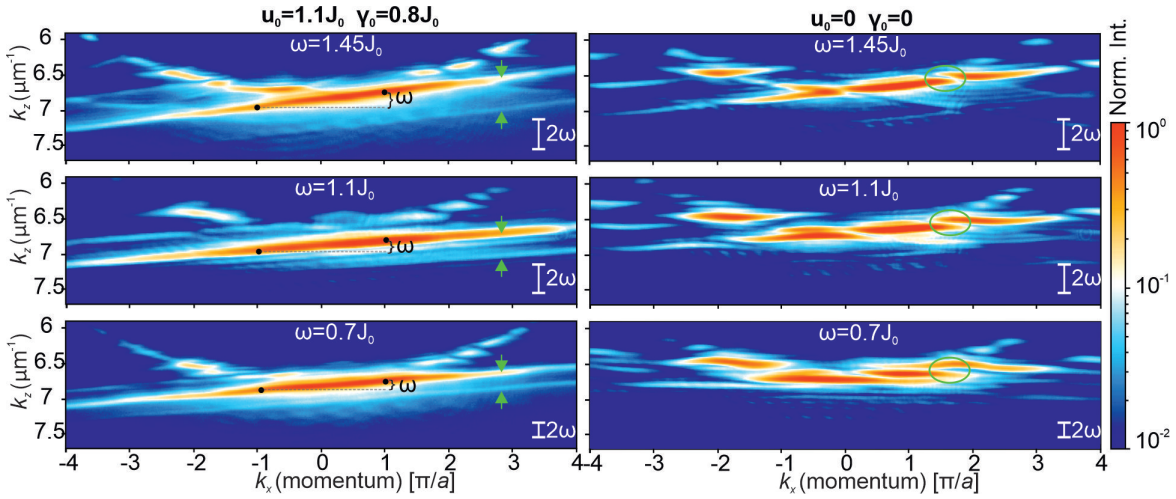

Figure 6.14: Fourier-space SPP intensity distributions for different driving frequencies and single-site excitation at waveguide A corresponding to the real-space measurements in Fig. 6.13 (a). The images on the left-hand side correspond to the case with cross-section modulation ($u_0 = 1.1J_0, \gamma_0 = 0.8$). As the frequency increases the Floquet bands get closer (see green arrows) and flatter, nevertheless, they remain continuous which is a hallmark of quantized displacement in real space. On the right-hand side the data for constant cross-section modulation is displayed ($u_0 = 0, \gamma_0 = 0$). Here, changing the frequency has an additional effect on the band structure: the gaps at the FBZ boarder start to open (see green circles). Such a behavior of the quasienergies results in the decreasing CoM shift as confirmed by Fig. 6.13 (b). The scale at the bottom right corner in every micrograph shows the size of two FBZs.

the band winds around the 2D FBBZ $\{-\omega/2 \leq k_z < \omega/2; -\pi/a \leq k_x < \pi/a\}$. This is a hallmark of a quantized pumping and confirms our theoretical predictions (see Fig. 6.7 (b)).

As a reference measurement, we consider the parametric cycle, where all parameters are changing with the same amplitudes as in the previous case but the phase is chosen as $\varphi = \pi/2$. Under these conditions the Hamiltonian is symmetric under space and time inversion. In Fig. 6.12 (c) we present the real-space SPP intensity distribution for this parametric cycle. In contrast to the previous case the wave packet is spreading and we do not observe CoM transport in x-direction. The corresponding momentum resolved spectrum shows a complicated band structure with multiple band gaps (see Fig. 6.12 (d)). Obviously, none of the bands winds around the 2D FBBZ.

We note, that directional transport of light in periodically curved waveguides can be in principle also achieved by using a simple combination of directional couplers with constant effective mode index, i.e., constant waveguide cross-section [63, 151]. However, due to periodic exchange of power between two coupled waveguides this effect has a resonant character and the period of modulation plays in this case a crucial role. In order to demonstrate that the directional transport in our system has a different origin, we repeat the experiment shown in Fig. 6.12 (a) for three different driving frequencies ω ($0.7J_0, 1.1J_0, 1.45J_0$). Moreover we prepare two sets of samples, one with modulation of the waveguide cross-section as before ($u_0 = 1.1J_0, \gamma_0 = 0.8J_0$) and the second with constant cross-section ($u_0 = 0, \gamma_0 = 0$). The measured real space intensity distributions are depicted in Fig. 6.13 (a). We extract from this data the CoM position after up to 4 complete periods as displayed in Fig. 6.13 (b). In the case with cross-section modulation (red markers) the CoM is shifted by one unit cell per period T at all chosen driving frequencies. We note that the somewhat lower than unit slope of the CoM plots

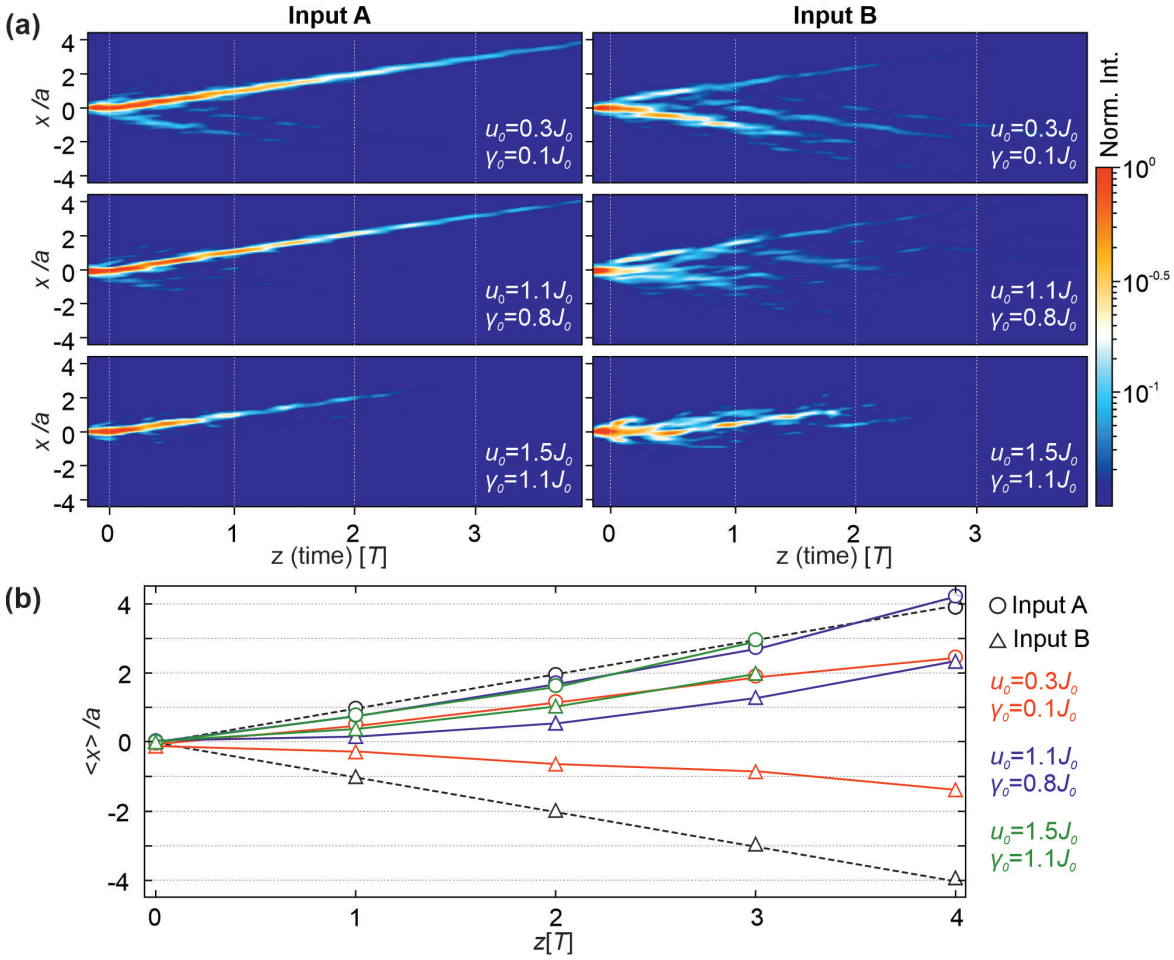

Figure 6.15: (a) Real-space SPP intensity distributions for the arrays with different strengths of the cross-section modulation ($u_0 = 0.3J_0$, $\gamma_0 = 0.1J_0$), ($u_0 = 1.1J_0$, $\gamma_0 = 0.8J_0$), and ($u_0 = 1.5J_0$, $\gamma_0 = 1.1J_0$). Measurements on the left-hand side show the SPP propagation after excitation at sublattice A (low-loss input). Measurements on the right-hand side show the SPP propagation after excitation at sublattice B (high-loss input) (b) The CoM position of the SPP intensity in dependence on propagation distance z calculated from the experimental results shown in (a). Note that the z-axis here is normalized to the period T. The black dashed line shows the anticipated adiabatic behavior.

in Fig. 6.13 (b) during the first pumping cycle is an artifact which arises from non-ideal excitation conditions, such as weak excitation of the neighboring waveguides. The deviations at large distance are statistical and result from increasing measurement errors due to camera noise and decaying signal intensity. In Fourier space changing the modulation frequency influences primarily the width of the Floquet BZ: the lower is the frequency, the smaller is the distance between the neighboring bands and the smaller is the tilt of these bands which reflects the wavepacket group velocity in absolute values (see Fig. 6.14).
Without cross-section modulation (blue markers in Fig. 6.13 (b)) the CoM displacement per period at these frequencies is much smaller than in the quantized case and depends on the driving frequency. These measurements confirm that the observed directional transport in our system is not a resonant

directional coupler effect.
Up to now we only considered experiments with excitation at sub-lattice A (low loss input). The numerical calculations predict that the transport in the opposite direction for single site excitation at sub-lattice B is strongly suppressed by the time-periodic losses. To test this, we perform additional experiments to study how the transport properties depend on the initial conditions for different strengths of cross-section modulation. In doing so we tune the amplitude of the on-site potential u_0 and simultaneously the loss amplitude γ_0. Fig. 6.15 (a) shows the real space intensity distributions for the excitation at the waveguides A (left column) and B (right column) for three different cross-section modulations and the driving frequency $\omega = 1.45J_0$. The CoM displacement derived from this data is depicted in Fig. 6.15 (b) (waveguide A: circles, waveguide B: triangles). In case of small modulation strength ($u_0 = 0.3J_0$, $\gamma_0 = 0.1J_0$, red markers) SPPs excited at site A and B are transported in $+x$ and $-x$ directions, respectively. However, for both inputs the mean displacement of the CoM is less than 1 unit cell per period. For the modulation strength ($u_0 = 1.1J_0$, $\gamma_0 = 0.8J_0$, blue markers) input A shows quantized displacement of the CoM while the sign of the mean displacement for input B switches from + to -. This effect becomes even stronger at higher modulation strength $u_0 = 1.5J_0$, $\gamma_0 = 1.1J_0$ (green) – as predicted by theory (compare with Figs. 6.8 (a-b)). In Fourier space (see Fig. 6.16) the increasing modulation strength has two main effects: first, the bands get broadened due to higher losses, second, the difference between inputs A and B gets more and more pronounced. In case of the input B the broadening effect is much stronger because of the populated high-loss band.

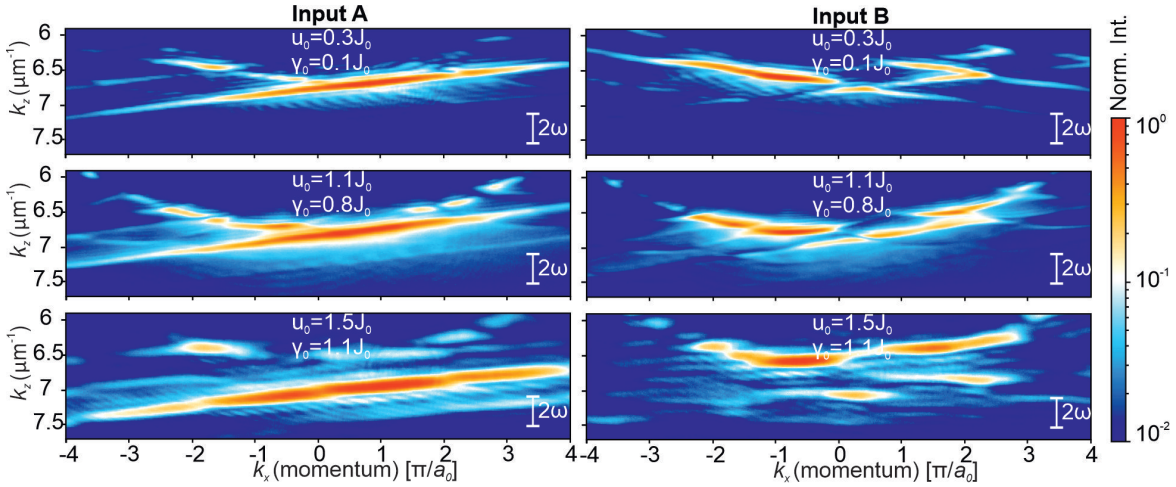

Figure 6.16: Fourier-space SPP intensity distributions for the arrays with different strengths of the cross-section modulation ($u_0 = 0.3J_0$, $\gamma_0 = 0.1J_0$), ($u_0 = 1.1J_0$, $\gamma_0 = 0.8J_0$), and ($u_0 = 1.5J_0$, $\gamma_0 = 1.1J_0$) corresponding to real-space measurements in Fig. 6.15 (a). Measurements on the left-hand side show the SPP propagation after excitation at sublattice A (low-loss input). Measurements on the right-hand side show the SPP propagation after excitation at sublattice B (high-loss input). Increasing the modulation strength results in a strong band broadening caused by a growing damping rate. This effect is more pronounced for the input B.

Summary

In conclusion, in this chapter we have considered the Thouless pumping, i.e. the quantization of particle transport that emerges in the slowly driven Rice-Mele model as a result of the non-trivial Chern number. We have learnt that at non-adiabatic driving frequencies the system becomes topologically trivial due to hybridization of the counter-propagating Floquet-Bloch bands. As a result, the particle transport deviates from perfect quantization, which poses a problem for the experimental observation of the Thouless pumping. To overcome this limitation we have introduced the non-Hermitain Floquet engineering. In particular, with the help of the non-Hermitian Floquet-Bloch theory we have shown that properly chosen periodic modulation of dissipation enables to restore the non-trivial Floquet-Bloch band structure and the associated quantized displacement of the Wannier center for the driving frequencies as large as the system's band gap. Our theoretical predictions have been confirmed by the experiments with plasmonic waveguide arrays, where the periodic losses were implemented by enhancing coupling to free-propagating SPPs with a decreasing waveguide cross-section.

CHAPTER 7

Dissipation engineered directional filter for quantum ratchets

Broadly speaking, ratchets are systems where a periodic drive together with the broken space-time symmetry give rise to a directed motion in the absence of a bias force [53]. Ratchets are found in classical [56, 57, 63] as well as in quantum systems [64, 65]. By operation mechanism ratchets are divided into those, that are based on dissipative forces and thermal motion, and lossless or Hamiltonian ratchets where directed transport arises from a coherence effect. One such example is Thouless pumping, where quantized particle displacement per period is given by the Berry phase accumulated during the closed loop in Hamiltonian parameter space. Since the driven Hamiltonian explicitly breaks space and time inversion symmetries, as long as we have a complete band filling any initial condition can carry a current. However, as we saw in the previous chapter, such a ratchet is not robust to non-adiabatic effects unless losses are introduced globally. This inevitably hampers practical applications since adiabatic conditions cannot be reached in most experimental situations and it is often desirable to minimize losses. In non-adiabatic Hamiltonian quantum ratchets, in contrast, transport efficacy sensitively depends on the initial state [64–67]. Due to periodicity in time, they can be described in terms of the Floquet-Bloch states with the well-defined group velocity. Since the system's Hamiltonian supports current in both directions, only the overlap with the initial conditions determines the contribution of different Floquet-Bloch states to the resulting current. Therefore, preparation of the initial state is crucial for optimal transport efficiency, which is often a challenging problem when dealing with real quantum systems.

From the previous chapter we have learnt, that properly designed time-periodic losses cause non-reciprocity of the wavepacket transport, i.e. favor the forward current but suppress the backward current. In this chapter we further develop this idea by constructing a direction-dependent filter for a non-adiabatic Hamiltonian quantum ratchet based on local impurity with engineered dynamic dissipation. Such a filter is aimed to relax strict initial-state requirements via suppressing the Floquet-Bloch states moving in the unwanted direction. Notably, being local it does not cause additional losses in the bulk.

As a simple ratchet model, we consider the driven SSH model that supports quantized transport for certain non-adiabatic driving frequencies once the space-time symmetry is broken by initial conditions. This model is introduced in Section 7.1. Its transport properties are analysed in the framework of the Floquet-Bloch theory in close cooperation with C. Dauer from the TU Kaiserslautern and A. Sidorenko

from the University of Bonn. In Section 7.2 we introduce time-dependent losses localized at a finite number of lattice sites. Motivated by the conditions of our experimental system, we implement these losses by the imaginary part of the potential. Our original premise is to use different spatio-temporal distributions of the moving Floquet-Bloch states to selectively absorb the states moving in one direction but transmit those that propagate in the opposite direction. Our ideas were proved by C. Dauer from the TU Kaiserslautern, who under the supervision of S. Eggert developed a numerical method based on the Floquet S-matrix theory and by its means computed the direction-dependent transmission coefficients for a broad range of the system parameters. His results are presented in this section because they clearly quantify the filter performance and allow to optimize the driving scheme. Furthermore, in Section 7.3 we provide the experimental observation of transport rectification in arrays of DLSPPWs with controlled losses. While in the previous chapter controlling losses was inseparable from changing the real part of the potential, here, we implement losses explicitly by locally depositing an absorber under the chosen DLSPPWs. In order to minimize the overall losses in the system we substitute gold by silver for sample fabrication. This chapter closely follows Ref. [152].

7.1 Ratchet model

Whereas in Sec. 5.1 we have analysed the properties of the static SSH model, here, we consider this model with parameters periodic in time. In the absence of losses the corresponding Hamiltonian for the chain of $N = 2M + 1$ unit cells reads

$$\hat{H}_{\mathrm{SSH}}(t) = -J_1(t) \sum_{j=-M}^{M} (|j,B\rangle\langle j,A| + h.c.) - J_2(t) \sum_{j=-M}^{M-1} (|j+1,A\rangle\langle j,B| + h.c.)\,, \tag{7.1}$$

where $J_1(t) = J_1(t+T)$ and $J_2(t) = J_2(t+T)$ are the T-periodic intra- and intercell hopping amplitudes. In our model these parameters are modulated such that $J_1(t) > J_2(t)$ holds for the first half of the period while the situation is inverted in the second half (see Fig. 7.1). As will be shown later, at certain driving frequencies this model supports almost dispersionless Floquet-Bloch states that can be selectively populated upon single-site excitation giving rise to unidirectional current.

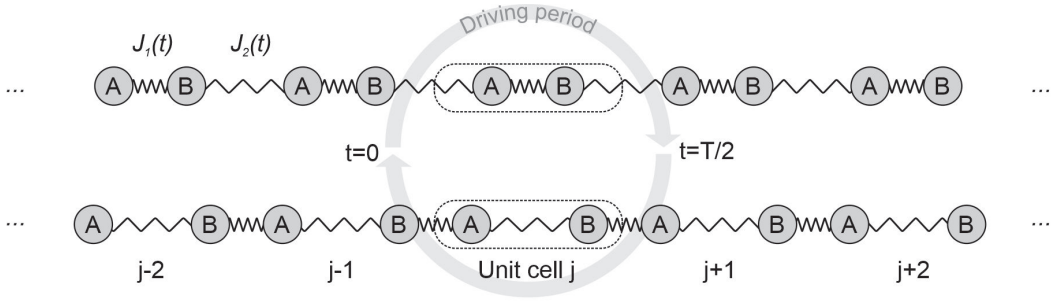

Figure 7.1: Sketch of the dimerized tight-binding Floquet chain with time-periodically modulated hopping amplitudes $J_1(t)$ and $J_2(t)$. The chain has two sublattices A and B, unit cells are labeled by j. In the first half of the period $J_1 > J_2$ (top) and in the second half $J_1 < J_2$ (bottom).

In order to reveal how the ratchet effect comes about in our model we again refer to the fully dimerized limit (see Sec. 5.1.3 and Sec. 6.1.4). In this limit it is assumed that the hopping amplitudes are modulated according to

$$\begin{aligned} J_1(t) &= \begin{cases} J & \text{if } t \in [0, T/2) \\ 0 & \text{if } t \in [T/2, T) \end{cases}, \\ J_2(t) &= \begin{cases} 0 & \text{if } t \in [0, T/2) \\ J & \text{if } t \in [T/2, T) \end{cases}. \end{aligned} \tag{7.2}$$

Next, we initiate the system at a single site on sublattice A of the unit cell j, i.e. $|\Psi_A(0)\rangle = |j, A\rangle$, and restrict ourselves to the first half of the period. Solution of the time-dependent SE yields that the time-evolution of the state $|\Psi_A(t)\rangle$ is governed by Rabi oscillations between the two lattice sites A and B from unit cell j with Rabi frequency $\Omega_R = J$

$$|\Psi_A(t)\rangle = \cos(Jt)|j, A\rangle - i \sin(Jt)|j, B\rangle \quad \text{for } t \in [0, T/2). \tag{7.3}$$

Thus, if the period of driving is chosen such such that the condition $JT_n = \pi + 2\pi n$ for $n = 0, 1, 2, \ldots$ is satisfied, then at the half period the system ends up with full population transfer between the two neighboring sites. In the terms of driving frequencies this condition reads

$$\omega_n = \frac{2J}{1 + 2n}, \quad n = 0, 1, 2, \ldots \tag{7.4}$$

Clear, that through this process the particle will be transported to the right with the quantized average group velocity of one unit cell per driving period. We note, that the optical analogue of such a system is a mesh of directional couplers, where the same principle enables to rectify light beams (see e.g. Ref. [63]). Let us emphasise the difference between the quantized transport in the driven SSH model and in the RM model from Sec. 6.1.4. In Thouless pump the population transfer was achieved by adiabatic state evolution and the period of driving played no role as long as the adiabatic condition was fulfilled. Here, in contrast, the transport is of resonant character and solely relies on the special choice of the driving frequency. For instance, if $JT'_n = 2\pi + 2\pi n$ or

$$\omega'_n = \frac{J}{1 + n}, \quad n = 0, 1, 2, \ldots \tag{7.5}$$

then at the end of the half cycle the full population returns to site A and with the flow of time the particle will always stay confined to the two neighboring lattice sites such that the average group velocity goes to zero.

Now we go away from the fully dimerized limit and use the functional form of the hopping amplitudes that resembles experimental conditions. Since in the experiments below we sinusoidally vary the spacing between the neighboring sites, the hopping amplitudes as functions of time become

$$\begin{aligned} J_1(t) &= J_0 e^{-\lambda(1-\sin(\omega t))}, \\ J_2(t) &= J_1(t - T/2). \end{aligned} \tag{7.6}$$

In the following, we set $\lambda = 2.11$, lattice constant $a = 1$ and all energies are in the units of J_0. In order

to access the band structure of our model, we impose periodic boundary conditions and transform the Hamiltonian (7.1) to momentum space (see Sec. 5.1.1 for details). The resulting Bloch Hamiltonian reads

$$\hat{H}_k(t) = -\begin{pmatrix} 0 & \rho(k,t) \\ \rho^*(k,t) & 0 \end{pmatrix}, \tag{7.7}$$

where $\rho(k,t) = J_1(t) + J_2(t)e^{-ik}$. It is easy to check that the Hamiltonian (7.7) obeys time-reversal, charge-conjugation, and chiral symmetries using the criteria for the Floquet-Bloch systems (2.61), (2.62), and (2) with $U_\mathrm{T} = \mathbb{I}$, $U_\mathrm{C} = U_\mathrm{S} = \hat{\sigma}_z$ and $t_0 = T/4$.
For theoretical analysis of our ratchet model we utilize the Floquet-Bloch theory outlined in Sec. 2.2.2. First, we calculate the quasienergy bands $\epsilon_\alpha(k)$, $\alpha \in \{1,2\}$. Fig. 7.2 (a) shows the result for three different driving frequencies $\omega \in \{0.597J_0, 1.195J_0, 2J_0\}$ exemplified in the 1st Floquet-Bloch BZ $\{-\omega/2 \leq \epsilon < \omega/2; -\pi \leq k < \pi\}$. Color code indicates the expectation value of the velocity operator in the corresponding Floquet-Bloch state $\langle v_{\alpha,k}\rangle$ calculated using Eq. (6.20). It is evident, that the driving frequency has a huge impact on the band shape: At $\omega = 1.195J_0$ (num. 2) the bands are nearly linear with the group velocity of $\pm 1/T$; in contrast, at $\omega = 0.597J_0$ (num. 1) the bands are almost flat with the close-to-zero group velocity. Due to chiral symmetry, the quasienergy spectrum is always symmetric with respect to $\epsilon = 0$. We can therefore choose to label the quasienergies and the corresponding Floquet-Bloch states according to the sign of the group velocity such that $\alpha = 1$ stands for $\langle v_{\alpha,k}\rangle \geq 0$ and $\alpha = 2$ for $\langle v_{\alpha,k}\rangle \leq 0$.
Next, we average the group velocity over all $\alpha = 1$ states

$$\langle \bar{v}_1 \rangle = \frac{1}{2\pi} \int_{-\pi}^{\pi} \mathrm{d}k \langle v_{1,k} \rangle \tag{7.8}$$

and plot it in dependence on the driving frequency ω in Fig. 7.2 (b). As predicted by the fully dimerized limit, the band-averaged group velocity oscillates with ω. C. Dauer from the TU Kaiserslautern derived the general analytical expressions for frequencies ω_n and ω_n' corresponding to maxima and minima of $\langle \bar{v}_1 \rangle$, respectively. These expressions resemble Eqs. (7.4) and (7.5) with the difference that $J/2$ is substituted by the period-averaged coupling $\int_0^1 \mathrm{d}\xi J_q(\xi 2\pi/\omega)$, $q = 1, 2$ (see Eq. (3-4) in Ref. [152]).
The frequency-dependent quasienergy spectrum for our model was calculated by A. Sidorenko from University of Bonn (see Fig. 7.2 (c)). She revealed that the observed oscillatory behaviour of $\langle \bar{v}_1 \rangle$ is directly connected to the oscillating size of the band gap opening at the boarders of the Floquet BZ, i.e. at $\epsilon = \omega/2 + m\omega$, $m \in \mathbb{Z}$. The ratchet transport is expected to be most efficient when the average group velocity reaches its maximum of one unit cell per driving period. These points correspond to gapless helical bands, which in turn feature minimal dispersion as seen from Fig. 7.2 (a).
In the view of our experimental setup, the achievable frequency range is roughly $\omega \in [0.7J_0, 2J_0]$. Thus, we focus only on the first maximum $\omega_0 = 1.195J_0$ as it lies in this range. In this case, the density of the periodic Floquet-Bloch states oscillates between the two sublattices (see Fig. 7.2): The density of a right-moving state $\alpha = 1$ is mostly concentrated on sublattice A at the beginning of the period, then it tunnels to sublattice B at $t = T/2$ and by the end of the period returns back to A. The time-reversal symmetry guarantees that this process is exactly inverted for the left-moving state $\alpha = 2$ with the same quasienergy. Note, that due to almost vanishing dispersion such a spatio-temporal distribution of the Floquet-Bloch states is largely independent of the magnitude of the quasimomentum k. The unidirectional transport in our model occurs when the asymmetric initial conditions are applied,

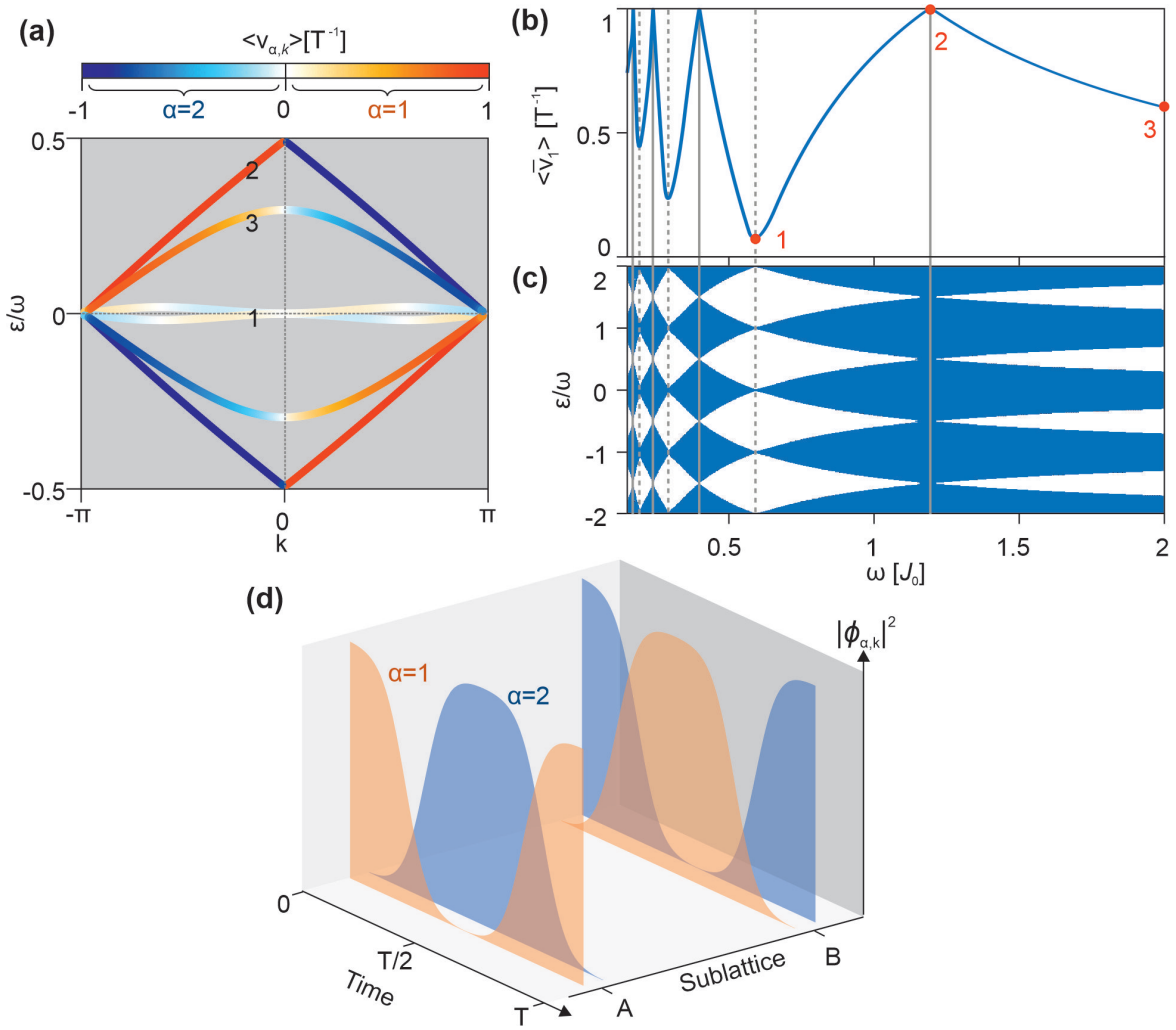

Figure 7.2: (a) Band structure in the 1st FBBZ at three different driving frequencies: 1: $\omega = 0.597J_0$, 2: $\omega = 1.195J_0$, 3: $\omega = 2J_0$. The color-code shows the corresponding group velocity $\langle v_{\alpha,k} \rangle$. (b) Average absolute value of the group velocity as a function of ω. Grey solid and dashed lines mark the local maxima and minima of the group velocity, respectively, while the numbers highlight the frequencies from (a). (c) Quasienergy spectra in dependence on the driving frequency calculated by A. Sidorenko from University of Bonn. (d) Squared absolute value of the state amplitude at $\omega = 1.195J_0$ with positive ($\alpha = 1$) and negative ($\alpha = 2$) group velocity along one period at sublattices A and B.

i.e. the system is initiated at one sublattice A or B. Via Fourier transform, this results in predominant population of only the left- or right-moving states, respectively. Such initial conditions effectively break space and time inversion symmetries thereby providing the necessary conditions for the ratchet effect.

7.2 Direction-dependent filter

Now, we additionally subject two central lattice sites, A and B from the central unit cell $j = 0$, to time-periodic losses oscillating at the same frequency ω as the bulk (see Fig. 7.3 (a)). As we know from the previous chapter, losses in our waveguide experiments are well described by the complex on-site potentials. The corresponding Hamiltonian is the sum of the SSH Hamiltonian (7.1) and the local impurity $V(t)$:

$$\begin{aligned} \hat{H}(t) &= \hat{H}_{\mathrm{SSH}}(t) + V(t), \\ V(t) &= -i\gamma_a(t)|0,A\rangle\langle 0,A| - i\gamma_b(t)|0,B\rangle\langle 0,B| \end{aligned} \tag{7.9}$$

The decay rates on sublattices A/B are denoted by $\gamma_{a/b}(t)$ and have a form of T-periodic step functions, i.e. the on-site losses can be turned on and off in a periodic manner as realized in our experiments below. The mathematical description is given by

$$\begin{aligned} \gamma_a &= \gamma_0 \Theta\{-\cos(\omega t + \varphi) - \cos(\pi L/T)\} \\ \gamma_b &= \gamma_a(t - T/2) \end{aligned} \tag{7.10}$$

where $\Theta\{x\}$ is the Heaviside function, γ_0 is the loss amplitude, L is the duration of the losses within one period T ($L < T$), and φ is the phase shift. Note, that for $\varphi = 0$ the losses are out of phase with

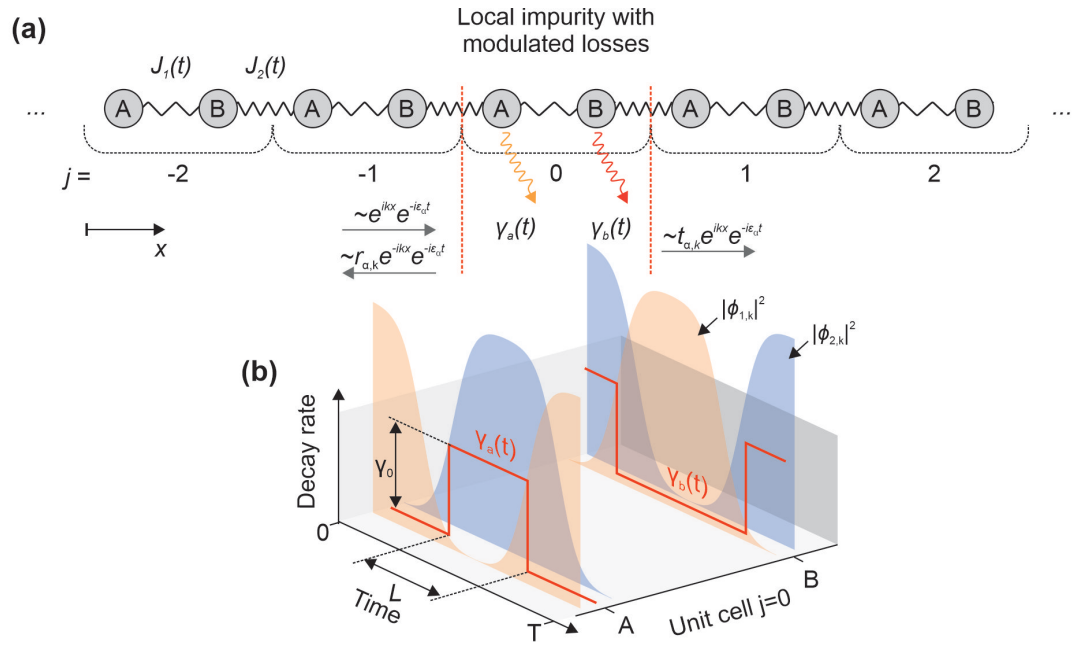

Figure 7.3: (a) Sketch of the driven SSH model with time-periodically modulated decay rates $\gamma_{a,b}(t)$. The reflection $r_{k,\alpha}$ and transmission $t_{k,\alpha}$ of the Floquet state with quasimomentum k and band index α are schematically indicated by grey arrows. (b) Loss functions $\gamma_{a/b}(t)$ on sublattices A/B of unit cell $j = 0$ in the case of $\varphi = 0$ that have a form of temporal intervals L of the constant decay rate γ_0. The probability densities of the Floquet modes $|\phi_{1,k}|^2$ and $|\phi_{2,k}|^2$ are adopted from Fig. 7.2 (d) to demonstrate that such time-periodic losses are able to selectively absorb $\alpha = 2$ states.

the coupling constants, i.e. they are centered at $t = (m + 1/2)\,T$ on sublattice A and at $t = m\,T$ on sublattice B (see Fig. 7.3 (b)).
Consider a quantum particle propagating along the driven SSH chain and scattered by the local dissipative impurity as shown by gray arrows in Fig. 7.3 (a). The transmission and reflection amplitude of the Floquet-Bloch state $|\phi_{\alpha,k}(t)\rangle$ are denoted by $t_{\alpha,k}$ and $r_{\alpha,k}$, respectively, while $T_{\alpha,k} = |t_{\alpha,k}|^2$ and $R_{\alpha,k} = |r_{\alpha,k}|^2$ stand for the corresponding transmission and reflection coefficients for the probability density. In what follows we want to explain descriptively that by choosing a proper driving scheme the transmission coefficients for the right-moving Floquet-Bloch states $\alpha = 1$ can be made much larger than for the left-moving states $\alpha = 2$, i.e. $|T_{1,k}| \gg |T_{2,k}|$. In order to understand the origin of such a non-reciprocal transmission induced by $V(t)$, assume that the system is driven with the resonant frequency ω_0, so that the bands are helical and the band-averaged group velocity is maximal. Here, it is central to look at the periodic exchange of the state density between the two sublattices. In the previous section it was shown that the counter-propagating Floquet-Bloch states have different spatio-temporal distributions which enabled to populate only states moving in the chosen direction by proper choice of the initial conditions. The same feature can be employed for direction-dependent filtering. In particular, introducing strong losses at space-time moments, where the maxima of $|\phi_{2,k}(t)|^2$ reside, the time-reversal symmetry and the oscillatory motion of the states guarantees that $|\phi_{1,k}(t)|^2$ is minimal at these moments. Thus, at $\varphi = 0$ we expect that such time-periodic losses should effectively absorb only the states moving in $-x$ direction ($\alpha = 2$), while the states moving in $+x$ direction ($\alpha = 1$) should stay almost unaffected.
Our expectations were confirmed by C. Dauer from the TU Kaiserslautern, who explicitly calculated the direction-dependent transmission and reflection coefficients for the scattering problem described by Eq. (7.9). For that, he developed the Floquet S-matrix formalism for a special case when the bulk and the impurity are both periodically modulated in time with the same frequency ω (see Ref. [152] for details). We briefly discuss his results because they allow to quantify the efficiency of our direction-dependent filter and thereby help to optimize the system parameters. The transmission coefficients for $\alpha = 1$ and $\alpha = 2$ states in dependence on L and γ_0 are shown in Fig. 7.4 (a) and (b), respectively. Here, $\omega = \omega_0$, $\varphi = 0$, and initial conditions correspond to the uniform superposition of either all the $\alpha = 1$ or $\alpha = 2$ states. Due to negligible dispersion at ω_0, the transmission coefficients were averaged over the 1$^{\text{st}}$ BZ, i.e. $T_\alpha = \frac{1}{2\pi}\int_{BZ} \mathrm{d}k T_{\alpha,k}$. Fig. 7.4 (a) reveals that for $L < 0.5T$ $\alpha = 1$ states are well transmitted with close-to-one T_1. In contrast, the transmission T_2 in Fig. 7.4 (b) drops sharply with increasing L and γ_0. Remarkably, the ratio T_1/T_2 can even exceed 10^3 in the examined parameter range, which clearly demonstrates that our dissipative impurity works as a perfect direction-dependent filter.
It is natural to wonder what happens if we change the phase shift φ in Eq. (7.10)? The band-averaged reflection and transmission coefficients for fixed $\gamma_0 = 1.5J_0$ and $L = 0.25T$ in dependence on φ are plotted in Fig. 7.4 (c). At $\varphi = 0$ and π the spatio-temporal loss distribution coincides with the maxima of the Floquet-Bloch states moving in $-x$ or $+x$ directions, respectively. In this case, the unidirectional transmission effect is most pronounced while the reflection coefficient is low and does not depend on the propagation direction. In contrast, at $\varphi = \pi/4$ and $3\pi/4$ the losses are centered at the points where the counter-propagating Floquet-Bloch states have equal support on both sublattices. At these points the transmission coefficients for $\alpha = 1$ and $\alpha = 2$ states become equal while the reflection coefficients reach their local maxima and turn to be direction-dependent.
Finally, the performance of our filter was analysed for various driving frequencies. Fig. 7.4 (d) shows

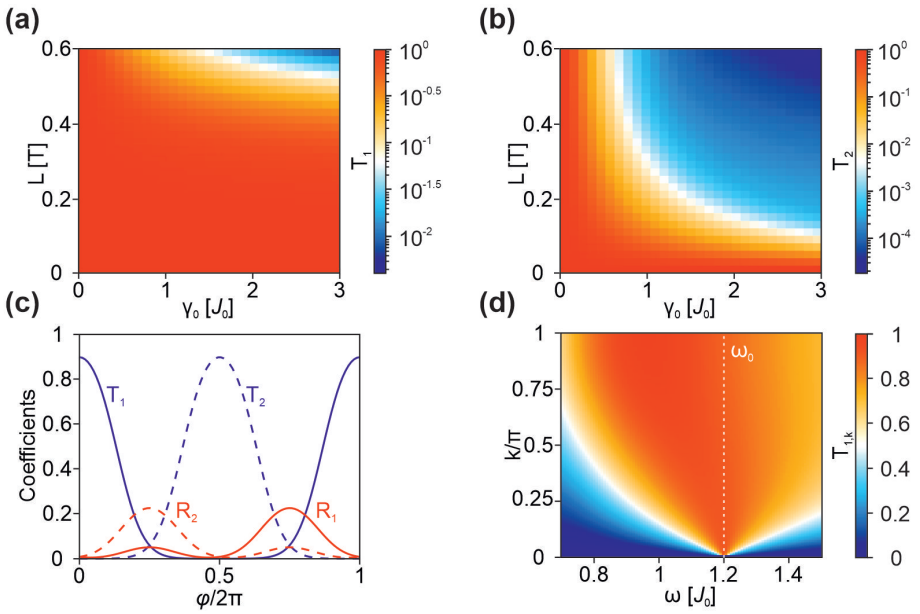

Figure 7.4: Results of the Floquet S-matrix analysis performed by C. Dauer from TU Kaiserslautern. Band-averaged transmission coefficient for (a) $\alpha = 1$ and (b) $\alpha = 2$ states in dependence on the impurity parameters γ_0 and L at $\omega_0 = 1.195J_0$, $\varphi = 0$. (c) Transmission (blue) and reflection (red) of $\alpha = 1$ (solid) and $\alpha = 2$ (dashed) moving states as functions of the phase shift φ for fixed $\gamma = 1.5J_0$ and $L = 0.25\,T$. (d) Transmission of $\alpha = 1$ states for $L = 0.25\,T$ and $\gamma_0 = 1.5J_0$ in dependence on the driving frequency ω and quasimomentum k. White dashed line highlights the resonant frequency ω_0.

that at ω_0 the transmission coefficient $T_{1,k}$ is maximal and homogeneous for all quasimomenta k, while away from the resonance it decreases for the states around $k = 0$. This is due to hybridization of the quasienergy bands. Note, that the corresponding reflection coefficient, in contrast, increases with with the detuning (see the corresponding data in Ref. [152]).

7.3 Experiments

Relying on the quantum-optical analogy described in Sec. 3.2.4 we realize unidirectional transmittance in arrays of DLSPPWs. According to this analogy, time is directly mapped into propagation distance z which enables us to mimic a Floquet system by periodic modulation of the corresponding parameters along the waveguide axis. The sketch of a typical sample is displayed in Fig. 7.5. Such a DLSPPW array is analogous to a one-dimensional Floquet chain with two sites (waveguides) per unit cell, A and B. The cross-sections of all the waveguides are kept constant. The sinusoidal modulation of the center-to-center distances $d_{1,2}(z)$ results in periodic modulation of the corresponding coupling constants. We introduce local periodic dissipation $\gamma_{a/b}(z)$ by deposition of chromium stripes below the waveguides. It was shown that Cr can cause strong losses with negligible effect on the real part of the effective refractive index [153]. Thus, in contrast to the approach from the previous chapter, this technique allows us to control the imaginary part of the propagation constant without need for change the real part. In order to minimize the overall losses, we use silver instead of gold for substrate

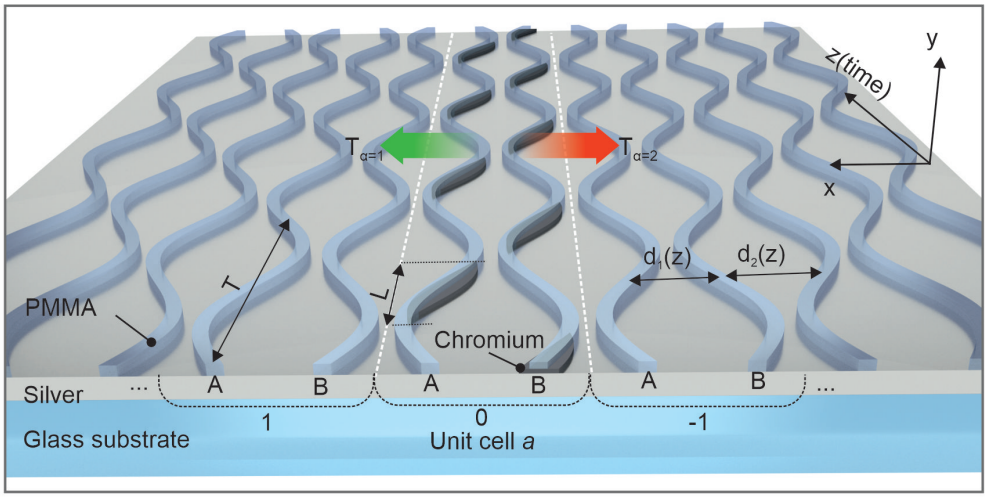

Figure 7.5: Sketch of a plasmonic waveguide array featuring unidirectional transmittance. Green and red arrows indicate the low and high loss directions, respectively.

preparation.

7.3.1 Fabricated samples

A scanning electron micrograph of a DLSPPW array with locally modulated dissipation is shown in Fig. 7.6. Such a sample is fabricated through a two-step process which combines the positive- and negative-tone electron beam lithography (see Sec. 4.1 for details). The sample preparation starts with evaporation of 62 nm of Ag and 2 nm of Cu for adhesion on a cleaned surface of a glass substrate. Then the sample is spin coated with the PMMA. In the first EBL step, we utilize PMMA as both positive- and negative-tone resist. While a template for the lossy regions are written with the low electron dose of 3 $\mathrm{C/m^2}$, the alignment markers are fabricated with high electron dose of 30 $\mathrm{C/m^2}$ that induces PMMA cross-linking. The reason is that cross-linked PMMA forms sufficiently high structures that stay clearly visible under the second layer of PMMA in the next lithography step. The areas exposed to low electron dose are dissolved in a developer and 15 nm of Cr is evaporated on top of the substrate. After the lift-off process, we end up with the Cr stripes and the alignment markers at the predefined positions. The width of each Cr stripe is set to 1.3 µm. Afterwards, the sample is again spin coated with PMMA and the second EBL step takes place. Now we fabricate the DLSPPW arrays on top of the Cr stripes with a constant electron dose of about 20 $\mathrm{C/m^2}$ using the markers for the alignment. In this step, PMMA acts only as a negative tone resist. Finally, the samples are developed in acetone.
The atomic force microscopy measurements revealed that the applied electron dose results in the mean waveguide height of 90 nm and the width of 270 nm, which allows us to work in a single mode regime at a vacuum wavelength of $\lambda = 0.98$ µm. For these geometrical parameters we numerically calculate the real part of the propagation constant of the guided mode using FEM (see Sec. 3.2.1) which yields $\beta' = 6.55\ \mu\mathrm{m}^{-1}$. Due to strong confinement of SPPs we can neglect the variation of a propagation constant caused by waveguide bending and thus consider the real part of the on-site potential to have a constant offset which be can always set to zero (see Sec. 5.3.1). The imaginary part

of the propagation constant is obtained by measuring the propagation length of SPPs and equals to $\beta'' = (7.3 \pm 0.02) \cdot 10^{-3}$ µm^{-1}. In our model system β'' is responsible for the constant decay rate caused by ohmic losses in the metal, imperfections of the fabricated film, and leakage radiation into the substrate. These losses are assumed to be homogeneous and independent of z, in contrast, to the dissipation induced by Cr stripes. Using FEM simulations we estimate the minimum loss strength caused by the Cr layer to be $\gamma_0 = 0.25$ µm^{-1}. Note, that $\gamma_0 \gg \beta''$. The width of the Cr stripe is designed to be much larger than the width of a waveguide (see Fig. 7.6). We can, therefore, assume the losses to be approximately constant along the whole length of the stripe L as given by Eq. (7.10). The distance between the adjacent waveguides varies as $d_{1,2} = 2 \pm 0.65 \cdot \sin \omega z$ µm, $\omega = 2\pi/T$. The sinusoidal modulation of $d_{1,2}(z)$ in turn results in periodic modulation of the corresponding coupling constants. This modulation can be expressed by Eq. (7.6) since the mode overlap decays as $\propto e^{-a \cdot d}$ with the distance d between the waveguides. The parameters from Eq. (7.6) are determined in an auxiliary experiment. For that experiment pairs of straight waveguides with different center-to-center distances are fabricated on top of a silver film. On this sample the real-space leakage radiation microscopy is performed under the excitation of one waveguide from each pair. Then the coupling length L_c in dependence on the distance between two waveguides d is extracted. According to Eq. (3.51), the measured coupling lengths give us direct access to the distance-dependent coupling constants $J(d)$ (see Fig. 7.7). Fitting the function $\ln J(d)$ by a line we obtain $\lambda = 2.11 \pm 0.21$ and $J_0 = 0.16 \pm 0.05$ µm^{-1}. Analogous measurements for gold films are described in details in Ref. [93]. As shown in Fig. 7.6 the modulated part of the array is preceded by a short straight interval of the length 6 µm. This region contains the grating coupler (red box) which is used for SPP excitation. The grating is deposited only onto the two waveguides at the left and right side from the dissipative region (inputs A and B), while the extension of others to this region is needed to prevent fire-end excitation of the adjacent waveguides.

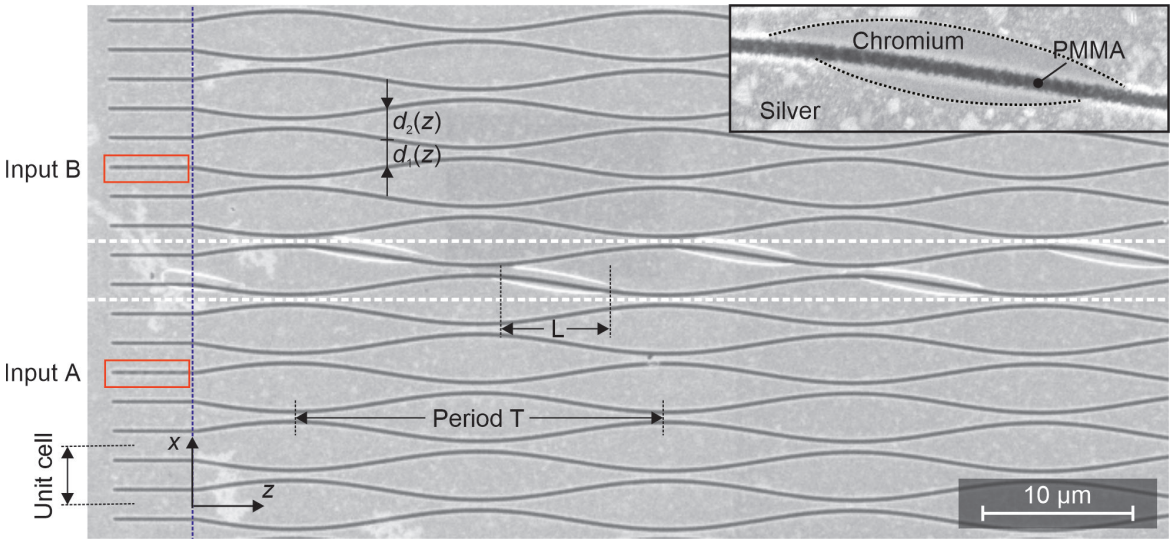

Figure 7.6: SEM scan of a typical sample. Inputs A and B are marked by red boxes and white dotted lines highlight the region with periodic dissipation. Blue dashed line corresponds to $z = 0$ and separates the excitation region from the modulated part of the array. The chromium stripe used to implement losses is magnified in the top right corner.

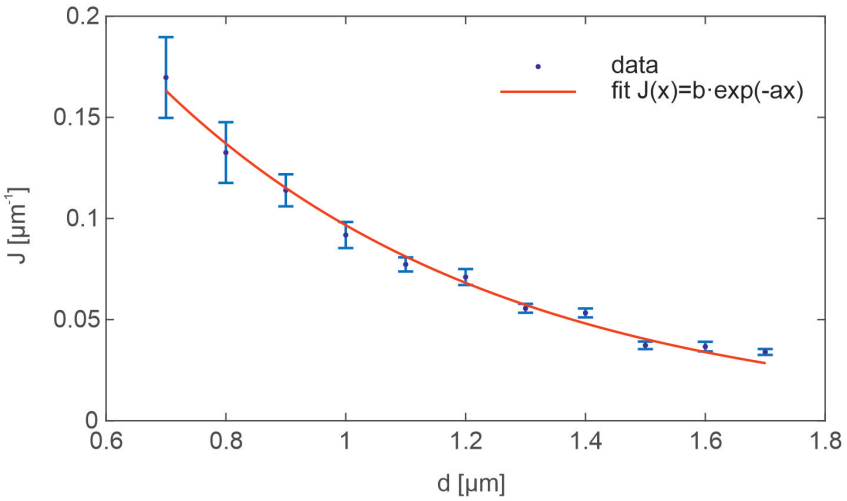

Figure 7.7: Experimental coupling constants plotted against the distance between the two straight DLSPPWs on silver films. The dependence $J(d)$ is fitted by an exponential function (red line).

7.3.2 Optical measurements

The propagation of SPPs in the fabricated arrays is monitored by the real- and Fourier space leakage radiation microscopy (see Sec. 4.2). First, we consider the case without engineered losses and determine the driving frequency ω at which the directed transverse motion of SSPs with the highest group velocity $\langle \bar{v} \rangle$ is achieved. Theory predicts for this case the absence of hybridization of the counter-propagating states and, therefore, the most pronounced one-way transmission effect. In order to find the group velocity maximum, arrays of modulated DLSPPWs (no Cr is deposited) with various frequencies of modulation are produced. For every array the real-space intensity distribution $I(x, z)$ (analogous to $|\Psi(x, t)|^2$) is measured after a single-site excitation at the sublattice A. Note that the corresponding data for the input B is just mirrored about $x = 0$. The experimental data is then used to extract the position of the center of mass $\langle x(z) \rangle$ of the wavepacket as a function of z (see Eq. (6.45)). The group velocity $\langle \bar{v} \rangle$ is found as the slope of the linear fit to $\langle x(z) \rangle$ and plotted in units of a unit cell per driving period a/T against ω in Fig. 7.8 (a). The resulting curve reaches the peak value of about 0.63 at $\omega = \Omega_1 \approx 0.23$ μm^{-1}. The measured peak value of the group velocity is smaller than 1 as would be expected from the completely filled band (see Fig. 7.2 (b)). We attribute this deviation to the contribution of camera noise and non-perfect excitation conditions. By the latter is meant that, first, the overlap of the states moving in the $-x$ direction with the initial conditions is not exactly zero, second, when guided SPPs are excited by shining laser light onto the grating coupler, the laser spot slightly excites the neighboring waveguides. These factors inevitably decrease the CoM displacement. The quantitative comparison with the theoretical value of ω_0 requires the value of J_0, which has an experimental uncertainty $1.09J_0 \geq \Omega_1 \geq 2.09J_0$ that is fully consistent with the theoretical value of $\omega_0 = 1.195J_0$. In Figs. 7.8 (b), (c) we compare the real- and Fourier-space intensity distributions for two frequencies Ω_1 (close to the resonance ω_0) and Ω_2 (maximum frequency in our measurements, away from the resonance). In real space at Ω_1 we observe that the wavepacket is confined, and the intensity maximum is transported in positive x-direction (Fig. 7.8 (b), top). The corresponding Fourier intensity distribution $I(k_x, k_z)$ shown in Fig. 7.8 (c) (top) reveals nearly linear dispersion and

predominant population of the Floquet states with $\langle v_{\alpha,k} \rangle > 0$. In contrast, at Ω_2 the wavepacket is spreading in both directions (see Fig. 7.8 (b), bottom) and in Fourier space (see Fig. 7.8 (c), bottom) the gaps between the quasienergy bands broaden, and the states with $\langle v_{\alpha,k} \rangle < 0$ become noticeably populated. Such a behaviour results from hybridization of counter-propagating states and is fully consistent with the theory (compare with Fig. 7.2 (b)).
Next, we fabricate DLSPPW arrays with local modulated losses using the optimal driving frequency Ω_1 determined above. For that we deposit Cr stripes of length $L = 0.3T$ beneath the two waveguides in between the inputs A and B, so that the phase shift in Eq. (7.10) is zero $\varphi = 0$ (see Fig. 7.3 (b)). The inputs are placed such that the excited wavepacket impinges upon the region of modulated losses from both sides. In Fig. 7.9 (a) the resulting real-space intensity distributions of SPPs for two input conditions are displayed. Here, the wavepacket impinging from the region $x > 0$ (top image) is strongly damped such that no SPPs are visible after the lossy region. Since the transmitted wave is lower than

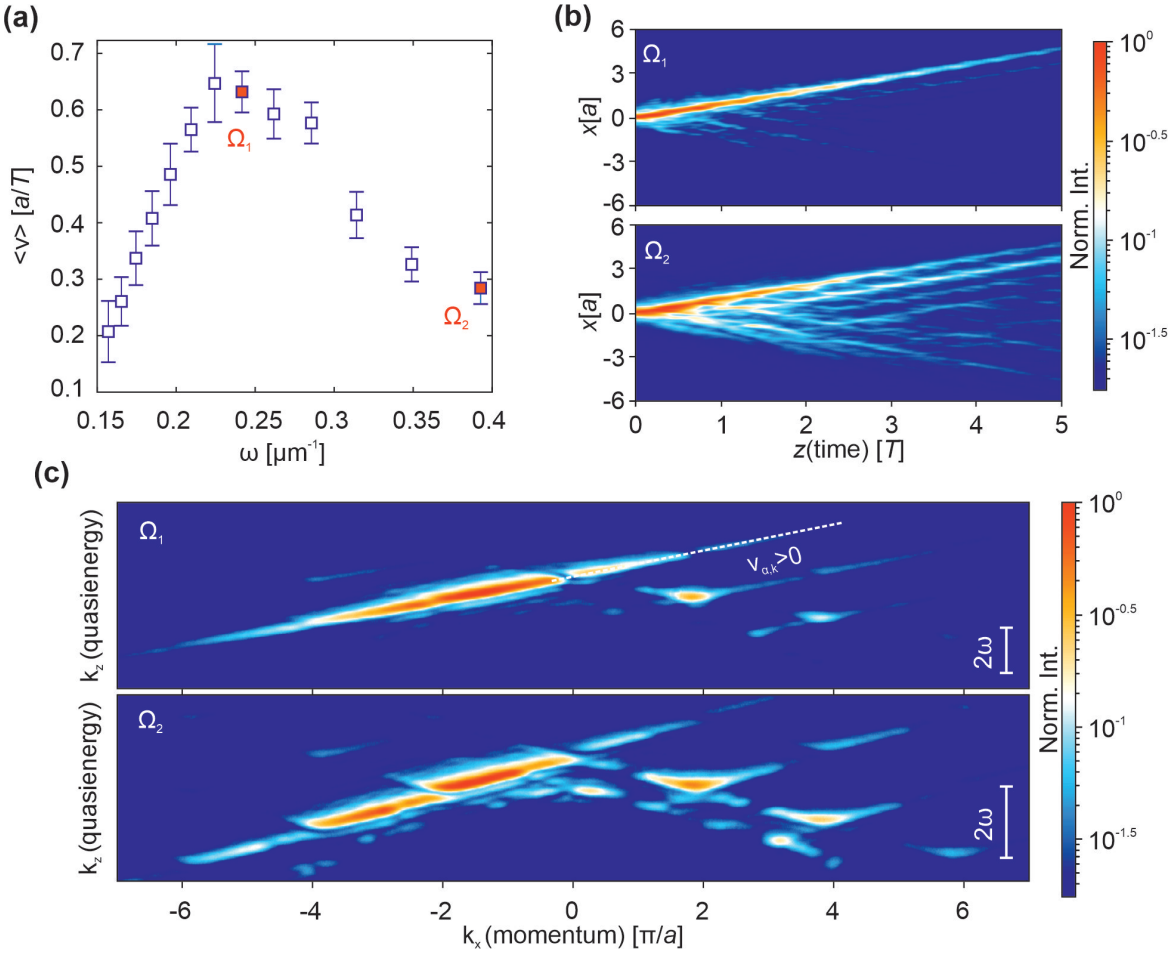

Figure 7.8: (a) Measured mean group velocity of a wavepacket versus driving frequency ω for the single-site excitation at the input A. (b) Real-space SPP intensity distributions corresponding to the arrays modulated with frequency $\Omega_1 = 0.23\ \mu m^{-1}$ and $\Omega_2 = 0.39\ \mu m^{-1}$. (c) Fourier-space SPP intensity distributions for the same arrays as in (b).

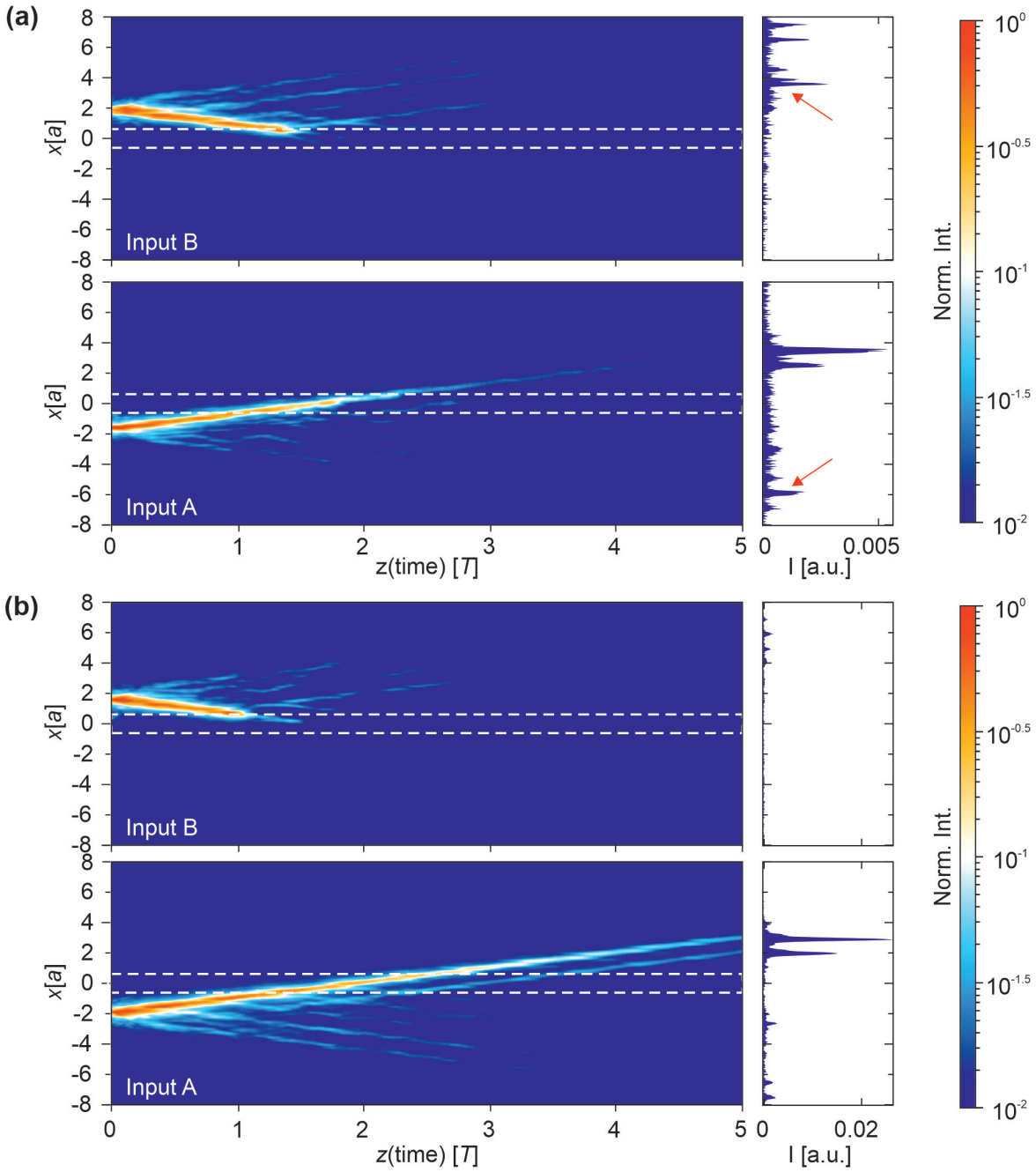

Figure 7.9: Real space intensity distributions for the DLSPPW arrays with local modulated dissipation (highlighted by white dashed lines) featuring unidirectional transmittance at Ω_1. The wavepacket is excited at $x > 0$ (input B, top) or at $x < 0$ (input A, bottom). The area plots at the right side from the real-space data show the intensity distribution after the propagation distance $z = 5T$. (a) Chromium stripes with $L = 0.3T$ were deposited below two waveguides. The red arrows point to reflected wave. (b) The same as in (a), but the length of the Cr stripe was reduced to $L = 0.15T$.

the noise level, the transmission coefficient must be $T_{\alpha=2} < 10^{-2}$. In contrast, when the wavepacket impinges from the opposite side, $x < 0$, it is partially transmitted (bottom image). By comparing to the case with no loss, we can estimate the transmission coefficient $T_{\alpha=1} \approx 0.53$. Additionally, the weak reflection from the interface is observed for both sides (see red arrows). This can be related to the slight shift of the Cr stripes in respect to the waveguides which leads to a non-zero phase shift φ. We now aim to improve the performance of the direction-dependent filtering in our system, in particular, we want to increase the transmission in the low-loss direction $T_{\alpha=1}$ while keeping the $T_{\alpha=2}$ below the detection limit of $\sim 10^{-2}$. Relying on the numerical calculations discussed above, at the constant loss strength γ_0 this can be realized by reducing the Cr stripe length L. Indeed, for $L = 0.15T$ (Fig 7.9 (b)) we again observe strong absorption in $-x$ direction such that $T_{\alpha=2} < 10^{-2}$, however, the transmission in the opposite direction is substantially increased $T_{\alpha=1} \approx 0.92$. In this case we see no reflection from the interface.

Summary

In conclusion, in this chapter we have employed the idea of the non-Hermitian Floquet engineering developed during the previous project to construct a direction-dependent filter for a fast Hamiltonian quantum ratchet. On the example of the driven SSH model, we have shown that a properly chosen driving scheme gives rise to a directional particle transport at certain resonant frequencies. However, the transport efficiency in this (in fact any) non-adiabatic Hamiltonian quantum ratchet depends critically on the initial conditions. In contrast, it is often desirable to achieve optimal transport efficiency without initial-state preparation. In order to circumvent this technical challenge we have proposed the filter based on a dissipative impurity that selectively suppresses the states moving in the chosen direction by taking advantage of the distinct spatio-temporal distributions of the counter-propagating Floquet-Bloch states. In addition, we have provided the direct experimental observation of the one-way transmittance in periodically modulated plasmonic waveguide arrays containing a local impurity with engineered losses. These losses were implemented explicitly by placing an absorber below the two central waveguides in a two-step lithographic process.

CHAPTER 8

Summary

In this thesis Floquet engineering was utilized to tailor topological and transport properties of one-dimensional tight-binding lattices. The systems of interest were analysed within the Floquet formalism and realized experimentally in arrays of evanescently coupled plasmonic waveguides. Our experiments relied on a mathematical equivalence of the single-particle Schrödinger equation in the tight-binding approximation and the coupled mode theory. The plasmonic samples were fabricated by electron beam lithography while their optical characterization was performed with the help of the real and Fourier space leakage radiation microscopy. Throughout this work we have observed a remarkable agreement of the experimental results with the numerical calculations based on the Floquet theory which unambiguously shows that arrays of plasmonic waveguides are a perfectly suited platform for Floquet engineering. Our theoretical and experimental findings illuminate new interesting aspects of Floquet engineering in the realm of topological and non-Hermitian systems.

In Chapter 5 we have demonstrated that local time-periodic driving of an edge in a system with non-trivial bulk topology can lead to a depopulation of a topological edge state. If the Hamiltonian obeys chiral symmetry, the energy of the topological edge state always remains symmetric with respect to zero. In the fully static case, this guarantees the energetic separation of the edge from the bulk states due to the presence of a band gap. Periodic driving splits the band structure into the Floquet replicas spaced by the energy of $\hbar\omega$. Since the edge is driven locally, only the Floquet copies of the edge state becomes populated, meanwhile the bulk spectrum stays almost unaltered. Although the topological character of the bulk cannot be changed by any local perturbation, we observe a dramatic change in the occupation and spectral characteristics of the topological edge state for a certain frequency window. This can only be explained by hybridisation with the bulk states because the depopulation happens once the Floquet replicas of the edge state overlap with the bulk energies. For the examined driving protocol, where the amplitude of the driving is smaller than the characteristic energy scale of the system, this effect is predominantly governed by the first-order replica. In the intermediate frequency range, enough energy is imparted to the system to destroy its topological protection, or, in more strict terms, the concept of topological protection is not valid any longer. Interestingly, if the driving frequency is high enough such that the Floquet replicas are well separated from each other, the localization of the edge state is not affected. This phenomenon was analysed theoretically with the help of the Floquet theory and demonstrated experimentally in arrays of plamonic waveguides for the longitudinal polarization of the perturbing field. Independent experiments based on the dielectric waveguides performed in the TU Kaiserslautern showed qualitatively the same behaviour for the

transverse polarization.
In Chapter 6 the concept of the non-Hermitian Floquet engineering has been introduced. Specifically, we considered a non-Hermitian extension of the periodically driven Rice-Mele model. For the theoretical analysis of such a system the Floquet theory has been generalized to the case of complex linear time-periodic Hamiltonians using the elements of biorthogonal quantum mechanics. While fast driving of the dissipationless systems always destructs the quantization of the Thouless pumping, we have demonstrated theoretically that time- and space-periodic dissipation can lead to the restoration of the quantized transport for non-adiabatic driving conditions. The reason is that periodic losses can modify the Floquet-Bloch band structure in such a way that they close the band gaps present in the Hermitian Floquet-driven system. It results in chiral quasienergy bands that wind around the two-dimensional Floquet-Bloch Brillouin zone, which thus carry a quantized transport given by the qusienergy winding number. Remarkably, that this is not due to a dissipation-induced band broadening, but a true renormalization of the real part of the energy eigenvalues, induced by the non-Hermiticity of the eigenvalue equation. Controlling the loss strength in the non-Hermitian Rice-Mele model one can restore topological transport quantization for an arbitrary fast driving frequency. Upon excitation of a single lattice site it was possible to homogeneously populate a single band, that is a necessary condition for probing the topological transport properties. We also have shown that systems with periodic loss modulation can be easily simulated by arrays of plasmonic waveguides. One way to implement such losses is to take an advantage of the enhanced coupling to free-propagating SPPs with a decreased waveguide cross-section. This effect allowed us to experimentally realize the non-Hermitian Rice-Mele model in arrays of plasmonic waveguides. In real space, the center of mass of the excited surface-plasmon polariton wavepacket was shifted by one unit cell per driving cycle. In Fourier space quantized pumping was seen as a chiral Floquet band that winds around the quasienergy Brillouin zone. Additional experiments showed that, first, unlike in a simple combination of directional couplers, the SPP transport in our system was independent on the driving frequency. Second, the transport in the opposite direction was strongly suppressed. Such a behavior perfectly agrees with the theoretical predictions based on the non-Hermitian Floquet-Bloch analysis.
Finally, in Chapter 7 the non-Hermitian Floquet engineering has been applied to construct a direction-dependent filter for a fast Hamiltonian quantum ratchet. The role of a ratchet system played the driven SSH model. The theoretical analysis based on the Floquet-Bloch theory has shown that in the case when space and time inversion symmetries were broken by initial conditions such a model supported a directional current at certain resonant frequencies. These frequencies were characterized by helical Floquet bands with a vanishing dispersion. The generation of a directional current by asymmetric initial condition was achieved due to the oscillations of the counter-propagating Floquet-Bloch states between the two sublattices. Such an oscillatory behaviour also predefined the design of the local periodic losses for the direction-dependent filtering. The resulting dissipative impurity enabled a largely nonreciprocal transport at all quasimomenta and a wide range of the system parameters. This was demonstrated by numerical calculations of the transmission and reflection coefficients conducted in the theoretical group from the TU Kaiserslautern. Theoretical predictions were confirmed by the direct experimental observation of the one-way transmittance in periodically modulated plasmonic waveguide arrays containing a local impurity with engineered losses. In contrast to Chapter 6, these losses were implemented explicitly by placing chromium stripes below the two central waveguides in a two-step lithographic process. This method allows to control the imaginary part of the propagation constant without changing the real part, which opens new possibilities to use the non-Hermitian Floquet engineering in the plasmonic waveguide arrays. In addition to that, the overall losses were

successfully reduced by substituting gold by silver in sample fabrication.

CHAPTER 9

Outlook

This thesis gives a valuable insight into the Floquet engineering as a tool for coherent control of topological and transport properties of surface plasmon polaritons in evanescently coupled waveguide arrays. Our findings are not only interesting by themselves for the broad scientific community, but also open up several new directions for the future research work both theoretical and experimental. Below I would like to mention some of them.

The first direction is to deepen our knowledge on the systems that were considered in this thesis. For instance, regarding the driven SSH model, it will be interesting to study how the spatial extent of the external driving field affects the topological protection of an edge state. On the one hand, we found out that if a single site at the boundary of the topologically non-trivial SSH model is driven at the frequency that lies within the bulk energies, then the edge state couples to the bulk states and its localization in real space is destroyed. On the other hand, it is known that if the SSH model is subject to time-periodic driving globally, i.e. in the whole bulk, then in the same frequency range it supports a localized edge state at zero energy [5, 136]. In addition to that, the overlap of the Floquet replicas of the bulk band structure results in the opening of the new band gaps at the boarder of the Floquet Brillouin zone that host anomalous topological edge states, the so-called π-modes. Such π-modes are also localized at the edge and were recently observed in our research group on the same plasmonic waveguide platform. However, it is unclear what happens during the transition between the local and global driving schemes. Specifically, how far the driving field has to be extended such that the wavepacket localization at the edge stabilizes and how it correlates with the system parameters?

The dissipative Rice-Mele model introduced in this thesis also leaves much space for the further research. The model parameters that were considered in this thesis were primarily inspired by the waveguide experiments, however, the driving scheme has not yet been optimized. Thus, one could try to find the best way to modulate time-periodic decay rates to efficiently restore a quantized transport with minimal intensity attenuation. In this context, the effect of coupling of the guided SPP mode to continuum of free propagating SPPs which was utilized to implement losses in the non-Hermitian Rice-Mele model also deserves a deeper analysis to improve the control over the system parameters. Another important issue is to address the stability of the dissipative quantized pumping against disorder. What is more, our experiments can serve as a starting point for future theoretical investigations of more elaborate many-body systems. Understanding the role of interactions in topological systems is still in its infancy and currently of growing interest. In our case, the observed stabilization of the topological transport in plasmonic wavegude arrays was due to the imaginary terms

in the single-particle Schrödinger equation. However, it is known that such imaginary terms in an effective single-particle equation of motion can also arise from many-body interactions. Thus, it will be interesting to see whether the topological transport stabilization at non-adiabatic conditions can be achieved not only by modulating losses, but rather by tailoring the interactions and whether this effect is feasible in ultracold gas experiments. In this realm, we note a closely related work on nonlinear Thouless pumping that has been recently published [154].

The second direction is to use the experimental and numerical expertise collected during this work to further study the interplay between Floquet drive, topology and non-Hermiticity. Of particular interest is the realization of non-Hermitian topological phases that have recently attracted much attention [155–157]. Another point to consider is that losses can serve not only as an instrument to change the topological properties of a non-Hermitian system, but also to detect topological invariants of the unitary dynamics. With this in mind, our plasmonic waveguide platform can be readily adopted for probing the topological invariants in one-dimensional tight-binding lattices via losses using the scheme proposed in Ref. [158]. The underlying idea is that the bulk winding number can be detected through the displacement of a single particle in the presence of the time-periodic losses applied to one sublattice. Such losses play a role of the repeated measurements that perturb the system dynamics in a periodic fashion. This detection scheme can be applied for static as well as time-periodic systems that respect chiral symmetry.

Last but not the least, the future work should be aimed towards the improvement of the existing experimental setup and finding the alternative solutions to mimic more complex Floquet topological systems with the tools of nanophotonics. Plasmonic waveguides allow for a very powerful detection technique but naturally suffer from ohmic losses that strongly limit the observation time of the modelled system. In spite of an advantage of strong field confinement, short propagation length additionally causes poor nonlinear performance of integrated plasmonic devices [159, 160]. In contrast, introducing nonlinearity is highly desirable for any photonic quantum simulator because it opens a path towards modelling systems with interparticle interactions. As already mentioned, addressing the affect of interactions in topological and Floquet systems is in turn an issue of fundamental importance.

In order to overcome the problem of metal absorption and at the same time keep using the same detection method, instead of SPPs one can try to build an experimental platform on the basis of Bloch surface waves (BSW). Such electromagnetic waves are exponentially confined to the interface constituted by a multilayered dielectric structure (one-dimensional photonic crystal) and a homogeneous dielectric medium due to the presence of a band gap in a photonic crystal. Such a configuration does not include a metallic layer and hence the propagation length of BSWs is substantially larger than for SPPs which has been pointed out in several works [161–165]. It has been demonstrated that Bloch surface waves can be manipulated by dielectric ridges at nanoscale and the same excitation and detection techniques as for SPPs are applicable. Of interest to us is that excitation by a grating coupler and detection via the leakage radiation microscopy have been already successfully realized [165]. Therefore, using BSWs it might be possible to keep all the advantages of the existing setup, but get additional benefits from the all-dielectric configuration. Although the propagation length would be still much shorter than in the usual optical waveguides, such a BSW-based platform opens new opportunities to realize nonlinearity, in comparison to SPPs. For instance, one can utilize for this purpose novel strongly non-linear materials, such as monolayers of transition metal dichalcogenides [166].

Bibliography

[1] A. Eckardt, *Colloquium: Atomic quantum gases in periodically driven optical lattices*, Reviews of Modern Physics **89** (2017) 011004 (cit. on pp. 1, 10).

[2] M. Holthaus, *Floquet engineering with quasienergy bands of periodically driven optical lattices*, Journal of Physics B: Atomic, Molecular and Optical Physics **49** (2015) 013001 (cit. on pp. 1, 13).

[3] J. W. McIver et al., *Light-induced anomalous Hall effect in graphene*, Nature physics **16** (2020) 38 (cit. on p. 1).

[4] M. C. Rechtsman et al., *Photonic Floquet topological insulators*, Nature **496** (2013) 196 (cit. on pp. 1, 2, 67).

[5] Q. Cheng et al., *Observation of anomalous π modes in photonic Floquet engineering*, Physical review letters **122** (2019) 173901 (cit. on pp. 1, 2, 119).

[6] R. Fleury, A. B. Khanikaev and A. Alu, *Floquet topological insulators for sound*, Nature communications **7** (2016) 1 (cit. on p. 1).

[7] H. Lignier et al., *Dynamical control of matter-wave tunneling in periodic potentials*, Physical review letters **99** (2007) 220403 (cit. on p. 1).

[8] S. Longhi et al., *Observation of dynamic localization in periodically curved waveguide arrays*, Physical review letters **96** (2006) 243901 (cit. on pp. 1, 39).

[9] M. Aidelsburger et al., *Measuring the Chern number of Hofstadter bands with ultracold bosonic atoms*, Nature Physics **11** (2015) 162 (cit. on p. 1).

[10] F. Cardano et al., *Statistical moments of quantum-walk dynamics reveal topological quantum transitions*, Nature communications **7** (2016) 1 (cit. on p. 1).

[11] M. Moskalets and M. Büttiker, *Floquet scattering theory of quantum pumps*, Physical Review B **66** (2002) 205320 (cit. on p. 1).

[12] S. A. Reyes et al., *Transport through an AC-driven impurity: Fano interference and bound states in the continuum*, New Journal of Physics **19** (2017) 043029 (cit. on p. 1).

[13] D. Thuberg et al., *Perfect spin filter by periodic drive of a ferromagnetic quantum barrier*, Physical review letters **119** (2017) 267701 (cit. on p. 1).

[14] M. S. Rudner and N. H. Lindner,
Band structure engineering and non-equilibrium dynamics in Floquet topological insulators,
Nature reviews physics **2** (2020) 229 (cit. on p. 1).

[15] P. Titum et al.,
Anomalous Floquet-Anderson insulator as a nonadiabatic quantized charge pump,
Physical Review X **6** (2016) 021013 (cit. on pp. 1, 3, 75, 83).

[16] K. v. Klitzing, G. Dorda and M. Pepper, *New method for high-accuracy determination of the fine-structure constant based on quantized Hall resistance*,
Physical review letters **45** (1980) 494 (cit. on p. 1).

[17] B. I. Halperin, *Quantized Hall conductance, current-carrying edge states, and the existence of extended states in a two-dimensional disordered potential*, Physical Review B **25** (1982) 2185 (cit. on p. 1).

[18] D. J. Thouless et al., *Quantized Hall conductance in a two-dimensional periodic potential*,
Physical review letters **49** (1982) 405 (cit. on p. 1).

[19] J. E. Moore, *The birth of topological insulators*, Nature **464** (2010) 194 (cit. on pp. 1, 2, 14).

[20] M. Sato and Y. Ando, *Topological superconductors: a review*,
Reports on Progress in Physics **80** (2017) 076501 (cit. on p. 1).

[21] B. Yan and C. Felser, *Topological materials: Weyl semimetals*,
Annual Review of Condensed Matter Physics **8** (2017) 337 (cit. on p. 1).

[22] M. Freedman et al., *Topological quantum computation*,
Bulletin of the American Mathematical Society **40** (2003) 31 (cit. on p. 2).

[23] Z. Yang et al., *Topological acoustics*, Physical review letters **114** (2015) 114301 (cit. on p. 2).

[24] L. Lu, J. D. Joannopoulos and M. Soljačić, *Topological photonics*,
Nature photonics **8** (2014) 821 (cit. on pp. 2, 51).

[25] D. N. Christodoulides, F. Lederer and Y. Silberberg,
Discretizing light behaviour in linear and nonlinear waveguide lattices,
Nature **424** (2003) 817 (cit. on pp. 2, 39).

[26] S. Longhi, *Quantum-optical analogies using photonic structures*,
Laser & Photonics Reviews **3** (2009) 243 (cit. on p. 2).

[27] Y. Chen et al., *Tight-binding model in optical waveguides: Design principle and transferability for simulation of complex photonics networks*,
Physical Review A **104** (2021) 023501 (cit. on p. 2).

[28] F. Bleckmann et al.,
Spectral imaging of topological edge states in plasmonic waveguide arrays,
Physical Review B **96** (2017) 045417 (cit. on pp. 2, 57, 70, 72).

[29] Z. Cherpakova et al., *Transverse Anderson localization of surface plasmon polaritons*,
Optics Letters **42** (2017) 2165 (cit. on p. 2).

[30] H. Trompeter et al., *Visual observation of Zener tunneling*,
Physical review letters **96** (2006) 023901 (cit. on pp. 2, 39).

[31] M. Segev, Y. Silberberg and D. N. Christodoulides, *Anderson localization of light*, Nature Photonics **7** (2013) 197 (cit. on pp. 2, 39).

[32] A. Block et al., *Bloch oscillations in plasmonic waveguide arrays*, Nature communications **5** (2014) 1 (cit. on p. 2).

[33] F. Dreisow et al., *Spectral resolved dynamic localization in curved fs laser written waveguide arrays*, Optics express **16** (2008) 3474 (cit. on p. 2).

[34] A. M. Essin and V. Gurarie, *Bulk-boundary correspondence of topological insulators from their respective Green's functions*, Physical Review B **84** (2011) 125132 (cit. on pp. 2, 58).

[35] O. Balabanov and H. Johannesson, *Robustness of symmetry-protected topological states against time-periodic perturbations*, Physical Review B **96** (2017) 035149 (cit. on pp. 2, 61).

[36] D. Thouless, *Quantization of particle transport*, Physical Review B **27** (1983) 6083 (cit. on pp. 2, 14, 75).

[37] S. Nakajima et al., *Topological Thouless pumping of ultracold fermions*, Nature Physics **12** (2016) 296 (cit. on pp. 3, 80).

[38] M. Lohse et al., *A Thouless quantum pump with ultracold bosonic atoms in an optical superlattice*, Nature Physics **12** (2016) 350 (cit. on pp. 3, 80).

[39] L. Privitera et al., *Nonadiabatic breaking of topological pumping*, Physical review letters **120** (2018) 106601 (cit. on pp. 3, 75, 82, 83).

[40] D. Linzner et al., *Reservoir-induced Thouless pumping and symmetry-protected topological order in open quantum chains*, Physical Review B **94** (2016) 201105 (cit. on p. 3).

[41] N. H. Lindner, E. Berg and M. S. Rudner, *Universal chiral quasisteady states in periodically driven many-body systems*, Physical Review X **7** (2017) 011018 (cit. on pp. 3, 75, 83).

[42] S. Longhi, D. Gatti and G. Della Valle, *Robust light transport in non-Hermitian photonic lattices*, Scientific reports **5** (2015) 1 (cit. on p. 3).

[43] Z. Lin et al., *Unidirectional invisibility induced by P T-symmetric periodic structures*, Physical Review Letters **106** (2011) 213901 (cit. on p. 3).

[44] L. Feng et al., *Experimental demonstration of a unidirectional reflectionless parity-time metamaterial at optical frequencies*, Nature materials **12** (2013) 108 (cit. on p. 3).

[45] T. E. Lee, *Anomalous edge state in a non-Hermitian lattice*, Physical review letters **116** (2016) 133903 (cit. on p. 3).

[46] D. Leykam et al., *Edge modes, degeneracies, and topological numbers in non-Hermitian systems*, Physical review letters **118** (2017) 040401 (cit. on p. 3).

[47] S. Malzard, C. Poli and H. Schomerus, *Topologically protected defect states in open photonic systems with non-Hermitian charge-conjugation and parity-time symmetry*, Physical review letters **115** (2015) 200402 (cit. on p. 3).

[48] M. S. Rudner and L. Levitov, *Topological transition in a non-hermitian quantum walk*, Physical review letters **102** (2009) 065703 (cit. on p. 3).

[49] T. Ozawa and I. Carusotto, *Anomalous and quantum Hall effects in lossy photonic lattices*, Physical review letters **112** (2014) 133902 (cit. on p. 3).

[50] C. M. Bender et al., *Faster than Hermitian quantum mechanics*, Physical Review Letters **98** (2007) 040403 (cit. on pp. 3, 84).

[51] S. Ibáñez et al., *Shortcuts to adiabaticity for non-Hermitian systems*, Physical Review A **84** (2011) 023415 (cit. on pp. 3, 84, 87).

[52] B. T. Torosov, G. Della Valle and S. Longhi, *Non-Hermitian shortcut to adiabaticity*, Physical Review A **87** (2013) 052502 (cit. on pp. 3, 84).

[53] S. Denisov, S. Flach and P. Hänggi, *Tunable transport with broken space–time symmetries*, Physics Reports **538** (2014) 77 (cit. on pp. 3, 101).

[54] M. Smoluchowski, *Experimentell nachweisbare, der üblichen Thermodynamik widersprechende Molekularphänomene*, Pisma Mariana Smoluchowskiego **2** (1927) 226 (cit. on p. 3).

[55] R. P. Feynman, R. B. Leighton and M. Sands, *The feynman lectures on physics; vol. i*, American Journal of Physics **33** (1965) 750 (cit. on p. 3).

[56] G. Mahmud et al., *Directing cell motions on micropatterned ratchets*, Nature physics **5** (2009) 606 (cit. on pp. 3, 101).

[57] V. Serreli et al., *A molecular information ratchet*, Nature **445** (2007) 523 (cit. on pp. 3, 101).

[58] H. Linke et al., *Experimental tunneling ratchets*, Science **286** (1999) 2314 (cit. on p. 3).

[59] M. V. Costache and S. O. Valenzuela, *Experimental spin ratchet*, Science **330** (2010) 1645 (cit. on p. 3).

[60] C. Drexler et al., *Magnetic quantum ratchet effect in graphene*, Nature nanotechnology **8** (2013) 104 (cit. on p. 3).

[61] J. Lehmann et al., *Molecular wires acting as coherent quantum ratchets*, Physical review letters **88** (2002) 228305 (cit. on p. 3).

[62] C. Zhang, C.-F. Li and G.-C. Guo, *Experimental demonstration of photonic quantum ratchet*, Science Bulletin **60** (2015) 249 (cit. on p. 3).

[63] F. Dreisow et al., *Spatial light rectification in an optical waveguide lattice*, EPL (Europhysics Letters) **101** (2013) 44002 (cit. on pp. 3, 97, 101, 103).

[64] T. Salger et al., *Directed transport of atoms in a Hamiltonian quantum ratchet*, Science **326** (2009) 1241 (cit. on pp. 3, 101).

[65] J. Ni et al., *Hamiltonian Ratchets with Ultra-Cold Atoms*, Annalen der Physik **529** (2017) 1600335 (cit. on pp. 3, 101).

[66] S. Denisov et al., *Periodically driven quantum ratchets: Symmetries and resonances*, Physical Review A **75** (2007) 063424 (cit. on pp. 3, 101).

[67] J. Gong, D. Poletti and P. Hanggi, *Dissipationless directed transport in rocked single-band quantum dynamics*, Physical Review A **75** (2007) 033602 (cit. on pp. 3, 101).

[68] S. A. Maier, *Plasmonics: fundamentals and applications*, Springer Science & Business Media, 2007 (cit. on pp. 21, 23, 25–28).

[69] J. D. Jackson, *Electrodynamics*, Wiley Online Library, 1975 (cit. on pp. 21, 22).

[70] M. Dresselhaus, *Solid state physics part ii optical properties of solids*, Lecture Notes (Massachusetts Institute of Technology, Cambridge, MA) **17** (2001) (cit. on p. 23).

[71] P. B. Johnson and R.-W. Christy, *Optical constants of the noble metals*, Physical review B **6** (1972) 4370 (cit. on p. 23).

[72] M. L. Brongersma and P. G. Kik, *Surface plasmon nanophotonics*, vol. 131, Springer, 2007 (cit. on p. 24).

[73] F. von Cube et al., *Spatio-spectral characterization of photonic meta-atoms with electron energy-loss spectroscopy*, Optical Materials Express **1** (2011) 1009 (cit. on p. 24).

[74] A. Vial and T. Laroche, *Description of dispersion properties of metals by means of the critical points model and application to the study of resonant structures using the FDTD method*, Journal of Physics D: Applied Physics **40** (2007) 7152 (cit. on p. 24).

[75] H. Raether, "Surface plasmons on smooth surfaces", *Surface plasmons on smooth and rough surfaces and on gratings*, Springer, 1988 4 (cit. on pp. 27–29, 33).

[76] E. Kretschmann, *Die bestimmung optischer konstanten von metallen durch anregung von oberflächenplasmaschwingungen*, Zeitschrift für Physik A Hadrons and nuclei **241** (1971) 313 (cit. on p. 27).

[77] A. Otto, *Excitation of nonradiative surface plasma waves in silver by the method of frustrated total reflection*, Zeitschrift für Physik A Hadrons and nuclei **216** (1968) 398 (cit. on p. 27).

[78] J. R. Lakowicz, *Radiative decay engineering 3. Surface plasmon-coupled directional emission*, Analytical biochemistry **324** (2004) 153 (cit. on p. 27).

[79] B. Hecht et al., *Local excitation, scattering, and interference of surface plasmons*, Physical review letters **77** (1996) 1889 (cit. on p. 27).

[80] S. I. Bozhevolnyi, I. I. Smolyaninov and A. V. Zayats, *Near-field microscopy of surface-plasmon polaritons: Localization and internal interface imaging*, Physical review B **51** (1995) 17916 (cit. on p. 28).

[81] A. Drezet et al., *Leakage radiation microscopy of surface plasmon polaritons*, Materials science and engineering: B **149** (2008) 220 (cit. on pp. 28, 29).

[82] E. Hecht, *Optics, 4th editio ed*, Addison-Wesley, San Francisco **2** (2002) 3 (cit. on p. 29).

[83] Z. Han and S. I. Bozhevolnyi, *Radiation guiding with surface plasmon polaritons*, Reports on Progress in Physics **76** (2012) 016402 (cit. on p. 30).

[84] S. A. Maier et al., *Local detection of electromagnetic energy transport below the diffraction limit in metal nanoparticle plasmon waveguides*, Nature materials **2** (2003) 229 (cit. on p. 30).

[85] K. Okamoto, *Fundamentals of optical waveguides*, Academic press, 2006 (cit. on pp. 30–34).

[86] J. Grandidier et al., *Dielectric-loaded surface plasmon polariton waveguides: figures of merit and mode characterization by image and Fourier plane leakage microscopy*, Physical Review B **78** (2008) 245419 (cit. on pp. 30–32).

[87] J.-M. Jin, *The finite element method in electromagnetics*, John Wiley & Sons, 2015 (cit. on p. 31).

[88] T. Holmgaard and S. I. Bozhevolnyi, *Theoretical analysis of dielectric-loaded surface plasmon-polariton waveguides*, Physical Review B **75** (2007) 245405 (cit. on pp. 32, 33).

[89] F. Bleckmann, *Controlling surface plasmon polaritons with dielectric nanostructures*, PhD thesis: Rheinischen Friedrich-Wilhelms-Universität Bonn, Mathematisch-Naturwissenschaftliche Fakultät, 2016 (cit. on pp. 32, 37).

[90] W.-P. Huang, *Coupled-mode theory for optical waveguides: an overview*, JOSA A **11** (1994) 963 (cit. on p. 33).

[91] A. Yariv and P. Yeh, *Photonics: optical electronics in modern communications (the oxford series in electrical and computer engineering)*, Oxford University Press, Inc., 2006 (cit. on p. 33).

[92] S.-L. Chuang, *A coupled-mode theory for multiwaveguide systems satisfying the reciprocity theorem and power conservation*, Journal of lightwave technology **5** (1987) 174 (cit. on p. 36).

[93] Z. Cherpakova, *Simulation of 1D tight binding systems with plasmonic waveguide arrays*, MA thesis: Rheinischen Friedrich-Wilhelms-Universität Bonn, Mathematisch-Naturwissenschaftliche Fakultät, 2017 (cit. on pp. 36, 44, 45, 50, 110).

[94] I. L. Garanovich et al., *Light propagation and localization in modulated photonic lattices and waveguides*, Physics Reports **518** (2012) 1 (cit. on p. 37).

[95] J. J. Quinn and K.-S. Yi, *Solid state physics: principles and modern applications*, Springer Science & Business Media, 2009 (cit. on pp. 6, 7).

[96] M. P. Marder, *Condensed matter physics*, John Wiley & Sons, 2010 (cit. on pp. 6, 7).

[97] S.-Q. Shen, *Topological insulators*, vol. 174, Springer, 2012 (cit. on p. 7).

[98] T. Ozawa et al., *Topological photonics*, Reviews of Modern Physics **91** (2019) 015006 (cit. on p. 39).

[99] T. Dittrich et al., *Quantum transport and dissipation*, vol. 3, Wiley-Vch Weinheim, 1998 (cit. on p. 10).

[100] H. Sambe,
Steady states and quasienergies of a quantum-mechanical system in an oscillating field,
Physical Review A **7** (1973) 2203 (cit. on p. 10).

[101] T. Oka and S. Kitamura, *Floquet engineering of quantum materials*,
Annual Review of Condensed Matter Physics **10** (2019) 387 (cit. on p. 11).

[102] A. Gómez-León and G. Platero,
Floquet-Bloch theory and topology in periodically driven lattices,
Physical review letters **110** (2013) 200403 (cit. on pp. 11, 13).

[103] M. Z. Hasan and C. L. Kane, *Colloquium: topological insulators*,
Reviews of modern physics **82** (2010) 3045 (cit. on pp. 14, 51).

[104] S. M. Girvin and K. Yang, *Modern condensed matter physics*,
Cambridge University Press, 2019 (cit. on pp. 14, 17).

[105] L. Fu and C. L. Kane, *Superconducting proximity effect and Majorana fermions at the surface of a topological insulator*, Physical review letters **100** (2008) 096407 (cit. on p. 14).

[106] J. K. Asbóth, L. Oroszlány and A. Pályi, *A short course on topological insulators*,
Lecture notes in physics **919** (2016) 997 (cit. on pp. 15, 17, 20, 52, 55, 57, 58, 77).

[107] J. Zak, *Berry's phase for energy bands in solids*, Physical review letters **62** (1989) 2747
(cit. on p. 16).

[108] P. Delplace, D. Ullmo and G. Montambaux,
Zak phase and the existence of edge states in graphene, Physical Review B **84** (2011) 195452
(cit. on pp. 16, 54).

[109] S. Yao, Z. Yan and Z. Wang, *Topological invariants of Floquet systems: General formulation, special properties, and Floquet topological defects*, Physical Review B **96** (2017) 195303
(cit. on p. 18).

[110] J. Cayssol et al., *Floquet topological insulators*,
physica status solidi (RRL)–Rapid Research Letters **7** (2013) 101 (cit. on p. 18).

[111] T. Oka and H. Aoki, *Photovoltaic Hall effect in graphene*,
Physical Review B **79** (2009) 081406 (cit. on p. 18).

[112] T. Kitagawa et al., *Transport properties of nonequilibrium systems under the application of light: Photoinduced quantum Hall insulators without Landau levels*,
Physical Review B **84** (2011) 235108 (cit. on p. 18).

[113] N. H. Lindner, G. Refael and V. Galitski,
Floquet topological insulator in semiconductor quantum wells, Nature Physics **7** (2011) 490
(cit. on p. 18).

[114] M. S. Rudner et al., *Anomalous edge states and the bulk-edge correspondence for periodically driven two-dimensional systems*, Physical Review X **3** (2013) 031005 (cit. on pp. 18, 66).

[115] C.-K. Chiu et al., *Classification of topological quantum matter with symmetries*,
Reviews of Modern Physics **88** (2016) 035005 (cit. on pp. 18, 19).

[116] A. Kitaev, "Periodic table for topological insulators and superconductors", *AIP conference proceedings*, vol. 1134, 1, American Institute of Physics, 2009 22 (cit. on pp. 18, 51).

[117] S. Ryu et al., *Topological insulators and superconductors: tenfold way and dimensional hierarchy*, New Journal of Physics **12** (2010) 065010 (cit. on p. 18).

[118] A. Altland and M. R. Zirnbauer, *Nonstandard symmetry classes in mesoscopic normal-superconducting hybrid structures*, Physical Review B **55** (1997) 1142 (cit. on p. 19).

[119] B. A. Bernevig, *Topological insulators and topological superconductors*, Princeton university press, 2013 (cit. on pp. 19, 79).

[120] R. Roy and F. Harper, *Periodic table for Floquet topological insulators*, Physical Review B **96** (2017) 155118 (cit. on p. 20).

[121] J. K. Asbóth, B. Tarasinski and P. Delplace, *Chiral symmetry and bulk-boundary correspondence in periodically driven one-dimensional systems*, Physical Review B **90** (2014) 125143 (cit. on p. 20).

[122] C. Vieu et al., *Electron beam lithography: resolution limits and applications*, Applied surface science **164** (2000) 111 (cit. on p. 41).

[123] K. M. McPeak et al., *Plasmonic films can easily be better: rules and recipes*, ACS photonics **2** (2015) 326 (cit. on p. 42).

[124] R. O'handley et al., *Residual gas and the optical properties of silver films*, Surface Science **50** (1975) 407 (cit. on p. 42).

[125] S. Popov, *Plasmonische Wellenleiter auf Basis dünner Silberfilme*, BA thesis: Rheinischen Friedrich-Wilhelms-Universität Bonn, Mathematisch-Naturwissenschaftliche Fakultät, 2019 (cit. on p. 42).

[126] I. Zailer et al., *Crosslinked PMMA as a high-resolution negative resist for electron beam lithography and applications for physics of low-dimensional structures*, Semiconductor science and technology **11** (1996) 1235 (cit. on pp. 43, 44).

[127] A. Hoole, M. Welland and A. Broers, *Negative PMMA as a high-resolution resist-the limits and possibilities*, Semiconductor science and technology **12** (1997) 1166 (cit. on p. 43).

[128] A. Broers, A. Hoole and J. Ryan, *Electron beam lithography—Resolution limits*, Microelectronic Engineering **32** (1996) 131 (cit. on p. 45).

[129] W. Hu et al., *Sub-10 nm electron beam lithography using cold development of poly (methylmethacrylate)*, Journal of Vacuum Science & Technology B: Microelectronics and Nanometer Structures Processing, Measurement, and Phenomena **22** (2004) 1711 (cit. on p. 45).

[130] R. Wagner et al., *Back focal plane imaging spectroscopy of photonic crystals*, Applied Physics Letters **101** (2012) 081904 (cit. on p. 47).

[131] J. A. Kurvits, M. Jiang and R. Zia,
Comparative analysis of imaging configurations and objectives for Fourier microscopy,
JOSA A **32** (2015) 2082 (cit. on p. 48).

[132] A. Drezet et al., *How to erase surface plasmon fringes*,
Applied Physics Letters **89** (2006) 091117 (cit. on p. 50).

[133] T. Zhang et al.,
Experimental demonstration of topological surface states protected by time-reversal symmetry,
Physical Review Letters **103** (2009) 266803 (cit. on p. 51).

[134] P. Dziawa et al., *Topological crystalline insulator states in Pb 1- x Sn x Se*,
Nature materials **11** (2012) 1023 (cit. on p. 51).

[135] M. Leder et al., *Real-space imaging of a topologically protected edge state with ultracold atoms in an amplitude-chirped optical lattice*, Nature communications **7** (2016) 1
(cit. on p. 51).

[136] V. Dal Lago, M. Atala and L. F. Torres,
Floquet topological transitions in a driven one-dimensional topological insulator,
Physical Review A **92** (2015) 023624 (cit. on pp. 51, 65, 119).

[137] M. Fruchart, *Complex classes of periodically driven topological lattice systems*,
Physical Review B **93** (2016) 115429 (cit. on pp. 51, 61).

[138] Z. Fedorova et al., *Limits of topological protection under local periodic driving*,
Light: Science & Applications **8** (2019) 1 (cit. on pp. 51, 72).

[139] W. Su, J. Schrieffer and A. J. Heeger, *Solitons in polyacetylene*,
Physical review letters **42** (1979) 1698 (cit. on p. 52).

[140] X.-G. Wen, *Symmetry-protected topological phases in noninteracting fermion systems*,
Physical Review B **85** (2012) 085103 (cit. on p. 59).

[141] K. Thyagarajan, M. Shenoy and A. K. Ghatak, *Accurate numerical method for the calculation of bending loss in optical waveguides using a matrix approach*, Optics letters **12** (1987) 296
(cit. on p. 69).

[142] R. Li and M. Fleischhauer,
Finite-size corrections to quantized particle transport in topological charge pumps,
Physical Review B **96** (2017) 085444 (cit. on p. 75).

[143] Z. Fedorova et al.,
Observation of topological transport quantization by dissipation in fast Thouless pumps,
Nature communications **11** (2020) 1 (cit. on pp. 76, 88, 89).

[144] M. Rice and E. Mele, *Elementary excitations of a linearly conjugated diatomic polymer*,
Physical Review Letters **49** (1982) 1455 (cit. on p. 76).

[145] W. Kohn, *Analytic properties of Bloch waves and Wannier functions*,
Physical Review **115** (1959) 809 (cit. on p. 77).

[146] D. Vanderbilt, *Berry Phases in Electronic Structure Theory: Electric Polarization, Orbital Magnetization and Topological Insulators*, Cambridge University Press, 2018 (cit. on p. 79).

[147] W.-K. Shih and Q. Niu, *Nonadiabatic particle transport in a one-dimensional electron system*, Physical Review B **50** (1994) 11902 (cit. on p. 82).

[148] A. Schnell, A. Eckardt and S. Denisov, *Is there a Floquet lindbladian?*, Physical Review B **101** (2020) 100301 (cit. on p. 86).

[149] D. C. Brody, *Biorthogonal quantum mechanics*, Journal of Physics A: Mathematical and Theoretical **47** (2013) 035305 (cit. on pp. 86, 87).

[150] J. E. Avron and Z. Kons, *Quantum response at finite fields and breakdown of Chern numbers*, Journal of Physics A: Mathematical and General **32** (1999) 6097 (cit. on p. 90).

[151] S. Longhi, *Rectification of light refraction in curved waveguide arrays*, Optics letters **34** (2009) 458 (cit. on p. 97).

[152] Z. Fedorova et al., *Dissipation engineered directional filter for quantum ratchets*, Physical Review Research **3** (2021) 013260 (cit. on pp. 102, 104, 107, 108).

[153] W. Song et al., *Breakup and recovery of topological zero modes in finite non-Hermitian optical lattices*, Physical review letters **123** (2019) 165701 (cit. on p. 108).

[154] M. Jürgensen, S. Mukherjee and M. C. Rechtsman, *Quantized nonlinear Thouless pumping*, Nature **596** (2021) 63 (cit. on p. 120).

[155] K. Takata and M. Notomi, *Photonic topological insulating phase induced solely by gain and loss*, Physical review letters **121** (2018) 213902 (cit. on p. 120).

[156] Z. Turker, S. Tombuloglu and C. Yuce, *PT symmetric Floquet topological phase in SSH model*, Physics Letters A **382** (2018) 2013 (cit. on p. 120).

[157] S. Wu et al., *Floquet π mode engineering in non-Hermitian waveguide lattices*, Physical Review Research **3** (2021) 023211 (cit. on p. 120).

[158] T. Rakovszky, J. K. Asbóth and A. Alberti, *Detecting topological invariants in chiral symmetric insulators via losses*, Physical Review B **95** (2017) 201407 (cit. on p. 120).

[159] M. Kauranen and A. V. Zayats, *Nonlinear plasmonics*, Nature photonics **6** (2012) 737 (cit. on p. 120).

[160] G. Li, C. M. De Sterke and S. Palomba, *Fundamental limitations to the ultimate Kerr nonlinear performance of plasmonic waveguides*, ACS Photonics **5** (2018) 1034 (cit. on p. 120).

[161] R. Dubey et al., *Experimental investigation of the propagation properties of Bloch surface waves on dielectric multilayer platform*, Journal of the European Optical Society-Rapid Publications **13** (2017) 1 (cit. on p. 120).

[162] D. Aurelio and M. Liscidini, *Electromagnetic field enhancement in Bloch surface waves*, Physical Review B **96** (2017) 045308 (cit. on p. 120).

[163] T. Sfez et al., *Bloch surface waves in ultrathin waveguides: near-field investigation of mode polarization and propagation*, JOSA B **27** (2010) 1617 (cit. on p. 120).

[164] K. A. Abrashitova et al.,
Bloch surface wave photonic device fabricated by femtosecond laser polymerisation technique,
Applied Sciences **8** (2018) 63 (cit. on p. 120).

[165] K. R. Safronov et al., *Multimode interference of Bloch surface electromagnetic waves*,
ACS nano **14** (2020) 10428 (cit. on p. 120).

[166] Q. Guo et al.,
Efficient Frequency Mixing of Guided Surface Waves by Atomically Thin Nonlinear Crystals,
Nano Letters **20** (2020) 7956 (cit. on p. 120).

Publications

Parts of this thesis have already been published in refereed scientific journals:

- Z. Fedorova, C. Jörg, C. Dauer, F. Letscher, M. Fleischhauer, S. Eggert, S. Linden and G. von Freymann *Limits of topological protection under local periodic driving*, Light: Science & Applications **8**.1 (2019) 1–12, DOI: 10.1038/s41377-019-0172-8
- Z. Fedorova, H. Qiu, S. Linden, and J. Kroha *Observation of topological transport quantization by dissipation in fast Thouless pumps*, Nature communications, **11**.1, (2020) 1–10, DOI: 10.1038/s41467-020-17510-z
- Z. Fedorova, C. Dauer, A. Sidorenko, S. Eggert, J. Kroha, and S. Linden *Dissipation engineered directional filter for quantum ratchets*, Physical Review Research, **3**.1 (2021) 013260, DOI: 10.1103/PhysRevResearch.3.013260

Acknowledgements

I want to acknowledge all the people who have supported me during my doctoral studies in Bonn and without whom this thesis would not have been possible.
First of all, I would like to express my deepest appreciation to my first supervisor Prof. Stefan Linden for his continuous support that is hard to overestimate and unwavering belief in me as a scientist. It is an honor to work in his group and I am looking forward to our further collaboration.
I would also like to extend my sincere gratitude to Prof. Johann Kroha for his invaluable contribution to the theoretical part of my work and for agreeing to be the second reviewer of my thesis. Furthermore, I am extremely grateful to Prof. Dieter Meschede and Prof. Peter Vöhringer for joining the doctoral committee. My special thanks also go to Prof. Michael Fleischhauer and Prof. Sebastian Eggert for giving me helpful advice and precious insight into Floquet theory and topology.
I would like to thank all the people from the collaborative research center OSCAR for interesting symposia, useful teaching activities, and, what is most important, creating a very friendly atmosphere that favored fruitful discussions and collaborations. I gratefully acknowledge the PhD students from OSCAR working with whom was a great pleasure: Christina Jörg, Christoph Dauer, and Haixin Qiu. Our collaboration within each project undoubtedly has put my research to a much higher level.
I would like to thank all the present and former members of the nanophotonic group of Prof. Linden, who worked with me side by side during my doctoral studies. Many thanks go to my fellow PhD students: Mike Prämassing, Till Leuteritz, Lok-Yee Yan, Alexander Faßbender, and Yuhao Zhang for a supportive environment in the group and for the exciting work trips where we have been together. I also had great pleasure of working with master and bachelor students who have contributed to my topic: Anna Sidorenko, Helene Wetter, and Stefan Popov.
I very much appreciate all the proof readers of my thesis for their valuable comments and suggestions that helped me to improve the quality of this work.
Finally, I would like to thank my family and my close friends for their unfailing love and support.